Narrow Gap Laser Welding of 316L Stainless Steel for Potential Application in the Manufacture of Thick Section Nuclear Components

A thesis submitted to The University of Manchester for the degree of

Doctor of Philosophy

in the Faculty of Engineering and Physical Sciences

2013

Ahmed Selim Ebrahim Elmesalamy

School of Mechanical, Aerospace and Civil Engineering
The University of Manchester

Abstract

Thick-section austenitic stainless steels have widespread industrial applications, especially in nuclear power plants. The joining methods used in the nuclear industry are primarily based on arc welding processes. However, it has recently been shown that the Narrow Gap Laser Welding (NGLW) technique can be used to join materials with thicknesses that are well beyond the capabilities of single pass autogenous laser welding. The heat input for NGLW is much lower than that of arc welding, as are the expected levels of residual stress and distortion.

The multi-pass laser welding technique, based on the narrow gap approach, is an emerging welding technology which can be applied to thick-section welds using a relatively low-power laser, but the process is more complicated than autogenous laser welding, since it is necessary to introduce filler wire to narrow gap weld configurations. Despite this complexity, the technique is very promising for improving the penetration capabilities of the laser welding process. However a limited amount of research has been conducted on the development of the NGLW technique; the control and optimization of weld bead quality inside the narrow gap is still an area of weakness.

The research described in this thesis involves investigations on NGLW of AISI grade 316L austenitic stainless steel, and the performance of the resulting welds. Design-of-experiments and statistical modelling techniques were employed to understand and optimize the welding process. A statistical model was used in order to understand the significant process parameters and their interactions, allowing improved control of the weld quality in ultra-narrow gap (1.5 mm gap width) welds. The results show a significant improvement in weld quality can be achieved through the use of statistical modelling and multi-variable optimisation.

The microstructure characteristics and mechanical properties (e.g. tensile strengths, fatigue, bending strength and fracture toughness) of the NGLW samples were examined and compared with those of other welding techniques - autogenous laser welding and gas-tungsten arc welding (GTAW). The work shows that NGLW of 316L steel sheets up to 20 mm thickness have generally better or comparable mechanical properties than those of GTAW but with much higher welding productivity.

The results of detailed investigations of the 2D residual stress distributions, material distortions, and plastic strain characteristics of the NGLW technique are described. The contour method was employed for residual stress evaluation of the NGLW technique, and the results were validated using X-Ray and neutron diffraction measurements. The results were compared with those obtained with GTAW. The results suggest that the longitudinal tensile residual stresses in NGLW joints are 30-40% lower than those for GTAW joints.

The influence of the laser power and number of passes for the NGLW technique, on the developed residual stress and plastic strain has been investigated, and the influence of welding strategy and the use of restraint during welding were also investigated.

To understand the thermal history in NGLW and its effect on residual stress, finite element analysis was carried out using ABAQUS to numerically model the behaviour of residual stress across the multipass NGLW weld joints. The model has been validated with the experiments using temperature measurements and in terms of residual stresses the model is compared with neutron diffraction and the contour method. There is a very good correlation between the model and experimental results. The influence of both the laser power and welding speed on the induced residual stress during the NGLW process was also investigated using the model.

The aqueous, pitting and stress corrosion cracking behaviour of the NGLW joints were investigated, and the results compared to those for GTAW joints under the same conditions. The results show that NGLW joints have better resistance to pitting corrosion than the GTA welds. Preliminary results also suggest that NGLW has better resistance to stress corrosion cracking.

Table of contents

List of Tables

List of Figures

ABBREVIATIONS

ANOVA	:	Analysis of variance
AR	:	As received conditions
AWI	:	Abaqus welding interface
BWR	:	Boiling water reactors
CAE	:	Computer aided engineering
CCD	:	central composite design
CMM	:	Coordinate measuring machine
DHD	:	Deep-hole drilling
EAC	:	Environmental assisted cracking
EDM	:	Electrical Discharge Machining
EDS	:	Energy Dispersive Spectroscopy
EBW	:	Electron Beam Welding
FCAW	:	Flux cored arc welding
GDOES	:	Glow-discharge optical emission spectroscopy
GTAW	:	Gas tungsten arc welding
ILW	:	Intermediate level radioactive waste
LBW	:	laser beam welding
NGLW	:	Narrow gap laser welding
OCP	:	Open circuit potential
PPM	:	Part per million
PREN	:	Pitting resistance equivalent numbers
PSD	:	position sensitive detector

PWR	:	Pressurized water reactors
RSM	:	Response surface methodology
SALSA	:	Strain Analyser for Large and Small scale engineering Applications
SAW	:	Submerged arc welding
SCC	:	Stress corrosion cracking
SCE	:	Saturated calomel electrode
SEM	:	Scanning electron microscope
SSRT	:	Slow strain rate test
SMAW	:	shielded metal arc welding
TEM	:	Transverse electromagnetic modes
TIG	:	Tungsten inert gas welding
VTR	:	Video tap recording
WRC	:	Welding Research Council
XRD	:	X-ray diffraction

NOMENCLATURE

A	Wire current
B	Stern–Geary constant
c	Speed of light
C	Specific heat
C_p	Thermal capacity
Cr_{eq}	Chromium equivalent
D	Beam diameter on the lens
d_{min}	focused beam diameter
d_i	individual desirability
E	Elastic modulus
E_i	Ionization potential for the neutral atoms
$d_{L(x, y)}$	Longitudinal lattice spacing at point (x, y)
$d_{ref(x, y)}$	Stress-free lattice spacing at point (x, y)
F	Faraday's constant
f	focal length of the lens
g_o	Degeneracy factors of neutral atoms
g_e	Degeneracy factors of electrons
$g_{i,}$	Degeneracy factors of ions
h	Planck constant
h_c	Convective heat-transfer coefficient
I_a	Attenuated laser beam intensity
$I_\circ$	Initial laser beam intensity

i_o	Corrosion current
k	Boltzmann constant
k_x, k_y, k_z	Thermal conductivities in the x, y and z directions
L_p	Length of plasma
M^2	Beam quality
m_e	Electron mass
N	Atomic mass
n	Number of free electrons per atom
N_o	Densities of neutral atoms
N_e	Densities of electrons
N_i	Densities of ions
Ni_{eq}	Nickel equivalent
p	Laser power
r	Laser beam radius
r_f	Reflectivity of the surface
R_P	polarization resistance
T	Current temperature
T_e	Electron temperature
T_m	Melting temperature
ρ	Density of the material
v	welding speed
$\varepsilon_{L\,(x,y)}$	Longitudinal strain component at point (x, y)
$\varepsilon_{N\,(x,y)}$	Normal strain component at point (x, y)

$\varepsilon_{T\,(x,y)}$	Transverse strain component at point (x, y)
$\sigma_{L(x,y)}$	Longitudinal stress component at point (x, y)
$\sigma_{N(x,y)}$	Normal stress component at point (x, y)
$\sigma_{T\,(x,y)}$	Transverse stress component at point (x, y)
v	Poisson's ratio
θ_o	Laser beam divergence angle
$\boldsymbol{\upsilon}$	frequency of emitted photon
λ	Beam wavelength
α	half of the divergence angle
$\omega_{\circ}$	radius of beam waist
ξ	Total desirability

DECLARATION

No portion of the work referred to in the thesis has been submitted in support of an application for another degree or qualification of this or any other university or other institute of learning.

COPYRIGHT

DEDICATION

For my parents

My loving mother – Nabila Ebrahim
My dear father – Selim Elmesalamy

And my small family

Acknowledgments

Firstly, I wish to give all praise to Almighty God for giving me the strength to complete this research.

I wish to express my deepest gratitude to my supervisors, Professor Lin Li and Dr John Francis. They have been always there, ready and happy to help. Their encouragement, guidance, helpful advice comments and suggestions during the undertaking of this research enabled me to develop an understanding of the subject and to gain a good experience.

I wish to thank all Laser Processing Research Centre (LPRC) group members at Manchester for providing cooperative environments and wonderful times.

I wish to thank my entire extended family for the sincere support and the supporting environment they provided.

Last but not least, this study would not have been possible without the financial support of my sponsor, the Egyptian Ministry of Defence. I would like to express my gratitude for giving me this precious opportunity to learn.

Publications

Some of the work described in this thesis appears in the following publications:

1- Elmesalamy, A.S., Li, L., Francis, J. A. and Sezer, H. K., **Understanding the process parameter interactions in multiple-pass ultra-narrow-gap laser welding of thick-section stainless steels.** *International Journal of Advanced Manufacturing Technology,* 64: 2013, p. 1-17.

2- Elmesalamy, A.S., Li, L., Francis, J. A., **A Comparison of Residual Stresses in Multi Pass Narrow Gap Laser Welds and Gas-Tungsten Arc Welds in AISI 316L Stainless Steel.** *International Journal of Pressure Vessels and Piping, accepted 14-11-2013.*

3- Elmesalamy, A.S., Li, L. and Francis, J. A., **Narrow gap laser welding of thick section stainless steel.** *In 31st International Congress on Applications of Lasers & Electro-Optics (ICALEO).* September 2012. Anaheim.CA. USA, Laser Institute of America.

4- Elmesalamy, A.S., Li, L. and Francis, J. A., **Narrow gap laser welding of thick section stainless steel for potential civil nuclear reactor fabrications.** *In 3rd International Laser Applications Symposium (ILAS), Association of Laser Users,* March 2013 Nottingham.UK.

5- Elmesalamy, A.S., Li, L. and Francis, J. A., **Effect of the welding parameters of narrow gap laser welding technique on the residual stresses in AISI 316L stainless steel.** under preparation.

6- Elmesalamy, A.S., Li, L. and Francis, J. A., **Finite element modelling for residual stress behaviour of multi-pass narrow gap laser welding and GTAW process with ABAQUS welding interface.** under preparation.

CHAPTER 1. **INTRODUCTION**

1.1 Overview

Electrical power plays a very significant role in modern life. It makes both direct and indirect contributions to most life activities (communications, transportation, education, medical care, manufacturing, agriculture etc). The world population is steadily increasing - it exceeded seven billion in 2012. Yet one-third of the population lacks access to electricity. The global energy demand for electricity is growing. According to the International Energy Agency IEA 2012, the energy demand is growing almost twice as fast as its total energy consumption [1]. The Royal Academy of Engineering in the U.K. estimates that the world will need to triple its energy production by 2050, even with extensive increases in energy conservation. Consequently, there is a need to improve electrical power generation resources.

The world is also concerned with global warming; the International Energy Agency (IEA) reports that the goal of limiting warming to 2 °C above the pre-industrial level is becoming more difficult and more costly with each year that passes. The average global temperature increase could reach 3.6°C [1]. It is regarded as the threshold for dangerous climate change. The energy generation and transportation sectors are considered to be the largest source of global carbon-dioxide (CO_2) emissions. Fossil fuel plants emit of a total about 8.5 billion metric tonnes of carbon into the atmosphere per year [2]. The critical need to meet ever-growing energy demands in an environmentally sustainable manner, and with a low level of carbon emissions has focussed attention to the potential for nuclear energy to play a significant role in future energy supply [3].

Nuclear power can provide a clean source of electrical energy with clear pricing of carbon emission. It is considered the key solution for providing mass electrical energy to decrease the gap between available power sources and the projected dramatic increase in world needs. It is also considered to be the means to limit the predicted increases in the price of electricity for consumers [2]. Finally it guarantees a high return to investors.

Nuclear power plants are the most efficient source of electrical energy. As of February 2013, there are 437 operating nuclear reactors for electricity generation in 30 countries

around the world, with an installed capacity of 370 GW [4]. These reactors represent less than 1 percent of the total number of global power plants. However they represents 12.5 percent of the world's electricity production capacity, according to International Atomic Energy Agency (IAEA) [4].

Safety and economy of nuclear power plants is dependent on precise and reliable structural integrity assessment of main components like pressure vessels and piping [5]. Operating conditions in nuclear power plants represent challenges for the overall structure, as well as for welded joints, due to the high temperatures, pressures and the aggressive environment. Welds are often considered as points of weakness and sources for failure initiation [6]. The selection of effective welding processes represents additional challenges in the fabrication of components in power plants, because of degradation of material properties due to severe thermal cycles and radiation damages.

In 2008, a significant report was issued by the Electric Power Research Institute (EPRI) [6] on a survey of welding and fabrication practices in nuclear plants. The survey identified welded joints as the locations that are most susceptible to failure in operating plants. Welding defects (porosity, cracks, lack of fusion....), phase transformation, segregation of some elements, sensitization, distortion, and residual stresses induced by welding process were identified as a major contributor to many types of failure mechanisms.

1.2 Research motivation

The recent requirements for increasing the lifetime of the new generation of nuclear power plants highlights the need to improved technologies for the construction. One of the key technologies that will underpin all of these activities is the joining of stainless steel components; most of the piping inside nuclear power plants is made from austenitic stainless steel. Developed stress corrosion cracking of welded stainless steel joints specially in pipes welding was a worldwide problem in boiling-water reactors [7]. The magnitude and distribution of residual stress has a significant influence on the structural integrity of power plant. The expected extension of design life of new power plant generations highlighted the significance for better understanding and controlling of residual stresses and their effects on the structure integrity [5].

The welding codes employed inside nuclear power plants depend mainly on arc welding processes. Currently, welding processes such as manual metal arc welding (MMAW), flux core arc welding (FCAW), and submerged arc welding (SAW) are commonly applied to power plants [8]. Gas tungsten arc welding (GTAW) is commonly employed for high quality welds [9]. These welding techniques have been well developed and investigated in the past. Consequently, there is a large body of experience and accumulated knowledge on the behaviour of arc weld joints. On the other hand, these techniques are associated with low welding speed. This results in a large accumulated heat input to the components being joined, increasing the likelihood of distortion, and susceptibility to stress corrosion cracking or decreased fatigue life due to high residual stresses [10, 11].

Design protocols for the new generation of nuclear power plants (generation IV) include a projected life span of over 60 years [6] . The safe operation of nuclear power plants is dependent upon their structural integrity, consequently the accurate design and life-span assessment of welded joints is critical to improving the life-span of the whole plant. The development of welding technology is essential to satisfy the requirement for the next generation of nuclear power plants. The new nuclear manufacturing technologies should aim to improve the life- span of structure, and reduce operating and maintenance costs, potentially saving the industry billions of dollars [6], and decrease the susceptibility of plants to unpredicted or sudden failures.

Laser welding is one of the highest power-density welding techniques currently available, and can be used efficiently for welding relatively thick-section components [12]. Laser welding technology has developed rapidly in recent decades; the improvements include increases in available beam power and beam quality, and laser beam wavelengths have been shifted toward values which are suitable for delivery through fibre-optic cables to improve the flexibility of control. The process can achieve high-welding speeds, and a high production rate. The welding time and total accumulated heat input during welding are reduced, consequently reducing distortion [13].

One of the biggest challenges in the field of laser welding is improving the maximum thickness of welded joints. Typical weld penetration depths for autogenous laser welding are on the order of 1-2 mm/kW [14]. Thicknesses higher than 25 mm are still

beyond the current laser limits of autogenous laser welding. This challenge limits the application of single-pass autogenous laser welding techniques for thick sections in heavy industries. The narrow gap laser welding (NGLW) technique enables thick section welding with relatively low laser power [15]. NGLW is a technique based on multi-pass laser welding with a filler wire; it has been recently demonstrated to be capable of welding materials with thicknesses well beyond that possible with single-pass autogenous welding [16].

The NGLW technique has many advantages over conventional multi-pass arc welding processes. One key advantage is that it allows higher welding speeds due to high power density. Therefore the overall heat input to the weld joint is decreased. Consequently the predicted distortion and residual stress are lower. Moreover, the technique produces a narrower heat-affected zone due to the very narrow bead width. In addition, the volume of added metal is lower than for arc welding, due to the narrow gap preparation for this technique; the reported gap width for NGLW is normally 1:5mm [14, 17]. Finally, the productivity of laser welding is higher than arc welding, due to the high welding speed.

Despite NGLW being a very promising technique, it has not been studied extensively. NGLW is considered to be a more complex process than autogenous laser welding, due to a large number of interrelated variables (laser control parameters, filler wire composition, wire feed rate, wire size, inclination angle of the wire with respect to laser beam, relative position of wire and laser on the welded surface, and speed) [15]. Joint gap geometry and process shrouding, combined with the previous factors, make the process more complicated. Consequently, there is a lack of a knowledge base for NGLW, for thick cross sections. Therefore this technique is not included in the welding codes inside nuclear power plants; highly conservative assumptions are still used in the design codes of power plants, which can limit their economic lifespan.

Austenitic stainless steels are one of the most commonly used materials in heavy industries, especially in power plants and in nuclear industries, as a result of their metallurgical stability, high corrosion resistance, and good creep and ductility properties at elevated temperatures [18, 19]. Most of the tubings inside nuclear reactors and intermediate level nuclear waste storage sites are made from stainless steels [20]. However there are many challenges during the welding of stainless steels using different techniques. The most critical challenges are related to the induced tensile residual

stresses, caused by the high thermal expansion coefficient of austenitic stainless steel, the lack of fusion between welding tracks and side walls, hot cracking, and porosity, causing degradation of both the mechanical properties and corrosion resistance of the material.

1.3 Aim and objectives

The aim of this research is to further understand the NGLW technique for joining 316L stainless steel in terms of process parameter relationships and weld characteristics. The objectives of the project are:

1) To optimise fibre laser NGLW parameters to achieve defect-free welds in 316L stainless steel using design of experiments and statistical modelling.
2) To understand the microstructure formation and residual stress characteristics in NGLW joints in comparison with those of GTAW welding and autogenous laser welding.
3) To understand the mechanical properties including tensile strengths, fatigue, bending and fracture toughness of NGLW joints in comparison to arc weld joints.
4) To investigate the induced residual stress across the welded joint with NGLW and compare it with GTAW by using contour, and neutron diffraction techniques to improve the reliability of the measurements.
5) To investigate the influence of the power and the number of filling passes of NGLW technique on the induced stresses and strain hardening, and the welding strategy, welding restraints on the residual stress development for both NGLW and GTAW.
6) To understand the thermal history and its effects on residual stress developments using finite element modelling.
7) To investigate corrosion and stress corrosion cracking characteristics of NGLW joints in comparison with those by arc welds

It is hoped that this preliminary study will provide an insight to the way in which NGLW affects some of the factors that have a critical influence on the integrity of nuclear welds, namely the development of residual stresses, and the cyclic hardening of the material during multipass welding, corrosion behaviour in nuclear environment. It is also hoped that this work will provide a foundation for future work involving welds in thicker sections of material.

1.4 Structure of thesis

Chapter.1 Introduction

Chapters 2-4 provide literature reviews on nuclear power plants, existing welding techniques applied to nuclear power plants, and the characteristics of laser welding and current and future applications in nuclear power plants.

Chapter 5 describes the experimental facilities, experimental procedures used in the project, and preliminary welding experiment.

Chapter 6 describes the design of experiments and statistical modelling for the optimisation of NGLW process using a 1 kW fibre laser for welds up to 20 mm thick. Multiple parameter interactions were studied and multi-objective optimisation was carried out.

Chapter 7 describes the microstructure, and the productivity of NGLW techniques compared to different welding techniques.

Chapter 8 describes the mechanical properties in NGLW joints up to 20 mm thick compared with arc weld joints.

Chapter 9 describes the residual stress characteristics of NGLW joints. The contour method was used, validated using neutron diffraction and the XRD measurements.

Chapter 10 describes the finite element modelling procedures and thermal history/residual stress prediction validated by experiments.

Chapter 11 describes corrosion and stress corrosion cracking performance of the welds to understand the effect of weld heat inputs, cooling rates and microstructure formation on the corrosion/stress corrosion cracking characteristics.

Chapter 12 provides conclusions of the research in terms of major findings, contribution to the advancement of welding science and technology, and further work.

Work Flow Plan

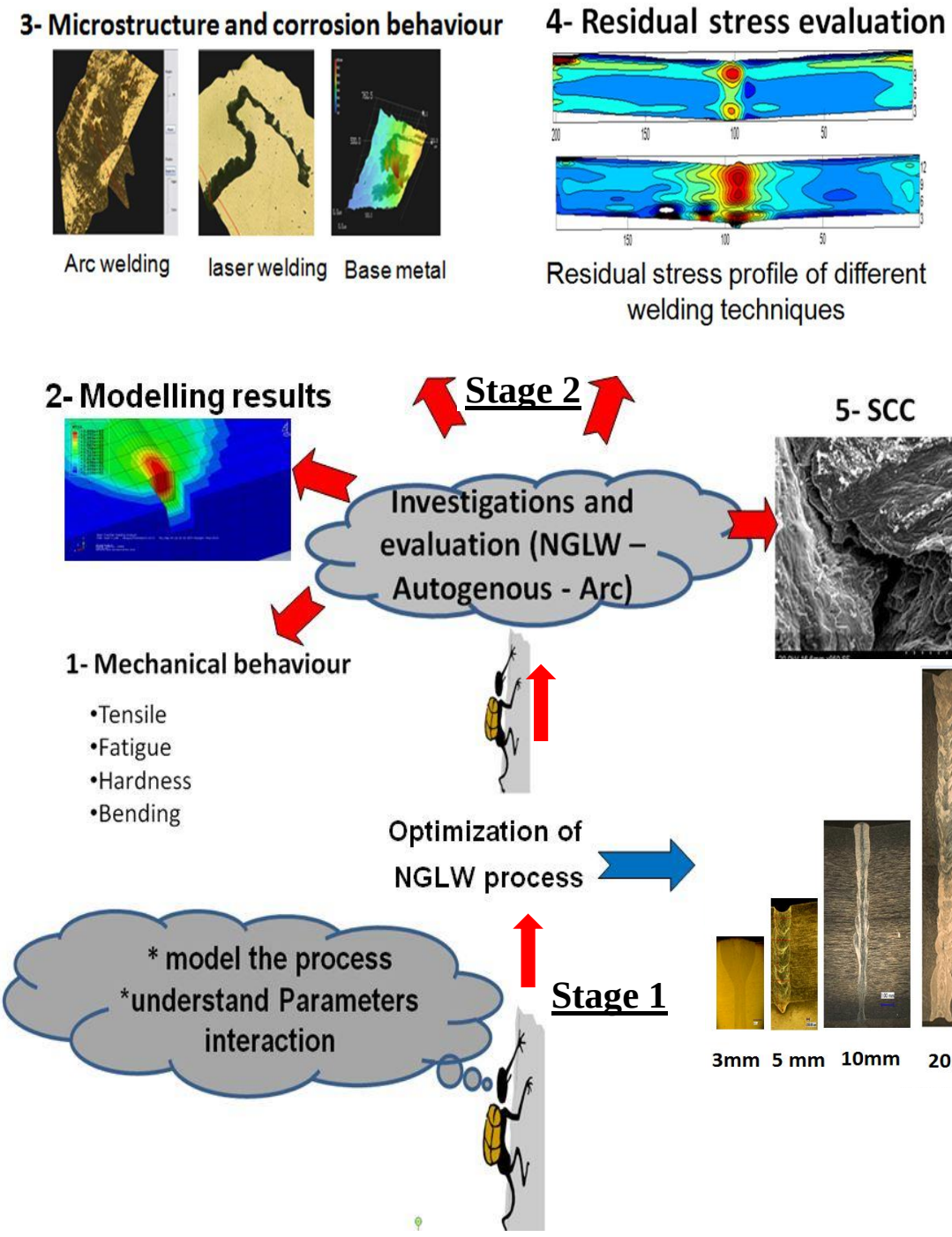

Are [NGLW] advantages promising?
What are limitations and challenges (How it could be resolved)
Evaluation of weld bead against other welding techniques

PART I - LITERATURE REVIEW

CHAPTER 2. LITERATURE REVIEW – OVERVIEW OF NUCLEAR POWER PLANTS

2.1 Introduction

A power station (generating station, power plant, or powerhouse) is an industrial facility for the generation of electrical power. Power plants are generating a large proportion of the electrical power that is used in almost all countries around the world. The generator is the centre element of nearly all power stations; its main function is to convert other energy forms into electrical power by creating relative motion between a magnetic field and a conductor through turbines.

The energy source harnessed to turn the generator varies widely. Most power stations in the world use fossil fuels, such as coal oil and natural gas, whereas others use nuclear power [21].

There is an increasing use of cleaner renewable sources of power, such as solar, wind, and hydroelectric. The power generation efficiency of the thermal power plants is higher than that of renewable techniques, and renewable techniques have a lower availability of power supply. The output of most renewable power plants depends on weather conditions (air speed and direction, sunrise, speed of flow of water in rivers or canals,); they cannot guarantee a continuous and reliable energy supply.

2.2 Fossil fuel power plants

Fossil fuel power stations transforms chemical energy into electrical energy, usually by burning coal or natural gas; thermal energy produced by combustion is used to produce supersaturated steam. The steam is used for the production of electricity through via a steam turbine. The kinetic energy of the spinning turbine is transformed into electrical power through electro-mechanical generators. Alternatively, in the case of natural gas power stations, the turbine is a gas turbine, which directly uses the dynamic pressure from flowing gases (air and combustion products).

The era of large-scale electrical power distribution began in July 1878, when the world's first power station was built by Sigmund Schuckert in the Bavarian town of

Ettal. It consisted of 24 dynamo electric generators which were driven by a steam engine. The first public power station was the *Edison Electric Light Station*, built in London at Holborn Viaduct, which started operation in January 1882 [22].

Fossil fired power plants have some environmental drawbacks, such as the production of large amounts of carbon dioxide, and also the production of sulphur dioxide which pollutes air and water. Fossil-fuelled plants are considered to have a lower efficiency for power generation, compared to that of nuclear power plants, as will be discussed below**.**

2.3 Nuclear power plants

Nuclear power plants are the most efficient power generation sources currently available. They are thermal power stations in which the heat source is a nuclear reactor, where heat is generated from a controlled nuclear chain reaction. The heat is used to generate steam, which drives a steam turbine connected to a generator to produce electricity.

Obninsk Nuclear Power Plant in Russia was the world's first nuclear power plant built to generate electricity for a power grid - it began operation in June 27th, 1954 [22] with capacity of around 5 megawatts of electrical power.

As of June 2012, the IAEA reported that there were 435 nuclear power reactors in operation, operating in 31 countries with total capacity 370,003 MW [21]

There are two main commercial reactor types, which are being actively considered for construction around the world; the Pressurized Water Reactor (PWR), and Advanced Boiling Water Reactor (ABWR) [2]. They represent more than 81% of total nuclear reactors [21]. The PWR represents the highest thermal efficiency of the two types, due to the high operating water pressure the feeding the turbine, with ~340 °C (15 MPa) steam instead of ~285 °C (7 MPa) for the ABWR, while the design pressure of the reactor is 21.5 MPa. The overall efficiency of the PWR can be up to 37%. [23].

2.3.1 Nuclear reactor (source of energy)

The nuclear reactor is the heart of a nuclear power plant, it is where the nuclear chain reaction occurs. When a neutron is absorbed by an atom of nuclear fuel, generally

uranium, a fission reaction takes place, which causes the splitting of the uranium atom into two smaller waste atoms. This process which results in the emission of a few more neutrons also releases energy, because the sum of the masses of the fragments will be less than the mass of the uranium nucleus as shown in equation (2.1) [24]. Increasing the number of fission events will lead to an increase in the amount of released energy [25].

$$235U + 1 \text{ neutron} \Rightarrow 2 \text{ neutrons} + 92Kr + 142Ba + \text{energy} \quad (2.1)$$

The newly released neutrons are the catalyst for the splitting of other atoms. Thus, the process is repeated in a chain reaction as shown in Figure 2-1

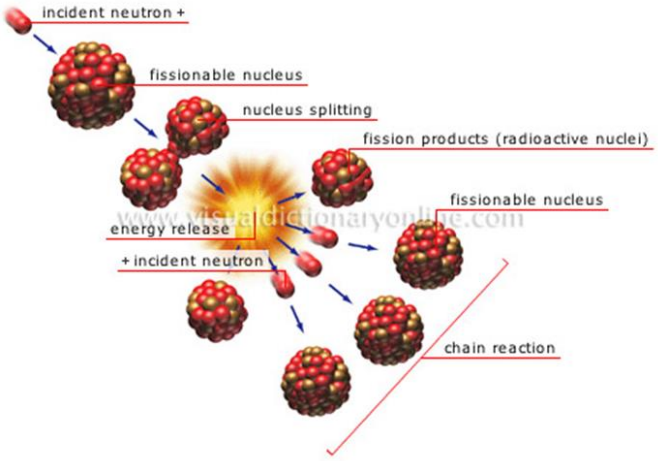

Figure 2-1 Fission chain reaction [24]

The chain reaction can be controlled through the use of water, and of graphite rods, since they act as a moderator, slowing down the neutrons. Rods of boron steel are also used as control rods to control the rate of the reaction, since they absorb neutrons without fission occurring. Heat is generated in the reactor core by controlled nuclear fission. Coolant is heated as it is pumped through the reactor and thereby removes the energy from the reactor - this is known as the primary cycle. The heat from the primary coolant is then used to raise the steam temperature through the steam generator. Steam is run through a secondary circuit to turbines, which in turn powers an electrical generator as shown in Figure 2-2.

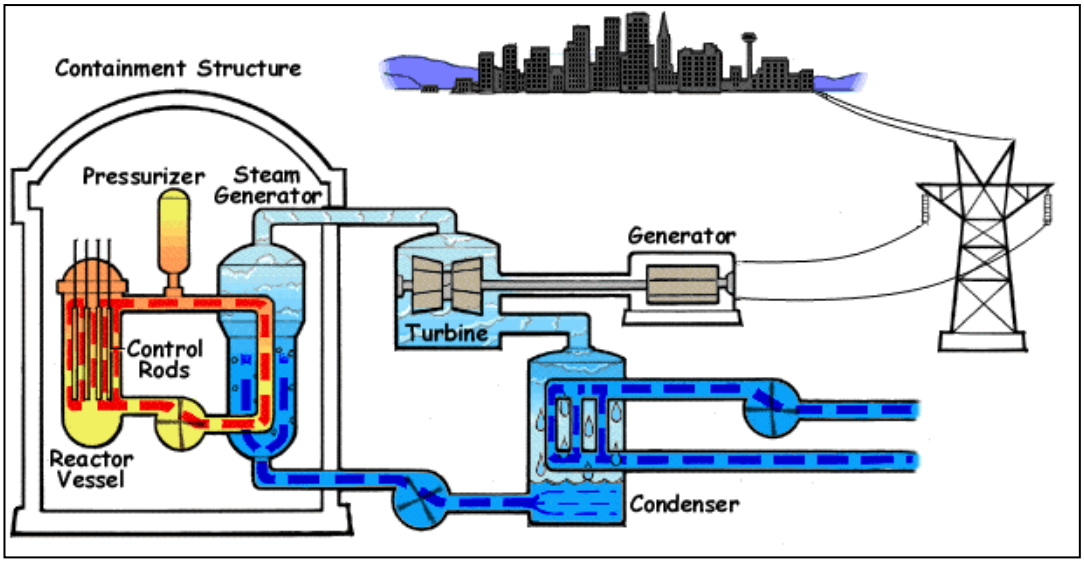

Figure 2-2 Pressurized water reactor system [26]

2.3.2 Nuclear power plant efficiency

A nuclear power plant is very effective electrical power generating facility. It uses less fuel compared to a fossil fired plant. It has been estimated that, to produce the same amount of electricity, the ratio of the fuel weights for nuclear and coal fired plants is 1: 17000 [27]. Nuclear power stations can generate great amount of energy from a single 1.65 cm nuclear fuel pellet. This is equivalent to the energy generated from burning 807 kilograms of coal, 677 litres of oil, or 476 cubic metres of natural gas as shown in Figure 2-3. Furthermore, the used nuclear fuels can be reprocessed and "charged" through a series of chemical and physical process to regain most of its spent energy to be used as fuels again.

Figure 2-3 Nuclear fuel efficiency [28]

The lifespan of most of currently operating nuclear power plants is limited to less than 40 years, due to the influence of the severe working conditions on their structural integrity [4]. Development of the increased lifespan for the new generation

of nuclear power plants is a major requirement, due to the high capital cost of the plants [29].

2.4 Current and developments of nuclear reactors

There are four main generations for nuclear reactors as shown in Figure 2-4. The first generation was developed between the 1950s and 60s. It worked as early prototype reactor. The second generation was developed in the 1970s as first large commercial power plants generation. A generation II reactor has an original design life of 30 or 40 years. However life could be extended to 50 or 60 years. Generation III was developed recently in the 1990s. This nuclear reactor generation represents current and near future technology. Generation IV reactors are mainly based on high temperatures and cooling by gas or liquid metals. They are generally safer and more efficient and reliable. The improvements in new generation designs make nuclear reactors less vulnerable to accidents — whether due to equipment malfunctions or human error [2].

It offers significant developments in safety and economics. Advances to generation III include improved safety systems and a 60 year design life [30]. Laser development of that generation resulted in Generation III+. New plants built between now and 2030 will likely belong to this generation.

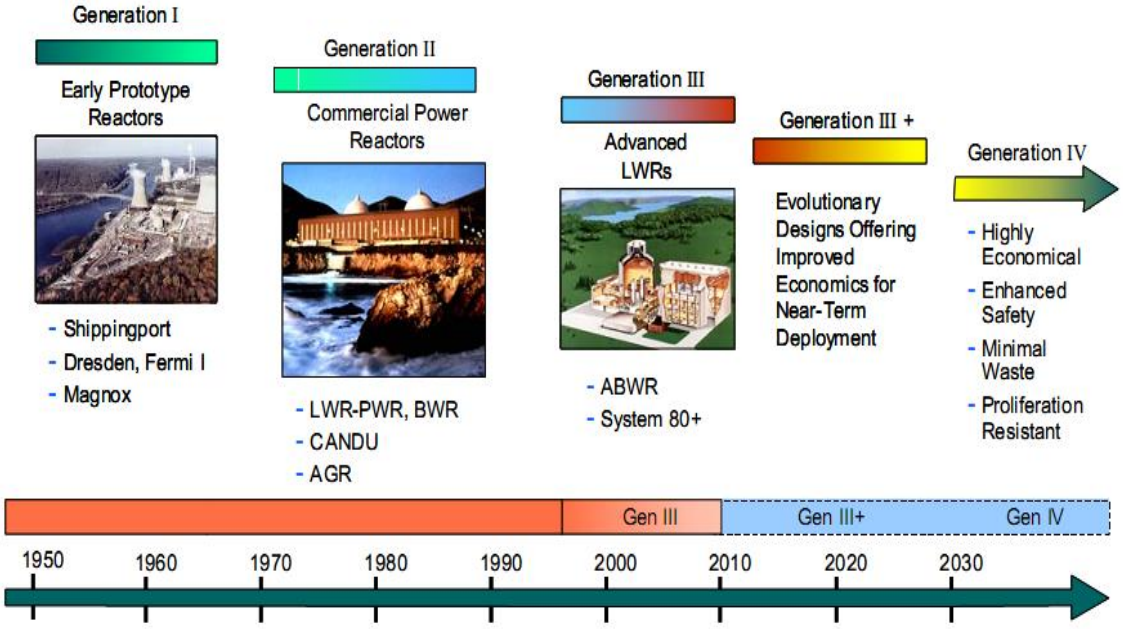

Figure 2-4 Progression of nuclear reactor grades [30]

The US Department of Energy, and the nuclear industry, have launched a program called NuStart to stimulate and support the development of evolutionary and revolutionary reactor designs for Generation III , and Generation III+ reactor designs. It covers both pressurized water reactors and boiling water reactors. Westinghouse nuclear corporation has submitted two pressurized water reactor designs belonging to this generation (Pressurized water reactorsAP600 and AP1000) for licensing to the US Nuclear Regulatory Commission. According to Westinghouse's description, these designs provide an enhanced level of safety. The enhancements include shortening large pipes, reducing the number of pumps on the primary circuit, and incorporating passive safety systems that rely on natural forces (Westinghouse Corporation, 2003) [21] .

AREVA nuclear corporation has made several major contributions in the area of safety, and accident prevention, including core damage (melt- down). It boasts significant strengthening of the civil engineering structures of the nuclear island, increasing its resistance to external hazards, including earthquakes, flood, fire, and strikes by military or large commercial aircraft. AREVA developed a boiling water reactor, the SWR1000 with the collaboration of German utilities. Its design was completed in 1999, with a capacity of 1250 MW and a 60 year expected lifetime. It has also designed the 1650 MW (e) European Pressurized Water Reactor (EPR), which meets the European Utility Requirements. Four are under construction in China, Finland and France [2, 21].

VVER-1200 AES-2006 is a Russian design for pressurized water reactor (PWR). It belongs to the third-generation of reactors [21]. The design uses water to cool the reactor and to generate steam. This is largely an evolutionary development of the VVER- 1000 reactor plant, with longer design life (50 rather 30 years), and increased efficiency (36.6 percent instead of 31.6 percent) [2, 21].

2.4.1 Nuclear reactor design for the Future (Generation IV)

Generation IV reactors are considered a step forward for the longer-term future of nuclear power generation; they are sets of theoretical nuclear reactor designs. There are two main international projects currently in progress contributing to the development of this generation [2]. Most of these designs are generally not expected

to be available for commercial construction before 2030 [2]. In February 2005, ten countries made an agreement on collaborative research and development of Generation IV systems. The main objective of this agreement is to implement an international generation IV forum (GIF), in order to develop future-generation nuclear energy systems.

The main goals for generation IV reactor design include development of a sustainable energy source with minimal waste, improved design lifetime for the structure, the development of a safe, reliable energy source using inherent safety features to improve public confidence in nuclear energy safety, and the realisation of a competitive energy source with low costs and short construction times. In addition, the design criteria include proliferation resistance, and physical shielding and protection (improved security from terrorist attacks) and decreased building running costs [2, 30] .

2.5 Hazard of nuclear power plants

There are two major hazards of nuclear power plants: exposure of radioactivity to the public and the environments, and the safe disposal of nuclear wastes.

The main hazard from nuclear power generation is the potential for exposing the public to radiation. A major health hazard would result if a significant portion of the radioactive inventory in the core of a nuclear reactor were released to the atmosphere. New development and safety considerations will decrease the probability of this happening. Various techniques are used, including conservative designs, safety equipment, and physical barriers. Analyses identify high-consequence accident frequencies of occurrence on the order of 10^{-7} per reactor-year (one event could occur every 10 million years) [2].

2.5.1 Disposal of nuclear wastes

Global concern over the accumulation of nuclear waste has encouraged most countries to be involved in investigating means of safe final waste disposal. Nuclear waste decays over time, but some of it remains hazardous for many thousands of years.

There are more than one possible technique for the safe disposal of nuclear wastes. One method of waste disposal involves the use of steel honeycomb capsules, encapsulated in a copper canister with a 50 mm wall thickness. It is anticipated that, when these are buried 500 m deep in specially prepared clay lined granite repositories, the leakage of radioactivity into the ground water will cease within 100 000 years [12].

Another waste disposal technique, used especially in the UK, depends upon packaging intermediate level radioactive waste (ILW) in glass-vitrified form in stainless steel containers, and then encapsulating them in a cementitious grout. These are stored in above-ground facilities to remain for several decades. Finally, the assemblies are buried in a permanent, underground rocky storage site, known as a geological disposal facility (GDF) as shown in Figure 2-5. The containers should maintain their integrity for extended periods of storage prior to final disposal, to ensure no significant or harmful quantities of radioactivity ever reach the surface environment. Welding regions and corrosion governed by the environmental conditions are the major challenges for the performance of the waste containers

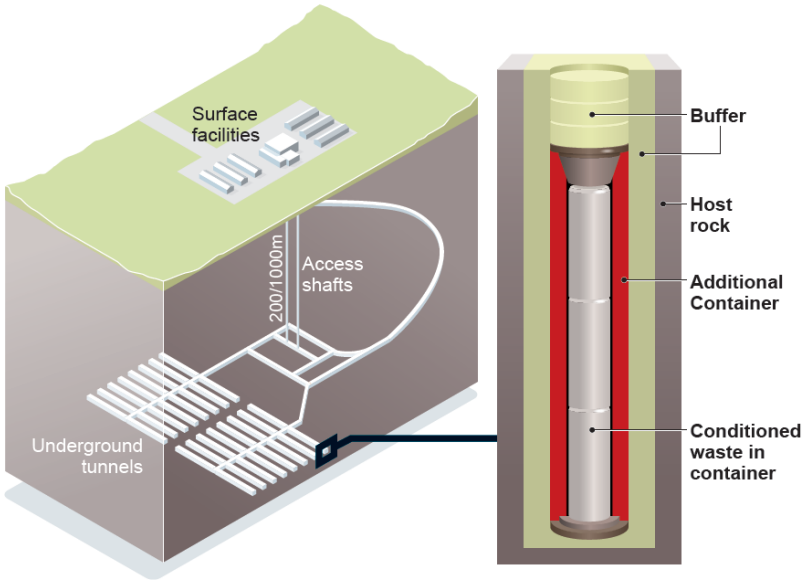

Figure 2-5 Geological disposal facility [20]

2.6 Materials in nuclear power plants

Power plants have very complicated structures - they contain large number of different systems, and components. These systems and components are made from

different alloys, and have different production methods according to their function and working conditions. These components are working under a high pressure and at high temperature [23]. They are subjected to a highly corrosive environment. Stainless steel is one of the main alloys used in power plant component fabrication [8, 31]. Stainless steels are used mainly for heat exchangers in boilers, bolted joints, and also used for the main pipe connections between steam generators and the reactor [8]. According to ASME codes for the construction of nuclear facilities, these alloys are used for some Class 1 components, such as main pipes, portions of pumps and valves, due to their high-temperature stability [31].

In fusion reactors, the inner and outer shells of the vacuum vessel are both formed from 60 mm-thick plates, and the stiffening ribs from 40 mm plates. These are made from SS 316L [9]. Austenitic 316LN stainless steel is also used in nuclear power plants, since the carbon has been reduced in order to decrease the probability of inter-granular corrosion. Nitrogen is added, mainly to conserve the elevated temperature strength and other properties associated with the loss of carbon, in comparison with the conventional 316 grade [32]. Figure 2-6 shows the different alloys used inside a PWR nuclear power plant.

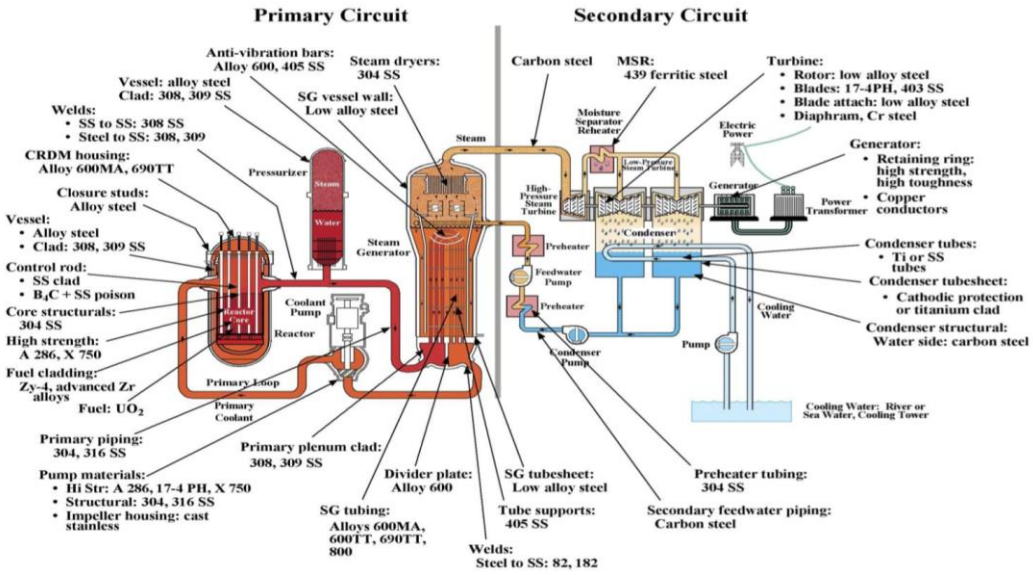

Figure 2-6 An Overview of Materials in a Pressurised Water Reactor [33]

There are three different alloy systems which cover the majority of power plant fabrication, namely austenitic stainless steels, ferritic steels, and nickel-based alloys.

This project involves a comprehensive study on austenitic stainless steel welding, in order to improve the welding quality and performance in service for different thickness ranges. This goal may be achieved through assessing the feasibility of introducing new welding technologies to the power generation industry, as well as by assessing the benefits and weld quality achieved with autogenous laser welding, narrow-gap laser welding, and arc welding.

2.7 Stainless steels

Stainless steels are widely used in many industries due to their high corrosion resistance. They are iron-based, and are primarily alloyed with at least 10.5% chromium, and often also with nickel, especially in the case of austenitic stainless steels [34, 35] . They have enhanced corrosion resistance due to a passive oxide film on the surface. Most stainless steels are weldable, but they can be very sensitive to heating in specific temperature ranges. They may suffer from changes in their phase balance due to grain growth, segregation, the formation of intermetallic constituents, and the presence of impurity elements. This can lead to changes in the properties and performance of the base metal [35].

2.7.1 Austenitic Stainless steels

Austenitic stainless steels are used generally in power industries due to their high ductility and fracture toughness [36]. Austenitic stainless steels have good corrosion resistance under normal conditions, and also good mechanical properties at both low and high temperatures. They are used in many industrial applications in both conventional and nuclear power plants, especially when it is necessary to weld high temperature components. A service temperature of up to 560ºC can be tolerated, but oxidation resistance and strength will be decreased at such high temperatures [35]. This type of stainless steel based on adding Ni in concentrations above 8 wt. %, and chromium, to form a ‘ternary system’. Adding nickel generally increases ductility and toughness. Carbon and nitrogen are also austenitic stabilising elements - nitrogen improves strength, and carbon improves strength at high temperature. Cr and Mo may also be added to improve pitting corrosion resistance. Austenitic stainless steels are non-magnetic. They are not suitable for use in highly corrosive environments

involving chloride ions, such as in seawater, as under these conditions they could be susceptible to stress corrosion cracking.

2.8 Austenitic stainless steel weldability

Austenitic stainless steels in the AISI 300 series usually solidify during welding as a mixture of austenite and ferrite. The ferrite almost fully transforms to austenite on normal cooling, but a few percent of the ferrite is often retained in the weld metal [32]. Austenitic grades have good corrosion and oxidation resistance up to 1200ºF (648 °C). They are generally very weldable alloys under normal conditions. However, problems may arise during welding if some precautions are not considered. The addition of sulphur and phosphorus to the steel is important in order to improve its machinability, however the addition of these elements has drawbacks with respect to solidification cracking behaviour [37]. One of the most critical problems in austenitic stainless steel welding is stress corrosion cracking due to high tensile residual stress near to the weld region, the risk of which may be increased if coupled with aggressive environments (high pressure, high temperature). Another problem relates to corrosion (sensitization) when austenitic alloys are subjected to their sensitization temperature range. Common welding defects for stainless steels will be discussed in the following chapter.

2.8.1 Austenitic stainless steel solidification behaviour

Referring to Figure 2-7, the liquidus surface exhibits a single dark line running from near the Fe corner to the Cr-Ni side, separating the solidification modes as primary ferrite above and to the left of the line, and a solidification mode as primary austenite below and to the right of the line. The solidus surface exhibits two dashed lines running in a similar direction, with a lower temperature than for the liquidus. Between the two lines is a region containing both ferrite and austenite, with liquid above the solidus surface; this region separates the pure austenite and pure ferrite regions [38]. There are two types of reactions: the peritectic reaction starts at Fe-4Ni, extending to where the liquidus continuous line crosses the Ni-rich solidus (dashed line), changing the peritectic to a eutectic reaction at the point specified by the blue

arrow as shown in the ternary diagram in Figure 2-7. The reaction becomes eutectic at Fe concentrations of less than 75% [32].

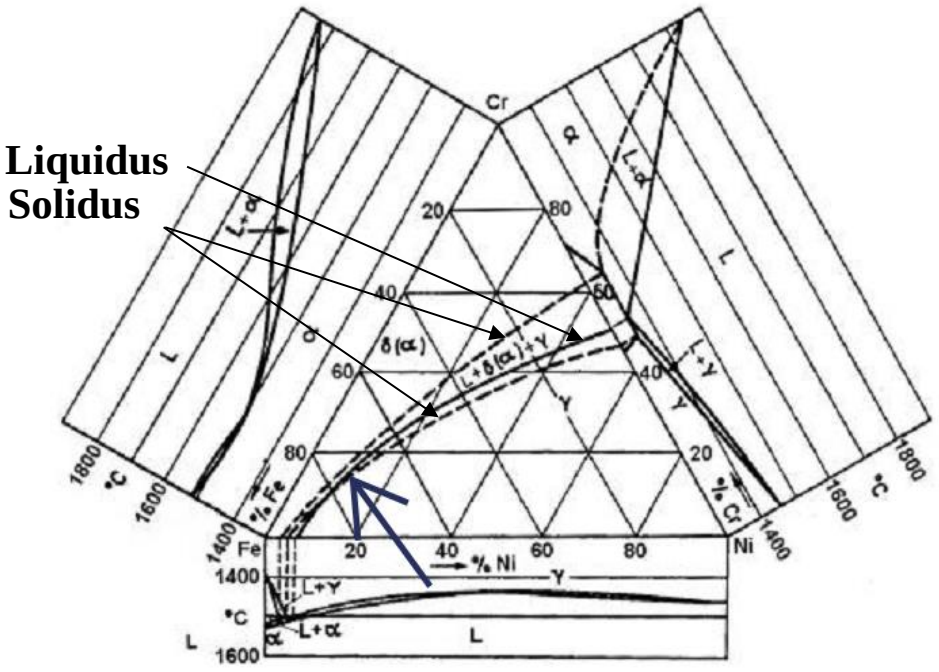

Figure 2-7 Liquidus and solidus projections of the Fe–Cr–Ni system [32]

Most commercial stainless steels contain less than 75% Fe, and often exhibit eutectic behaviour. The term eutectic is taken from the Greek language, and means “easy or well melting”. The eutectic reaction is formed when adding an alloying element causes a lowering of the liquidus lines from both melting points of the two pure elements as shown in Figure 2-7.

The alloy composition has the lowest melting point of the system where the mixed solid-liquid phases (L + δ and L + γ) vanish. The eutectic composition also solidifies completely at a single temperature, and is referred to as an invariant point. In a eutectic reaction, a liquid freezes to form two solid solutions according equation (2.2).

$$\text{L liquid} \quad \Rightarrow \quad \delta \text{ ferrite} + \gamma \text{ austenite} \qquad (2.2)$$

A pseudo-binary diagram is 2D phase diagram based on a constant Fe content (70 wt. %) [32], as shown in Figure 2-8. Austenitic stainless steel welds can solidify as primary ferrite or austenite phase. The primary solidification mode depends on the

composition of the alloy; alloys at the left hand side of the pseudo-binary diagram, close to high Ni percentage represent primary austenitic solidification, and alloys on the right hand side to the small triangle between the solidus and liquidus show primary ferritic solidification modes as shown in Figure 2-8 .

There are two solidification modes in the case of primary austenite [38]. The first mode is completely austenitic - if the composition of the stainless steel is sufficiently far from the eutectic trough, the solidification will be fully austenitic. The eutectic trough is the small triangle in the pseudo-binary diagram which represents a combined austenitic-ferritic phase solidification region. As the composition approaches the eutectic trough, some ferrite can form during the last stages of solidification by the eutectic reaction as previously discussed. The solidification mode is described as austenite-ferrite (AF) as indicated in Figure 2-8. This ferrite would be confined to the solidification cell boundaries and is called eutectic ferrite.

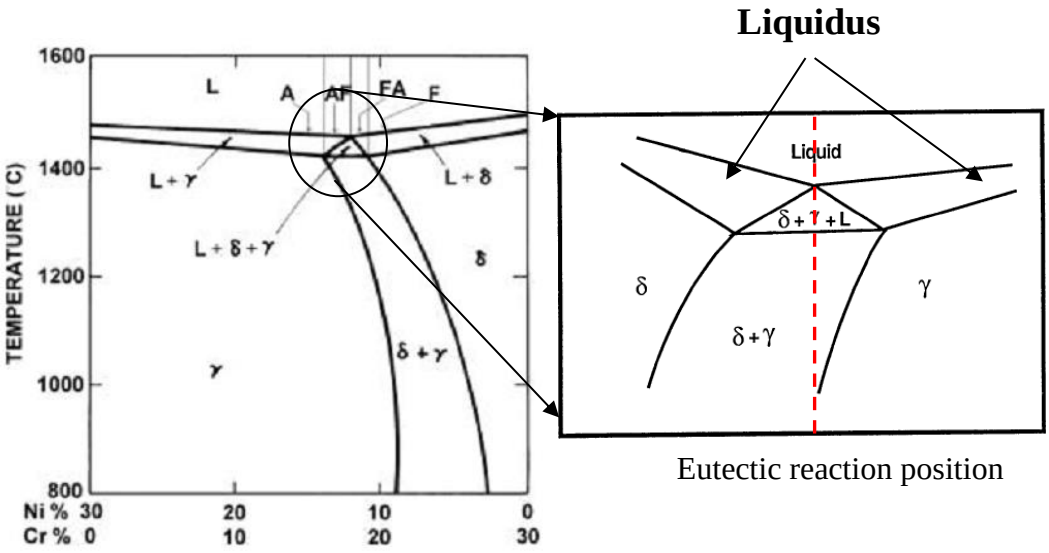

Figure 2-8 Vertical sections of Fe-Ni-Cr ternary diagram, at constant Fe70%[32]

The primary ferrite solidification mode is shown in Figure 2-9. The alloy may have an equilibrium structure of 100% ferrite at high temperatures, but still be partly or completely austenitic at lower temperatures, depending on the extent to which equilibrium is approached, as shown in Figure 2-9. The transformation of the primary solidified ferrite to austenite results in many different ferrite morphologies [38]. A second mode of solidification can be described as ferrite-austenite (FA) as

shown on Figure 2-8. This occurs when dendrites solidify as primary ferrite, but upon slow or moderate cooling through the two phase region, they transform to austenite. This results in the formation of austenite along the ferrite cell and dendrite boundaries, except for thin rods or strips of ferrite along the core of the original dendrite. This is called 'skeletal ferrite' as shown in Figure 2-9. If the cooling rate is high, or the ferrite-promoting elements are increased, the ferrite morphology changes to a lathy structure along the dendrite axis. Restricted diffusion (e.g. due to a rapid cooling rate) during the ferrite-austenite transformation leads to reduced diffusion distances and more tightly spaced laths [38]. Consequently, a reduced amount of austenite is formed, as shown in Figure 2-9. Alloys sufficiently far from the eutectic trough, with an increased Cr/Ni ratio, solidify with a ferrite matrix and grain boundary austenite. Solidification will be primary ferrite, with a Widmanstätten austenite structure along the ferrite boundaries [38].

For a simplification of the phase transformation behaviour and solidification modes during the welding of stainless steels, another method is used, and it is based on the calculation of the chromium equivalent (Cr_{eq}), nickel equivalent (Ni_{eq}), and ferrite number, as will be introduced in the next sections.

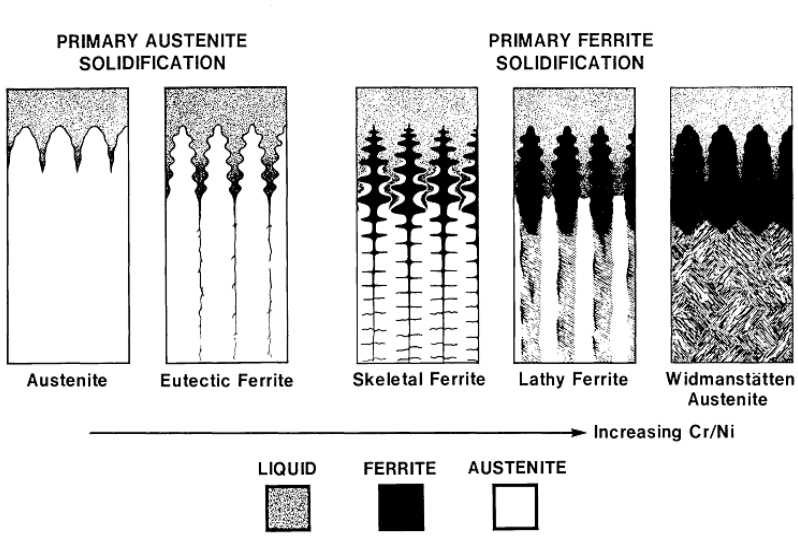

Figure 2-9 Solidification behaviour morphologies in austenitic stainless steel [38]

2.8.2 Control and calculation of ferrite number

The amount of ferrite and austenite in an alloy is very important in determining the solidification behaviour. It can be estimated through the ferrite number. This number is very important for predicting the mode of solidification (primary solidification phase). A ferrite number greater than 3 and less than 20 indicates that the most likely solidification mode is ferritic-austenitic (FA) solidification. This mode has a high resistance to solidification cracking [35]. The ferrite number can be computed through the calculation of chromium equivalent (Cr_{eq}) and nickel equivalent (Ni_{eq}) compositions. Both the Cr_{eq} and Ni_{eq} depend on the composition of the stainless steel alloy and can be calculated according to the Schaefler diagram using equations (2.3),(2.4) [19]:

$$Cr_{eq} = Cr + Mo + 1.5Si + 0.5\ Nb + 2Ti \tag{2.3}$$

$$Ni_{eq} = Ni + 0.5\ Mn + 30C \tag{2.4}$$

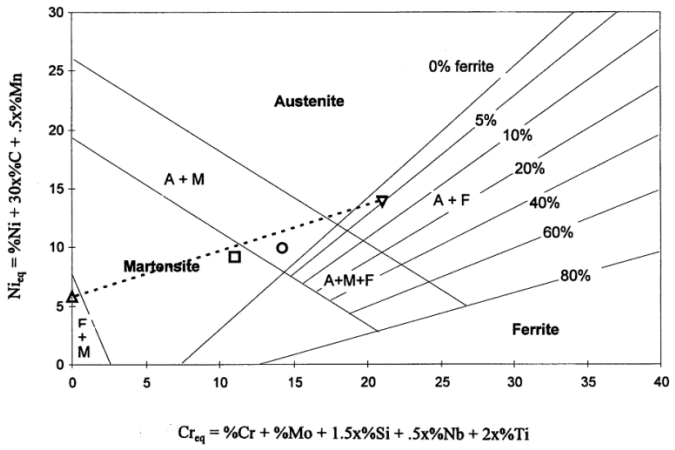

Figure 2-10 Schaefler diagram [39]

The Schaefler diagram is shown in Figure 2-10 [39]. The diagram was published in 1947. Since then, there have been many refinements to this diagram, and corresponding refinements to the equations for both of chromium equivalent (Cr_{eq}) and nickel equivalent (Ni_{eq}). The first modification was by Delong et al. in 1956 [35], followed by modifications suggested by Hull in 1973 [35], then Hammer and Svenson in 1979 [40], and Espy in 1982 [35]. The final diagram was developed by

Kotecki and Siewert in 1988 and (WRC 1992) [35]. This resulted in the Welding Research Council diagram (for solidification mode, ferrite number). The definitions of Cr_{eq} and Ni_{eq} are shown in Figure 2-11.

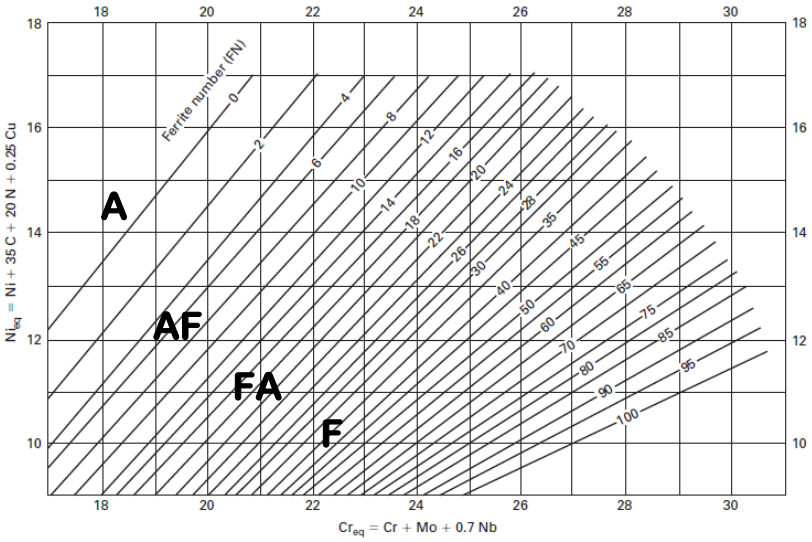

Figure 2-11 Kotecki and siewert 1992 [41]

Kell et al. [41] studied the ferrite number prediction with autogenous welding of 316L austenitic stainless steel by calculating the chromium equivalent (Cr_{eq}) and nickel equivalent (Ni_{eq}) for the chemical composition is shown in Table 2-1. The calculated values were Cr_{eq} = 19.173 and Ni_{eq} = 11.72. The WRC 1992 diagram is used to identify the ferrite number; according to the Cr_{eq} and Ni_{eq} values, the ferrite number is approximately 6%. This ferrite value corresponds to dual solidification (F-A) region, and a small amount of ferrite is likely to be present after cooling to room temperature for normal welding conditions.

Table 2-1 Chemical composition of austenite stainless steel 316L [41]

Element	C	Cr	Mn	Mo	N	Ni	P	S	Si	Fe
%weight	0.020	16.820	1.214	2.353	0.042	10.200	0.026	0.002	0.038	69.247

Another study was performed by Clayton et al. [42] in the laser welding of austenitic stainless steel (316Ti). The chemical composition for this grade is shown in Table 2-2. The calculation of chromium/nickel equivalents for the given material gives a

value of 1.57, which corresponds to FA solidification. The ferrite number was calculated for this alloy according to different solidification mode diagrams. The obtained values for the ferrite number was between 5 and 8%, and values in this range all correspond to FA solidification [42].

Table 2-2 Chemical composition of austenite stainless steel 316LTi [42]

Composition (wt%)										
Fe	C	Cr	Ni	N	Mo	Si	S	P	Mn	Nb	Cu
68.04	0.02	17.22	10.81	–	1.98	0.56	–	0.01	0.85	0.09	0.41

No solidification cracks were noticed, which suggests that compositions in this range are not susceptible to solidification cracking. The microstructure of the weld cross-section is shown in Figure 2-12. Two phases are identified: austenite phase with ferrite phase dendrites, which are clearly visible appearing in black. This structure is called vermicular or skeletal delta ferrite.

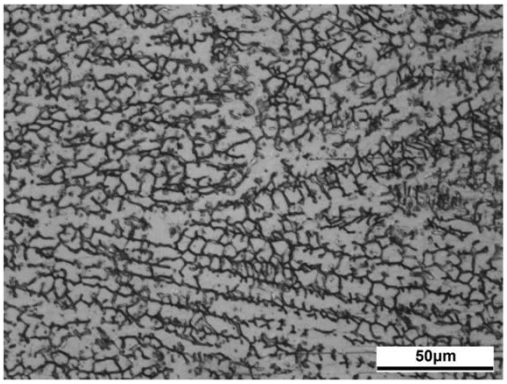

Figure 2-12 Typical microstructure of the cross section [42]

2.8.3 Filler material and solidification behaviour

Welding processes using filler material techniques improve the performance of the welded joint. This technique of welding controls the solidification behaviour of the welded zone according to the combination of base and filler material, and the dilution ratio between them at the welding region. Figure 2-13 shows two different cases in which an austenitic base metal has been welded with a filler metal, having a

known ferrite number of 10. The final composition of the weld metal will lie on the tie-line between the compositions of the base and filler, and the exact position will depend on the dilution of the filler metal. Point 1 specifies the final composition if the dilution is 50%, it is lying at FN = 1 - this suggests AF solidification. If the dilution for another case is 20%, perhaps due to a low heat input, the weld metal composition will be shifted to position 2 at FN = 6. This suggests a change to FA solidification [35]. The NGLW technique has the flexibility to change the filler material in order to control the solidification behaviour, such that welding joint will be free of solidification defects and mechanical or corrosion resistance degradation.

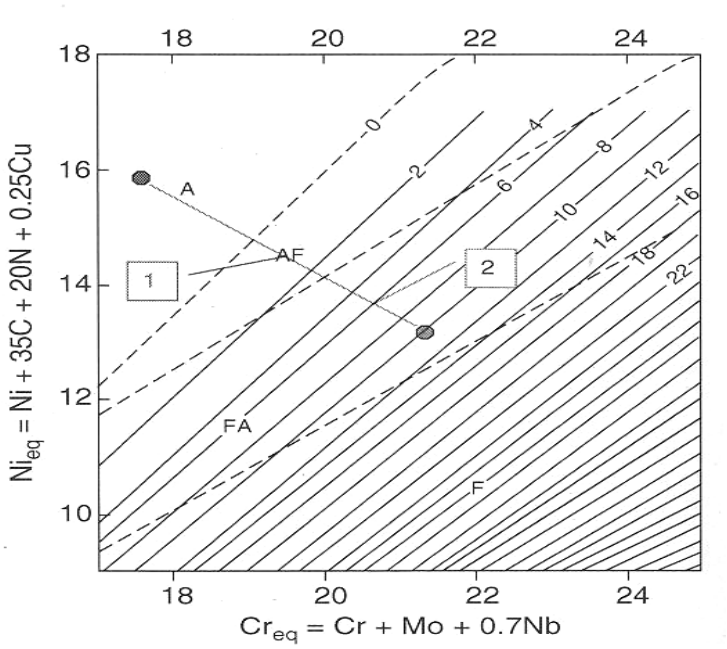

Figure 2-13 Influence of filler material on ferrite number [35]

CHAPTER 3. LITERATURE REVIEW - CURRENT WELDING TECHNOLOGIES FOR NUCLEAR POWER PLANTS

3.1 Introduction

Welding is the process of joining two different parts from the same or different materials to become one part [43]. It is the most common method of joining parts [44]. Welding processes can be applied to most metal products in manufacturing and repair operations. The field of welding technology is still growing in both the number of available technologies and the variety of applications. Welding takes place through forming chemical (or metallurgical) bonds across the joint interface under different conditions of heat and pressure. When carried out successfully, welding achieves homogeneity between the welded parts. Welding is also one of the cheapest joining processes. Due to the large number of available technologies for welding, it can be used to join most metallic materials. It is considered to be a flexible joining process [44]. It represents the optimum utilization of metal, and it gives the designer flexibility in casting construction.

Power plant construction involves the use of a number of welding techniques in order to join a variety of structural components of different sizes and materials. Severe working conditions inside power plants mean that the welding processes employed are subject to a large number of strict constraints - many components are working at high temperature and pressure, and in a corrosive environment. The huge scale and complexity of the reactor structures in nuclear power plants have created challenges for the used welding technologies [12], such as the need to weld substantial material thicknesses with severe service performance requirements, and over extended distances.

This chapter will review different welding processes, which are included in the welding codes inside nuclear power plants, according to the ASME Boiler and Pressure Vessel Code [45], the welding challenges in nuclear reactor conditions, and evaluation procedures for different types of weld joints.

3.2 Welding technologies for nuclear power plant components

The harsh operating environment in power plants presents challenges for both the materials that are used in the different components, and also for the welding techniques employed. Several processes are used for welding inside power plants, dependent on the components being joined (material, size, accessibility to the welding region, and shape of weld). These processes will be discussed in the following sections.

The ASME boiler and pressure Vessel Codes Section IX relates to the qualification of welding and brazing processes for nuclear components and pressure vessels [45]. Many welding techniques are included and approved for welding stainless steel nuclear power components: shielded metal arc welding (SMAW), gas tungsten arc welding (GTAW), submerged arc welding (SAW), and flux cored arc welding (FCAW) - these welding techniques will be discussed in the following sections. The investigation will include consideration of the application of the techniques to nuclear components, and the advantages and limitations of each welding process.

3.2.1 Submerged Arc Welding (SAW)

Submerged Arc Welding (SAW) can be used for joining ordinary steels, austenitic stainless steel, and duplex stainless steels while achieving acceptable properties. It was developed between the 1930s and 1940s. A high amount of heat input is used to join the materials, but the corrosion characteristics have been found to be acceptable [46]. Submerged arc welding produces clean welds due to protective action of the flux and molten slag. The spatter is minimised and also heat losses are decreased due to the weld area being submerged. This process has a high deposition rate and two or more electrodes may be used.

SAW technique is used efficiently for blade attachments in rotors of turbines since it achieves deep penetration and high welding rates [47]. It is used also in build-up welds for the repair of creep damaged rotor blade grooves, or for the repair of damages caused by stress corrosion cracking. Multiple-layer submerged arc welds can be used also for joining vessel sections [48].

Figure 3-1 shows the main configuration of the process. It is limited to down hand welding of flat plates and pipes [49]. Decreasing the height of the flux layer could

lead to an uncovered arc. The weld will have a poor appearance and porosity will increase. If the height of the flux layer is too thick the generated gases during welding will be entrapped and the surface of the weld will be distorted [50].

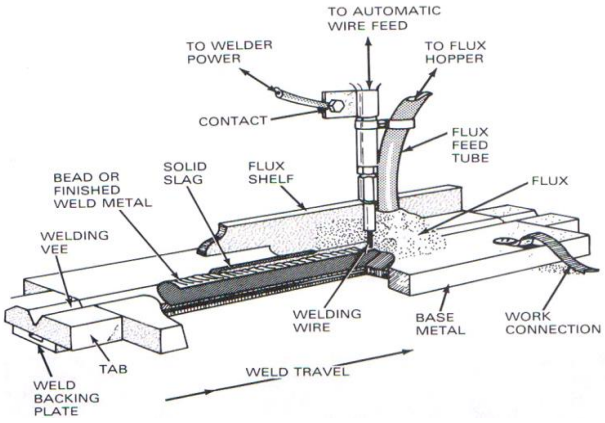

Figure 3-1 Submerged arc welding configuration [50]

3.2.2 Manual Metal Arc Welding (MMAW)

Manual metal arc welding induces an arc between a coated electrode and the work-piece. The electrode is a consumable item - the metallic core is melted by the arc. The electrode coating also melts, and serves to protect the molten pool from contamination from the atmosphere, by forming slag on the surface of the weld pool, and a shielding gas around the arc and the weld pool.

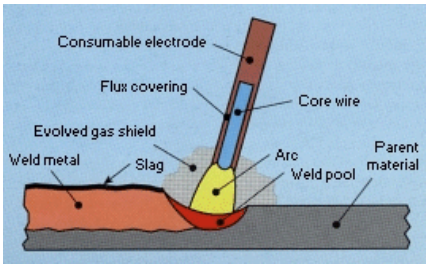

Figure 3-2 Manual metal arc welding [51]

This process can be applied successfully for structural steel, including low alloys, and also higher strength steels. High quality welds are achieved on all steels both in the workshop and on site [52]. This technique has the flexibility to deal with difficult welding positions, with ease of mobility. The process has a number of applications, such as in power plant pressure vessels and piping, and cryogenic plant pipelines.

However, MMAW is considered to be a low-speed welding technique, and the control for the process depends mainly on the skill of the welding technician. In addition, the process is limited to low joint thicknesses due to its limited deposition rate.

3.2.3 Flux cored arc welding (FCAW)

This welding technique employs a metal sheath with a core of powdered materials, and is often shielded by a gas as shown in Figure 3-3. The method is considered as an alternative to manual metal arc welding for thick cross section site welds, especially in large excavations, as shown in Figure 3-3. Welding of a joing with FCAW may take less than half the time compared to manual metal arc welding.

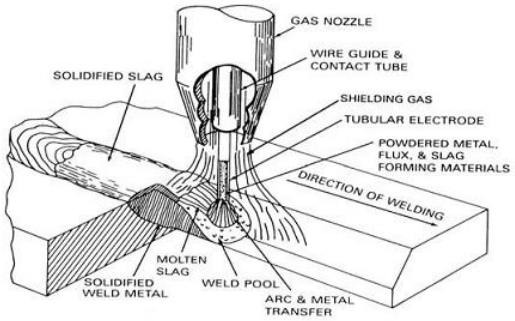

Figure 3-3 Illustration of FCAW process [53]

FCAW can also be used for joining in-situ boiler panels (mild steel), and for stainless steel and duplex stainless steel repair to pitting damage [53]. However, it has limited usage due to the large size and lower flexibility of the instruments used.

3.2.4 Gas Tungsten Arc Welding (GTAW)

GTAW is the most common form of non-consumable electrode arc welding. The method includes tungsten inert gas (TIG) welding, when the shielding gas is an inert gas; this process is used for welding a wide range of materials. Tungsten is used as the electrode for TIG welding, as it has melting temperature of approximately 3400ºC [54]. The electrode is shielded by a specific shielding gas to protect it as shown in Figure 3-4.

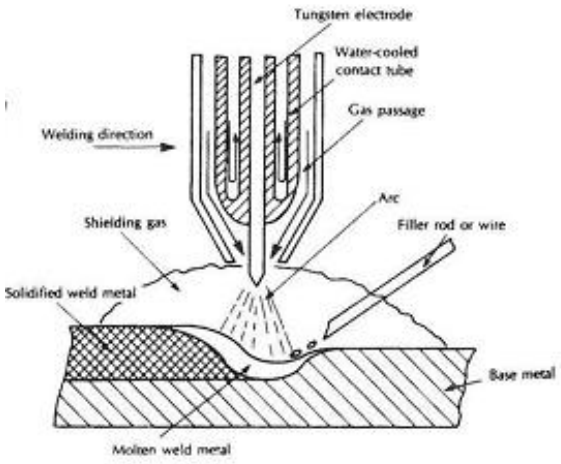

Figure 3-4 Schematic of a Tungsten inert gas welding process [55]

In GTAW, an inert gas like argon or helium may be used, or alternatively an active gas such as CO_2 or N_2. The arc current affects the weld penetration; direct current electrode negative polarity generally offers better weld penetration - approximately 70% of the heat is generated at the anode [50]. The arc voltage is the voltage between the two electrodes, which depends on the arc current. The weld pool width generally increases with an increase in the arc length. The travel speed affects the width and heat affected zone more than depth of penetration. The ratio of the wire feed speed to the travel speed determines the quantity of material deposited per unit length. An increase in the wire feed speed generally leads to a decrease in penetration.

In comparison with other techniques, the GTAW process provides a high quality weld, free of defects, with low spatter, and it can be used for welding most kinds of metals. It can be used with or without a filler material. It permits a independednt control of the heat source and the addition of filler material. GTAW has some applications inside power plants; it is used for weld joints between two halves of the sector of a vacuum vessel for the fusion nuclear reactor as shown in Figure 3-5. It consists of a double wall design. The thickness of the welded plates of the shells was 40 to 60 mm.

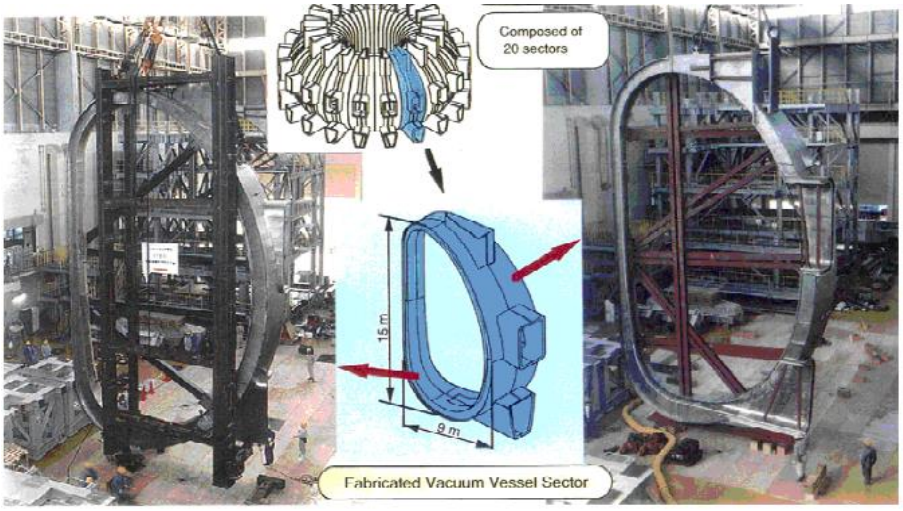

Figure 3-5 Welding of sectors of vacuum vessel [9]

3.3 Integrity of power plant welds

Welding inside power plants is different to most other applications, due to the severe working environment. Many power plant components are subjected continuously to elevated temperatures and pressures. Austenitic stainless steel alloys are commonly used, thus there are many challenges for welding stainless steel, which will be covered in the next sections.

3.3.1 Hot cracking of austenitic stainless steel

Sulphur is known to be an undesirable element in the welding of stainless steels, especially with respect to solidification cracking. It causes the formation of low-melting sulphide films along the inter-dendritic boundary and grain-boundary [32]. Sulphur and phosphorus impurities are among the main causes for hot cracking. A fully austenitic solidification (A) mode is the most crack-susceptible mode. Conversely, a ferritic austenitic solidification (FA) mode has the lowest cracking susceptibility, therefore this mode is preferred due to its high resistance to solidification cracking, as shown in Figure 3-6 [35]. The FA mode is also less susceptible to hot cracking because phosphorus and sulphur have a higher solubility in ferrite [35, 56]. The ferrite boundaries exhibit less wetting with respect to austenite boundaries. Crack propagation is more difficult along irregular grain

ferrite-austenite boundaries than it is for boundaries of one phase. Moreover, the coefficient of expansion of ferrite is less than that for austenite.

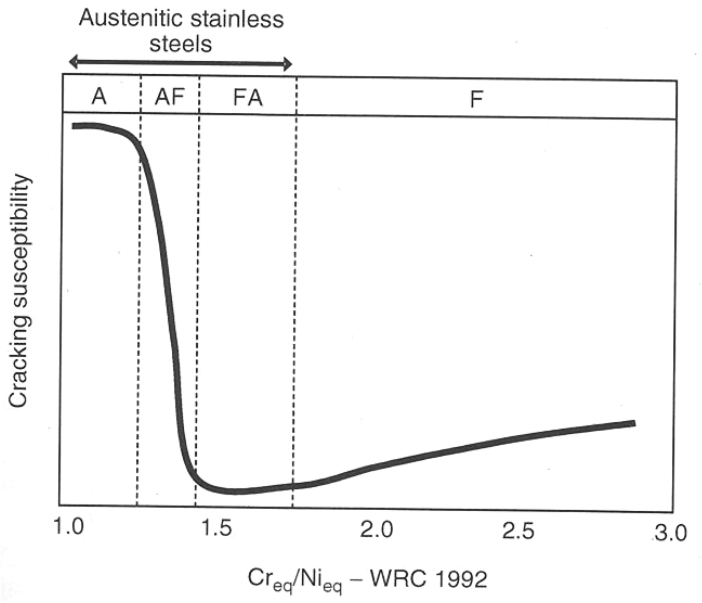

Figure 3-6 Cracking susceptible and solidification mode [35]

Ferrite presents a reduced shrinkage stress during solidification. Sauutala. et al. 2003 [40] studied the relationship between the solidification mode and the impurities ratio with respect to hot cracking. It is clear that the critical value for the ratio (Cr_{eq}/Ni_{eq}) is close to 1.48 as shown in Figure 3-7. If this ratio is lower than approximately 1.48, the solidification mode will be primary austenite, and will exhibit greater susceptibility to crack formation. This value is approximately equivalent to a ferrite number of 3. If this ratio is increased above the critical value, the solidification will be primary ferrite solidification. Most of the filler materials have a ferrite number greater than this value, with typical grades having a ferrite numbers between 5 and 15. In order to avoid crack formation with primary austenitic solidification, it is necessary to control the impurity levels so that their sum is less than 0.02%.

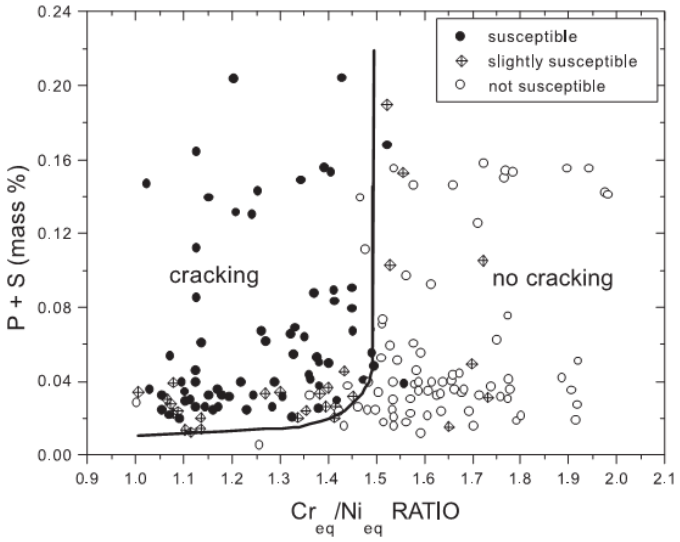

Figure 3-7 Sauutala diagram [32]

3.3.2 Hot cracking of stainless steel due to laser welding

Austenitic stainless steels have a high thermal expansion coefficient, coupled with a low thermal conductivity [57]. These properties increase the probability of distortion and cracking when using welding techniques with a high heat input. Laser welding offers advantages over conventional welding methods due to its low heat input; increasing the laser power density permits an increase in the welding speed. On the other hand, the use of laser welding affects the relevance of the Suutala diagram, due to the rapid thermal cycles and different cooling and solidification conditions [40]. Under conditions of rapid cooling, the dendrite tip promotes austenite instead of ferrite as the primary phase of solidification [35]. A modified curve was proposed by Lippold. et al. This diagram is based on the ratio (Cr_{eq}/Ni_{eq}), where the ratio is calculated according to the following relationships, which were developed by Hammer and Svenson [58].

$$Creq = \%Cr + 1{:}37 \times \%\,Mo + 1.5 \times \%Si + 2 \times \%Nb + 3 \times \%Ti \qquad (3.1)$$

$$Ni_{eq} = Ni + 0.31 \times \%Mn + 22 \times \%C + 14.2 \times \%N + \%Cu \qquad (3.2)$$

Lippold studied the influence of laser welding on different kinds of austenitic stainless steels [40]. There are two vertical lines, one dotted, the other dashed, which separate three regions, as shown in Figure 3-8. Each region has a different

solidification mode, depending on the composition of the alloy. The zone (I) primary austenitic solidification region occurs when the ratio (Cr_{eq}/Ni_{eq}) is below approximately 1.59. Region (II) alloys, having a Cr_{eq}/Ni_{eq} value above approximately 1.59 and below 1.69, exhibit primary ferrite solidification or dual austenitic and ferrite solidification [40]. Region (III) alloys, having a Cr_{eq}/Ni_{eq} value above approximately 1.69, exhibit primary ferrite solidification - no cracks were observed within this region. It is clear from Figure 3-8 that when these alloys solidify as austenitic base metal, they are much more susceptible to cracking when the combined impurities (P+S) are greater than approximately 0.02% at area I(a). If the impurities within austenitic base metal are less than approximately 0.02%, cracking will not exist at area I(b). Within region (II) the minimum value of impurities where cracking may occur is 0.04 % or more. The shift of the curve from a critical value of 1.48 in the case of conventional welding, to 1.69 for laser welding, reflects the rapid cooling conditions of laser welding. Despite the fact that the implemented values for the curve were developed using pulsed Nd: YAG laser welding, the same curve could be used for different welding processes with rapid thermal cycles, such as continuous wave laser welding and electron beam welding [40].

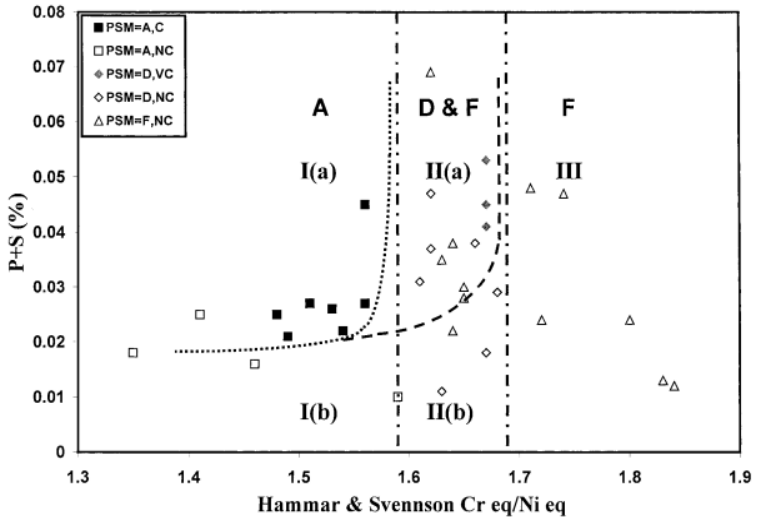

Key:
A = Austenitic PSM
D = Dual (F&A) PSM
F = Ferritic PSM
C = Cracking
NC = No Cracking
VC = Variable Cracking

PSM:
Region I: Austenitic PSM only
Region II: F or Dual PSM
Region III: Ferritic PSM only

Cracking:
Region I(a): Solidification cracking likely
Region II(a): Solidification cracking possible
Regions I(b), II(b) & III: No solidification cracking

Figure 3-8 Modified Sauutala diagram for laser weld stainless steel [40]

A recent study was performed by Karhu. et al. [59] 2008 on testing the hot cracking susceptibility of a laser welded thick section of ANSI 316LN austenitic stainless steel, using a multi-pass laser hybrid welding process (3 kW Nd: YAG-laser + GMAW). The values of Cr_{eq}, Ni_{eq} were calculated for base metal; Cr_{eq} = 21.47, Ni_{eq} = 14.33, and Cr_{eq}/Ni_{eq} = 1.50. The values of Cr_{eq}, Ni_{eq} for filler metal were Cr_{eq} = 24. 69, Ni_{eq} =20.43, and Cr_{eq}/Ni_{eq} = 1, 21.

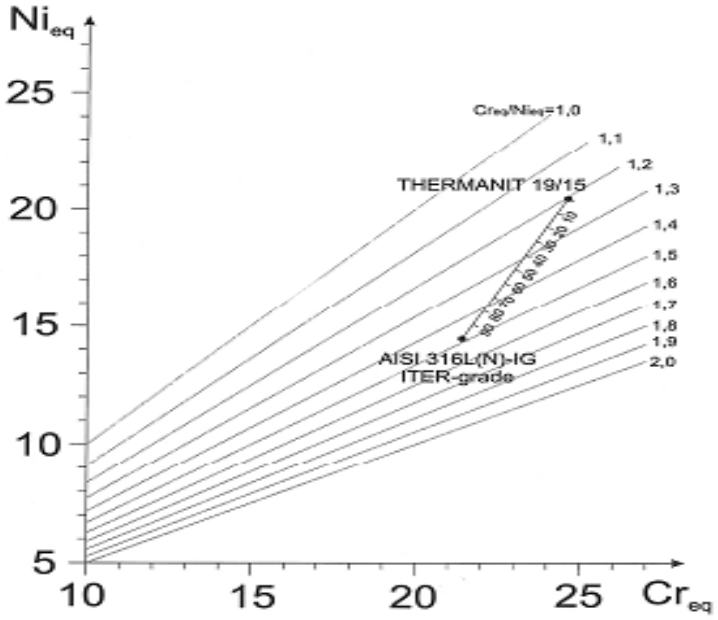

Figure 3-9 Cr_{eq} - Ni_{eq} for base metal and filler [59]

According to the values of Cr_{eq}/Ni_{eq} for both base metal and filler and dilution, the ratio is 10:30%. The value of Cr_{eq}/Ni_{eq} ratio is 1.23:1.27 in weld metal, which is below risk value according to the modified Sauutala diagram shown in Figure 3-8. A hot crack was observed on a certain pass of the welding. Filler wire material with higher ferritic ratio was used previously to improve the Cr_{eq}/Ni_{eq} value [59], and to prevent hot cracking. Another study was performed by Xudong. et al. 2010 [60] on the welding of 50mm thick 316L, using a multi-pass narrow-gap welding technique with an 8 kW disc laser. A hot crack was initiated in the build-up layers, as shown in Figure 3-10a. The ferrite number was less than 1%, due to the use of nitrogen as a shielding gas.

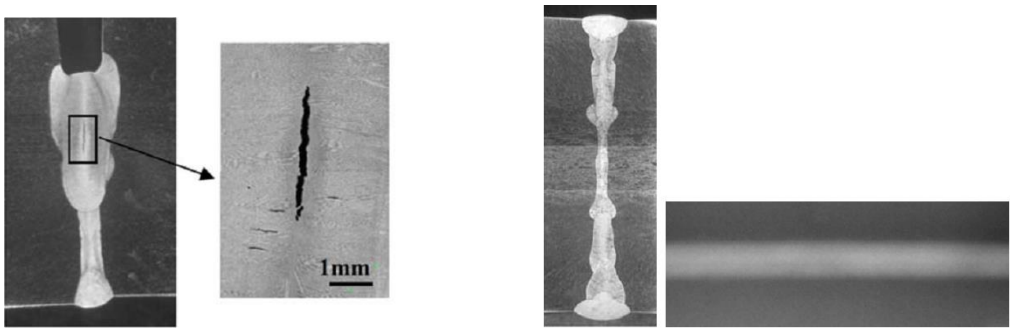

a- crack initiated b- No crack due to increase ferrite content(X-ray)

Figure 3-10 Cross section influence due to ferrite percent [60]

When filler material is used with higher ferrite content steels, it can inhibit crack occurrence. Table 3-1 shows 4 types of materials; cracks were observed for all the weld metal (A, B, C). but no cracks were observed when the filler wire (d) was used with different welding conditions as shown in Figure 3-10 b. The observed ferrite concentration in the weld metal was decreased to 6:11%, due to the influence of nitrogen.

Table 3-1 Effect of welding conditions and wire composition on welding crack [60]

Welding conditions			Wire composition (ferrite %)			
Laser power (kW)	Welding speed (m/min)	Defocused distance (mm)	A (5.9)	B (9.2)	C (9.4)	D (16.8)
4	0.15	7	○	○	○	○
6	0.225	7	—	—	×	○
	0.3	7	×	—	×	○
		10	×	×	×	○
		15	×	—	×	○
	0.4	10	—	—	×	○

○:No crack ×:Crack -:no data

3.3.3 Corrosion of austenitic stainless steel

Austenitic stainless steel has a good corrosion resistance under normal conditions and at room temperature, due to a passive film formation of chromium oxide on its surface. However, due to welding conditions and severe working conditions inside nuclear reactors (increased temperature and pressure), its susceptibility to corrosion increases. Nuclear power plants, which use seawater for cooling, are considered to

have an extremely high potential for chloride stress corrosion cracking at elevated temperatures.

3.3.3.1 Intergranular corrosion due to carbide precipitation (sensitization)

Intergranular corrosion in austenitic stainless steel is a very serious problem. It is mainly caused by sensitization, which is the formation of chromium carbide precipitation in the grain boundaries. It will lead to a decrease in the chromium ratio near to the grain boundaries, causing them to become anodic for the alloy, and leading to the formation of corrosive media. The main factors relating to this phenomenon are temperatures from 600ºC to 850ºC, and also the carbon content of the alloy [35]. In austenitic stainless steel, the presence of nickel decreases the solubility of the carbon, which may increase the probability of sensitization occurring. As shown in Figure 3-11, as the percentage of carbon in the steel decreases, the probability of sensitization is reduces; at 0.08% carbon, the sensitization starts at 600-900ºC only after 30 seconds, whereas at 0.03% carbon content, the sensitization starts at 600-750ºC after 50 minutes.

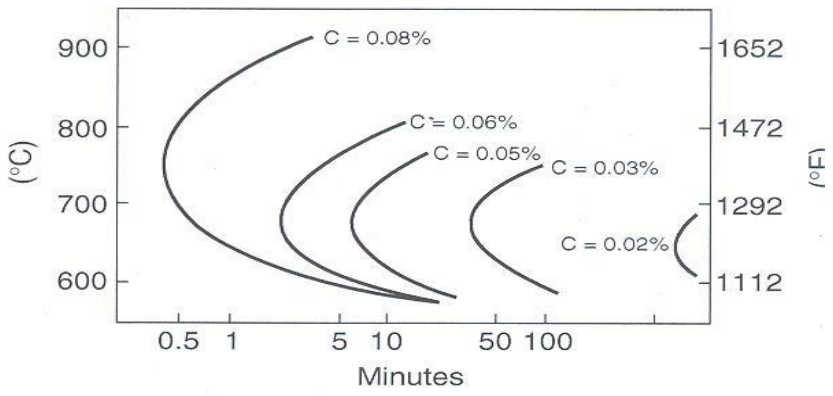

Figure 3-11 Intergranular corrosion at different carbon content [35]

Sensitization can be prevented by using low-carbon austenitic stainless steel grades [35]. It can also be prevented by using stabilized stainless steel, created by adding niobium or titanium, such as in 321 or 347 austenitic stainless steels [34], or by increasing the cooling rate, leading to a decrease in the time the steel is exposed to sensitization temperatures.

3.3.3.2 Knife-line attack

If the temperature is increased to 1299ºC, steel stabilized against chromium carbide formation may be susceptible to another defect known as knife-line attack [58]. This defect is caused by the dissolution of Ti carbides, which forms free carbon atoms. These atoms can combine again with chromium to form chromium carbides, at a high cooling rate in a narrow area near to the fusion zone [34, 35].

3.3.3.3 Stress corrosion cracking (SCC)

Stress corrosion cracking represents the most serious corrosion mechanism in metals and specially stainless steel. It is defined as corrosion mechanism that forms a cracks and could lead to an unexpected sudden failure of metals and alloys subjected to a tensile stress in a highly corrosive environment [35]. SCC is related to the percentage of Ni present in the steel - the maximum susceptibility to SCC occurs when the Ni percentage is between 5-20% [35]. Austenitic stainless steels are subjected to stress corrosion cracking under specific conditions, severe thermal cycles, where micro-segregation of some elements like molybdenum occurs, and due to induced residual tensile stresses, leading to a decrease in SCC resistance.

Working environments inside power plants are considered to be another cause of SCC, due to aggressive conditions such as chloride rich media, reactor water cleanup, and core spray. In such environments, attack in the form of pitting or SCC may occur [36]. This type of corrosion can be avoided by using a certain type of welding which induces minimum residual stresses, using ferritic or duplex stainless steel instead of austenitic, or by preventing sensitization. Preheating for stress relief leads to a decrease in stress and consequently in SCC, but on the other hand it may lead to sensitization if the preheating temperature is in the range of sensitization [35].

3.3.3.4 Pitting and crevice corrosion

A local breakdown of the passive film on the surface of stainless steel occurs at the sites of small pits in the protective oxide layer. This takes place under certain conditions involving corrosive environments and elevated temperatures. This type of corrosion is associated with metallurgical features such as grain boundaries [35]. The metal surface is subjected directly to corrosive media at these pits. This kind of

corrosion is dangerous since it is not clearly visible on the surface of the metal; it forms as small pinholes on the top surface.

Crevice corrosion conditions are similar to pitting, but do not require grain boundary conditions for initiation. It mainly takes place in bolted structures, due to the space between the bolt head and surface. A potentiodynamic test was performed on 316L stainless steel, to determine the pitting potential as shown in Figure 3-12. The test compares the potentiodynamic curves for the base metal as received, and after welding and after heat treatment (annealing) [42]. The results show a small difference, between the pitting potential for the as-received and the welded samples, of about 0.6 V. The result also shows a reduction of around 0.4 V in the pitting potential for the heat treated sample, due to the formation of a large amount of chromium carbides, sensitized during the heat treatment, resulting in the depletion of chromium in some areas, which then became more susceptible to pitting. This result indicates that laser welding of AISI 316LTi did not significantly affect the corrosion properties of the base material.

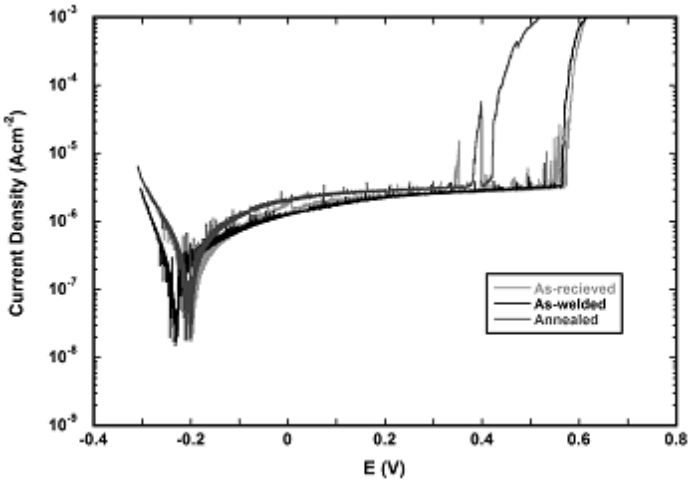

Figure 3-12 Potentiodynamic tests results [42]

3.3.4 Hydrogen embrittlement

Hydrogen is a very small atom. It can diffuse more rapidly than large atoms between metals atoms. The presence of hydrogen may be a reason for the fracture of metal, by making cleavage easier or by developing local plastic deformation. These influences lead to embrittlement of the metal [61]. Ferrite stainless steel has a body-centred

cubic (BCC) crystal structure, which means that small holes are present between the metal atoms, but the channels between these holes are relatively wide. Consequently, hydrogen has a relatively high diffusion coefficient and low solubility. In contrast, the austenite FCC (face-centred cubic) lattice has larger holes between the metal atoms but the channels between the lattice are smaller, so austenitic stainless steel has a higher hydrogen solubility and a lower diffusion coefficient. Consequently, austenitic materials tend to take longer to become embrittled by hydrogen diffusion, comparing to ferritic materials.

3.3.5 Irradiation Embrittlement

Neutron irradiation embrittlement can affect the predicted service life of pressure vessels in nuclear reactors. The operating condition of the reactor pressure vessel (RPV) is severe; temperatures of around 290°C at pressures ranging from 7 MPa in boiling water reactors to 14 MPa in pressurized water reactors [48]. This combination of temperature and pressure conditions can result in rapid unpredictable fracture, if the vessel steel is sufficiently brittle [48]. Embrittlement due to exposure to neutrons usually occurs at a vessel's "beltline," that is a wall closest to the reactor fuel. Irradiation embrittlement is usually characterized by the increase in the ductile-to-brittle transition temperature (DBTT). Steels with a higher proportion of copper and nickel will tend to be more susceptible to embrittlement. Vessels in nuclear reactors are exposed to neutron energies in the order of several million electron volts (MeV) - these high-energy neutrons are the source of embrittlement [48].

3.3.6 Residual stresses

Residual stresses are stresses that still affect the component after the original cause of the stresses (external load, heat gradient) has been removed. [62]. It arises mainly because of misfits (incompatibilities) between different regions of the material.

Controlling, and understanding the behaviour of residual stresses in welding region is important because no external evidence appears on the components suffering from residual stresses, making it a particularly dangerous phenomenon. Moreover, residual stress can combine with other types of stresses in the body and contribute to failure.

A stress field is induced in the body by applying forces or displacements. The strain field is termed ‘compatible’ if it arises purely from elastic deformation. Such strains are reversible and, upon removal of the load, the body will not be subject to residual stress.

When a body contains some form of inelastic strain, such as plastic flow strain, thermal strain or phase transformation strain, and if the elastic deformation cannot recover this strain to produce an equilibrium between stress and strain in all places, consequently residual stress field will remain [63].

Residual stresses have different origins due to mechanical or thermal effects. In welding, the residual stress is mainly tensile near the weld region due to thermal stresses [64]. Tensile residual stresses occur within the welding processes due to either restraints against thermal contraction, or where the thermal contraction strain is greater than the yield strain of the material [65].

Residual stresses have a significant influence on the fatigue lives of engineering components. Tensile residual stresses in the surface of components are generally undesirable. Near surface tensile residual stress tend to accelerate the initiation and growth phases of the fatigue process and stress-corrosion cracking [10, 11].

On the other hand, compressive residual stresses near a surface may lead to improvements in the fatigue lifetime [11, 66]. Generally, residual stresses improve the operation of any object when they act in the plane of applied load in opposite sense.

There is a large volume of previous investigations of residual stresses distributions in conventional arc welding and autogenous laser welding. However, detailed study of the residual stress behaviour for NGLW has not so far been much reported. There is only one previous study that investigated the surface residual stress distribution for a NGLW process without validating the results [60]. Therefore there is a knowledge gap in understanding the cross sectional residual stress characterisations and on how various welding procedures and parameters affect residual stresses in NGLW.

Bang *et al*. (2010) compared the residual stress change between a 304 stainless steel sample welded with hybrid laser-arc welding and submerged arc welding, as shown in [67] Figure 3-13.

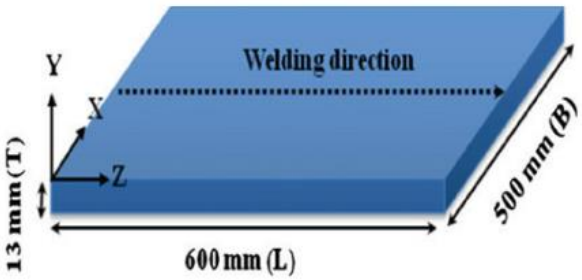

Figure 3-13 Dimension of welded specimen

The values of residual stresses were measured at 1 mm in depth and z =300mm. The maximum residual stress in the Z direction σ_{zz} (welding line direction) is the tensile stress, which occurs in the welded joint, owing to the material resistance to contraction produced by cooling after welding. The residual stress exceeds the tensile stress value - the maximum value appears at the HAZ limit. The value of the total residual stresses was approximately 10% lower in case of hybrid laser welding compared to submerged arc welding, due to the high cooling rate for the hybrid laser - arc welding. Outside the HAZ, the residual stresses become compressive for balancing as shown in Figure 3-14 [67].

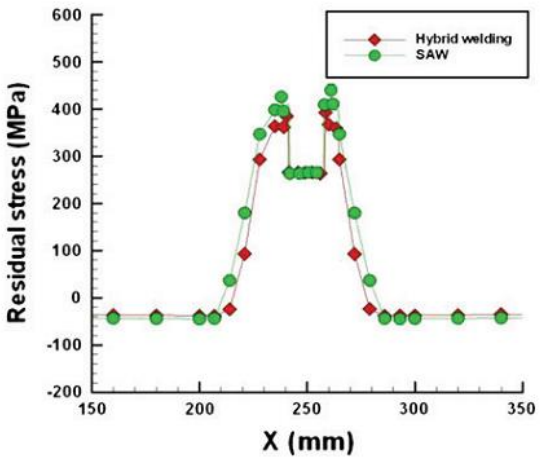

Figure 3-14 Residual stresses along the welding pass direction σ_{zz}, across the the plate at Z = 300 mm and the plate at Z = 300 mm and = -1 mm

The residual stresses in the width direction σ_{xx}, and in the thickness direction σ_{yy}, are found to be totally tensile and to reach the maximum value in the heat affected zones as shown in Figure 3-15.

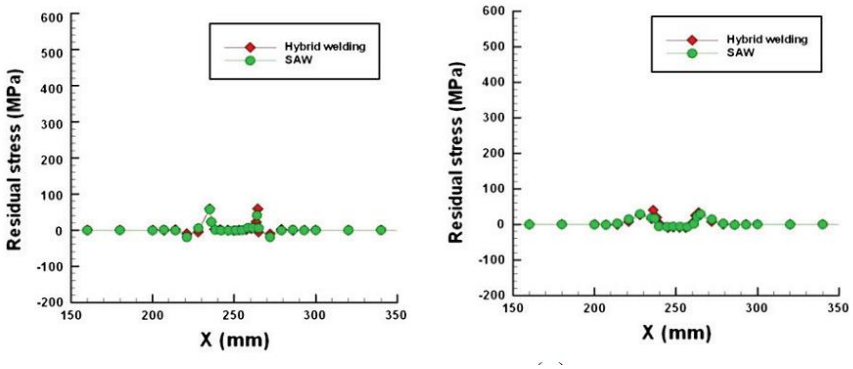

a) Thickness direction σ_{yy} b) Width direction σ_{xx} b

Figure 3-15 Residual stresses in welding joint , across the the plate at Z = 300 mm and the plate at Z = 300 mm and = -1 mm

3.3.7 Creep

The strength of metals generally decreases with increasing body temperatures. By increasing the temperature the strength become more time sensitive. Creep in metals is defined as the slow plastic deformation under load and high temperature, and it is time dependent. A Creep test measures strain versus time at constant high temperature and constant load. Test time is typically 2,000 to 10,000 hours. Creep testing is very important and provides more useful information for components, which are under constant load or high temperature conditions like steam power plant. It is useful also for long term applications, which are strain limited, such as turbine blades. The Creep Curve is divided into three partitions as shown in Figure 3-16. Primary creep proceeds at a diminishing rate due to work hardening of the metal. Secondary creep (steady state) proceeds at a constant rate because a balance is achieved between the work hardening and annealing (thermal softening) processes. Tertiary creep in which the creep rate increases due to necking of the specimen and the associated increase in local stress and failure occurs [68]. Creep is much more hazardous in fossil fuelled power plants due to high operating temperatures. In contrast, in nuclear reactors, the operating temperature is around 290°C [48]. This temperature limit will not affect reactor structure with creep, since it is very low temperature comparing to the melting temperature of the materials.

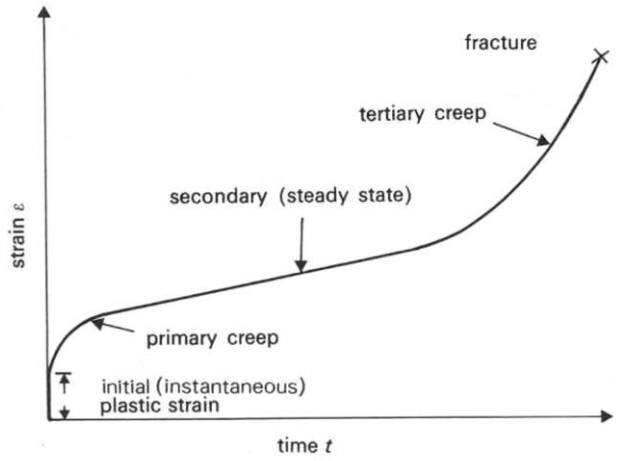

Figure 3-16 Stages of creep [68]

3.4 Residual stresses measurements

It is important to quantify the residual stress field in a welded region using a reliable technique; it is considered to be a key design factor to prevent failure and manage the lifetime of any engineering structure [10]. However, welding residual stresses are difficult to predict because several complex transient phenomena are involved in the welding process.

Residual stress can be measured by different techniques; however, few of these can offer a complete spatial distribution of residual stress. Measurement of residual stresses in thick section weld presents challenges [62]. There are two measurement concepts for residual stresses (destructive and non-destructive): the contouring method is a destructive method, whereas deep hole drilling is a semi-destructive method. Both methods, which rely on stress relaxation, can offer characterisation of the residual stress distribution across the workpiece [69]. X-ray diffraction and neutron diffraction techniques are non-destructive techniques, and will be introduced in the next sections.

3.4.1 Stress relaxation technique

This technique relies on measuring the magnitude and the direction (tension or compression) of released strain, by cutting the sample which contains the stress, to create a stress free surface. The stress is released in the form of surface deformation,

and is determined by measurement of the magnitude of the deformation of the cut surface. There are different methods of sample cutting: drilling, partitioning and milling, consequently the concept has limited usefulness with complex workpiece shapes.

3.4.1.1 Deep hole drilling technique

The deep-hole drilling (DHD) technique is a semi-invasive residual stress measurement method for thick section metallic components [70]. DHD relies on the measurement of strain relaxation after material removal. A small-diameter hole is drilled through the component. The diameter of the hole is measured accurately at different angular positions and equal intervals along the hole axis. A column of material with the reference hole as its axis is then trepanned from the specimen using electro discharge machining (EDM), allowing the residual stresses in the column to relax as shown in Figure 3-17. The diameter of the hole is re-measured using an air probe at the same angular positions around the reference hole. The air probe works by calculating the clearance between the gauge and the hole from the pressure required to blow air from the gauge into the gap. The residual stresses are then calculated from the change in diameter of the hole.

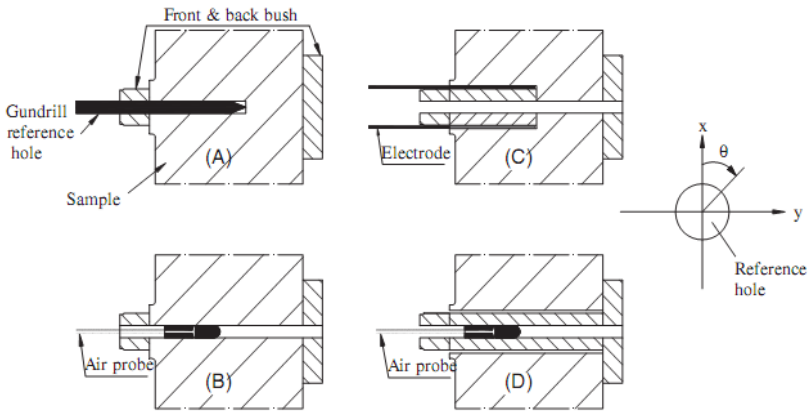

Figure 3-17 Deep hole drilling for measurement of residual stresses [70]

The normalised radial distortion $\overline{U_{rr}}$ is related to the in-plane residual stresses σ_{xx}, σ_{yy}, σ_{xy} as shown in [70].

$$\overline{\mathbf{U_{rr}}} = \frac{\mathbf{1}}{\mathbf{E}}\left[\boldsymbol{\sigma}_{\mathbf{xx}}\,\mathbf{f}(\boldsymbol{\theta}) + \boldsymbol{\sigma}_{\mathbf{yy}}\,\mathbf{g}(\boldsymbol{\theta}) + \boldsymbol{\sigma}_{\mathbf{xy}}\,\mathbf{h}(\boldsymbol{\theta})\right] \quad (3.3)$$

$$\overline{\mathbf{U_{rr}}} = \frac{\boldsymbol{\Delta}\mathbf{d}(\boldsymbol{\theta})}{\mathbf{d}(\boldsymbol{\theta})} \quad (3.4)$$

$$\boldsymbol{\Delta}\mathbf{d}(\boldsymbol{\theta}) = \mathbf{d}'(\boldsymbol{\theta}) - \mathbf{d}(\boldsymbol{\theta}) \quad (3.5)$$

where: d (θ) and d′ (θ) correspond to the diameter of the reference hole before and after trepanning, and

$$f(\theta) = (1 + 2\cos 2\theta)\,,\ \ g(\theta) = (1 - 2\cos 2\theta),\ h(\theta) = (4\sin 2\theta) \quad (3.6)$$

This is repeated at m different angular measurements. The previous equation can be formed in the matrix form as shown in :

$$\overline{\mathbf{U_{rr}}}(\boldsymbol{\theta}) = -\frac{\mathbf{1}}{\mathbf{E}}[\mathbf{M_{2D}}\boldsymbol{\sigma})] \quad (3.7)$$

Residual stresses can be calculated according to

$$\boldsymbol{\sigma} = -\mathbf{E}\mathbf{M}^{*}_{\mathbf{2D}}\overline{\mathbf{U_{rr}}}(\boldsymbol{\theta}) \quad (3.8)$$

Where M^{*}_{2D} is the inverse of matrix $M_{2D.}$

3.4.1.2 The contour method

The contour method is considered one of the destructive residual stresses measurement techniques. The method involves four steps: specimen cutting, contour measurement, data reduction and stress analysis. The first step is a flat cut - which is very important in order to achieve good accuracy - therefore wire electric discharge machining (EDM) is used instead of hard cutting tools, as shown in Figure 3-18. The ideal cut for contour method should be zero width, and introduce no stresses, and allow no plasticity at the tip of the cut [71]. This requirements is practically impossible, however EDM skim cutting conditions is the closest technique to satisfy these requirements.

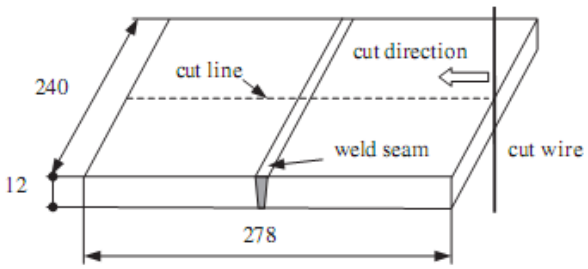

Figure 3-18 Cutting direction through weld sample [72]

After cutting, the relief of stress acts normal to the created surface. It causes the surface to deviate if the residual stress is not zero. The second step is contour measurement. It is preferential to use a coordinate measurement machine (CMM) with a contact probe, or a laser detector measurement head, in order to achieve sufficient accuracy. The third step is data reduction; the measured data sometimes contains errors due to cutting stresses or measurement conditions, poor surface flatness, or distortion due to welding operations. Smoothing of the measured data digitally in order to minimize the errors in the data is therefore crucial in order to achieve an accurate stress evaluation with the contour method [72]. Figure 3-19 shows a scanned surface before and after data reduction and smoothing of the scanned surface.

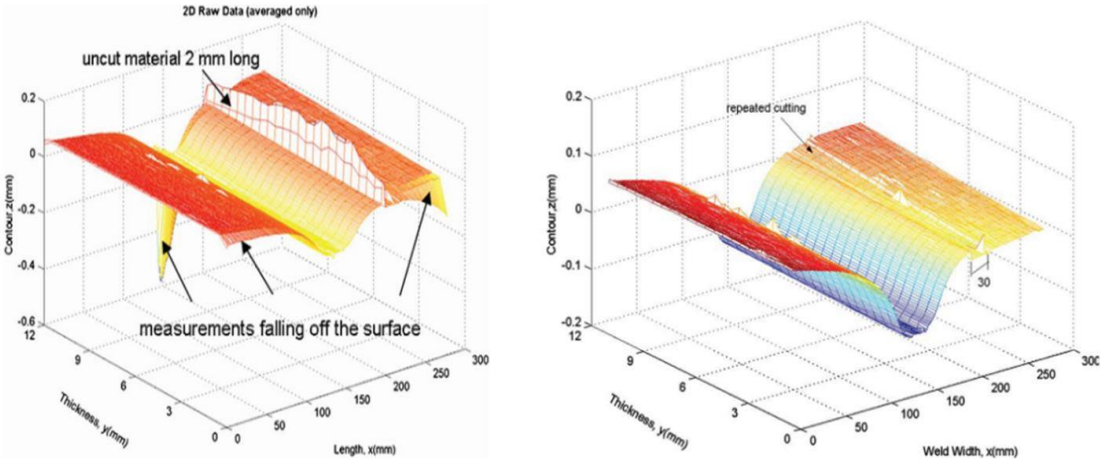

Figure 3-19 Scanned data before and after data reduction (smoothing) [72]

The final step is stress analysis using a FE model applying the smoothed deformation data of the profile, with opposite sign.

Output results appear as shown in Figure 3-20. The tensile residual stress is concentrated in the middle cross section around the welding area, and a compressive residual stress emanates from both sides. In the right-hand section of the diagram, the result is not reliable due to cutting error.

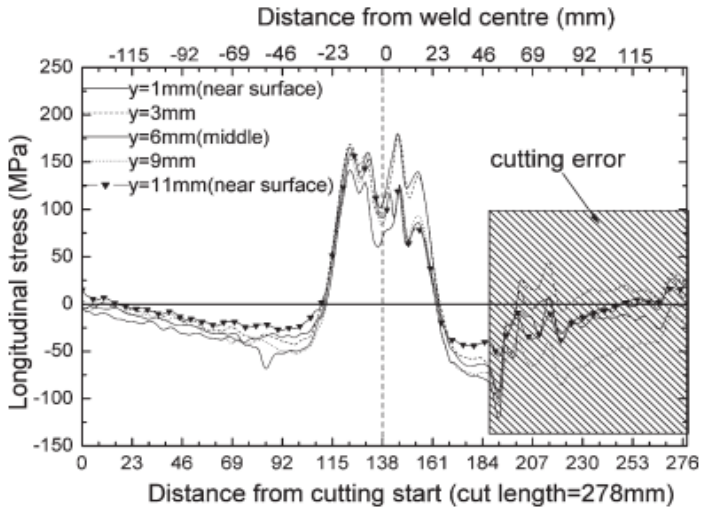

Figure 3-20 Residual stress profile [72]

3.4.2 Non-destructive measuring methods

There are two main non-destructive measuring methods; X ray, and neutron diffraction. Interactions between electromagnetic radiation such X Ray and condensed matter result in scattering from the individual atoms of a regular crystal structure causes an initially parallel beam of incident radiation to be diffracted from its original path. Diffraction angle depends on the spacing between the scattering atoms. Neutron beams also follow the same behaviour. However, X-rays are scattered by the electron clouds of atoms, while neutrons are scattered by atomic nuclei. This results in weaker interaction between most of the materials with neutrons than with X rays. Consequently neutrons penetration capability is higher with respect to X ray. The penetration depth of X-rays for most of metallic materials within tens of microns, however it could be few centimetres in neutron diffraction [62, 73].

3.4.2.1 Neutron diffraction

Neutron diffraction is considered as a non-destructive measurement method for residual stresses. Neutrons penetrate readily into most materials, making the method

more efficient compared to X-ray diffraction, as neutrons are not easily absorbed, so can penetrate deeper into most metallic components, permitting measurement of lattice spacing, strain, residual stresses in thick welded cross-sections [74].

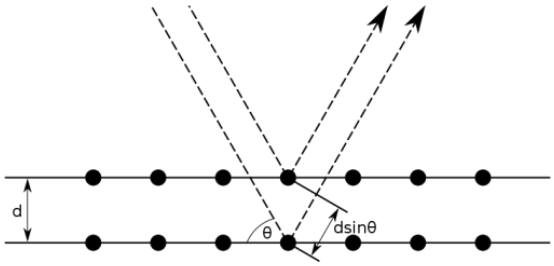

Figure 3-21 Bragg diffraction planes [75]

Bragg explained this result by modelling the crystal as a set of discrete parallel planes separated by a constant parameter d, where λ is the wavelength of incident wave, d is the spacing between the planes in the atomic lattice, and θ is the angle between the incident ray and the scattering planes, as shown in Figure 3-21. The diffracted beam is produced when the difference in the travelled distance between two successive diffracted beams is equal to the wavelength, as stated by Bragg's law:

$$\lambda/2 = d \sin \theta \tag{3.9}$$

To derive a strain value, the lattice spacing d is determined at two positions: far from the welding position a reference spacing d_{ref}, and near to the welding position at spacing d. The strain at any measurement point on each sample is then calculated from:

$$\boldsymbol{\varepsilon} = \frac{\boldsymbol{d - d_{ref}}}{\boldsymbol{d_{ref}}} \tag{3.10}$$

Strain is measured in three orthogonal directions with respect to the welding directions A (axial), T (transverse) and N (normal). The strain components are along the sample axis (axial strain ε_A), transverse to it (transverse strain ε_T) and through the wall (normal strain ε_N), as shown in Figure 3-22.

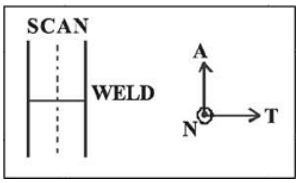

Figure 3-22 Directions of strain measurement [74]

With the three measurements of strain at each position, the residual stress can be calculated through a generalized Hooke's law.

$$\boldsymbol{\sigma_A} = \frac{\mathbf{E}}{\mathbf{1+\nu}}\left[\ \boldsymbol{\varepsilon_A} + \ \frac{\boldsymbol{\nu}}{\mathbf{1-2\nu}}(\boldsymbol{\varepsilon_A}\ + \boldsymbol{\varepsilon_T}\ + \boldsymbol{\varepsilon_N}\ )\right] \qquad (3.11)$$

$$\boldsymbol{\sigma_T} = \frac{\boldsymbol{E}}{\mathbf{1+\nu}}\left[\ \boldsymbol{\varepsilon_T} + \ \frac{\boldsymbol{\nu}}{\mathbf{1-2\nu}}(\boldsymbol{\varepsilon_A}\ + \boldsymbol{\varepsilon_T}\ + \boldsymbol{\varepsilon_N}\ )\right] \qquad (3.12)$$

$$\boldsymbol{\sigma_N} = \frac{\boldsymbol{E}}{\mathbf{1+\nu}}\left[\ \boldsymbol{\varepsilon_N} + \ \frac{\boldsymbol{\nu}}{\mathbf{1-2\nu}}(\boldsymbol{\varepsilon_A}\ + \boldsymbol{\varepsilon_T}\ + \boldsymbol{\varepsilon_N}\ )\right] \qquad (3.13)$$

Where E is the Young's modulus and ν the Poisson's ratio

3.4.2.2 X-Ray diffraction (XRD)

X-ray diffraction (XRD) has been in use since the 1960's; XRD stress measurement can be a powerful tool for failure analysis or process development studies. The residual stresses present in a component may either accelerate or arrest fatigue or stress corrosion, depending on the type of residual stress [73]. XRD can be applied to fine-grain crystalline materials; these materials give good diffraction peaks with high intensity and free from interference for any orientation of the sample surface. Both X-ray and neutron diffraction methods measure the strain in a material from changes in the crystal lattice, and from this the residual stress producing the strain is calculated, assuming a linear elastic distortion of the crystal lattice; atoms are irradiated by X-ray beams or neutrons, and the scattered radiation undergoes interference. In certain directions the interference is constructive, whereas in other directions it is destructive, depending on the spacing between planes and the wavelength of the incident radiation. Bragg's law governs constructive interference as shown in equation (3.9). Knowing the wave length of the x-ray beam, and measuring the diffraction angle 2θ using a Diffractometer as shown in Figure 3-23 , it is possible to determine the spacing d.

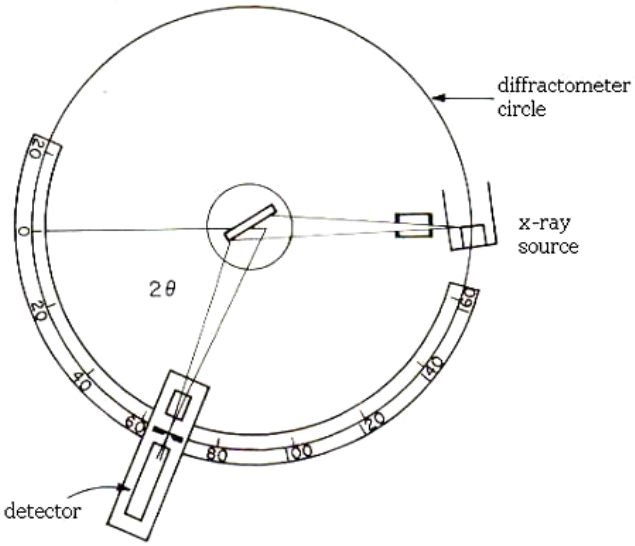

Figure 3-23 Circular diffractometer [76]

In a similar way to the previously described techniques, the spacing is calculated at a stress-free area, and therefore the strain in the stressed area can be calculated and consequently the stresses can be calculated according to equation (3.10)

The limitation of X-ray diffraction technique is the depth of penetration (tens of micrometers) as mentioned previously due to beam absorption [62].

3.5 Mechanical properties of welded joints

Welded joints are potential sites of weakness in any structures. Severe thermal cycles can lead to property degradation of the base materials due to the probability of weld defects, phase transformation, and the influence on the grain size. Welding parameters have a major effect on the solidification structure and geometry of the melting region of weldment for all welding techniques [77]. The filler materials used in multi-pass welding processes and the use of shielding gasses can have an influence on the microstructure and properties of the welded joints. Brittle sigma- phase propagation in stainless steel is considered as the main reason to change the mechanical properties of the welded joint. The ASME qualification standards for welding and brazing in boilers and pressure vessels include procedures for the mechanical qualification of welding process [45]. There are several standard

qualification tests for welds: QW-150 (tensile testing), QW-160 (guided-bend tests), QW-170 (notch-toughness tests) and QW-182 (fracture tests).

3.5.1 Tensile test

Tensile tests are the most common tests used to characterise welds. The tests are carried out on a standard test specimen; they provide information on proof stress, yield point, maximum tensile strength, elongation, and ductility behaviour. Weld beads above the parent material surface are usually removed in cases where they are removed in service. If failure occurs outside of the welded cross-section area, a specimen with a reduced cross-section may be used to measure the actual values of the tensile strengths at the weld joints, since weld material strength exceeds the base metal strength. Failure will occur at limiting strain; poor welded material ductility will fail first, while high ductile material will sustain the load [55].

Benjamin et al. [78] have characterized arc-welded austenitic 316LN stainless steel using the tensile test. The results show improved strength for the welded region with respect to the base material, as shown in Table 3-2. The tensile test was performed according to ASTM E8M-04 guidelines, with sample dimensions as shown in Figure 3-24.

Table 3-2 Tensile test results for austenitic stainless steel [78]

Specimen No.	1	2	3
Ultimate tensile strength (MPa)	593.15	601.29	591.52
Base Material Strength (MPa)	560		

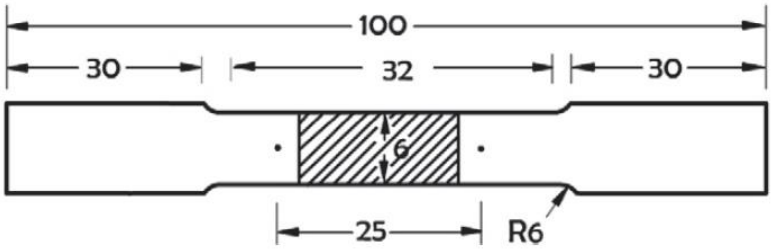

Figure 3-24 Flat tensile test sample specifications, all dimensions in mm [79]

Yilmaz et al [77] studied the effect of GTAW and GMAW on 316L stainless steel. The results show an increase in strength near to the weld bead, however the increase in strength is higher for GTAW due to the narrower weld pool and higher power concentration.

Another study compared autogenous laser welding with tungsten inert gas (TIG) welding of stainless steel [80]. It concentrated on the relation between the microstructure and mechanical properties of the welded region in 304-grade stainless steel. The TIG welded joint was called (J_T); it was subjected to high heat input and low welding speed, which causes a wider HAZ. The laser-welded joints were denoted by J_L, and characterised by higher welding speed due to the higher power density, which also led to a narrower HAZ. The higher cooling rate led to the formation of finer grains, and resulted in higher tensile strength compared to J_T. The results showed that the laser weld pool will be less susceptible to the micro-segregation of some important alloying elements, and will also be less subject to Cr depletion region sensitization, thereby resulting in lower degradation of mechanical properties. Thus, laser welding shows promising properties for stainless steel elding, however knowledge of the NGLW technique for thick-section welding is still limited, and more research is needed.

3.5.2 Bend test

This test is carried out to evaluate the joint performance, the weld zone characteristics, and the ductility of the welded joint across the seam [79]. This test cannot be considered as a quantitative means of predicting service performance in bending operations. The severity of the bend test is dependent on the angle of bend, and also the inside diameter of the bent specimen, and of the cross-section of the specimen. There are three types of bending test: transverse, longitudinal, and side bend, along the axes of bending with respect to the welding direction [55]. Bend tests can be performed according to ASTM E190-92 specifications.

The bending test rig is shown in Figure 3-25. The angle at which either fracture occurs or a crack initiates is recorded. The bend angle and fracture appearance provide a guide to the ductility of the joint and the weld quality. A previous study of austenitic stainless steel welded joint mechanical behaviour shows very good

ductility behaviour, using the bending test [78]. The samples are qualified by the value of angle at which crack is initiated, and how the depth and width of crack at full bending angle = 180º.

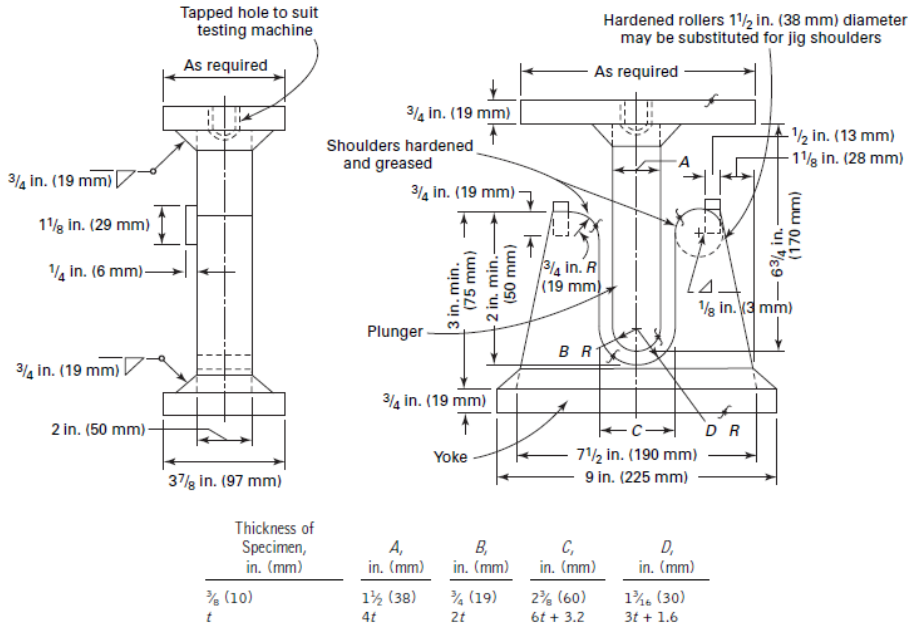

Thickness of Specimen, in. (mm)	A, in. (mm)	B, in. (mm)	C, in. (mm)	D, in. (mm)
3/8 (10)	1 1/2 (38)	3/4 (19)	2 3/8 (60)	1 3/16 (30)
t	4t	2t	6t + 3.2	3t + 1.6

Figure 3-25 Bending test set up [45]

3.5.3 Impact fracture toughness test

The impact test is a method of measuring the toughness of a material; the resistance of a material to fracture under dynamic loading is often critical. A test specimen is cut such that the longitudinal axis of the test specimen is perpendicular to the direction of welding, as shown in Figure 3-26. A drop weight is used to assess the energy absorbing characteristics of the tested sample.

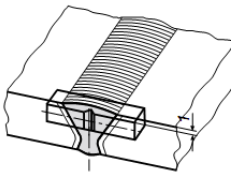

Figure 3-26 Impact test specimen [81]

The most common used test is the Charpy test, where a V or keyhole notched specimen is cut from thick section welded plate, such that the notch is machined at the weld centre, as shown in Figure 3-27. This test is required for weld qualification

in boiler and pressure vessel component welding codes. The amount of energy absorbed in the fracture is recorded, and the absorbed energy is defined as the impact toughness of the material according to ASTM E23-05 specifications for preparing and testing the impact specimens.

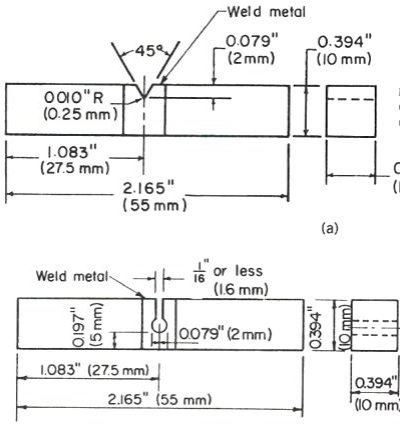

Figure 3-27 Impact test sample [55]

Impact testing can be used in conjunction with tensile tests in distinguishing between different welding conditions. A welded joint may show a tensile strength equivalent to the parent material, whereas the absorbed Charpy impact energy for the weld may be less than 50% of that of the parent material. Yilmaz et al. [77] studied the influence of the GTAW and GMAW welding process on 316L, and 304L austenitic stainless steel. The toughness was increased in the welded bead region with respect to base material for both techniques, and the toughness of 316L is higher than that of 304L due to the molybdenum content. GTAW weld bead toughness is higher than that of GMAW for both alloys, due to the higher oxygen potential in the GMAW process, and higher delta ferrite percentage near to the weld bead.

Benjamin et al. [78] studied the influence of the welding parameters of electron beam welding on the toughness of austenitic stainless steel. Their results show that the resultant toughness of the welded region is directly proportional to the cooling rate, due to the variation in the grain size. The toughness is reduced at lower temperature, mainly due to delta ferrite brittleness behaviour at low temperature. However, there is still a lack of accurate and reliable data on impact fracture resistance for laser welding processes, especially NGLW toughness behaviour.

3.5.4 Fatigue test

Fatigue behaviour is a very important factor in weld bead quality evaluation, especially for core components. It is considered to be one of the dominant mechanisms in the degradation of pressure boundaries, in addition to stress corrosion cracking [19]. The largest number of weld failures is attributed to either the high-cycle fatigue caused by flow induced vibration, or to fatigue in general. Fatigue damage is induced by cyclic variations of pressure, temperature and flow induced vibration, thereby reducing the lifetime of structures and components. Fatigue test should be performed according to ASTM standard E466-90 as shown in Figure 3-28.

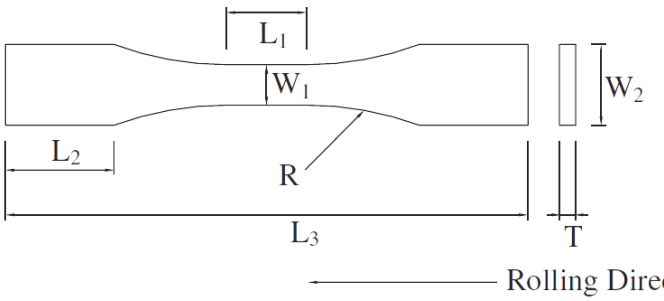

Designations	T (mm)	W_1 (mm)	L_1 (mm)	W_2 (mm)	L_2 (mm)	L_3 (mm)	R (mm)	$\frac{W_1}{T}$	$\frac{L_1}{W_1}$	$\frac{W_2}{W_1}$	$\frac{R}{W_1}$	Reduced cross section area ($T \times W_1$)
Large (Standard specimen)	5	10	30	30	40	190	85	2	3	3	8.5	50 mm^2
Subsize specimen	2.6	5.2	10.4	10.4	14	67	41.6	2	2	2	8	13.52 mm^2
ASTM E466 specifications	≧2.54 (as possible as)							2～6	2～3	> 1.5	≧8	19.4 mm^2～645 mm^2 (preferable)

Figure 3-28 Dimensions of standard of high-cycle fatigue specimens

3.5.5 Hardness Test

Hardness is defined as the resistance of a material to localized deformation. The term can apply to deformation from indentation, scratching, cutting or bending, and relates to the ability of a material to resist plastic deformation by penetration. Welding is a very aggressive process; it involves intense localized heating to melt the surfaces to be joined, and may also involve the introduction of molten weld filler metal. The welding area will be subjected to rapidly changing, concentrated thermal cycles,

which will lead to changes in the micro-structure of the material. These thermo-mechanical cycles significantly influence the hardness of the material. The resultant change depends on the type of material, and the welding technique and parameters. This investigation of these changes is very important in understanding the influence of different welding techniques on the strain hardening and phase changes at the welding bead and heat affected zone. The Vickers hardness test method will be used for hardness measurements; this consists of an indenter with diamond shape, which has a square base. The angle between opposite phases is 136^{o}, as shown in Figure 3-29 . Load values are 1-100 kgf, and loading time is 10 - 15 seconds. The two diagonals of the indent are measured after removing the load [82].

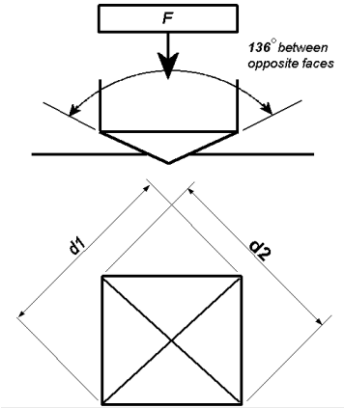

Figure 3-29 Vickers hardness test [82]

F = load in (N)

α = the plane angle of indenter

d = mean indentation diagonal length , and defined as shown in [82]

$$d = \frac{\boldsymbol{d_1+d_2}}{\mathbf{2}}\, mm \qquad (3.14)$$

HV = Vickers hardness can be defined according to ISO 6507-1 as:

$$HV = 0.102 \times \frac{2Fsin[\frac{\alpha}{2}]}{d^2} \qquad (3.15)$$

Yilmaz et al. [77] studied the influence of arc welding on the hardness distribution across the weld and base metal of 304L and 316L austenitic stainless steel. Their

results show an increase of the hardness near to the welding bead for both techniques, however the hardness value near to the welding bead of 316L was approximately 210 HV, whereas for 304L it was 270 HV. The increase in hardness is mainly due to the multi-pass welding process used, which leads to a work-hardened state with dislocation density exceeding 10^{10} cm^{-2}, compared with a dislocation density of 10^{6}-10^{8} cm^{-2} in the base materials.

Another study by Kwok et al. (2006) investigated the hardness across laser welded beads for austenitic stainless steels [83]. The study is based on X-ray diffraction spectra for the volume fractions of ferrite C_{δ}, for different stainless steel alloys, both as received (AR), and after laser welding (LW). It is clear from Table 3-3 that the greatest increase in the ratio of C_{δ} is for LW S30400, due to the welding. On the other hand, the sample of S31603 did not have an increase in C_{δ} after welding.

Table 3-3 δ -ferrite volume fraction and micro-hardness (AR) and (LW) [83]

Stainless steels	C_{δ} (AR) (%)	C_{δ} (LW) (%)	Difference in C_{δ} (%)	$Hv_{0.2}$ (AR)	$Hv_{0.2}$ (LW)
S30400	0	14	+14	176	301
S31603	0	0	0	179	194
S31803	60	62	+2	268	316
S32760	54	50	−4	290	314

It is clear from Figure 3-30 that the greatest increase in hardness was detected in LW of S30400 alloy, with an increase of about 70% from 176 HV to 301HV. This indicates that the increase in hardness is mainly related to presence of hard fractions of ferrite C_{δ} , and also to the refinement of grain size. This may be another reason why the results of Yilmaz et al. [77] show that the induced hardness of arc-welded 304 austenitic stainless steel is higher than that the hardness values of welded 316L alloy.

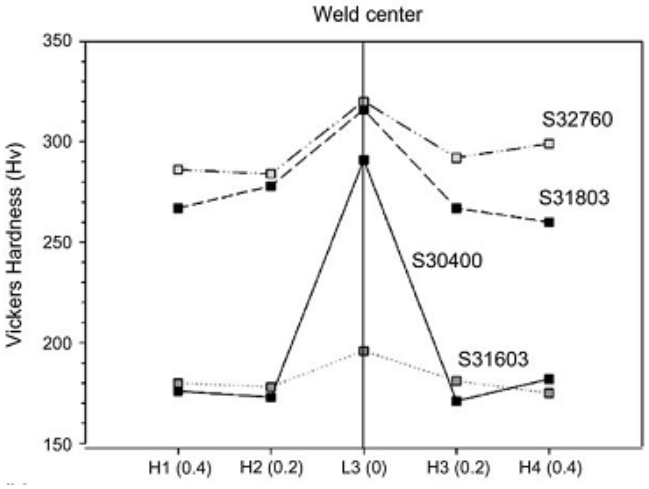

Figure 3-30Hardness distribution change in welding zone [83]

Another piece of research on austenitic 304 stainless steel welding, using a 10 kW fibre laser welding machine shows that, although the structure has an increased tensile strength due to rapid cooling and fine grain structure, the results of the hardness test show that there are no significant increases in the hardness when using argon as a shielding gas as shown in

Figure 3-31a [84]. When nitrogen is used as a shielding gas, the hardness may decrease in the fusion zone, due to decreases in ferrite phase formation, as shown in

Figure 3-31b. The NGLW technique for thick cross sections is weak in this respect, and not recognised previously for mechanical evaluation of austenitic stainless steel welding.

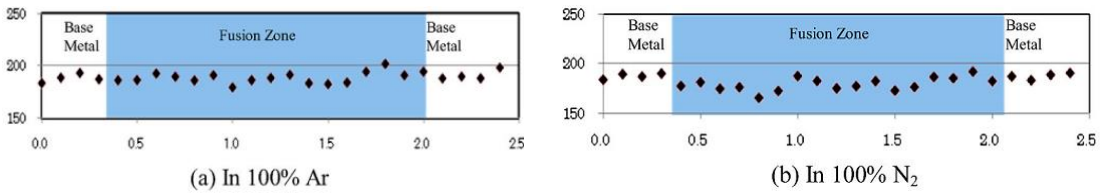

Figure 3-31 hardness test samples [84]

Koshiishi et al. [85] studied the influence of the surface hardening on the SCC in simulated boiling water reactor (BWR) environment. The results are shown in Figure 3-32. It has been found that, increasing the surface hardness beyond 300 HV (Vickers hardness) has a significant influence on the SCC crack depth. Consequently it is very critical for better weld joint performance to keep the hardness distribution below the specified critical value for SCC propagation.

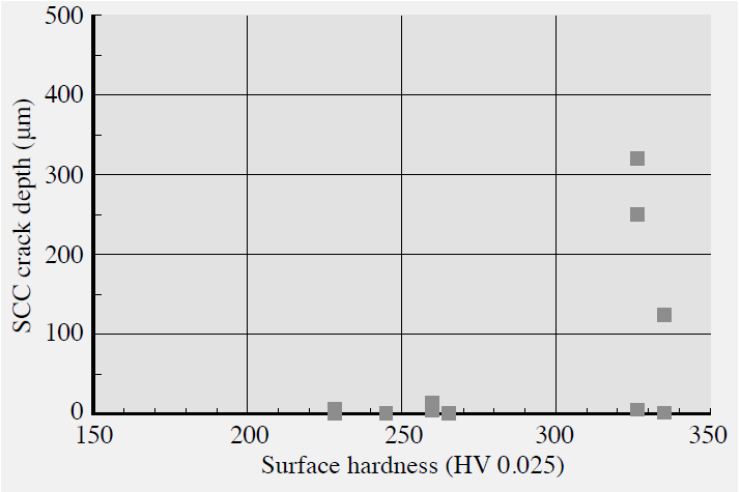

Figure 3-32 Relationship between SCC crack depth and surface hardness

CHAPTER 4. LITERATURE REVIEW ON LASER WELDING AND APPLICATIONS IN NUCLEAR POWER PLANTS

4.1 Introduction

High power-density welding processes are typically fusion welding methods, utilizing a heat source capable of producing extremely high power-density welds. In most modern manufacturing industries, there is a vital need to improve productivity without sacrificing the quality of the product. Welding speed must be increased to improve productivity; consequently the energy should be increased to satisfy the heat energy requirement for fusion welding operations. This highlights the importance of developing suitable high-power density welding processes [86].

The density of the energy is often more important than the absolute source energy. There are two welding technologies which can be classified as high power-density processes: electron beam welding (EBW) and laser beam welding (LBW) [87]. Both processes use a very high-intensity beam as a heat source, and can operate in keyhole mode producing narrow parallel-side fusion welds with higher welding speeds. They can produce a narrower heat affected zone with minimum distortion and thermal contraction. The energy density can reach 10^{13} W/m^2, whereas in conventional welding process (e.g. arc welding) the power density is typically 10^8 W/m^2 [87]. There are some limitations in the use of the EBW technique, due to the solidification and brittleness of weld, and the requirement for a vacuum chamber which results in greater constraints on the product size, due to the size of the available vacuum chamber. In addition, the method has a high operating cost [88], although new developments in reduced vacuum and local vacuum electron beam welding have overcome the need for a vacuum chamber. The vacuum level inside welding the chamber is around 5×10^{-3} m bar, which can result in sealing difficulties [12]. This equipment was not available for this PhD and hence the evaluation of EBW is outside of the scope of this thesis.

4.2 Laser welding

Laser welding is one of the highest power density welding processes. It has the capability of focusing the laser beam down to a very small spot diameter (typically 50-500 μm). High precision and concentrated heat input helps in minimizing micro-structural modifications in the weld, reducing residual stresses and distortions in the welded specimens. Laser welding is used on a wide scale in many industries, ranging from nanoscale structures to heavy industries such as nuclear and aerospace [89]. It could be used efficiently for welding relatively thick-section components [12].

A laser is a coherent electromagnetic radiation with a very small divergence angle (almost parallel). Therefore, the beam can be focused through an optical device such as a lens or mirror to increase the intensity. The focused laser beam is used to produce sufficient heat to cause fused welding [90]. New generations of lasers, such as fibre lasers, are receiving significant attention due to their high efficiency, high power and improved beam quality. They can produce an ultra-high peak power density in the order of 10^{12} W/m^2 [91]. This higher power density permits high weld penetration and high welding speed, with a very narrow heat affected zone. High welding speed can achieve high productivity and reliability, and decreased heat input to the welded joint [92]. However, more research is still required into laser welding techniques before they can be widely adopted by the nuclear industry [92].

Due to decreased overall heat input per unit joint length during laser welding process with respect to conventional arc welding, the predicted distortion, and influence on the welded material properties are expressed lower. Consequently joints will be less subject to failures due to the different applied loads inside nuclear power plants. Moreover, the wavelengths of advanced laser beams are moving toward values suitable for delivery through fibre-optic cables, allowing improved flexibility and control.

4.3 Basic laser beam characteristics

Laser light is an electromagnetic wave; the process of stimulated emission is accomplished by an active medium placed between a pair of mirrors that act as a feedback mechanism. During each pass between the mirrors, the light waves are amplified by the active medium and reduced by internal losses and laser output. The

amplitude of a light beam is increased in a laser by multiple passes of coherent light waves through the active medium. It has certain unique properties, namely, high monochromaticity, coherence and directionality, compared to ordinary sources of light, though both are electromagnetic radiation. These properties are briefly discussed in the following sections.

4.3.1 Monochromaticity

The energy of a photon determines its wavelength through the relationship

$$E = hc/\lambda \qquad (4.1)$$

Where c is the speed of light, h is Planck's constant, and λ is wavelength.
Laser light consists of essentially one wavelength, having its origin in stimulated emission from one set of atomic energy levels. In an ideal case, the laser emits all photons with the same energy, and thus the same wavelength and they are in phase to each other, it is said to be monochromatic.

4.3.2 Coherence

The waves are said to be coherent when they have a defined phase relationship over a long length of propagation. When an excited atom at the higher energy level drops down to a lower energy level, a photon is emitted, corresponding to the following equation

$$n\,(h\upsilon) = E_2 - E_1, \qquad (4.2)$$

Where υ is the frequency of the emitted photon, n is number of emitted photons, and E_2 and E_1 correspond to the higher and lower energy levels respectively. This process is called spontaneous emission; it is characterized by the lifetime of the upper excited state, at the end of which the atom spontaneously returns to its lower state, and radiates energy by emission of a photon. This passing photon can stimulate a transition from a higher level to the lower level in another atom, thus resulting in the emission of two photons, which is a gain as shown in Figure 4-1.

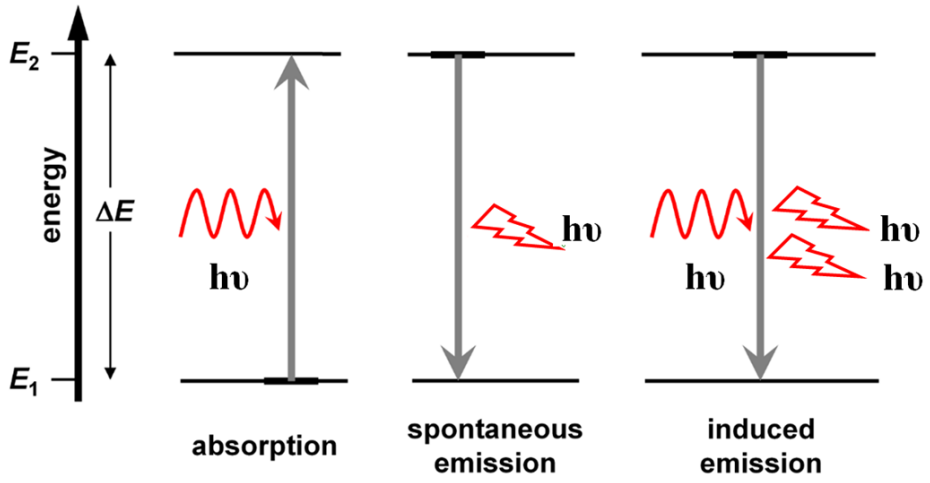

Figure 4-1 Spontaneous emission

The two emitted photons are said to be in phase, which means that the crest or the trough of the wave associated with one photon occurs at the same time as on the wave associated with the other photon. This results in the generated laser beam having the property of coherence.

4.3.3 Directionality and beam divergence

High directionality is one of the most important properties of laser. Collimation refers to the degree to which the beam remains parallel with distance. A perfectly collimated beam would have parallel sides and would never expand. Its divergence angle would be zero. Diffraction plays an important role in determining the size of a laser spot that can be projected at a given distance.

The high degree of collimation arises from the fact that the cavity of the laser has very nearly parallel front and back mirrors, which constrain the final laser beam to a perpendicular path to those mirrors.

Multiple reflections produce a well-collimated beam, because only photons travelling parallel to the cavity walls will be reflected from both mirrors. The oscillation of the beam in the resonator cavity produces a narrow beam that subsequently diverges at some angle depending on the resonator design, the size of the output aperture, and the resultant diffraction effects on the beam.

The divergence angle θ_o describes the directionality of the laser. Beam divergence is direct proportional with the wavelength, and beam waist radius w_o, and beam quality M^2 which will be discussed in next sections, and is defined as

$$\theta_o = (M^2 \lambda / \pi w_o) \quad (4.3)$$

4.3.4 Beam diameter

The intensity of laser light is not the same throughout the cross section of the beam. This is because the cavity also controls the transverse modes, or intensity cross-sections. The ideal beam has a symmetric cross-section; the intensity is greater in the middle and tails off at the edges. This is called the transverse electromagnetic mode (TEM $_{00}$) beam, which has a perfect Gaussian profile.

$$I(r) = I_0 e^{\frac{-2x^2}{r^2}} \quad (4.4)$$

I_o maximum intensity of the beam.

r radius of the beam.

x distance from beam axis.

Beam diameter is defined as the distance across the beam where the intensity drops to a certain fraction of its maximum value. The common definitions are half intensity i.e. full width at half maximum (FWHM). In other words, beam diameter is the diameter of the laser beam cross section between points near the outer edge of the beam where its intensity is only 50 % of the intensity at the beam centre.

4.3.5 Beam quality

The use of high-power lasers in industrial applications increases the importance of focussing the laser beams 'tightly' to produce highest possible radiance with minimum collateral damage. A dimensionless beam propagation parameter, M^2 was developed in 1970. This term is a quantitative measure of the quality of the laser beam; better beam quality translates into better delivery of optical power to the target in the far field with limited diffraction. The M^2 beam quality factor limits the degree to which a laser beam can be focused for a given beam divergence, which in turn is limited by the numerical aperture of the focusing lens. The design of optical delivery

systems for laser systems is highly dependent on the laser's beam quality. According to ISO standard 11146, M^2 is defined as the beam parameter product (BPP) divided by λ / π. BPP is the product of a laser beam's divergence angle and the diameter of the beam at its narrowest point "beam waist". $M^2 = 1$ only occurs where a single-mode TEM_{00} Gaussian beam is used.

4.3.6 Brightness

The radiance of laser is defined as the power emitted per unit surface area per unit solid angle (watts per square metre per steradian). The steradian is the unit of solid angle, which is three-dimensional analogue of a conventional two-dimensional (planar) angle expressed in radians. The radiance of a milli-watt laser is greater than 10^6 Watts/m^2/steradian. It is calculated according to equation 4-1.

$$\text{The radiance} \quad B = \frac{C\,P}{\lambda^2 (M^2)^2} \tag{4.5}$$

Where P is the power, λ is the wavelength, M^2 is the beam quality (assuming a radially symmetric beam), and C is a constant that depends on the definition of beam size and divergence angles [93].

4.3.7 Transverse Mode

The transverse mode of a laser output characterizes the intensity distribution of a laser beam in the transverse plane, which is perpendicular to the direction of propagation. The configuration of the optical cavity determines the transverse mode of the laser beam. Transverse electromagnetic modes are called (TEM). Two indices are used to indicate the TEM modes – TEM_{pq}, where p and q are integer numbers indicating the number of points of zero illumination (between illuminated regions) along the x-axis and y-axis respectively, as shown in Figure 4-2. Different combinations of mirrors in the process of stimulated emission, such as plane and curved types, have been utilized in practical lasers to control the transverse mode of the laser beam.

The lowest-order mode, $TEM_{00,}$ has an essentially ideal Gaussian profile with a certain spot size. This mode depends on the spacing and radii of the mirrors, and the wavelength of the light, and not on the mirror diameter, which is assumed to be very large, typically four to five-times that of the beam size. This spot size, called the "Gaussian spot size" can be estimated in terms of the cavity length L, the end mirror radii r_1 and r_2, and the wavelength. The fundamental TEM_{00} mode is only one of many transverse modes that satisfy the round-trip propagation criteria.

The TEM_{00} mode is considered to be the most desirable beam mode, on the other hand multi-mode beams can often deliver more power with a poorer beam quality. Other modes may be acceptable in applications where power is the main criterion.

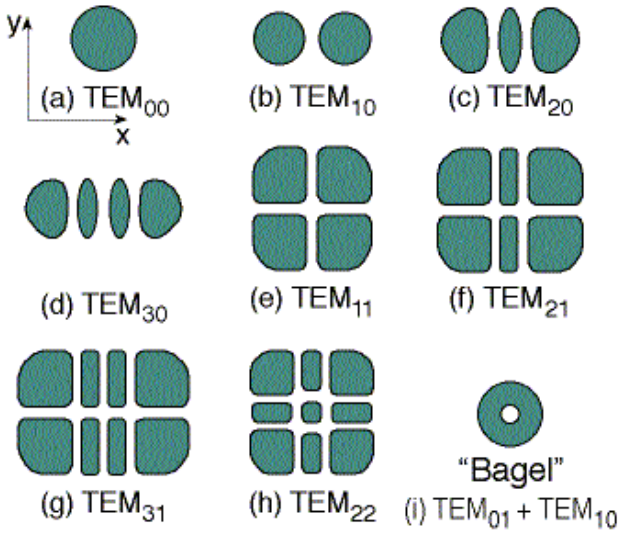

Figure 4-2 Laser beam transverse modes [94]

4.4 Laser welding and applications in power plants

The huge scale and complexity of reactor structures in nuclear power plants has placed new demands upon fabrication technology and material performance. The need to weld high thicknesses of different materials with severe service performance requirements, over extended distances, presents a tough series of challenges. Recent developments in laser beam welding technology can offer an ideal solution for welding challenges inside nuclear power plants; they can minimize the welding time, control the predicted distortion and decrease residual stress, especially for stainless steel where the expansion coefficient is large [12, 95]. However, the

methods are limited by the available laser power. Recently, a number of high-power laser machines have been implemented, which also combine different welding techniques such as laser-hybrid welding in order to improve the welding penetration capability of the laser. The maximum recorded limit of stainless steel cross-section welding for a laser technique is in the order of 50 mm [60]. The laser technique requires more research in order to increase its penetration to satisfy the requirement to weld challenging, thick cross sections, especially in power plants and nuclear reactors. Generally, the huge stainless steel structures used in nuclear reactors, especially generation IV designs, range from 50-80 mm thick, and are planned to be welded by using this technique [17, 92] . Detailed reviews of laser welding process will be discussed in the following sections.

4.4.1 Advantages of laser welding

Laser welding is one of the modern high power density welding techniques. It depends on a laser source, which emits a laser beam with a certain power density (irradiance). This power density relates to the heat energy absorbed by the material surface. Laser welding has a number of advantages compared to other welding methods:

Laser welding process works at normal atmospheric pressure. This enhances the process flexibility for welding different weld sizes.

It is a non-contact welding process, it has a parallel-sided fusion zone, narrow weld width and high penetration due to its high power density [96], a laser beam can be focused through laser optics into a small spot and can be positioned precisely over the required welding location [90].

Laser welding has the ability to use a filler material in the form of a wire-feed or in the form of powder [90]. Increasing the welding speed is possible due to high power-density; this leads to a decrease in the heat energy input to the workpiece, and consequently a narrow heat-affected zone and limited residual stresses [85]. A rapid cooling rate results in formation of fine solidification microstructures [90]. However, the high capital cost of laser welding is considered to be a disadvantage in comparison with conventional welding processes, but this can be mitigated through

the increased productivity, quality and flexibility of the laser welding process [90, 97].

4.4.2 Laser welding modes

There are two basic modes for welding according to power density [43, 98].

4.4.2.1 Conduction welding mode

The conduction welding mode occurs when the power density is not high enough to cause evaporation of the melted pool; the power density is below approximately $5x10^9$ W/m^2. The energy is transferred into the welded material by conduction [90]. Absorption of heat below the surface is small, consequently a low aspect ratio (depth to width ratio), and a hemispherical weld bead is formed, as shown in Figure 4-3. It is considered to be a stable welding mode [99]. This mode cannot be used in deep penetration welding

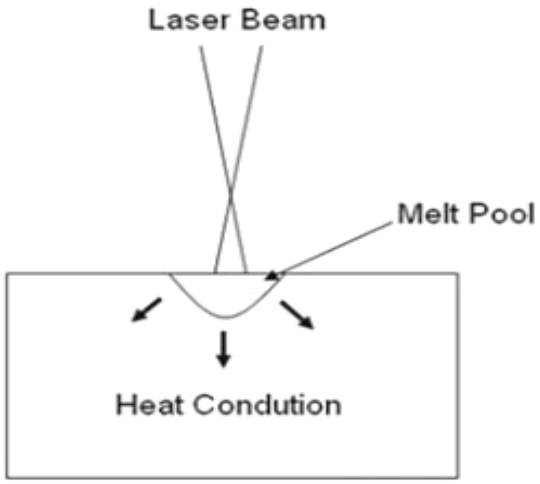

Figure 4-3 Conduction welding mode [43]

4.4.2.2 Keyhole welding mode

When the power density is sufficient to cause evaporation of the melted pool, it will form the second mode, known as keyhole welding [100, 101], as shown in Figure 4-4. Most metals require a power density of 10^{10} W/m^2 or greater in order to initiate a keyhole mode. Once the beam strikes the surface of the workpiece it tends to make a cylindrical shape through evaporation of the surface [102]. Absorption of heat energy over the surface of workpiece results in the development of the nail head shape

within the keyhole, due to the widening of the bead near to the surface [103]. In addition, improved absorption of laser beam means temperature within the keyhole may reach 2 x 10^4°C [104]. As the laser beam moves, the keyhole is translated through the material. Surface tension causes the molten metal to flow around the hole and fill in behind it. The keyhole is bent in the opposite direction to the welding, and the angle of this bend depends on the welding speed [105]. The wall of the keyhole also absorbs energy from the laser beam [98]. Since energy is transferred to the workpiece along the depth of the keyhole, deep penetration can be achieved [106]. Keyhole welding is more efficient with respect to conduction. Multiple reflections of the laser beam inside the keyhole lead to increased beam absorption and inverse Bremsstrahlung absorption by the laser induced plasma also occurs inside the keyhole [96], known as Fresnel absorption [105]. There is a reduction in heat loss by thermal conduction compared to conduction laser welding, as keyhole welding is considered to be a cylindrical heat source below the workpiece surface [98] .

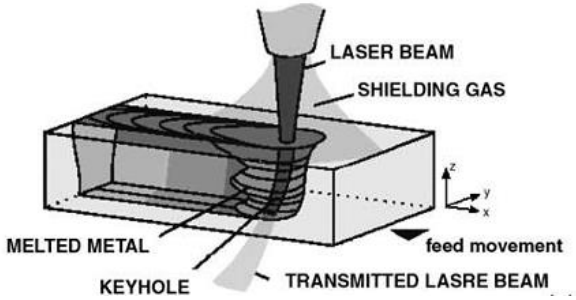

Figure 4-4 Deep penetration welding process keyhole mode [97]

4.4.3 Plasma formation

Plasma is an undesirable product for a laser welding process. It consists of ions and electrons of ionized gas and metal vapour, caused by laser beam interaction, and is associated with deep penetration laser welding [107]. The plasma has a three distinct periods: formation, growth and disappearance [108]. It is a high pressure high temperature ionized gas. It has two sources: metallic plasma, which consists of vaporized metal ions, and shielding gas plasma, which is generated by shield gas ionization. Metal plasma is a result of interaction between high power laser and metal vapours, and is evidence of keyhole welding mode formation. Metal plasma significantly influences the welding process [109].

There are two types of plasmas according to location: external plasma (plasma plume) and internal plasma (keyhole plasma) [107]. If the plasma is external to the workpiece surface, a part of the laser beam is refracted by the vapour plume. This changes the beam intensity distribution on the workpiece [110]. Moreover, the photons of the laser beam are absorbed by the electrons in the plasma through the inverse Bremsstrahlung mechanism [111, 112]. The laser beam may also be subjected to scattering by ions. Plasma formation at high welding powers is unavoidable, consequently, increasing the power may actually reduce the laser power reaching the surface [42] . At a certain power density, the plasma intensity will totally impede the welding process.

Conversely, a keyhole plasma may help the energy transfer if the plasma is inside the keyhole, because it consists of vaporized metal ions, which are considered to be a good energy-transfer medium [107, 113]. The height of the plasma plume also has a direct effect on laser energy absorbed by the workpiece, as shown in Figure 4-5.

The plasma formation (ionization) is described by the Saha equation [107]:

$$\frac{N_e N_i}{N_\circ} = \frac{g_e g_i}{g_\circ} \frac{[2\pi m_e k T_e]^{3/2}}{h^3} exp[\frac{-E_i}{kT_e}] \quad (4.6)$$

$N_{e,i,o}$ are the densities of electrons, ions and neutral atoms respectively, $g_{e,i,o}$ are the degeneracy factors of electrons, ions and neutral atoms respectively, h is the Planck constant, m_e the electron mass, T_e the electron temperature, E_i is the ionization potential for the neutral atoms, and k the Boltzmann constant. If the direction of the shielding gas is inclined, it will cause deflection of the plasma and decrease the height [42]. The interacting height of inclined plasma is smaller, consequently the laser energy absorbed by the workpiece is increased, and deep penetration can be satisfied - if $h_2 < h_1$, it will lead to $Z_2 > Z_1$ [114]. The Beer-Lambert law describes this relationship:

$$I_a = I_\circ \, e^{-\mu_a Lp} \quad (4.7)$$

where I_a and $I_\circ$ are the attenuated and the initial laser beam intensity respectively, μ_a is the absorption coefficient and L_p is the length of the plasma [115].

The plasma absorption coefficient for the laser beam is directly proportional to the wavelength. In other words, the absorption by plasma is increased by increasing the

laser beam wavelength. This gives a significant advantage for shorter-wavelength lasers for welding [116]. The wavelength of a Nd-YAG laser beam is 1.06 μm, whereas a carbon dioxide laser beam has a wavelength of 10.6 μm. Therefore the predicted plasma influence for a CO_2 laser is greater than that for Nd-YAG and fibre lasers.

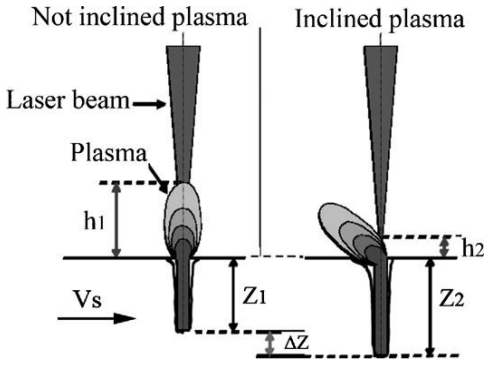

Figure 4-5 Relationship between interacting plasma height and penetration [114]

4.4.4 Laser welding parameters

According to previous investigation for laser welding process, there are five significant parameters, which control the laser welding process [90, 96]. These parameters are: output power, welding speed, focal position spot size, and shielding gas. These parameters should be determined carefully to achieve complete penetration and produce a small heat affected zone and a good weld profile [117].

4.4.4.1 Laser output power

There are two types of output power delivery in laser welding processes: continuous wave (CW) and pulsed wave (PW). Laser power has a direct effect on the penetration depth, for the same welding speed for a given material. The penetration depth increases by increasing the laser output power, as shown in Figure 4-6. The laser power has more influence on the penetration in comparison with weld profile and heat affected zone [117]. Equation 4.8 shows the governing equation for maximum depth with respect to power [116]

$$0.483\ P\ (1 - r_f) = v\ w\ g\ \rho\ Cp\ Tm \qquad (4.8)$$

Where *0.483P* is the net laser power used for welding taking account of conduction losses, r_f is the reflectivity of the surface to the laser beam, w is the weld bead width, g is the weld penetration, v is the maximum welding speed, ρ is the density of the material, C_p is the thermal capacity of the material, and T_m is the melting temperature of the material. Laser output power is considered, along with spot size, as the main parameters for transition welding from the conduction mode into the keyhole mode. A high-power laser delivers high energy density to the welded joint, thereby permitting an increase in the welding speed [118].

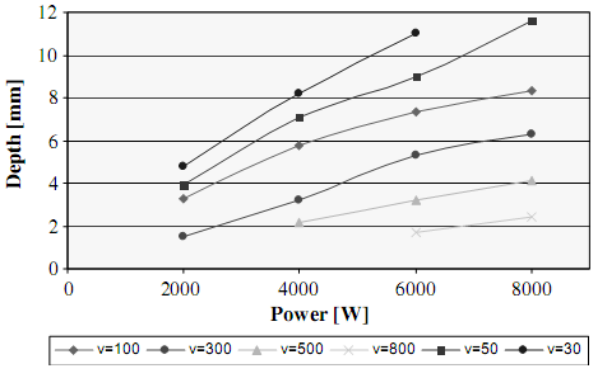

Figure 4-6 Typical relationship between laser power and weld penetration depth at various speeds [118]

4.4.4.2 Welding speed

The welding speed has a big influence on the welding process, and also on the properties of the fusion zone and shape defects. Increasing the welding speed leads to a decrease in the penetration depth [119] as shown in Figure 4-7.

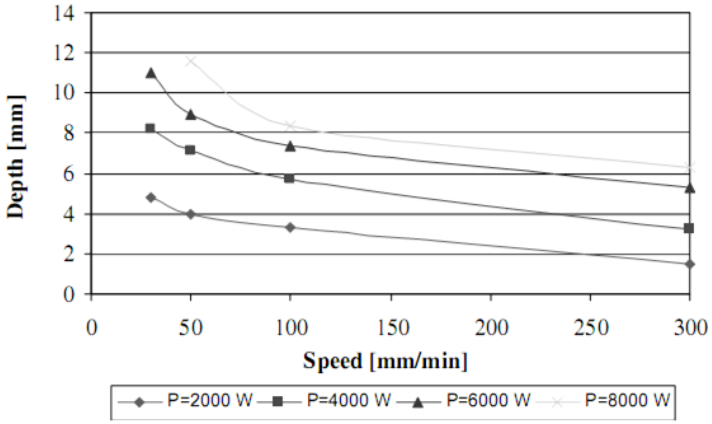

Figure 4-7 Effect of welding speed on depth [118]

On the other hand, as the welding speed increases, it leads to decreasing plasma effect. Consequently laser beam will interact directly with the workpiece surface [117]. The welding speed has to be optimized in order to obtain the required penetration with minimum heat input to workpiece. High welding speed extends the hot metal away from the shield gas quickly, which will expose to air contamination. Increasing the welding speed will lead to narrower heat affected zone and the grain size will not be highly enlarged in this zone with respect to other welding processes [120, 121]. Decreasing welding speed leads to an increase in heat input to the workpiece. It has also a direct effect on the keyhole stability and the porosity formation [122]. This issue will be discussed briefly in porosity formation section. It has also a big influence on the shape defects of the welded zone, such undercut due to high speed welding and dropout defect due to low welding speed.

4.4.4.3 Laser beam focal position

The focal position of a laser beam is the position of the minimum beam diameter, and consequently the maximum power density. The focal position in the welding process has an important role in achieving the required quality, and also in achieving maximum penetration. Several attempts have been made to define the optimum focal position, and most of them state that the preferred position for the focal plane for thin work-pieces is located at a depth of around 1 mm, in order to achieve maximum penetration [116]. The focal position on the workpiece surface has the smallest weld width and smallest spot size, so it should be positioned where the maximum penetration depths and best process tolerances are required.

The focal position should be moved deeper into the material for thicker work-pieces [123]. The focus position is shifted up according to plasma density by 1-2mm. The position of the de-focusing plane will affect the keyhole stability, and consequently the porosity formation. Kim. et al. (1995) studied the effect of beam defocusing value on porosity [124] ; they confirmed that the position of the focal point influences the porosity formation, especially in aluminium. The uniform weld zone was obtained at 3-4 mm below and above the focal plane, respectively. The optimum position of the focal plane will depend on the quantity of light elements in the welded metal, such *Mg*, which has a low evaporation temperature [124]. The porosity is increased within the focus position between 1mm above and below the workpiece

surface. This is mainly due to the instability of the keyhole when the beam is focused close to the surface as shown in Figure 4-8.

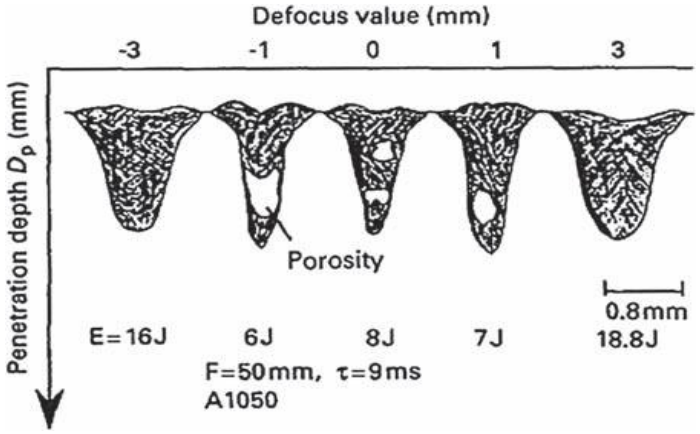

Figure 4-8 Porosity formation possibility against defocusing position [124]

A recent study was performed by Xudong. et al. (2008) [125]. They studied the deep-penetration welding of stainless steel. A laser power of 10 kW was used, with 0.3 m/min welding speed and 12 l/min gas flow rate, at different gas jet angles. It is clear from Figure 4-9 b that increasing the defocus distance will lead to increased penetration. The maximum penetration depth was approximately 24 mm at -13mm defocusing distance, and the angle of gas jet nozzle was 60°, as shown in Figure 4-9 a. Moreover, from the same figure, we can understand the influence of the gas jet angle; increasing the angle will lead to an increase in the penetration depth.

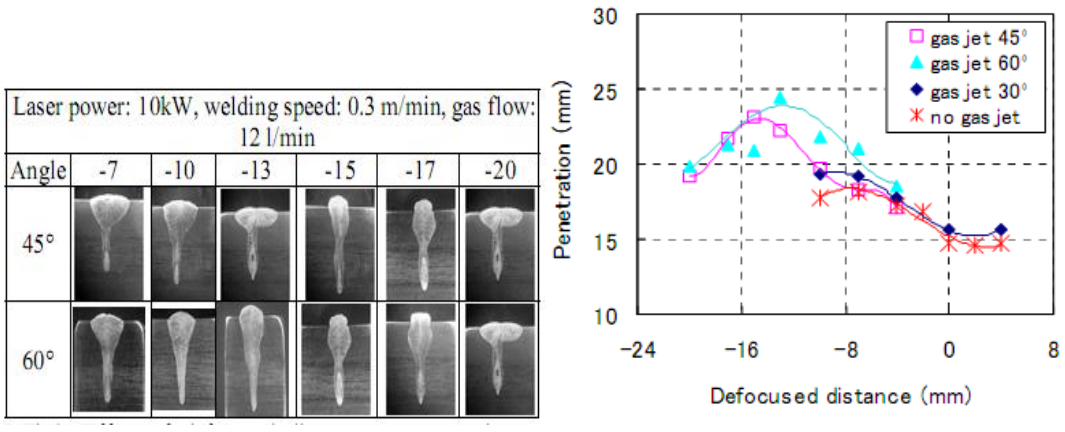

Figure 4-9 Effect of defocusing distance and angle on penetration depth[125]

4.4.4.4 Laser beam spot size

The smaller the spot size, the higher the power density. Laser optics plays an important role in releasing the desired spot size. The focusability of a laser beam is often referred to by another term, the beam product parameter (BPP) [118].

$$(\text{BPP}) = \alpha\ \omega_{\circ}\ \ (\text{mm.mrad}) \qquad (4.9)$$

where α is half of the divergence angle and $\omega_{\circ}$ is the radius of beam waist. The smaller the value of the BPP, the better the beam quality (M^2) [126]. A diffraction limited beam has an M^2 factor of 1 and is said to be a Gaussian beam; the M^2 factor determines the ability of the beam to be focused to a small spot for a given beam divergence angle. In addition, the initial beam diameter is inversely proportional to the final spot size. If the initial diameter is large, this implies a smaller spot size and higher energy density for a given welding speed.

For a Gaussian laser beam TEM_{00}, the spot size is calculated according to following equation.

$$d_{min} = 2.44\ \lambda f/D \qquad (4.10)$$

where

d_{min} is the diffraction limited spot size (focused beam diameter).

f is the focal length of the lens.

D is beam diameter on the lens.

For a non-Gaussian laser beam, the following equation can be used to calculate the focussed beam diameter for a high order mode $T_{m,n}$ such that m or n or both ≠ zero [57].

$$d_{min} = 2.44\ (\lambda f/D)(2M_{mn}+1) \qquad (4.11)$$

Where M_{mn} is the laser beam mode number for $TEM_{01} = 0.01$ and for $TEM_{10} = 0.10$

4.4.4.5 Shielding gases

The shielding gas is a very important parameter in the laser welding process. It protects the workpiece surface from oxidization, and protects the laser optics from spatter, and from high temperature plasma which could be formed on the surface of

the workpiece and affects the penetration of the welding. The height of laser induced plasma is inversely proportional to the shield gas inclination angle, and consequently the penetration depth of welding [127]. Shielding gases participate in suppressing the plasma plume [108]. Helium has a very good thermal conductivity, and a better ability to suppress plasma formation as it has a high ionization potential compared with other shielding gasses. On the other hand, argon produces insufficient penetration with respect to helium [108], but its density is high and can replace atmospheric gases in the weld pool more efficiently than nitrogen [42]. When using carbon dioxide as a shielding gas, it is decomposed into carbon monoxide and oxygen, thus good penetration can be obtained, but the carbon monoxide gas is entrapped, and could be a source of porosity as shown in Figure 4-10. Nitrogen enhances the penetration in comparison to argon, but it may lead to porosity formation due to dissociation [108].

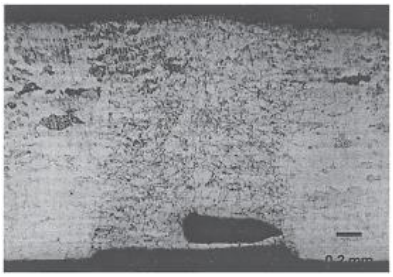

Figure 4-10 Porosity due to using CO_2 shielding gas [108]

A comparative study of helium and argon shielding gases with laser gas metal arc hybrid welding was performed, as shown in Figure 4-11. The result indicates that helium is more effective in suppressing the laser induced plasma due to high ionization potential [127]. In pure helium, the induced plasma was very small, but as the ratio of helium to argon decreases, the plasma will become more effective.

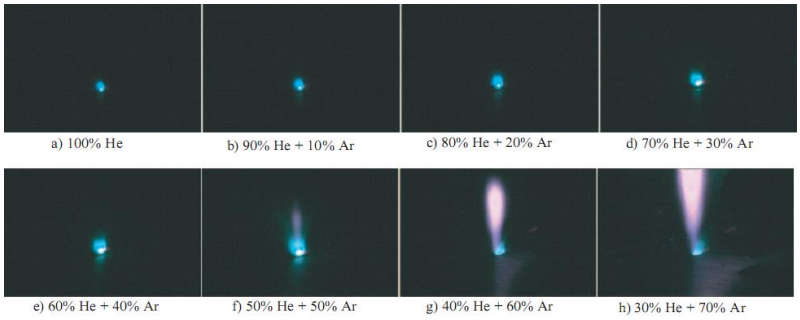

Figure 4-11 Plasma generated for different shielding gas [127]

To achieve efficient shielding for thick material welding, root gas shielding must be used in order to achieve acceptable weld quality. Without using root gas shielding, the welding process becomes unstable, especially the root quality. Oxidization of the root side is the most likely cause of the instability, but output heat from the oxidation exothermic reaction may also lead to the introduction of excessive energy into the process [128].

4.4.4.6 Gas flow rate

The gas flow rate has a direct effect on the welding operation. If the flow is too small, the plasma will be thicker, and consequently penetration will be lower. Conversely, a high gas flow rate results in increased penetration, but if the flow rate is too high, the keyhole will be widened, resulting in a reduction in the heat absorbed by the weld [57]. A recent study was performed by Xudong. et al. (2008) on the influence of the gas flow rate on the weld bead and the welding penetration [125]; using a 10 kW fibre laser, the BPP was 4.5 mm/mrad for welding stainless steel of 30mm thickness. As shown in Figure 4-12, increasing the gas flow speed will lead to deeper penetration and narrower welding width, but at a certain limit the process becomes unstable and may transform into a cutting operation.

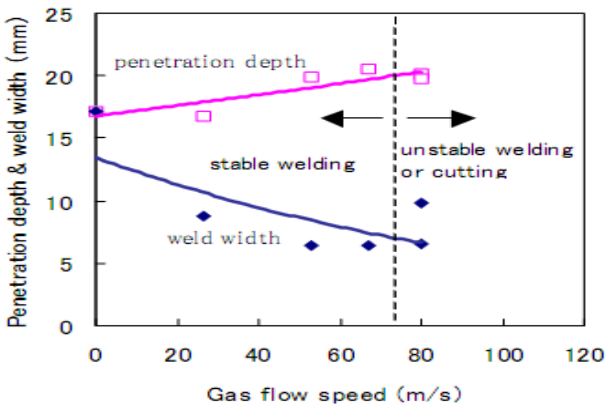

Figure 4-12 Effect of gas flow speed and penetration depth and weld width [125]

4.4.5 Fibre laser welding

The fibre laser is considered to be one of the new generations of lasers for industrial applications; it has been receiving considerable attention recently because of high power, high beam quality and high efficiency. It can produce extremely high peak power density, in the order of 10^9 W/mm^2. It is considered a very promising heat source for thick cross-section welding, with high speed and deep penetration [129].

The first fibre laser used for material processing was in the year 2000 with a power of 100 W. Today, multi-kW power with lower divergence angles is available [118]. The active medium of a fibre laser is a core of optical fibre doped with a rare earth element.

The fibre laser is type of solid-state laser, where emission of the laser beam depends on three main elements: The first element is the active medium, a silica-based optical fibre, which is core-doped with rare earth ions such erbium or ytterbium, as shown in . Figure 4-13

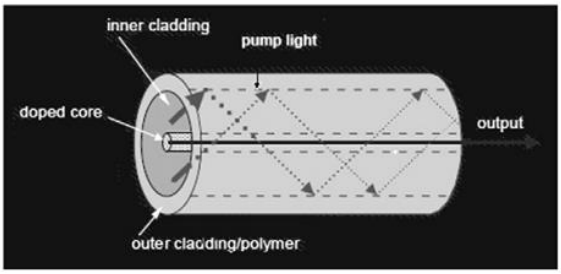

Figure 4-13 Doped core clad fiber [118]

The second element is the reflector, which uses two Bragg gratings, formed from a section of fibre core with a reflective index sufficiently different to allow it to operate as a reflecting mirror [118]. The wavelength of the laser depends on the rare earth material inside the fibre core. Ytterbium doped fibre has an emission wavelength of 1.07–1.08 μm, and thallium doped fibre has a wavelength of 1.8–2 μm. The third element of the fibre laser is the pumping system, which is used to reach the threshold rate. The diode pumping energy is transmitted to the active doped fibre through multimode fibre; Figure 4-14 shows a schematic drawing of a fibre laser system [118].

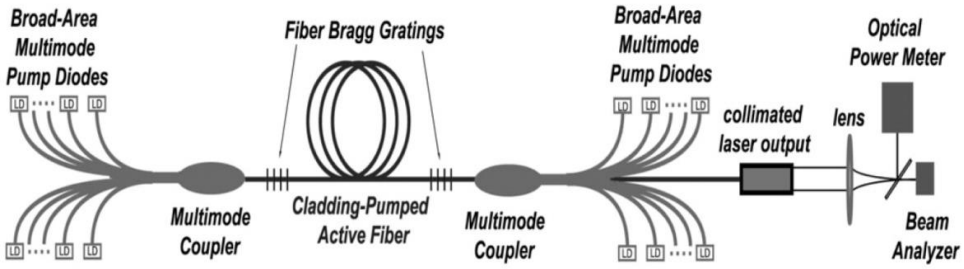

Figure 4-14 Schematic drawing for fiber laser system[118]

4.4.5.1 Advantages of fibre laser

The fibre laser has a high beam quality (small beam divergence angle and focal spot diameter) with Gaussian transverse electromagnetic modes, and consequently a small beam focus diameter [129]. This leads to welds with higher aspect ratio (deep penetration and smaller width). The fibre laser has better overall efficiency, around 25% [130]. Flexible beam delivery is possible, through fibre cables leading to the laser head, resulting in a compact size laser beam source with high reliability. Due to the short wavelength of 1070 nm, most materials have good absorption for this type of laser beam. The system has low maintenance costs, high efficiency and compact size. The lifetime of the diode pumped beam source is expected to be longer.

4.5 Laser welding influences on the base material

Laser welding has a relatively small influence on the changes in material properties, particularly near to the welded region, with respect to conventional welding

techniques. This is due to small amount of total heat input to the workpiece, resulting in a very narrow heat affected zone. The heat required for material fusion during the welding process, and also the high cooling rates associated with laser beam welding, affects the base material properties, such as strength, hardness, ductility, corrosion resistance and residual stresses components [131]. These effects are due to metallurgical changes such as micro-segregation, solidification cracking and grain growth, especially in the fusion zone (FZ) and heat affected zone (HAZ) [80]. Moreover, the weld cross-section shape and dimensions change due to material vaporization. In addition, the formation of defects in the fusion zone such as porosity, cracking and geometry defects such humping, spatter, dropout, etc are affected due to welding parameters [132].

4.5.1 Mechanical defects

The influence of the laser welding process on the mechanical properties of metals (tensile strength and hardness distribution) has been discussed in sections 3.3.9.1 and 3.3.9.4.

4.5.2 Defect Formation in laser welding

Forming defects are defined as unpredicted, undesirable changes in the welded cross-section, due to changes in specific welding parameters. These defects will deteriorate the weld joint performance. This section will mainly discuss the formation of these defects, such as porosity and cracks in the fusion zone and heat affected zone.

4.5.2.1 Porosity

Porosity is considered as a serious problem in laser welding. It mainly affects the mechanical properties of the welded zone [124]. This problem arises in deep-penetration welding or during welding by the keyhole mechanism. The keyhole suffers from unstable dynamic loads even at constant speed and constant power [133]. This is considered as the main reason for porosity formation [134-136]. The non-uniform evaporation of the front wall of the keyhole due to humping will lead to severe evaporation directed at the rear wall, as shown in Figure 4-15. Continuous vibration of the rear wall due to strong dynamic pressure of the evaporated metal makes the keyhole unstable [137].

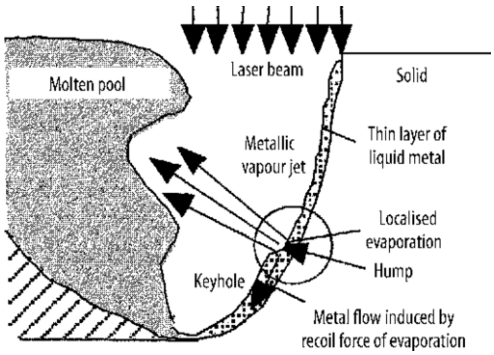

Figure 4-15 Interaction of laser beam with the front wall hump [138]

Optimization of the welding speed during welding is the most significant welding parameter in order to gua rantee a weld bead free of porosity. Katayama [122] states that a lower welding speed may lead to increased porosity formation.

Keyhole collapse takes place due to an increase in the duration of the interaction between the laser beam and keyhole surface [136]; the instability is caused by the strong melt flow at this position, as shown in Figure 4-16.

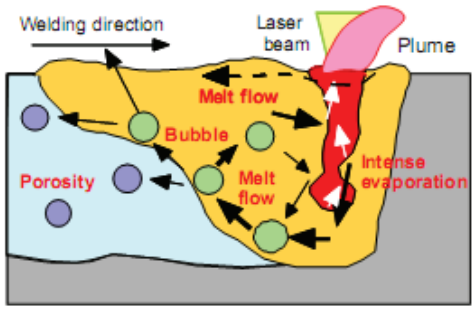

Figure 4-16 Melt flow inside keyhole at low welding speed [122]

The relationship between ablation pressure and surface tension forces controls the keyhole stability [134]. If the instability of the keyhole is greater than the surface tension of the base material, a sudden depth decrease of the keyhole will take place, due to keyhole bottom area collapse; typical bubble formation processes are illustrated in Figure 4-17. Moreover, the laser beam has a weak intensity in the bottom of the keyhole due to shielding by molten metal and absorption by plasma. This weakness will decrease the ablation pressure, and will cause the keyhole tip to be broken by the capillary instability [139].

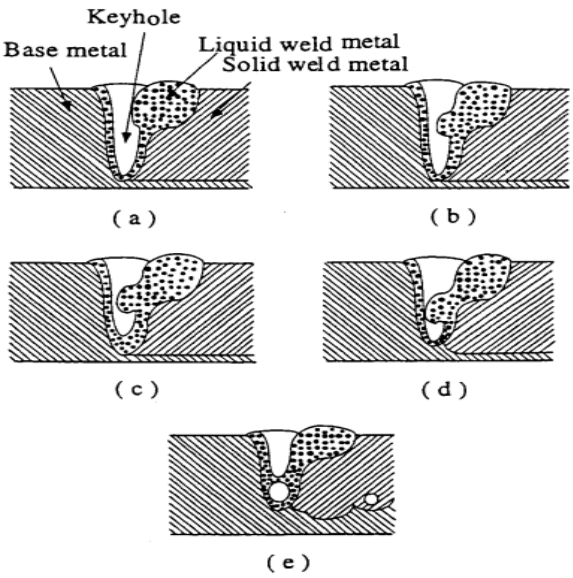

Figure 4-17 Porosity formation procedures during keyhole welding [134]

4.5.2.2 Undercut

High speed welding leads to a strong flow of molten metal within the welding pool. The direction of this flow toward the centre of the weld is shown in Figure 4-18a. High-speed welding leads to the rapid solidification of this area, forming the undercut defect, as shown in Figure 4-18b.

a) Undercut shape [116]

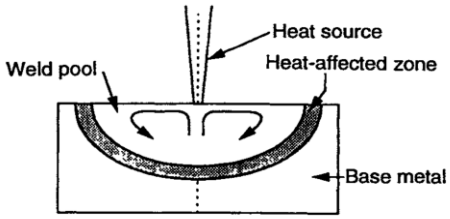

b) Flow direction in the welding pool

Figure 4-18 Undercut formation [140]

4.5.2.3 Drop out

A decrease in welding speed will enlarge the welding pool, and may lead to a drop out defect, as shown in Figure 4-19. Drop out defects mainly occur because the ferrostatic head pressure is larger than the surface tension.

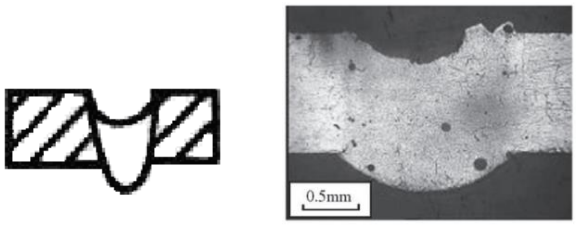

Figure 4-19 Defects of the welding profile (drop out) [116, 141]

4.5.2.4 Spatter formation

During the welding process, the laser beam strikes the surface of the workpiece. The molten metal is forced upward, and other ingredients are ejected to form the keyhole. The volume ratio between the molten metal that is pushed away when the keyhole is formed, and the volume pushed down, will result in spatter [131] . The amount of spatter depends on a number of variables, such as vapour pressure and processing parameters such as power. Increasing the power will lead to an increase in the amount of spatter [142]. Moreover the spatter is affected largely by the incidence angle as shown in Figure 4-20; when the incidence angle is zero, the spatter is more than twenty degrees inclination forward, whereas the plume in the second case tends to suppress spatter formation. Increasing the welding speed severely affects the stability of the keyhole and the formation of spatter [84].

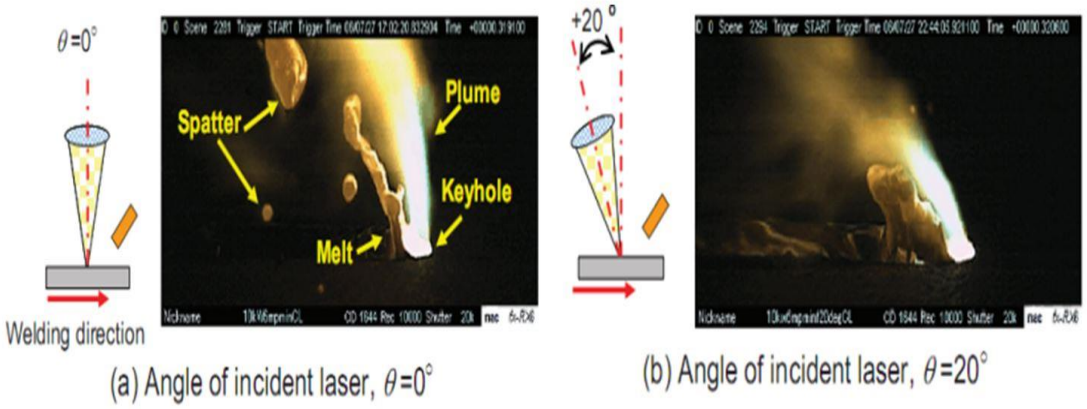

Figure 4-20 Effect of angle on spatter formation [122]

The formation of spatter also depends on the size of the molten zone. A large molten pool has slow metal flow, whereas a small pool has a fast flow, and will lead to increased spatter, as shown in Figure 4-21.

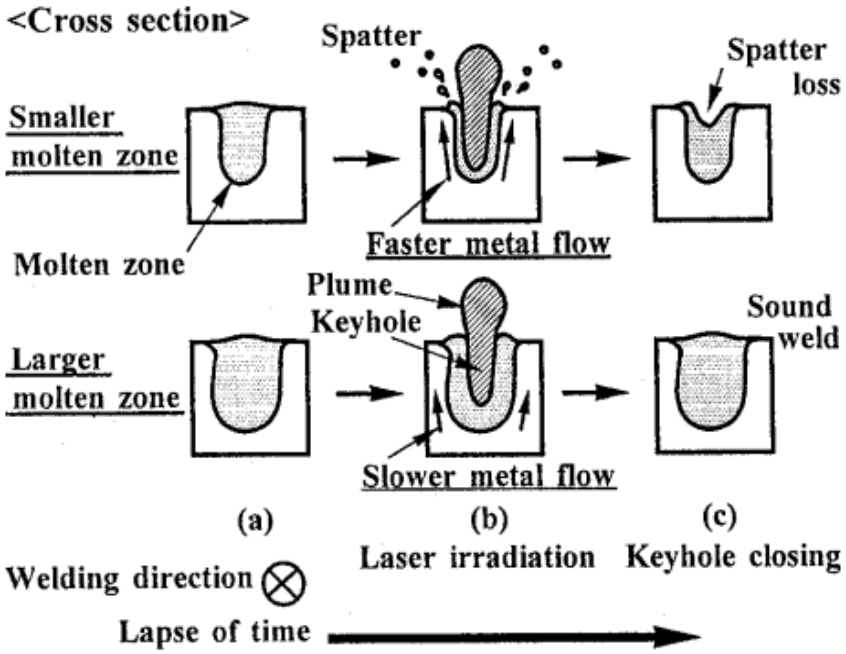

Figure 4-21 Relation between volume of molten zone and spatter [131]

4.5.2.5 Humping

Humping is mainly caused by high speed welding. An increase in the welding speed leads to a reduction in the flow of metal within the weld pool [143]. Once the humping is formed, it can be seen easily at the rear of the welding pool. The possibility of humping formation is increased with smaller spot diameters; it is due to weak melt back-flow and higher surface tension, as shown in Figure 4-22 [122].

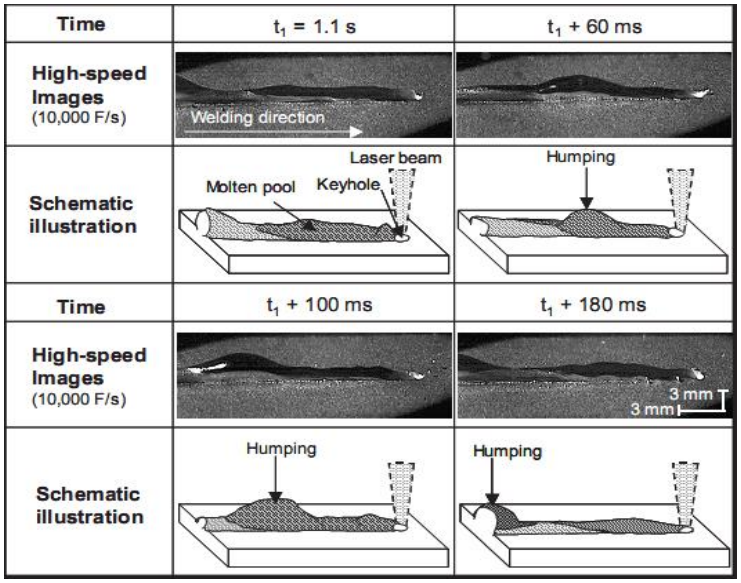

Figure 4-22 Humping formation sequence [122]

4.6 Candidate welding techniques for welding thicker sections

4.6.1 Autogenous laser welding

Laser welding technology is being increasingly utilized in heavy industrial manufacturing processes, especially those which require deep penetration. Laser welding technology is one of the highest power density welding techniques, due to the distinctive characteristics of laser beam, which can be focused into a very small beam spot diameter.

Several attempts have been made to study the characteristics of thick cross-section welding: Penetration depths of up to 11 mm in 304 stainless steel have been achieved using a 10 kW fibre laser with a spot diameter of 130 μm [122]. Another study on welding of SUS 304 plate succeeded in achieving penetration of up to 20 mm in one pass using a YAG laser beam with power of 7.6 kW and a speed of 0.2m/min. [137]. Vollertsen et al. [144] (2008) increased the welding thickness to 20.5 mm in mild steel plate, with a one-pass 30 kW laser combined with an arc source. Zhang et al. [16] (2011) developed recently gas jet assisted laser welding technique. He used a jet gas to increase the keyhole depth with no need for higher power. 10 kW fibre laser was used successfully for penetration into 40 mm thick plates in two passes from both sides as shown in Figure 4-23. N_2 used as shielding gas with get flow 12 l/min.

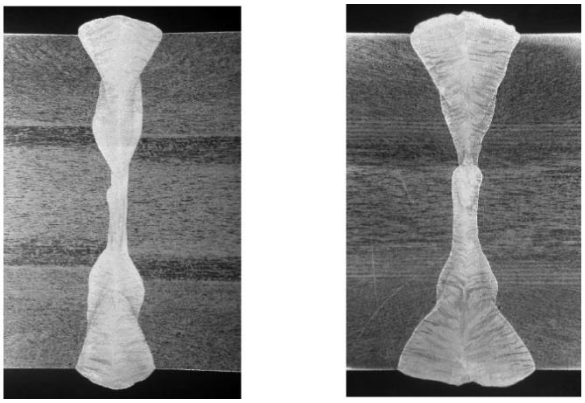

(a) v= 0.3 m/min (b) v= 0.2 m/min

Figure 4-23 Gas jet assisted laser welding of 40 mm thick plates

The power of the laser and the spot diameter are key factors in increasing the power density in order to increase the penetration of laser welding. However, increasing the power in some cases will not be an economical solution, and will also lead to increased plasma formation - at a certain power density the plasma will block the laser beam totally. Increasing the power may also lead to evaporation of the welded area, due to excessive heat input to material. In order to increase the depth of welding without an excessive increase in power, new candidate techniques were developed for improving the power efficiency of welding. One of these techniques is hybrid laser/arc welding, and the other is narrow-gap laser welding. Both techniques will be discussed in the following sections.

4.6.2 Hybrid laser welding

This technique is based on adding a second heat source to the laser beam during the welding process [145] The primary heat source could be a laser beam such as a Nd-YAG, CO_2 or a fibre laser [146]. The secondary heat source, from an arc welding system, is directed into the keyhole or into the interaction zone produced during laser welding. Combining arc welding with laser welding leads to an increase in the power density, which improves the keyhole stability [43]. The welding speed is increased compared to the pure laser beam welding process, and it can be observed that the undercut typical of high-speed laser welding is prevented [145]. This leads to improved weld quality, increased welding thickness, and improved process stability

and efficiency [146]. Two general types of hybrid laser welding exist: high power diode assisted laser welding, and arc-augmented laser welding (TIG, MIG or PLASMA) [146, 147] .

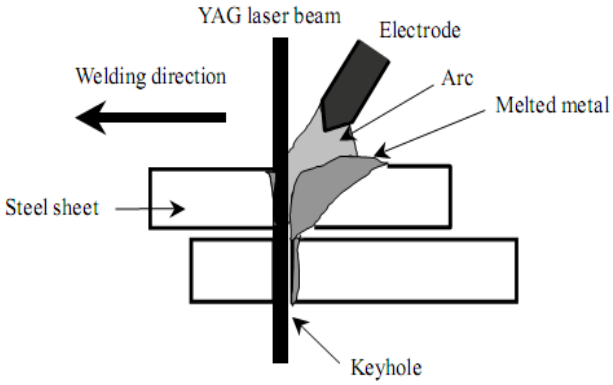

Figure 4-24 Laser arc hybrid welding [148]

4.6.2.1 Arc-Augmented Laser Welding

In this method, an electric arc is the secondary heat source, which is integrated with the laser through a special head as shown in Figure 4-25. The combination of arc and laser beam will lead to improvements in the operation for the two heat sources.

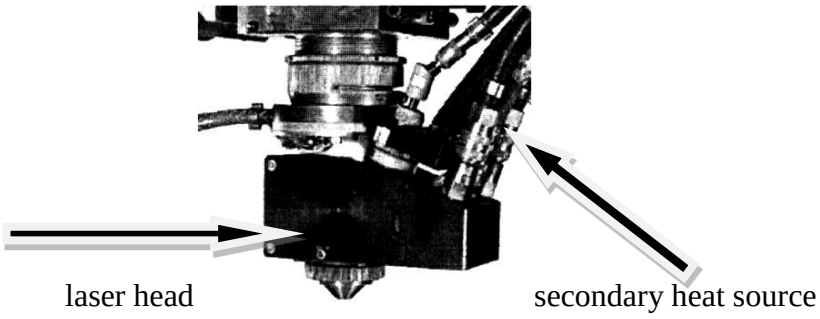

Figure 4-25 Integrated hybrid laser welding head [149]

The welding arc consists of a discharge of electrons in an ionized medium between cathode and anode. It depends on the current intensity and degree of ionization of the shielding medium. The arc ionization increases due to a combination of the effect of the laser and the current intensity of the arc, which cause a decrease in the ionization resistance [100]. The arc created during hybrid welding is squeezed, and

consequently concentrates the energy since it discharges from around the narrow spot of the laser, as shown in Figure 4-26.

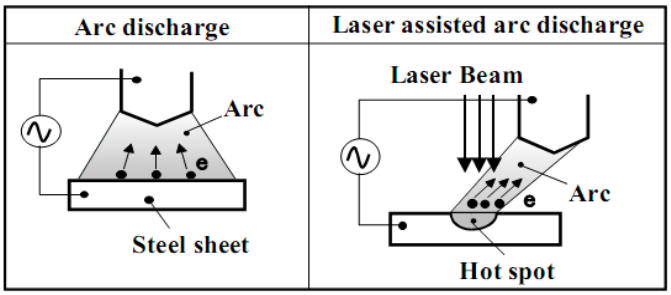

Figure 4-26 Arc discharge squeeze due to laser beam [148]

During arc-augmented laser welding, the thermionic emission is higher in the keyhole area, due to the presence of the laser radiation and the high temperature and high electron density 10^{17}–10^{23}/cm^2 in the keyhole; this will improve arc stability even at high welding speeds [148]. The combination of the electric arc and laser beam has a positive effect upon laser properties - the electric arc improves energy transfer to the surface from the laser beam, by reducing reflection from the metal. The surface of most metals reflects laser light at normal temperature. The presence of the electric arc increases the temperature of the material, consequently the reflectivity is decreased and the absorptivity is improved, as shown in Figure 4-27

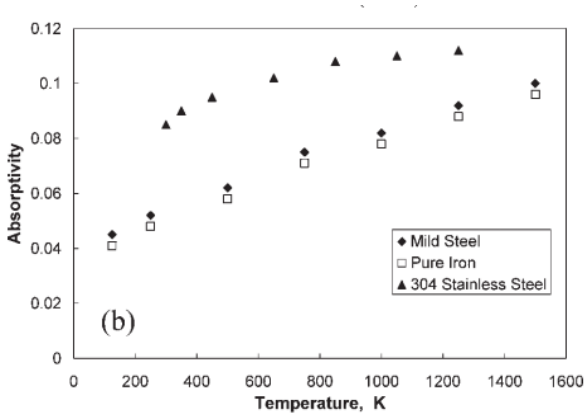

Figure 4-27 Temperature effect on absorptivity [115]

4.6.3 Narrow gap laser welding

Typical weld penetration for autogenous laser welding techniques is in the order of 1-2 mm/kW of laser power [14]. The welding of cross-sections greater than 30 mm is

still beyond capability of currently available laser powers. Narrow-gap laser welding is another laser welding technique, which depends on a multi-pass strategy with filler wire, based on a narrow-gap approach. It is an emerging welding technology, which can be applied to thick-section welds by using relatively low laser power, as described by Zhang et al. [60], and Starling et al. [150].

It is possible to use a NGLW technique with a low welding power density and high welding speed, to weld a thick plate, by using an optimum root gap [151]. Design of the gap is an important requirement in improving the welding quality. The width, and the taper angle of the groove should be as small as possible to minimize the volume of the gap, but the groove angle should be more than the divergence angle of the laser beam in order keep the laser beam and filler wire reaction point at the bottom of the gap [95]. According to recent research, the gap width is 1-5 mm, according to sample thickness, filling wire diameter and laser welding power. The taper angle is 0-6 degrees [14, 16, 95]. Figure 4-28 shows an example of the modelling of a narrow gap configuration. The sample shown is 10 mm thick; the root gap width is 1 mm, and taper angle is 3º. It required to add 10 passes to achieve a full weld, as shown in Figure 4-28 b.

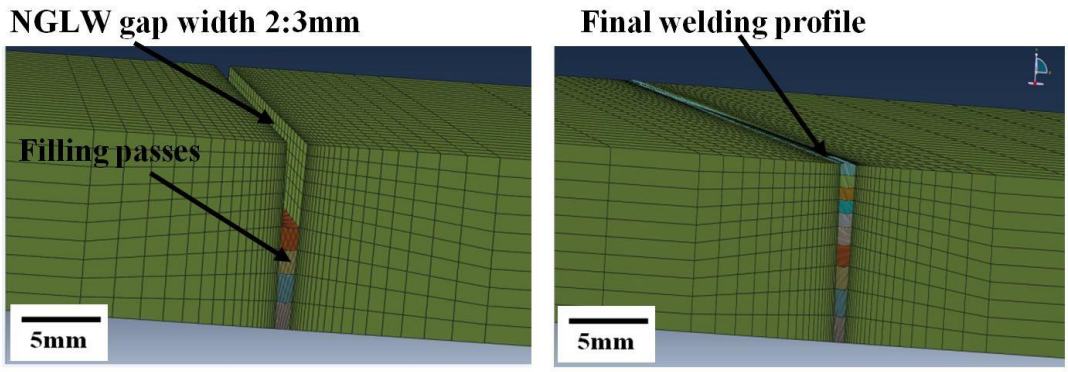

a) Partially weld 4 filling passes b) complete welding 10 filling passes

Figure 4-28 Modelling for multi pass NGLW 10 mm thick sample

There are potential metallurgical advantages associated with NGLW techniques, such as the effect of the filler material composition on the metallurgy and properties of the weld pool for laser welds. For example, Zhang effectively controlled the chemical composition of the filler wire to suppress solidification cracks [60]. This technique decreases the required tolerance tightness requirements for the welding

gap. Despite the advantages of multi-pass laser welding with a filler wire, it is considered a more complex process than autogenous laser welding, as it has more interrelated variables. The laser welding parameters include power, focal position and traverse speed. Using the multiple-pass narrow gap welding technique will add more parameters, which will also influence the process. These may include the filler wire composition, the filler wire diameter, the angle between the wire and the laser beam, the relative position between the wire and laser focus, and the wire feed rate. The combination of these factors, together with the joint gap geometry and process shrouding, make the process more complicated [15]. Indeed, there is often a limited window of acceptance for many process variables. For example, the laser beam and filler wire need to be aligned to within 0.2 mm inside the weld groove, and the wire feed rate fluctuation should not be more than ± 0.5% during a weld run, if uniform weld beads are to be achieved [15, 39].

Few studies use narrow gap techniques to investigate welding parameters and different gap preparations. Jokinen et al. [95] uses a Nd-YAG laser for welding plates with 20 mm thickness. The gap preparations are shown in Figure 4-29 a. Six passes were required to fill the gap. The parameters were: laser power 3 kW, welding speed 0.5 m/min, filler wire speed 4.5 m/min, groove angle 10º, interaction point 2 mm below focus plane and wire inclination angle 45º. The results show an acceptable quality for the weld cross-section, as shown in Figure 4-29b. This indicates that the main variable parameter in this process is the interaction between the filler wire and laser beam.

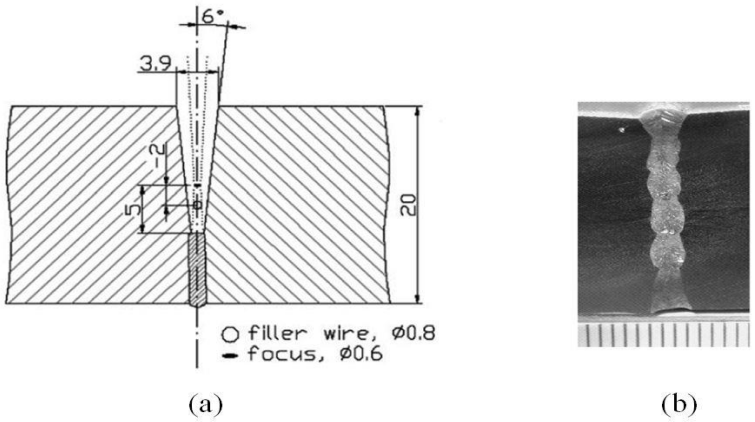

Figure 4-29 Cross-sections of the welds [95]

Zhang et al. have recently made a significant advance in NGLW, succeeding in welding 50 mm thick plates of austenitic stainless steel 316 by using a multi-passes narrow gap welding technique with a laser power of 8 kW [16]. The gap and configuration for the welding process is shown in Figure 4-30.

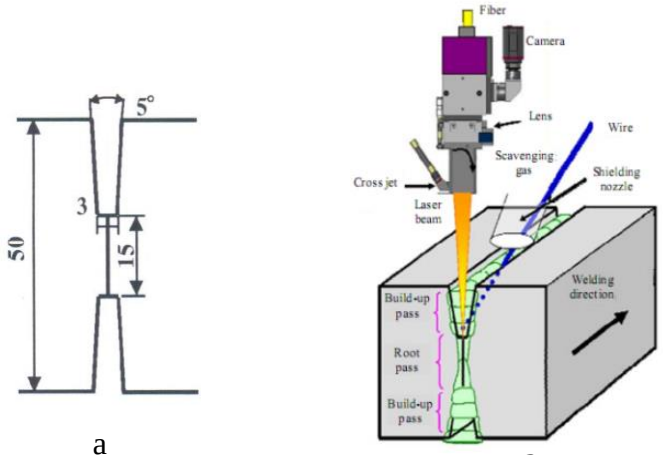

a

Figure 4-30 Configuration of narrow gap dimensions [60]

The pass for the welding root with a 15 mm thickness is performed without filler material. It is followed by 8 passes with a Y308L austenitic stainless steel filler wire. For welding the root condition, the optimum value of power is 6 kW, with speed 0.5 m/min [17]. For the filling passes, it was found that the optimum laser power for good bead formation was 6 kW, the welding speed 0.4 m/min, and the filler feed 5.5 m/min. Changing this value affected the integrity of the welding bead. If the filler feed rate is increased, it will lead to lack of fusion due to insufficient energy with respect to the wire feed; it will cause a gap between the upper welding layers and root cross section, as shown in Figure 4-31a, and lack of fusion due to re-melt of the root section due to insufficient wire feed with respect to input power (wire suppression) as shown in Figure 4-31b. The results of the optimum welding parameters are shown in Figure 4-31c.

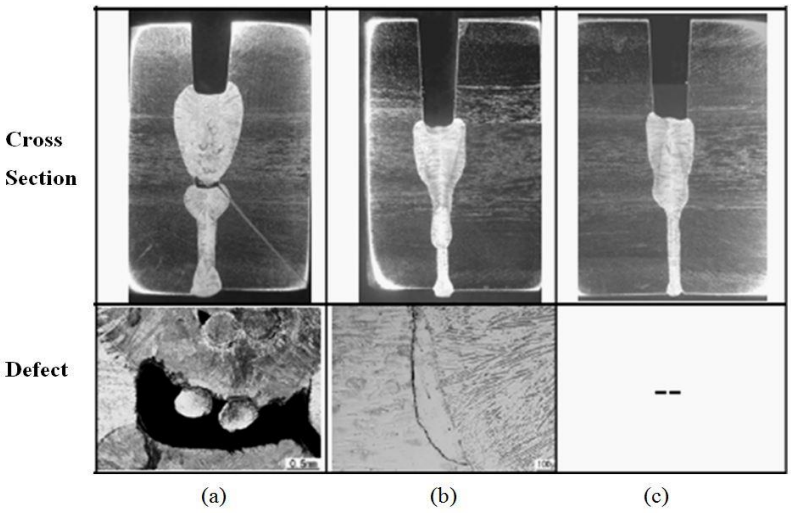

a) Power suppression b) wire feed suppression (c) good welding

Figure 4-31 Lack of fusion in multi pass laser welding zone [16]

Phaoniam et al. (2013) [152] studied the influence of the hot wire on the NGLW technique. The welding configuration is shown in Figure 4-32. 3 kW laser power was used with travelling speed 0.5 mm/min, wire feed rate 8 m/min, wire current 137 A, angle 80º to horizontal direction, and argon shielding gas. The results show improved welding efficiency due to increased laser power absorptivity of hot wire, and improved deposition rate. Low dilution and narrow heat affected zone

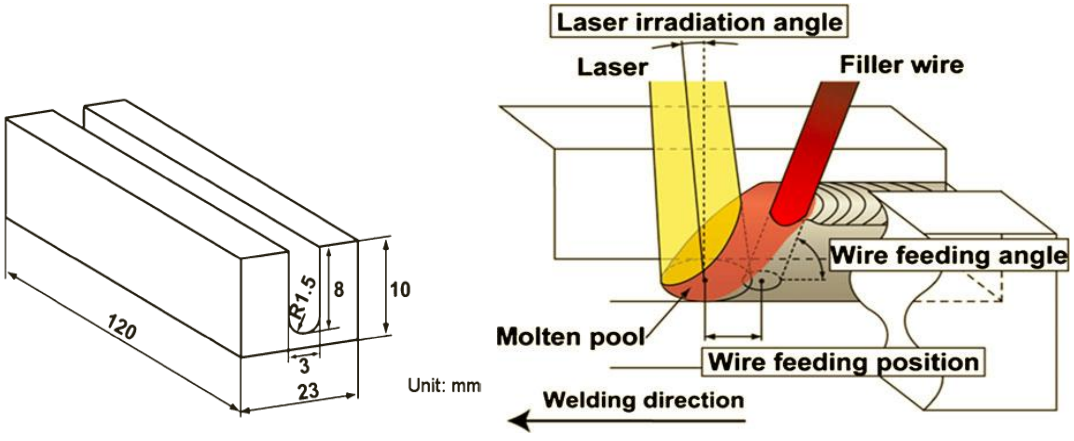

Figure 4-32 Hot wire NGLW configuration

4.6.3.1 Factors affecting the efficiency of narrow gap laser welding

Salminen et al. 2010 studied the laser beam interaction during laser welding with filler wire [153]. The efficiency of laser welding using filler wire depends on two

main factors: absorptivity and melting efficiency. The absorptivity depends on the material, laser light wavelength and welding system; when the laser beam interacts with the filler wire, it absorbs part of the power. Part of the beam passes through the wire and part of it is reflected away. The ratio between the reflected and absorbed value of the laser power depends on the beam power, the wire feed rate, the wire - beam interaction point and the power density [153].

Increasing the wire feed rate leads to an increase in the reflectivity, and consequently a decrease in the absorptivity. Preheating the wire will lead to a decrease in the reflectivity and improve the welding efficiency [153]. The optimum value for the wire feeding angle α_w is= 45° - 60°, as shown in **Error! Reference source not found.**.

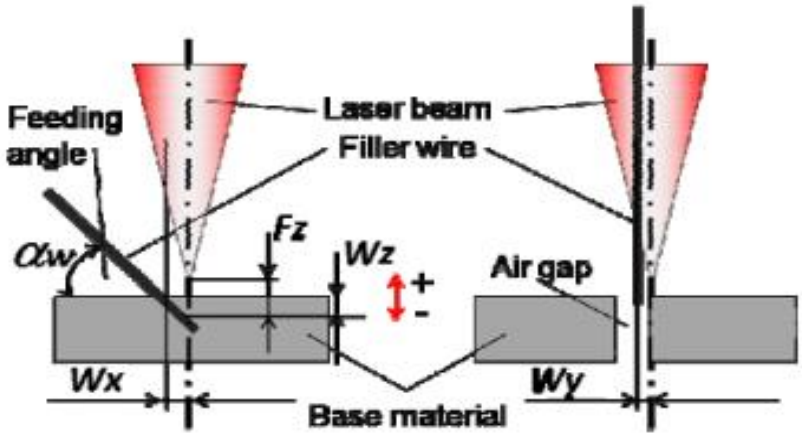

Figure 4-33 Relative position between filler wire, laser beam, workpiece [153]

Decreasing the angle will lead to losses in the reflected beam, since it is reflected outside of the keyhole, consequently the optimum value for this angle approximately 45°, in order to keep most of the reflected light inside the keyhole and improve the total welding efficiency. The melting efficiency will be affected by the accuracy of the alignment between the laser beam and the wire position. The feed position error, transverse to the welding direction (W_y), leads to a decrease in the melting efficiency. For an error of 0.25mm, the efficiency of 2 mm wire is reduced by 30%, and 36% for a 1mm wire. The wire is usually fed to the leading edge of the keyhole which offers more evenly distributed filler. The wire – laser beam interaction level should be on the workpiece top surface or slightly below it. Salminen et al. pointed

out that the optimization of the process requires further research to achieve good welding results [153].

Laser power, and wire feed rate are very significant factors for the weld bead quality in NGLW technique. Zhang et al. [16] studied the influence of laser power intensity, and deposition area on the weld bead. He found a limited windows of acceptance for NGLW technique as shown Figure 4-34. Increasing the deposition area will lead to lack of fusion A (Power suppression), and increasing the laser power intensity will lead to lack of fusion B (wire feed suppression) as shown previously in Figure 4-31.

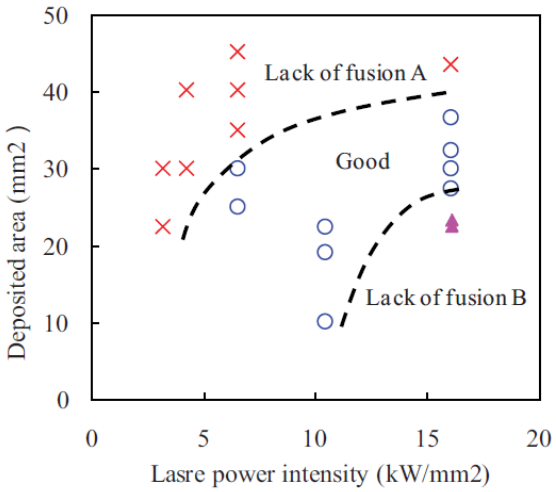

Figure 4-34 Influence of laser power intensity and deposition area on the weld bead quality [16]

4.7 Current and future applications of narrow gap technique in nuclear industry

Current usage of laser welding, and particularly NGLW technique in nuclear industry is still limited. Despite the promising behaviour of the NGLW technique in terms of low heat input to the weld joint and limited power required for welding thick sections, it represents a challenge to satisfy good weld performance. This is mainly due to high number of interacting parameters as discussed. Consequently, to produce weld joints without defects was the main objective for most of previous studies of NGLW technique[16, 95] .

There are a few research studies developing this technique for potential nuclear applications. Jokinen et al. [95] investigated the influence of the interaction between laser power and the wire for welding 20 mm stainless steel to develop a new joining method for the ITER vacuum vessel sectors with minimum defects and lower distortion, as mentioned in detail in section 4.6.3.

Recent development of NGLW technique was investigated by GE Hitachi nuclear in Japan, which started a project to develop a NGLW technique for welding thick section stainless steels. They studied the usage of NGLW technique in stainless steel welding for current and future applications in nuclear power plants. The main objective was to use the NGLW technique to weld thick sections with no defects, and to suppress the tendency of weld joint to SCC in nuclear reactor components as shown in Figure 4-35 [85].

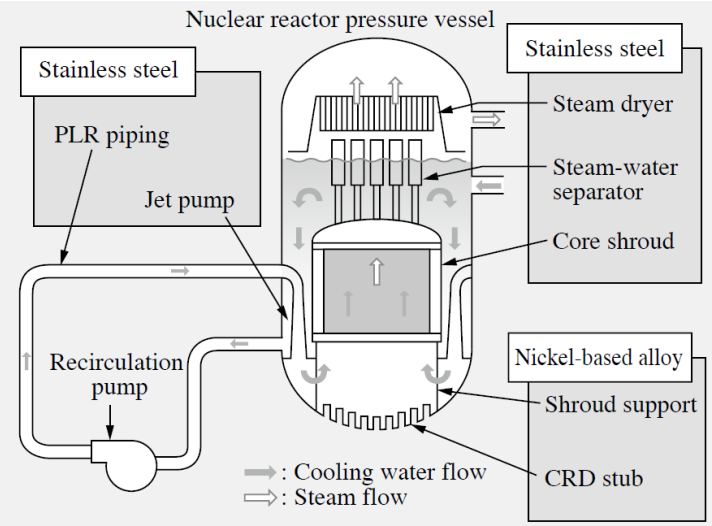

Figure 4-35 Stainless steels used in (boiling water reactor) BWR power plant [85]

The research investigated how to satisfy welded joint specifications without the lack of fusion and porosity. They succeeded in (2011) applying this welding technique for thicknesses up to 50 mm with a power 6 kW disk laser in 8 passes from both sides [16] as shown in Figure 4-36, and discussed in detail in section 4.6.3. Then they investigated the influence of the work hardened outer layer on SCC behaviour, and how the performance could be improved by removing this layer. However residual stresses were evaluated only at the surface, and the results were validated by using another technique [60].

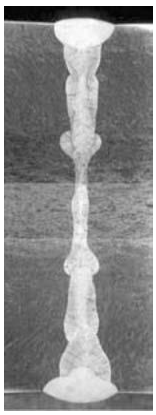

Figure 4-36 Narrow gap welding of 50 mm thickness stainless steel [16]

The influence of the welding parameters on the weld bead quality and the developed residual stress is unknown, and needs more investigation. Optimization of the welding parameters for that technique to satisfy the optimum weld joint cross section without welding defects is still a point of weakness and needs more investigation [154]. Moreover, corrosion behaviour of NGLW technique and comparison with conventional welding processes has not yet been studied. The influence of the residual stress on SCC also needs more investigation.

4.8 Summary

Austenitic stainless steel alloy is used widely inside nuclear reactors. It has a good mechanical properties, and high resistance for corrosion, however it is very sensitive to heat input during welding process. Welding codes inside nuclear power plants mainly includ high heat input process due to lack of accumulated knowledge of the high power density welding processes. Despite the promising potential of NGLW technique in terms of thick cross section welding with low heat input, and low expected residual stresses, it is very difficult technique due to tight requirements of accuracy, and high number of interacting parameters. Literature review highlights the gap of accumulated knowledge of that technique because a few number of articles explore the detail behaviour of NGLW technique.

The workspace of the current study will concentrate on filling this gap by improving the knowledge base of NGLW technique in terms of optimization of welding

parameters to improve the weld bead quality, mechanical and microstructure evaluation of weld bead, residual stress study, and modelling the process to validate the results, and finally the behaviour in corrosion environment.

Part II Current Study

CHAPTER 5. EXPERIMENTAL FACILITIES, AND PRELIMINARY WELDING EXPERIMENTS

5.1 Introduction

This chapter includes details of the developed welding system components, and the experimental setup for the NGLW experiments. The developed fixture for the wire feeder nozzle to the laser head, and also the workpiece clamp configuration are introduced. This chapter includes also some screening and preliminary experiments for laser deposition by using a wire feeder. The aim of these experiments is to demonstrate the relationship between the laser parameters, wire feeding rate, and the homogeneity and size of the deposition layer; these results are critical to acceptable NGLW results and for further optimisation.

5.2 Experimental equipment and facilities

The NGLW technique is based upon a multi-pass concept, using a filler wire. The system used in this project is shown in Figure 5-1. It consists of the following facilities:

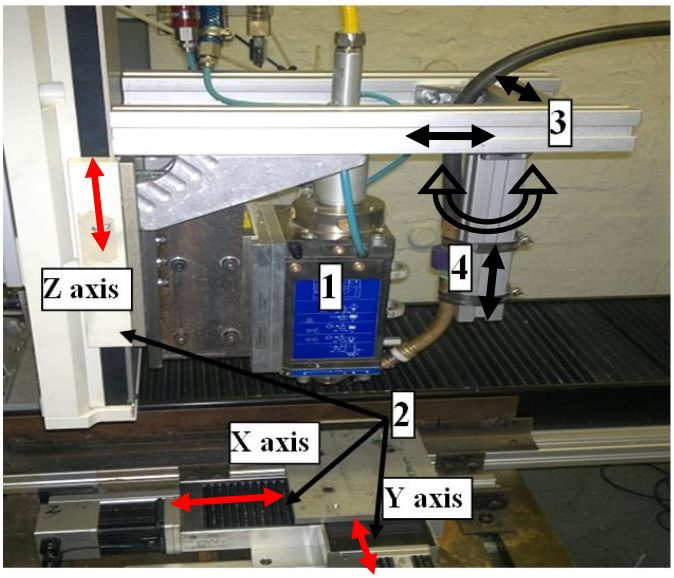

Figure 5-1 Experimental work set up

(1- Laser head, 2- Stage moving axis, 3- Wire feeder fixture, 4- Wire feeder nozzle)

A continuous wave (CW) IPG fibre laser, model YLR-1000-SM Ytterbium with 1 kW power. The fibre laser uses a coaxial shielding nozzle, and can emit a beam in the near-

infrared spectrum at 1060 - 1080 nm wavelength, with a beam quality factor $M^2 < 1.07$. The beam is delivered via an optical fibre, with a fibre core diameter of 14 μm, to the output lenses, and focused to a minimum spot size of 70 μm in diameter using a 190.5 mm focal-length lens.

A two dimensional stage provides X-Y axis control of workpiece movement, and a third stage with an axis in the Z direction, controls the laser head movement as shown by the red arrows in Figure 5-1.

5.3 Experimental system setup

NGLW weld bead quality depends significantly on the accuracy of alignment between the laser beam nozzle and the wire feed nozzle and the wire position with respect to the focal position, in order to achieve acceptable results with the NGLW technique. Sun et al. [15] stated that the laser beam and filler wire need to be aligned to within 0.2 mm inside the weld groove. The gap width in the NGLW technique is very narrow, and is dependent on laser power and wire diameter [14, 95, 153]; consequently the designed fixture should be flexible, and provide accurate relative alignment between the laser beam and the wire inside the narrow gap. The implemented fixture shown in Figure 5-1 has 3 translational degrees of freedom in the X, Y, Z directions, and there is a rotational degree of freedom, to control the angle between laser beam and wire feed direction, as shown in the black arrows in Figure 5-1.

5.4 Stainless steel wire deposition screening experiments

The first set of experiments investigated the influence of the welding parameters such as laser beam power, wire feed rate and traverse speed, considering two responses; the weld bead (solidification zone) geometry (width - height), and homogeneity of the deposition layer. These experiments are important for determining windows of acceptance of each welding parameter, which can meet acceptable weld bead quality and size requirements. These parameter ranges will then be the key targets for optimization of the NGLW technique welding parameters in the next set of experiments. The experiments for wire deposition were performed with the test configuration shown in Figure 5-2, where N is the standoff distance, α is the angle between wire and laser

beam (set at 45° according to previous recommendations for best weld quality in [154]), and *H* and *W* are the height and width of the bead, in mm.

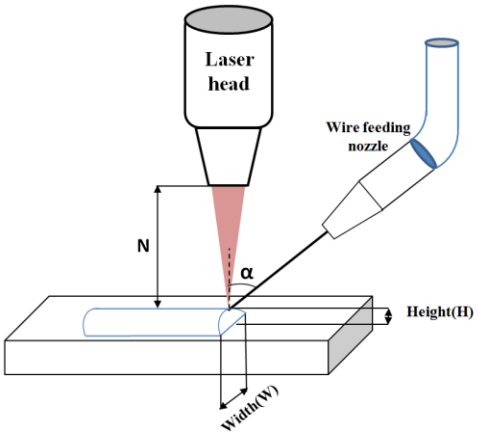

Figure 5-2 Configuration of deposition experiment

5.4.1 Influence of wire feed rate on bead size - homogeneity

These experiments were designed to examine the influence of the wire feed rate on weld bead size and homogeneity. The experiments were performed with a laser nozzle diameter of 6mm, and a wire diameter of 0.8 mm. Argon was used as the shielding gas, with a flow rate of 30 l/min. The base material and wire were AISI 316L stainless steel. Weld bead homogeneity is defined according to:

$$Weld\ bead\ homogeneity\ \% = \frac{length\ of\ continuous\ bead}{total\ length\ of\ the\ bead} \times 100 \qquad (5.1)$$

Length of continuous bead is defined as following:

$$= \frac{total\ length\ of\ bead\ segments\ + length\ of\ maximum\ bead\ segment}{2}$$

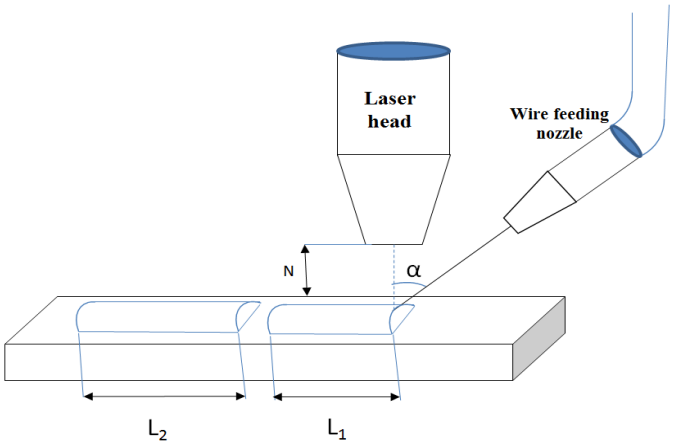

Figure 5-3 Bead homogeneity definition

Total length of bead segments: $L_1 + L_2$.

Length of maximum bead segment: L_1.

The results of these experiments show that an increase in the wire feed rate leads to an increase in the height of the deposition and a decrease in the clad width, as shown in Table 5-1. The weld bead homogeneity increased with wire feed rate increases, up to a peak value, after which it degraded dramatically.

Table 5-1 Wire feed influence on bead size- homogeneity

No	Stand of N[mm]	Power [w]	Focus [mm]	Traverse speed [mm/s]	Wire feed rate [mm/s]	Homogeneity %	W [mm]	H [mm]
1	10	950	10	6	10	45	2.29	0.62
2	10	950	10	6	15	82	2.22	0.71
3	10	950	10	6	17	98	2.1	0.9
4	10	950	10	6	25	78	2.02	1.26

Increasing the wire feed rate led to an increase the laser power required for a proper fusion; moreover, the percentage of reflected power will be increased [153], consequently the depth of penetration of the deposition layer into the base metal is decreased. Decreasing the penetration of base metal will lead to an increase in the deposition layer height.

Increasing the wire feed rate to 25 mm/s without optimizing the laser power resulted in a reduction in the welding efficiency, due to non-homogeneity between wire feed rate

and power required for proper fusion, consequently homogeneity of the deposition pass is interrupted. The homogeneity was decreased as the wire feed rate was decreased below certain values as shown in Table 5-1. Decreasing the wire feed to 10 mm/s or less was noted to generate a discontinuous deposition layer with higher error margins, as shown in Figure 5-4. The size of the homogenous welding bead is small at low wire feed rates, due to the wire deposition rate being insufficient to achieve a continuous deposition. The size of the homogeneous welding bead increases gradually as the wire feed rate is increased, until it reaches a peak value at 17 mm/s, but it then starts to decrease again due to insufficient power in the wire to allow the formation of a homogeneous bead with proper fusion; as a consequence, the bead is interrupted, causing unsatisfactory bead homogeneity .

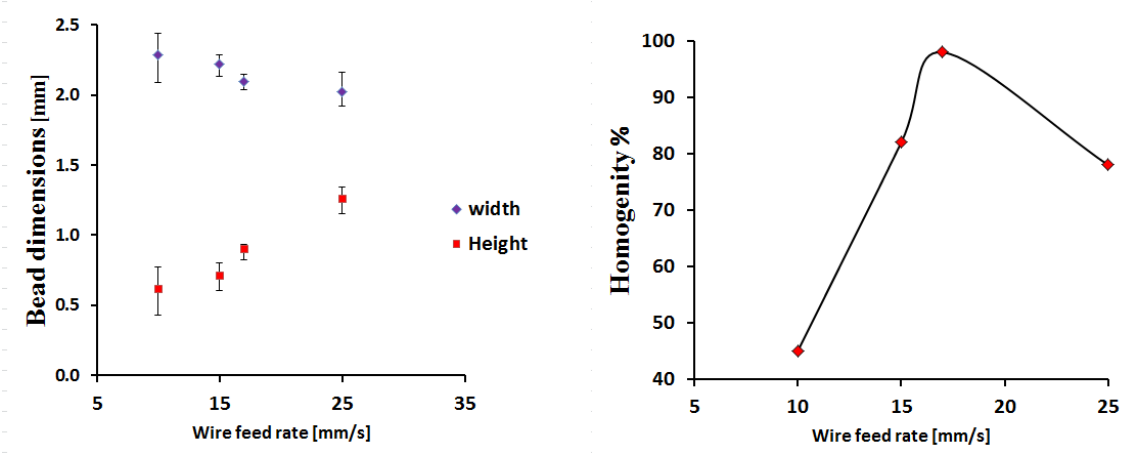

Figure 5-4 Wire feed influence on bead size

5.4.2 Influence of traverse speed on the bead size - homogeneity

The second set of experiments was designed to study the influence of the welding speed on bead size and homogeneity. The results show that the speed of the welding is inversely proportional to the deposition height and width; increasing the speed led to a decrease in the height and width of the weld bead, since the energy delivered per unit length was decreased. The penetration of the sub-layer was also decreased, as was the delivered wire volume per unit length; both of these factors led to decreasing the deposition height and width, as shown in Figure 5-5.

Table 5-2 Welding speed influence on bead size- homogeneity

No	Stand of N[mm]	Power [w]	Focus [mm]	Traverse speed [mm/s]	Wire feed rate [mm/s]	Homogeneity %	W [mm]	H [mm]
1	10	950	10	4	17	46	2.27	1.19
2	10	950	10	6	17	71	2.1	1.04
3	10	950	10	8	17	84	2.02	0.85
4	10	950	10	10	17	95	1.96	0.61

The tolerance values (shown by the error bars) for the width and height graphs were decreased by increasing the welding speed, due to improvement in homogeneity and continuity of the bead, as shown in the homogeneity diagram in Figure 5-5 b.

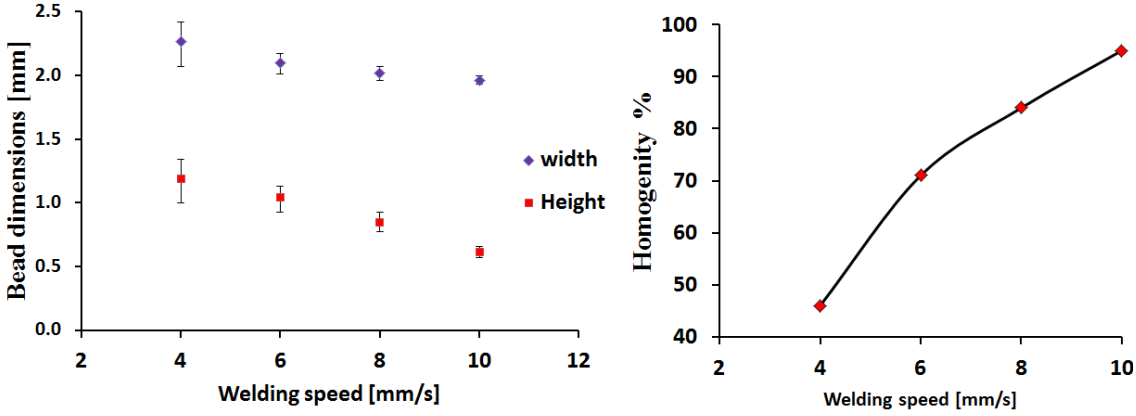

Figure 5-5 Speed influence on deposition bead size- homogeneity

5.4.3 Influence of power on the bead size – homogeneity

This set of experiments was designed to examine the influence of the laser power on the size and homogeneity of the weld bead. The experimental results are shown in Table 5-3.

Table 5-3 Power influence on bead size- homogeneity

No	Stand of N[mm]	Power [w]	Focus [mm]	traverse speed [mm/s]	Wire feed rate [mm/s]	Homogeneity %	W [mm]	H [mm]
1	10	950	10	10	17	98	1.8	1.12
2	10	800	10	10	17	95	1.5	1.22
3	10	700	10	10	17	91	1.4	1.28
4	10	600	10	10	17	77	1.3	1.37

The graphical representation of the results is shown in Figure 5-6; it shows that as the laser power increases, the weld bead width generally increases, but the deposition pass height reduces due to the increase in base metal penetration with the increases in the laser power. This leads to a decrease in the height of the deposition, as shown in Figure 5-6, and consequently an increase in the width. The homogeneity of the weld bead is improved at high power as shown in Figure 5-6 b, due to an improvement in the fusion efficiency of the wire and improves the heat transmitted to the sub layer for a proper fusion between layers. It is therefore recommended that laser powers ≥ 700W are used to improve the weld bead homogeneity.

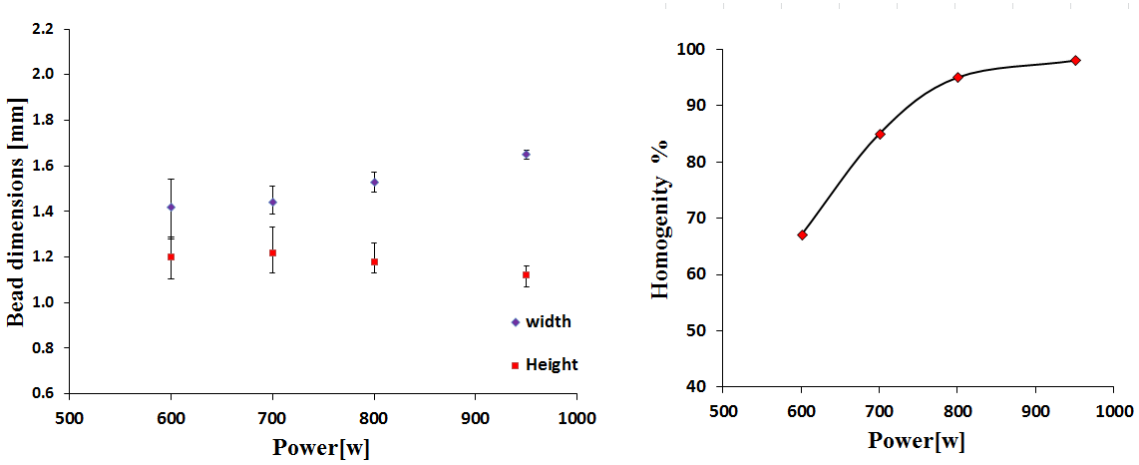

Figure 5-6 Power influence on cladding height- width

5.5 Challenges of NGLW with stainless steel

Some challenges were highlighted during the preliminary experiments for the multi-pass NGLW process. The next section will describe these challenges, and will present techniques developed to minimize their influence.

5.5.1 Surface oxidation

Surface oxidation is considered as a critical challenge for the multi-pass NGLW technique, due to the difficulty of shielding when welding in an open environment. Shielding inside a narrow gap is more difficult; back shielding of the root surface must be efficient to protect the surface during multi pass welding process, otherwise The welding surface will suffer from severe surface oxidation, as shown in Figure 5-7a.

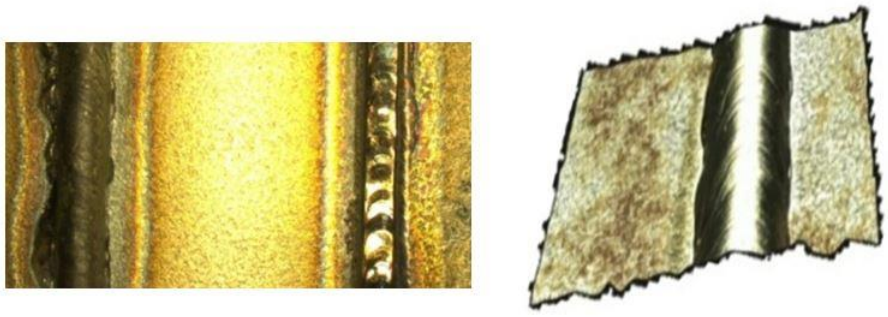

a- Oxidized surface b- shielded surface

Figure 5-7 Bead surface shielding

5.5.1.1 Improving shielding efficiency

Special techniques were implemented for improving experimental results (bead surface shielding – Bead surface uniformity) as shown in Figure 5-7b.

a- Increase the coaxial laser nozzle diameter – used diameter (d= 6mm).

The use of a larger-diameter nozzle may affect the life of laser lens by causing an increase in back-reflection from the welding surface; however the use of a larger nozzle is very important in improving the shielding efficiency. An increased nozzle diameter leads to a more stable gas flow and a decrease in gas turbulence over the shielded surface - consequently the shielding efficiency is improved. An increased nozzle diameter will also increase the protected area over the shielded surface, and a decrease in the pressure of the shielding gas over the surface during the welding operation.

b- Shielding gas showering tube

A new design of shielding gas shower tube was developed to improve the shielding efficiency (specially for NGLW); it consists of a thick metal tube, with a longitudinal groove machined along its main axis, connected to the shielding gas, and sealed at the other end. A special small fixture was designed to align the tube in the right position just behind the laser nozzle. Figure 5-8 shows a schematic and photograph of the laser nozzle, filler wire nozzle and shielding gas shower tube. The shielding efficiency was improved dramatically by using this configuration, as shown in Figure 5-7b.

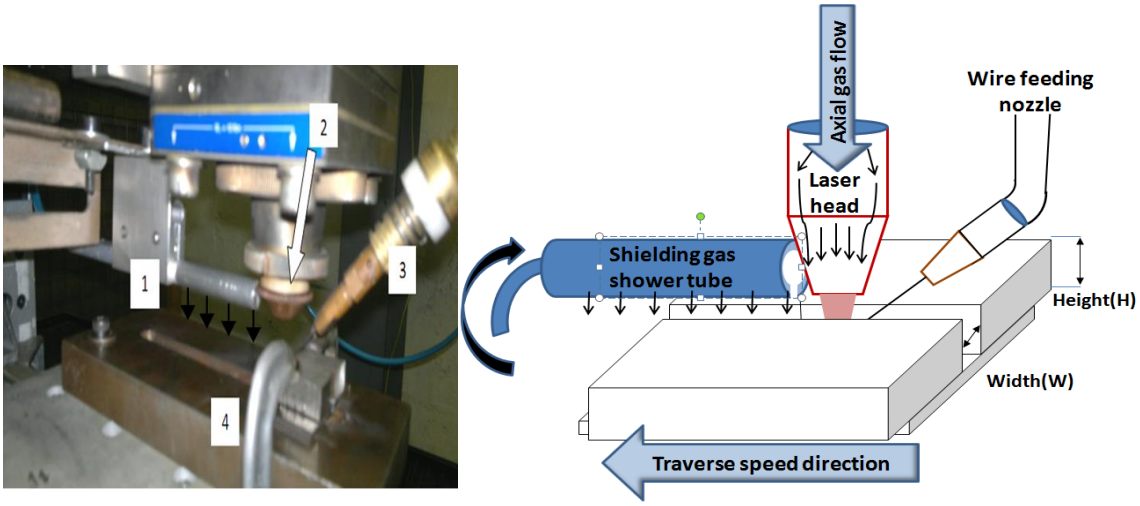

a) Real configuration b) schematic drawing

Figure 5-8 Shielding gas shower tube construction

1-Shielding gas shower tube 2- laser nozzle 3- Filler wire nozzle 4- Welding joint fixture

c- Back shielding fixture

Back shielding of the root surface is very important in order to provide full protection of the welded joint; it was achieved with a specially designed fixture, which provided a proper shielding gas flow for the back surface during the welding process, especially during the welding of the root pass. The fixture was designed with an internal chamber, which was connected to shielding gas input tube. It directed the gas to the lower surface of the workpiece during the welding process, shown by the black arrows in Figure 5-9.

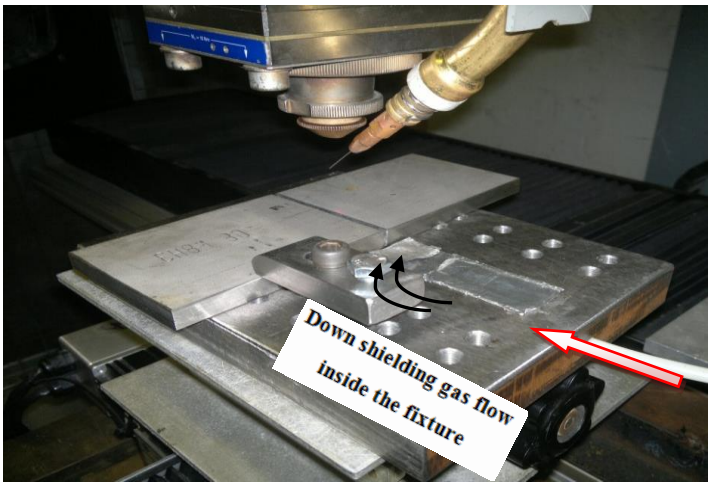

Figure 5-9 Back shielding fixture

5.5.2 Under-cut

Under-cut defects are mainly caused by improper filling of the upper pass of multi-pass laser welds, as shown in Figure 5-10 . The main reason for this improper filling is a non-optimized combination of welding parameters, particularly the welding speed, deposition rate, or if the width of the weld bead is not covered by the width of the narrow gap. This problem will be considered in the optimization criteria described in the statistical model in the next chapter.

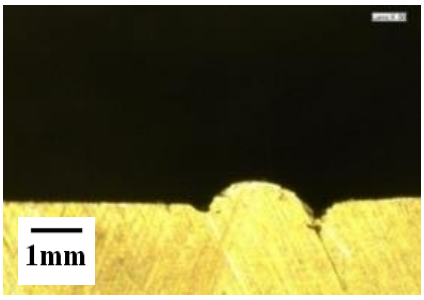

Figure 5-10 Undercut for upper welding pass

5.5.3 Lack of fusion to the side wall

This defect is mainly due to improper wire delivery system, and narrow gap configuration. These two conditions may lead to inaccurate positioning of the wire in the centre of the gap and result in this defect. Straightening of the wire and accurate and flexible clamping are very important to guarantee appropriate wire delivery.

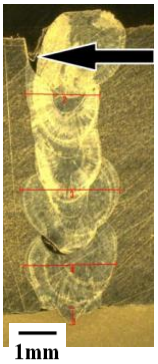

Figure 5-11 Lack of side fusion in welding

5.5.4 Lack of fusion between layers

A lack-of-fusion defect is mainly caused by the use of an incompatible combination of values of laser power and wire feed rate. If the laser power is suppressed, it will be insufficient for proper melting of the wire, and for fusion with the sub–surface, as shown in Figure 5-11, and Figure 5-12. Optimization of the welding factors (power, wire feed rate and welding speed) is a key in order to achieve optimum gap filling without a lack of fusion.

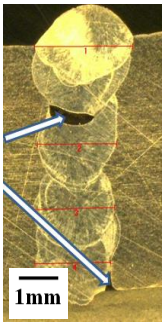

Figure 5-12 Lack of fusion

5.5.5 Distorted welding gap

This defect is mainly due to the high thermal expansion coefficient of the material being welded, and increases with the number of filling passes. Non-optimum gap design with respect to laser beam can lead to severe heat influence on the narrow gap side walls during multi-pass welding - consequently the gap size will be affected. Distortion of the workpiece is due to insufficiently rigid clamping during the welding operation. In the preliminary experiments, the initial gap width was 1 mm with parallel sides. The gap contracted to a width of 0.705 mm after three welding passes, as shown in Figure 5-13. This defect may be minimized by increasing the welding speed to decrease the heat input to the welding gap, or by decreasing the number of filling passes. In addition, the gap should be prepared with a ‘V-shape’ cross section, with a small angle, instead of with parallel sides, and clamped with a suitably rigid fixture. Figure 5-13 b shows the recommended gap configuration for welding 10 mm thick samples using the NGLW technique, using the system discussed in section 5.3.

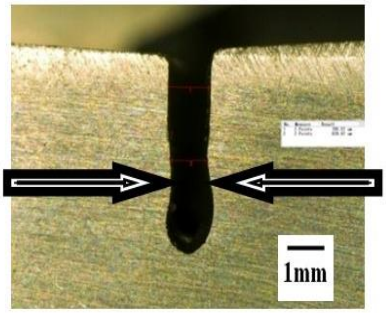

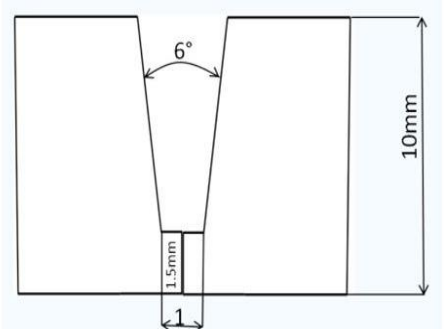

a) Closed gap b) Optimum gap configuration for 10 mm thick plates

Figure 5-13 Narrow gap configuration

5.6 Summary

In this chapter an experimental setup for evaluating the NGLW technique has been introduced; the setup includes facilities and developed systems designed to improve the welding performance. This chapter also includes the results of preliminary screening experiments for wire deposition, intended to specify the working range windows for different welding parameters to achieve an acceptable weld bead with high homogeneity. Finally this chapter describes the main challenges which affect the multi-pass NGLW technique, and the facilities developed to overcome these challenges.

CHAPTER 6. DESIGN OF EXPERIMENTS AND STATISTICAL MODELLING OF NGLW OF 316L STEEL

6.1 Introduction

Narrow gap laser welding is a very promising technique for thick- section welding, due to its low heat input and high production efficiency, compared to conventional arc welding techniques. As a consequence, it produces low distortion and reduced levels of residual stress [60]. Traditionally, very thick section welding has been achieved with submerged arc welding and other high-productivity welding processes. In the power generation industry, oscillating narrow-gap GTA has also been employed, using a welding gap of typically 8-15 mm in width; the use of narrow-gap TIG weld configuration dramatically reduces production times and overall heat input with respect to conventional arc welding [155]. This trend underlines the need to better understand the behaviour of ultra-narrow-gap (< 5 mm) laser welding, including the influence of discrete laser welding parameters, and also their interactions, on weld bead quality. The quality of a weld joint is directly influenced by the welding parameters, and it can be characterised in terms of properties such as weld bead geometry, mechanical properties and distortion [156, 157].

The NGLW technique is considered to be more complex than autogenous laser welding, due to a larger number of interacting parameters, including laser parameters, narrow-gap shape, and wire feeding nozzle parameters. The required positional and alignment accuracy between the system components further increases the complexity of this technique [15].

A great deal of previous research has focussed on the behaviour of single-pass autogenous laser welding; for example, Manonmani *et al.* [158] and Benyounis *et al.* [96] investigated the influence of laser autogenous welding parameters on the weld-bead geometry. Torkamany *et al*. [159] studied the influence of the welding parameters on the quality of the weld bead, and the keyhole behaviour in bead-on-plate welding. In contrast, investigations regarding NGLW are not frequently conducted. It has been stated previously that the NGLW technique is still in need of more research effort in order to achieve better optimization of the welding parameters [153, 154] . Due to

complex parameter interactions in the NGLW, one parameter at a time experimental approach cannot provide their interactions and sensitivity to their variations, thus difficult to optimise the process. In this chapter an design of experiment and statistical modelling technique was used to better understand the parameter interactions in NGLW of 316L stainless steel sheets and to optimise the welding parameters and procedures.

Reisgen et al. applied a statistical modelling approach to the study of single-pass autogenous laser welding of steels to optimise the process parameters. Clearly, statistical modelling is a useful approach for the study of multiple parameter interactions. This chapter aims to establish a statistical model to understand and control multiple process parameter interactions and to achieve optimum welding parameters for ultra-narrow-gap (< 2 mm, not previously reported) multi-pass laser welds. The influences of laser power, welding speed and wire feed rate on the integrity of the weld bead, the gap bridgability (lateral fusion), weld bead overlap factor, surface oxidation, welding efficiency, and weld joint strength have been studied and optimised for material thicknesses ranging from 5 to 20 mm, and with the maximum laser power limited to 1 kW. It is hoped that the general findings arising from this study will be applicable to welds made in much thicker sections of material, using higher laser powers.

This work will be followed by detailed investigations of the weld joint properties (tensile strength, fatigue strength, fracture toughness, bending strength, corrosion resistance, stress corrosion cracking, microstructure and residual stress), and the results will be compared with those of arc welding of similar material thickness, to give a full understanding of the behaviour of the NGLW weld bead with respect to other welding techniques.

6.2 Design of experiments and statistical modelling approach

Statistical modelling is one of the most efficient tools for developing a relationship between processing parameters and a particular response, whilst requiring a minimal number of experiments [156, 160]. The main objectives of using this approach are:

1- To establish a relationship between control factors and responses, which can predict the response values for given values of the control factors.

2- To determine individual and interacting significance of the factors on the responses.

3- To identify the optimal welding parameter and procedures to achieve peak performance of the response according to required optimization criteria.

6.2.1 Response surface method (RSM)

Response surface methodology (RSM) is one of the most commonly applied statistical modelling methods; it was introduced by Box and Wilson [161] in 1951. RSM is aimed at reducing the cost, time, and complexity of different analysis methods such as the finite element method or CFD analysis, and their associated numerical noise, to design optimization methods. RSM can be used in the development of adequate functional relationships between a response of interest, y, and input variables denoted by x_i, x_j, as shown in equation (6.1), which has the general form of a polynomial:

$$Y = \boldsymbol{\varepsilon_\circ}+\sum_{i=1}^{k} \boldsymbol{\beta_i x_i}+\sum_{i<j} \sum_{i=1}^{k} \boldsymbol{\beta_{ij} x_i x_j} +\sum_{i=1}^{k} \boldsymbol{\beta_{ii} x_i^2}+\boldsymbol{\beta_\circ} \qquad (6.1)$$

Where, ε_o is a random experimental error, β is a vector of p unknown coefficients, β_0 is the response at the centre point; β_i is the coefficient of the main linear components; β_{ij} is the coefficient of the two linear factor interactions, and β_{ii} the coefficient of the quadratic factor. RSM can be used to predict the response behaviour, with sufficient accuracy, inside the working ranges of the factors to be investigated. This technique had been used successfully with autogenous laser welding in order to investigate the relationship between welding parameters and the output weld bead responses [96, 158]. It has also been used for optimizing the welding process parameters. However, statistical modelling for NGLW to control the weld bead behaviour through the welding parameters has not been found in any previous work.

The scheme of the implemented NGLW model is shown in Figure 6-1. It consists of 3 variables and 6 responses, and the data flow direction through the model is shown. Modelling starts by creating a design matrix according to operating variables with defined limits. The response is evaluated at each design point of the experimental matrix. A control model is created for each response, and the overall model is modified using analysis of variance (ANOVA) statistics [162, 163]. Finally, a numerical and graphical optimisation process is carried out to obtain results according to the optimisation criteria.

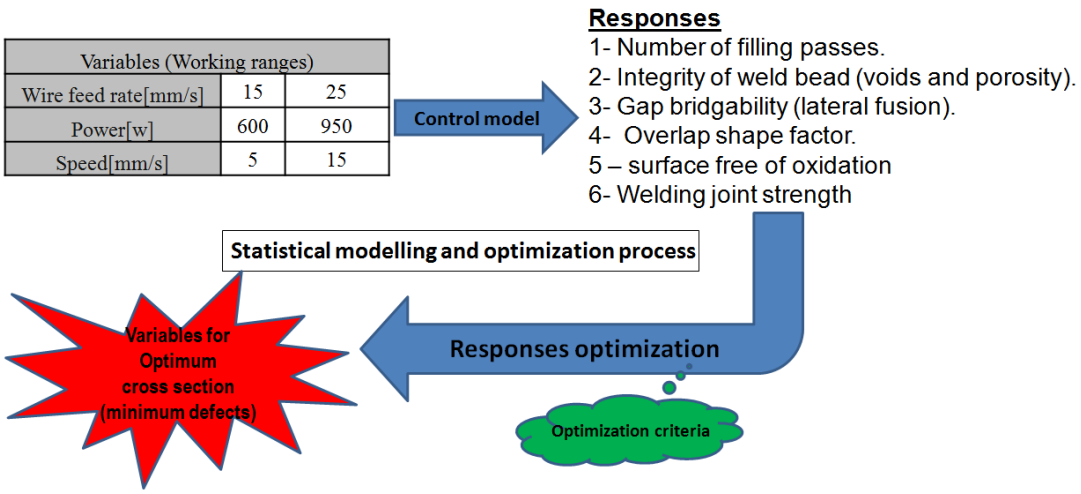

Figure 6-1 Statistical modelling and optimization process

6.2.1.1 Modelling Approach

A sub-method of RSM, called central composite design (CCD) was used to develop a second order polynomial model, which can also be used to optimise the responses of interest in the process. The CCD is three or five level experimental plan. It can fit second order polynomial with high accuracy, and represent a good accuracy for process optimization. CCD can be represented graphically by a cube for representing three factors as shown in Figure 6-2. It consists of 3 types of design points, central, axial, and factorial. [164].

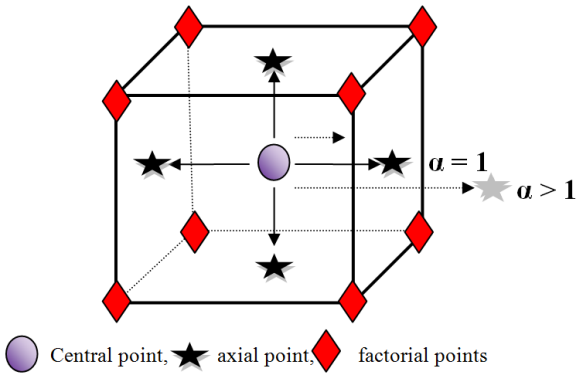

Figure 6-2 Central composite design points

The experimental design depends on applying one run or more at each point of the design matrix. For *k* factors, there are 2^k factorial points, *2k* axial points, and one central

point. The centre point is separated by α, to the axial points, and separated by unit to factorial points [164].

The value of α is always specified in coded values. If $\alpha = 1$, the design will be a surface design, since the axial points will be on the surface of the design cube, and the factors have 3 levels at (-1, 0, 1). In contrast, if α has a value greater than 1, the axial points will be outside of the design cube and two levels are created at $-\alpha, \alpha$. Consequently the factor will run at five different levels ($-\alpha$,-1, 0, 1, α), according to Figure 6-2.

The working range for each factor was established by preliminary screening tests. These screening tests were carried out by varying one of the process parameters at a time to identify the working ranges for acceptable welding quality, as presented in Chapter 5. From the results of the screening experiments, the ranges for process parameters for the design of experiments and statistical modelling were selected as shown in Table 6-1**.**

Table 6-1 Factor levels and process parameter ranges

Variable	Level 1	Level 2	Level 3	Level 4	Level 5
Power [w]	775	802.5	857.5	912.5	940
Speed[mm/s]	6	7	9	11	12
Wire feed rate mm/s]	15	17	21	25	27

The model was used to establish a relationship between the control variables and the responses. It was also used to determine the significant individual and interacting factors, and to optimize process settings, to achieve optimum performance according to specified optimization criteria.

6.2.2 Model validation

The adequacy of the implemented models is tested using analysis of variance (ANOVA) statistics [162, 163]. The ANOVA results show the significance of the models, which were tested against regression data using the same statistical package. An F-test was applied on each term of the model to measure the significance levels; it compares model variance with residual (error) variance. If the two values are close, the ratio will be close to one, and it is less likely that any of the factors have a significant effect on the response. The F-test is calculated from the model mean square value divided by the residual mean square. The 'lack of fit' represents the variation of the actual data around the fitted model; if the 'lack of fit' is insignificant according to the F-test results, this

implies that the model fits the data. R^2 and the adjusted R^2 values are the other two criteria, used to indicate the adequacy of a fitted regression model [165]. R^2 is a measure of the variation around the mean, and the adjusted R^2 value is a measure of the variation around the mean of the adjusted model terms (significant terms only). "R^2 adj." is calculated according to equation:

$$\boldsymbol{R^2_{adj} = \frac{(n-1)}{(n-p)} + (1 - R^2)} \qquad (6.2)$$

Where p is the number of model parameters and n is the number of experiments. The values of R^2 and adjusted R^2 for the models ranged from 86:99% and 78:97%. These values indicate that the models can be used to navigate the design space. The adequate precision parameter measures the signal-to-noise ratio for each model. A ratio greater than 4 indicates that the model has an acceptable signal [157]. The adequate precision values range from 11.8 to 22.5 for the models. Scatter diagrams were also used for regression. Perturbation curves and response surface graphs were derived for each model.

6.3 Results and Discussion

A set of 17 multi-pass narrow-gap laser welding experiments was performed, with different welding parameters according to the design matrix shown in **Table 6-2**. The statistical software package 'Design-Expert V.0.0' (Stat-Ease, Minneapolis, MN, USA) was used to code the variables and to establish the design matrix, based on a 5-level experimental plan. The number of experiments required to establish a model are calculated as follows:

Number of factorial points = $(2)^k = (2)^3$=8 points
Number of axial points = 2k = 2*3 =6 points.
Such that, k number of factors is equal to 3.
Repetition at centre point = 3 times. Total number of experiments = 8 +6+3=17 experiments.

Table 6-2 Design matrix of statistical model

Runs	Point type	Factors			Responses					
		Wire feed rate[mm/s]	Power [W]	Welding speed [mm/s]	Number of filling passes	Gap bridge-ability Width [µm]	Integrity of bead (Lack of fusion) [%]	Surface chemistry integrity [%]	Strength [MPa]	Overlap shape factor [µm]
1	Fact	25	802.5	11	6	1570	80	80	550	100
2	Fact	17	802.5	7	5	1727	65	80	510	200
3	Fact	17	912.5	11	7	1705	100	95	630	70
4	Fact	25	802.5	7	4	1907	85	70	550	300
5	Fact	17	802.5	11	5	1658	95	85	600	125
6	Fact	17	912.5	7	5	2085	95	90	610	150
7	Fact	25	912.5	7	6	1882	80	65	450	300
8	Center	21	857.5	9	5	1670	85	85	500	75
9	Fact	25	912.5	11	5	1754	80	90	500	120
10	Center	21	857.5	9	6	1611	90	80	550	100
11	Axial	21	857.5	6	4	2160	40	85	540	240
12	Axial	15	857.5	9	6	1588	95	75	610	126
13	Axial	21	775	9	5	1778	90	95	600	115
14	Axial	21	857.5	12	6	1628	95	85	620	80
15	Axial	21	940	9	5	1667	85	95	600	90
16	Center	21	857.5	9	5	1635	85	85	530	105
17	Axial	27	857.5	9	4	1840	80	80	460	230

The investigated material thickness was 5 mm. Figure 6-3 shows some of weld bead cross sections related to different welding parameters. The following output responses were evaluated for each weld bead to complete the design matrix as mentioned in Table 6-2: overlap shape factor, number of filling passes, bead width or lateral fusion, integrity of weld bead, weld joint strength, and surface chemistry. The output results of the experiments were qualified and described through 6 models. Each model defines a specific quality response for the welding joint, as will be discussed in the next sections.

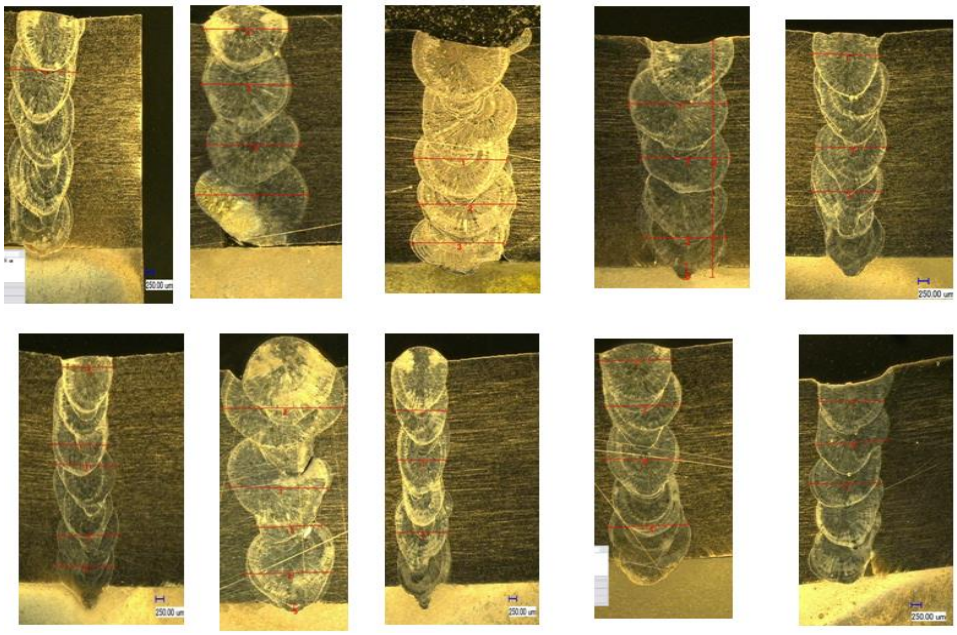

Figure 6-3 Various bead geometry according to table (6.2)

6.3.1 Lateral fusion (Gap Bridgability) model

The first model is concerned with lateral fusion, which is defined as the ability of the weld bead to fill the prepared gap without leaving voids. The better the lateral fusion is, the higher the gap bridgability will be, but if the weld bead is too wide, productivity will decrease. Establishing a suitable value for the lateral fusion will also improve the mechanical properties (i.e. strength) of the welded joint. At this stage of the investigation, the objective of this model was to maximize the lateral fusion, in order to develop an efficient welding process, as well as to achieve mechanically sound welded joints.

6.3.1.1 ANOVA of the models (scatter diagrams)

The lateral fusion model and the verification are shown in the Analysis of Variance statistics in Table 6-3. The ANOVA (F test) results indicate that the wire feed rate *A*, the laser power *B*, the welding speed *C*, and the interaction of the wire feed rate and the speed, *AC*, C^2 are significant process parameters. The second-order effect B^2 is an insignificant model term, such that R^2 =96%, adjusted R^2 = 91%, and Adeq. Precision = 14.65.

Table 6-3 ANOVA table for gap bridgability

Source	Sum of Squares	df	Mean Square	F Value	p-value Prob > F	
Block	4589.55	1	4589.55			
Model	4.012E+00	9	44582.6	19.64	0.0009	Significant
A-Feed	86777.78	1	86777.7	38.23	0.0008	
B-Power	37977.68	1	37977.6	16.73	0.0064	
C-Speed	1.961E+00	1	1.961E+	86.37	< 0.0001	
AC	35511.12	1	35511.1	15.64	0.0075	
B^2	10931.13	1	10931.1	4.82	0.0706	
C^2	18872.48	1	18872.4	8.31	0.0279	
Residual	13620.20	6	2270.03			
Lack of Fit	12162.20	5	2432.44	1.67	0.5262	Not significant
Pure Error	1458.00	1	1458.00			
Cor Total	4.195E+00	16				

The values in Table 6-3 represent adequate signals from the model with respect to noise influence, and they can be used to navigate the whole design space whilst maintaining good correlation between the measured and fitted values of the weld bead width. The scatter diagram plots the measured values of the response against the fitted values from the model, as shown in Figure 6-4. Most of the points have a small deviation from the diagonal line, which corresponds to perfect agreement between the measured and the predicted values. This indicates a good fit for the developed model [165].

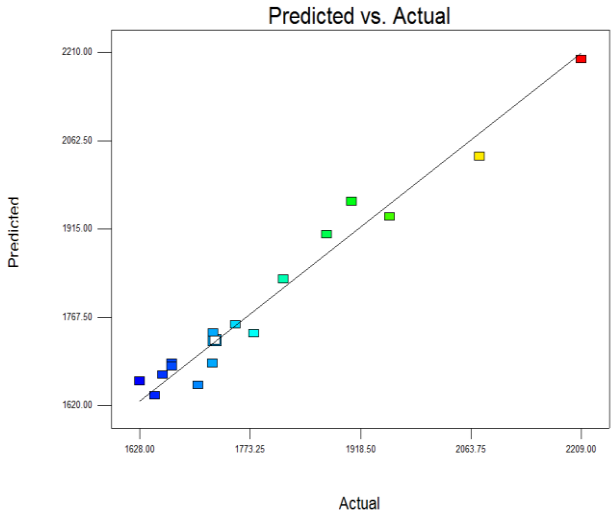

Figure 6-4 Validation graph - comparison of predicted gap bridgability with measured values

6.3.1.2 Model results and discussion

The perturbation plot for the gap bridgability model is shown in Figure 6-5. It illustrates the overall influence of the control parameters (A is wire feed rate, B is the power, and C is the welding speed. The X axis shows the value of the factor in coded form, and the Y axis represents the value of the response (i.e. the bead width). As the traverse speed increases, the weld bead width (lateral fusion) reduces. Increases in power and wire feed rate both lead to increases in lateral fusion. The average value of the bead width was around 1.9 mm at a speed of 7 mm/sec and a wire feed rate of 25 mm/sec. Increasing the welding speed to 9 mm/s, and decreasing the wire feed rate to 21 mm/s resulted in the average value of the bead width decreasing to 1.6 mm. Increasing the power simply increases the energy delivered per unit length, leading to more lateral melting, and consequently increases in bead width. Figure 6-5 shows a macrograph for the weld bead in both conditions. Decreasing the speed and increasing the wire feed rate are the key considerations for improving the gap bridgability, due to increased wire deposition rate per unit length.

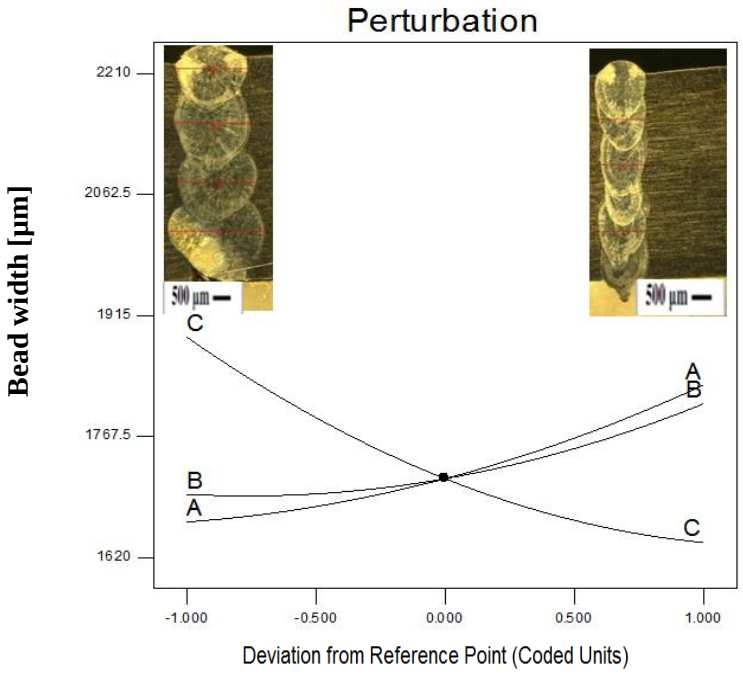

Figure 6-5 Perturbation curve for gap bridgability model

The model reveals that the welding speed has a strong influence on the bead width, while the wire feed rate has a stronger influence on the bead height. The response surface graph is shown in Figure 6-6. It indicates that the bead width is more sensitive

to changes in wire feed rate at low speeds (e.g. speed= 7 mm/s). The bead width is also more sensitive to changes in welding speed at higher wire feed rates, such as 25 mm/s. These results confirm the general trends for the model as shown in the perturbation curve.

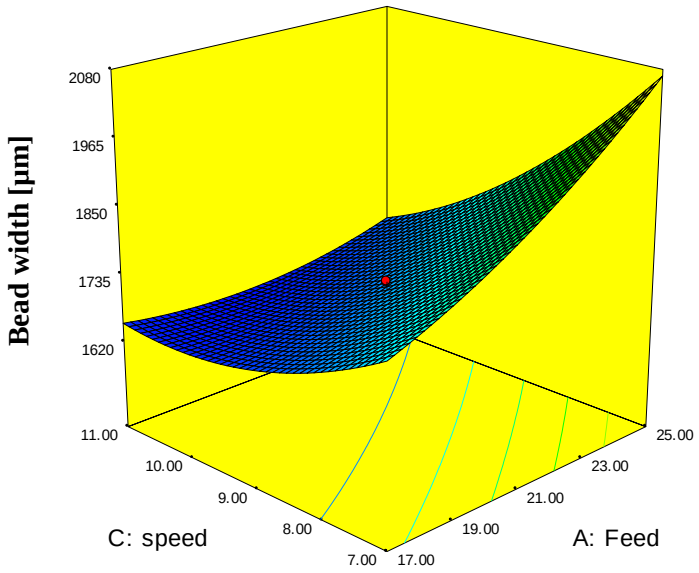

Figure 6-6 Response surface for gap bridgability model

6.3.2 Weld integrity model

6.3.2.1 ANOVA investigation for integrity model

The weld integrity was defined as a factor describing the ability of the weld bead to fill the welding gap. It was defined as 1 minus the volume fraction of voids with respect to the total weld bead area. The objective of the weld integrity model is to maximise this factor for improved strength and a more homogeneous weld bead. The ANOVA results for the weld integrity model indicate that the welding speed *C*, the interaction between the welding speed and the wire feed rate *AC*, the interaction between laser power and speed *BC*, as well as A^2 *C* and A^3, are significant terms as shown in **Table 6-4**. The 'lack of fit' is insignificant, and the other model validation measures are given as R^2 =89%, Adjusted R^2 = 84%, Adeq. Precision 13.5. This result implies a good ratio between model signal and noise.

Table 6-4 ANOVA table for integrity of weld

Source	sum of squares	df	mean square	f value	p-value prob > f	
Block	0.19	1	0.19			
Model	711.23	5	142.25	17.20	0.0001	Significant
C-speed	312.50	1	312.50	37.79	0.0001	
AC	50.00	1	50.00	6.05	0.0337	
BC	50.00	1	50.00	6.05	0.0337	
A^2C	98.00	1	98.00	11.85	0.0063	
A^3	248.73	1	248.73	30.08	0.0003	
Residual	82.70	10	8.27			
Lack of	70.20	9	7.80	0.62	0.7627	Not significant
Pure Error	12.50	1	12.50			
Cor Total	794.12	16				

The scatter diagram corresponding to Table 6-4 is shown in Figure 6-7; most of the points lie close to the diagonal line corresponding to agreement between measured and fitted values. Thus, the model for weld integrity describes the data effectively within the design space.

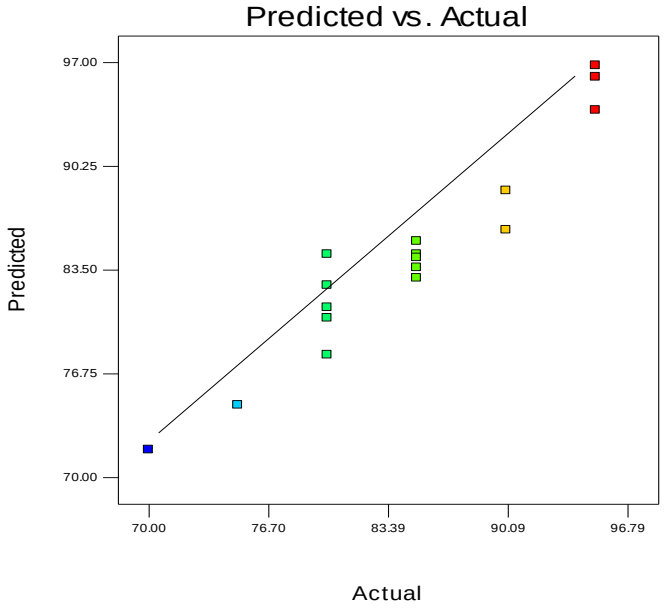

Figure 6-7 Validation graph for the weld integrity model – a comparison of measured and predicted values

6.3.2.2 Model results and discussion

The weld bead integrity increases directly with welding speed, and to a lesser extent the laser power, while decreasing with increases in the wire feed rate. Measurements obtained from polished macrographs indicate that, at high welding speeds (12 mm/sec), the integrity reached 93 %, while it was only 75 % at a welding speed of 7 mm/sec, as shown in Figure 6-8.

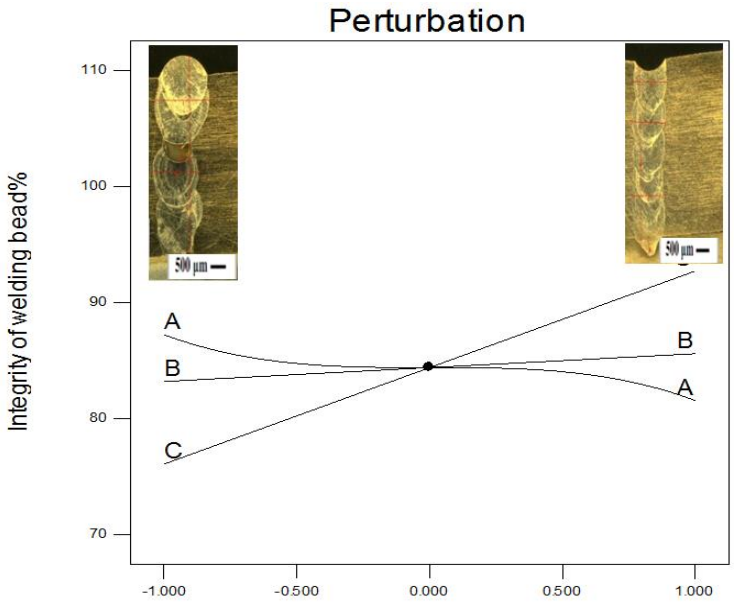

Figure 6-8 Perturbation curve for the integrity of the weld bead

The response surfaces for the weld integrity model are shown in Figure 6-9; two significant interactions can be seen. The first interaction is between the welding speed and laser power; the integrity of the weld bead can be improved by increasing both the laser power and the welding speed, and the integrity is more sensitive to changes in speed, as shown in Figure 6-9 a. The second interaction is between the welding speed and wire feed rate; Figure 6-9 b shows the integrity of the weld bead, which can also be improved by decreasing the wire feed rate at a high welding speed. At low welding speeds, the values of the integrity are generally smaller compared to those at higher welding speeds. This result agrees with that found by Salminen *et al*. *** [154] - they observed that increasing the power would improve the weld integrity and reduce the risk of imperfections for narrow gap laser welding technique.

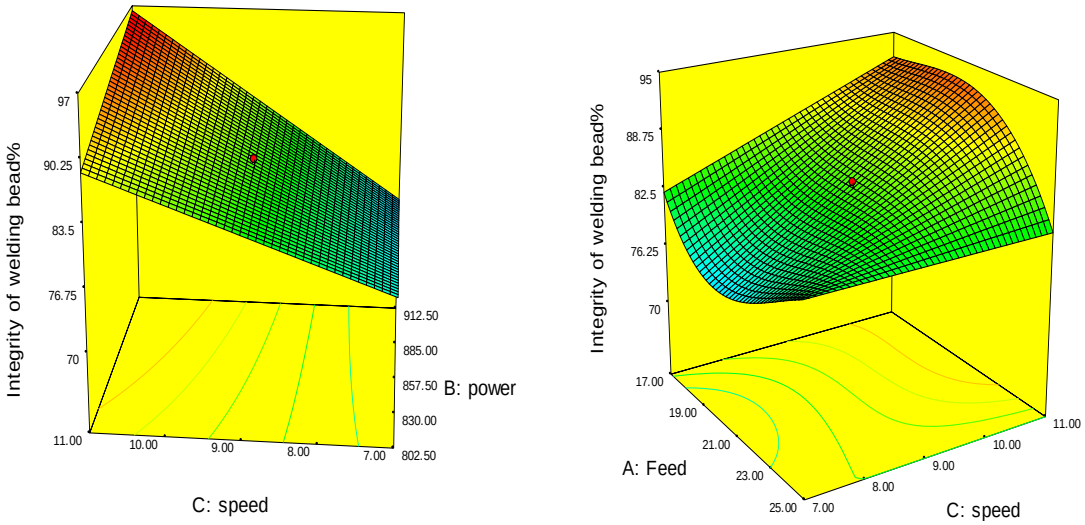

(a) welding speed – laser power (b) wire feed rate – welding speed

Figure 6-9 Response surface graphs for the integrity of the weld bead

6.3.3 Overlap shape factor model

The profile of the beads within the gap has a significant influence on joint quality, with it being desirable to have overall fusion profiles that are approximately straight on each side of the gap. If the profiles of individual beads are such that the overall fusion profiles deviate significantly from a straight line, then the probability of voids forming between individual beads will increase. This model controls the overall shape of the fusion boundary through calculating an overlap shape factor, *D*, which is defined as follows:

$$D = (d_{outer} - d_{inner})/2 \qquad (6.3)$$

where d_{outer} is the maximum weld bead width and d_{inner} is the minimum weld bead width. Definitions of these values are shown in detail in Figure 6-10. The dark black lines show the weld bead geometry, with D_1 and D_2 representing higher and lower values of weld bead overlap shape factor respectively. The diagram in Figure 6-10a schematically represents a high overlap shape factor, while Figure 6-10b shows a low overlap shape factor. The objective of this model is to minimize the overlap shape factor, in order to achieve a continuous and near-straight fusion profile on each side of the weld, since such overall profiles decrease the likelihood of void formation between passes.

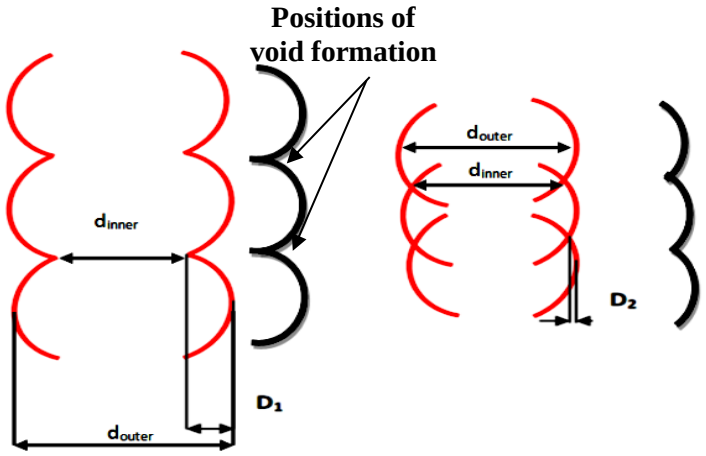

(a) High overlap shape factor (b) Low overlap shape factor (target shape)

Figure 6-10 Overlap shape factor

6.3.3.1 ANOVA investigations for overlap model

The analysis of variance for the overlap shape factor model indicates that the wire feed rate, A, the laser power, B, and the welding speed, C, are significant factors. Furthermore, interactions between the wire feed rate and the laser power, *AB*, and wire feed rate and the welding speed, *AC*, and second order terms A^2 and C^2 are also significant, as shown in Table 6-5. Model validation measures are given as R^2 =98%, adjusted R^2 = 96%, and Adeq. precision = 22.4. The 'lack of fit' is not significant.

Table 6-5 ANOVA table for overlap shape factors

Source	Sum of Squares	df	Mean Square	F Value	p-value Prob > F	
Block	711.26	1	711.2605			
Model	90600.13	7	12942.88	67.64308	< 0.0001	significant
A-Feed	14860.88	1	14860.88	77.66711	< 0.0001	
B-power	1200.5	1	1200.5	6.274148	0.0367	
C-speed	48050	1	48050	251.1227	< 0.0001	
AB	1953.125	1	1953.125	10.20758	0.0127	
AC	6328.125	1	6328.125	33.07255	0.0004	
A^2	12770.13	1	12770.14	66.74029	< 0.0001	
C^2	8007.74	1	8007.742	41.85069	0.0002	
Residual	1530.72	8	191.3407			
Lack of Fit	1218.22	7	174.0323	0.556903	0.7779	not significant

The analysis of variance for the overlap shape factor model indicates that the wire feed rate, A, the laser power, B, and the welding speed, C, are significant factors. Furthermore, interactions between the wire feed rate and the laser power, *AB*, and wire feed rate and the welding speed, *AC*, and second order terms A^2 and C^2 are also significant, as shown in Table 6-5. Model validation measures are given as R^2 =98%, adjusted R^2 = 96%, and Adeq. precision = 22.4. The 'lack of fit' is not significant.

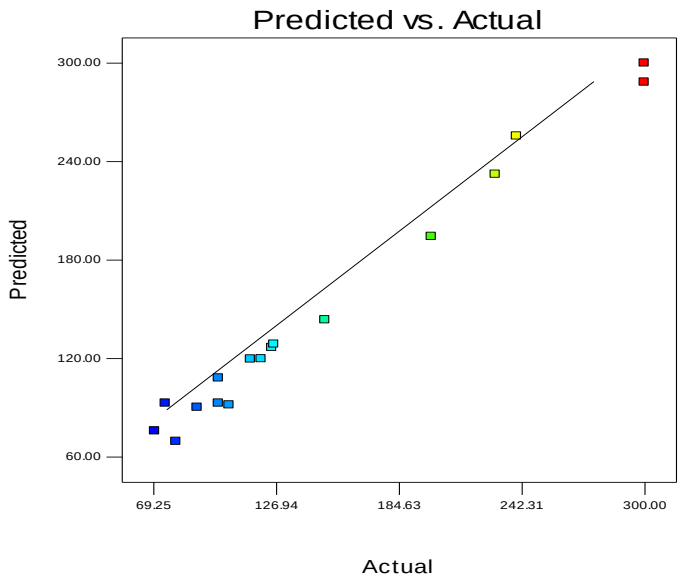

Figure 6-11 Validation graph (predicted vs. measured values) for the overlap shape factor

6.3.3.2 Influence of variables on overlap shape factor

The influences of the process parameters on the overlap shape factor are shown in Figure 6-11. The speed (C) is inversely proportional to the overlap shape factor, while the wire feed rate (A) is directly proportional, and the Power (B) is also inversely proportional to the overlap shape factor, but with less significance. The value of the overlap shape factor decreased to 80 μm at a welding speed of 9 mm/s, and a wire feed rate of 21 mm/s. However, decreasing the welding speed to 6 mm/s and increasing the wire feed rate to 25 mm/s led to the overlap shape factor increasing to 190 μm.

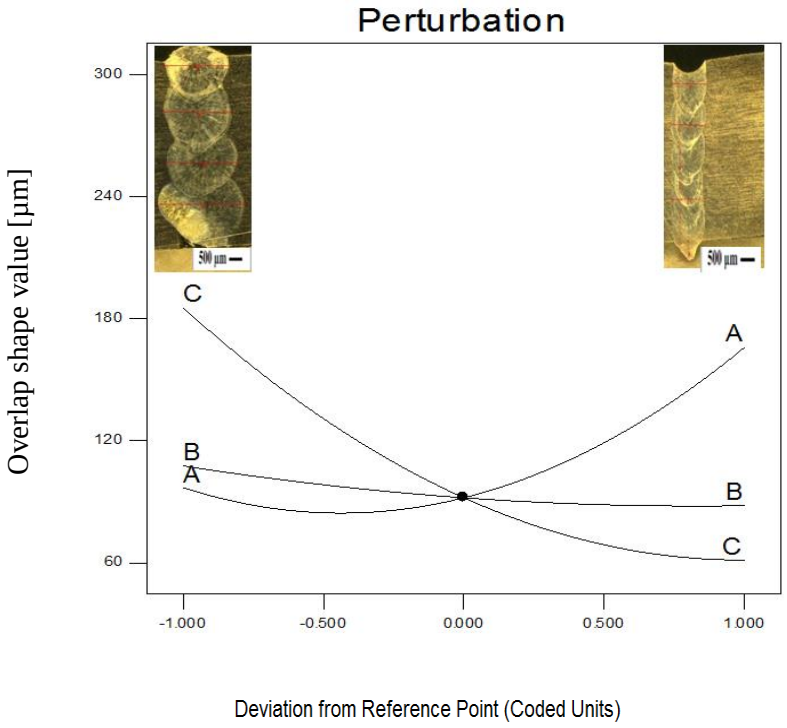

Figure 6-12 Perturbation curve for the overlap shape factor

The experimental results for the overlap shape factor experiment indicate that the welding speed has a more significant effect than the wire feed rate. Increasing the welding speed or decreasing the wire feed rate leads to a decrease in the wire deposition per unit length [153]. There are two significant interactions in this model, between the laser power and the wire feed rate, and between the welding speed and the wire feed rate - these are represented by the response surface graphs in Figure 6-13. The overlap shape factor is more sensitive to the wire feed rate than the laser power, as shown in Figure 6-13a, and it is more sensitive to the welding speed than the wire feed rate, as shown in Figure 6-13b. The overlap shape factor can be improved (i.e. it can be reduced) by increasing the welding speed and decreasing the wire feed rate.

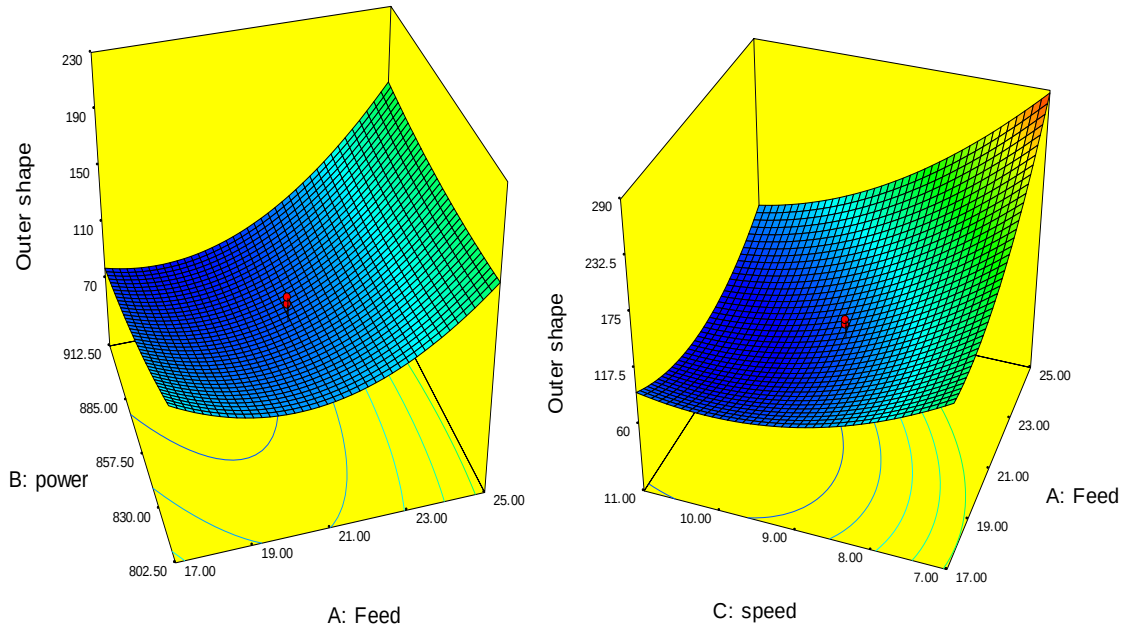

(a) Laser Power [W] – wire feed rate[mm/s] (b) Wire feed rate – welding speed [mm/s]

Figure 6-13. Response surface graphs for overlap shape model.

6.3.4 Number of filling passes model

This model was developed to study the number of filling passes that are required to fill the gap. The objective of the model was to investigate the influence of the welding control parameters (i.e. power, wire feed rate, traverse speed) on the number of filling passes required. The optimization objectives were to minimize the number of passes in order to decrease the total heat input to the weld, and to increase productivity.

6.3.4.1 ANOVA investigation for number of filling passes model

The analysis of variance for the number of filling passes model indicates that the welding speed *C*, and the interactions *AC*, *ABC*, A^2B, and A^3 are significant model terms. The 'lack of fit' is insignificant, as shown in Table 6-6. Validation measures for the model are given as R^2 = 87 %, adjusted R^2 = 81 %, and Adeq. Precision = 14.2. These values show that model has a good signal-to-noise ratio.

Table 6-6 ANOVA table for number of filling passes

Source	Sum of Squares	df	Mean Square	F Value	p-value Prob > F	
Block	0.27	1.00	0.27			
Model	8.08	5.00	1.62	13.77	0.0003	Significant
C-speed	1.62	1.00	1.62	13.80	0.0040	
AC	1.13	1.00	1.13	9.58	0.0113	
ABC	1.13	1.00	1.13	9.58	0.0113	
A^2B	1.13	1.00	1.13	9.58	0.0113	
A^3	3.09	1.00	3.09	26.31	0.0004	
Residual	1.17	10.00	0.12			
Lack of Fit	0.67	9.00	0.07	0.15	0.9705	Not significant
Pure Error	0.50	1.00	0.50			
Cor Total	9.53	16.00				

The scatter diagram shown in Figure 6-14 represents the validation results of the developed model. The results indicate that the model can describe the response data reasonably well within the design space - all of the values of actual response against model predicted values are close to the diagonal line, as shown in Figure 6-14.

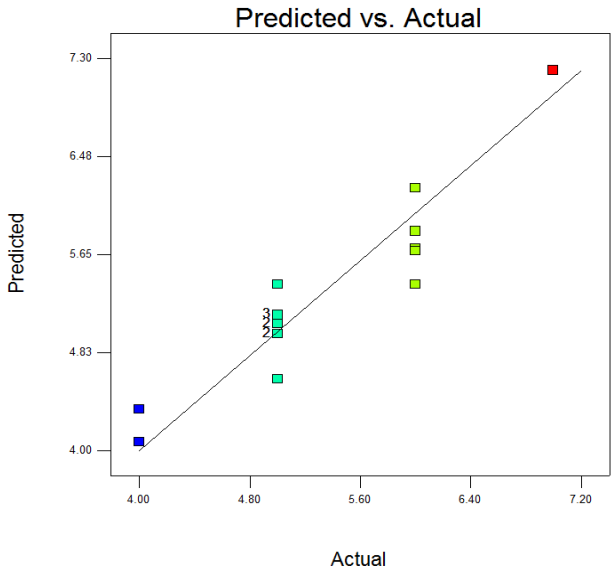

Figure 6-14 Validation graph for the number of filling passes model – (predicted numbers of filling passes against measured values)

6.3.4.2 Results of model and discussion

The perturbation plot for the number of filling passes is shown in Figure 6-15. It can be seen that the laser power had a very small influence on the number of filling passes. The wire feed rate and welding speed were more significant factors with respect to power. Consequently, increasing the wire feed rate and decreasing the welding speed would be an effective strategy for decreasing the number of filling passes within the windows of acceptance for the parameters. The effect is shown in Figure 6-15, through a comparison of the optical images obtained from the two weld cross sections.

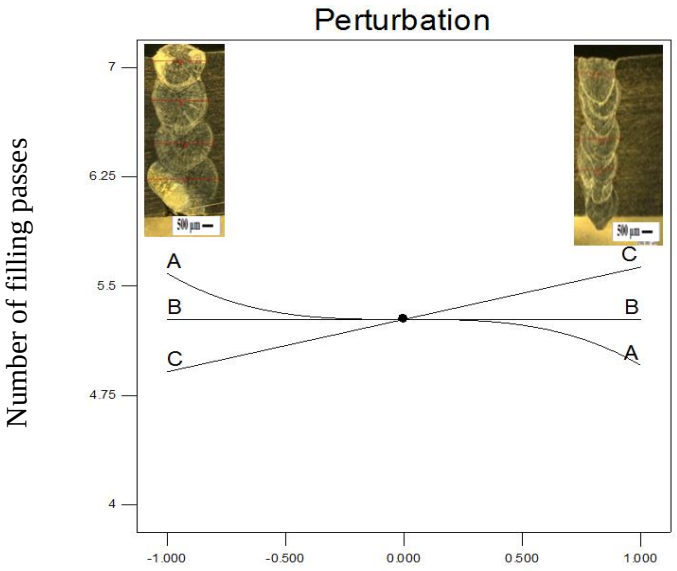

Figure 6-15 Perturbation curve for number of filling passes model

Six passes were needed to fill the gap with a welding speed of 11 mm/s, a wire feed rate of 17 mm/s, and a laser power of 802 W (the gap height is 5 mm), while only four passes were needed with a welding speed of 7 mm/s and a wire feed 25 mm/s. The number of passes decreased due to the decrease in speed and the increase in the wire feed rate, which led to an increase in the quantity of wire deposited per unit length and, consequently, the average height of each pass. The response surface representation for the significant interactions between the welding speed and the wire feed rate is shown in Figure 6-16. This indicates that the welding speed has more significant influence on the number of filling passes at low wire feed rates. On the other hand, at high wire feed rates, the welding speed has less significant influence on the number of filling passes.

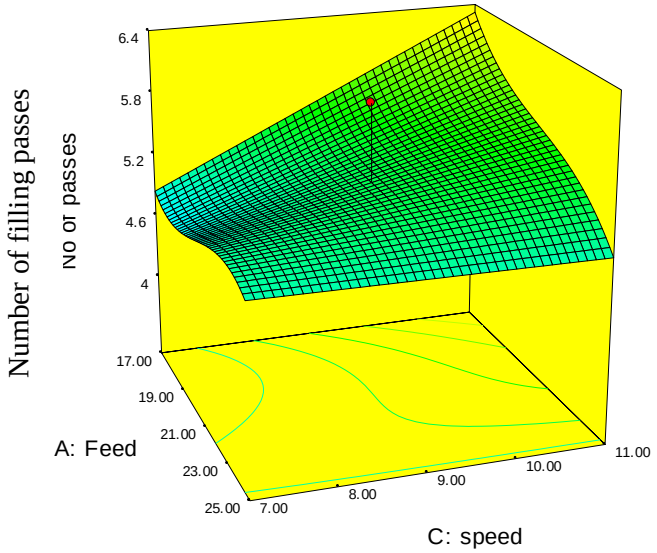

Figure 6-16 Response surface graph for the number of filling passes model

6.3.5 Surface chemistry integrity *(*free of oxidation) model

This model predicts the degree of surface oxidation. The surface chemistry integrity is defined in equation (6-4). The surface oxidation level was quantified according to the surface colour, using the surface oxidation chart in Table 6-7 [166]. The heat tint or temper colour is caused by the progressive thickening of the surface oxide layer upon heating. The colours that arise can be used as an indication of the temperature to which the steel has been heated.

Surface chemistry integrity (Free of Oxidation) % = 100% – Surface Oxidation % **(6.4)**

Table 6-7 Surface oxidation colour chart [19]

Colour	Temperature C°	Surface chemistry integrity%
silver	-	100%
pale yellow	143.3	95%
dark yellow	187.7	90%
brown	198.8	85%
purple brown	215.5	80%
dark purple	232.2	77%
blue	282.2	75%
dark blue	315.5	70%

In order to introduce the surface chemistry integrity evaluation technique, two different examples for surface oxidation levels are presented: the first example is of a weld near

to blue in colour, as shown in Figure 6-17a, while the second is bright silver in colour, as shown in Figure 6-17b. According to the surface oxidation chart the surface chemistry integrity (% free of oxidation) levels are 75% and 100% for the blue and silver surfaces respectively.

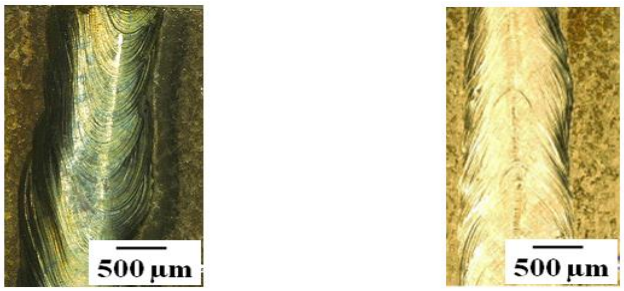

Figure 6-17 Surface oxidation levels

(a) 75% free of oxidation bead surface (b) 100% free of oxidation bead surface

6.3.5.1 ANOVA table for weld surface oxidation model and validation

The analysis of variance for the surface oxidation model indicates that the welding speed, *C*, the laser power, *B*, and the interactions *AB*, *AC*, A^2,B^2,A^2B, and AB^2 are significant model terms. The 'lack of fit' is insignificant as shown in Table 6-8. The output values of R^2 = 95 %, Adjusted R^2 = 86.8%, and Adeq Precision = 12.2 indicate the adequacy of the regression fit to the data.

Table 6-8 ANOVA table for weld surface chemistry integrity (% free of oxidation)

Source	*Sum Of squares*	*DF*	*mean*	*F*	*p-value*	
Block	50.44	1	50.44			
Model	671.67	10	67.17	10.89	0.0083	*Significant*
B-power	50.00	1	50.00	8.11	0.0359	
C-speed	112.50	1	112.50	18.25	0.0079	
AB	50.00	1	50.00	8.11	0.0359	
AC	12.50	1	12.50	2.03	0.2138	
A^2	124.09	1	124.09	20.13	0.0065	
B^2	26.97	1	26.97	4.37	0.0907	
ABC	12.50	1	12.50	2.03	0.2138	
A^2B	60.50	1	60.50	9.81	0.0259	
A^2C	18.00	1	18.00	2.92	0.1482	
AB^2	200.00	1	200.00	32.44	0.0023	
Residual	30.83	5	6.17			
Lack of Fit	18.33	4	4.58	0.37	0.8261	*Not significant*
Pure Error	12.50	1	12.50			
Corrected Total	752.94	16				

The scatter diagram for the surface chemistry integrity model shows that the measured points generally fall close to the diagonal line representing perfect agreement between the measured and fitted data, as shown in Figure 6-18.

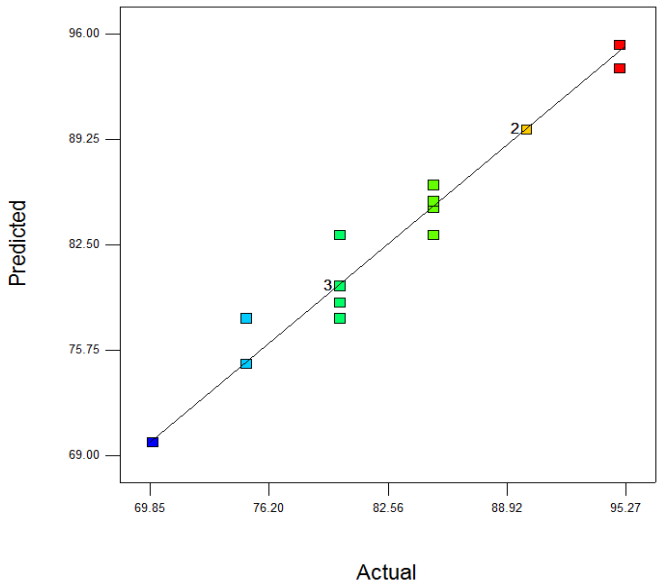

Figure 6-18 Validation graph for the surface chemistry integrity model

6.3.5.2 Results of model and discussion

Increasing the wire feed rate until the centre design point leads to a reduction in the surface oxidation, but the trend is reversed when the wire feed rate is increased further, as shown in Figure 6-19. Increases in welding speed and reductions in laser power will lead to a decrease in the heat input to the welded joint, and consequently the temperature of the workpiece surface will be reduced below the critical temperature before the weld bead leaves the area protected by the shielding gas. This will reduce the thickness of the oxidation layer on the upper weld surface.

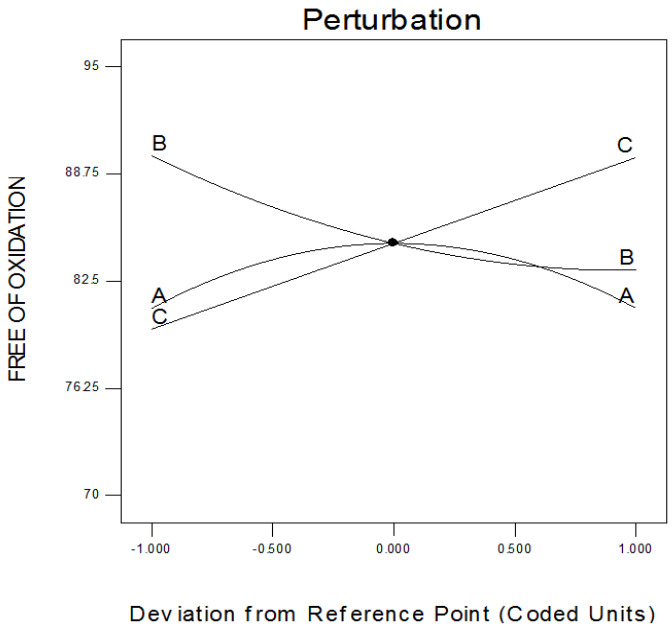

Figure 6-19 Perturbation curve for surface chemistry integrity model

The use of the shielding gas shower tube that was introduced earlier in this work led to a reduction in surface oxidation. The technique allows prolonged shielding of the weld surface outside of the region that is in the vicinity of the coaxial laser gas nozzle. Response surface graphs for the significant interactions when the shower tube is used are shown in Figure 6-20. The first significant interaction is found between the welding speed and the wire feed rate: at a low welding speed of 7 mm/s, the surface chemistry integrity was increased to 80% at a wire feed rate of 21mm/s, at a higher welding speed the surface chemistry integrity was increased up to 90% at wire feed rate = 21 mm/s, but then it decreased as shown in Figure 6-20**a**. The second interaction is found between the laser power and the wire feed rate: the surface chemistry integrity was improved at high powers by decreasing the wire feed rate, and at low powers the surface chemistry integrity was improved until the wire feed rate reached 21 mm/s, then it decreased again as shown in Figure 6-20**b**. Thus increasing the welding speed improves the surface protection by decreasing the amount of heat which enters the joint during the welding process.

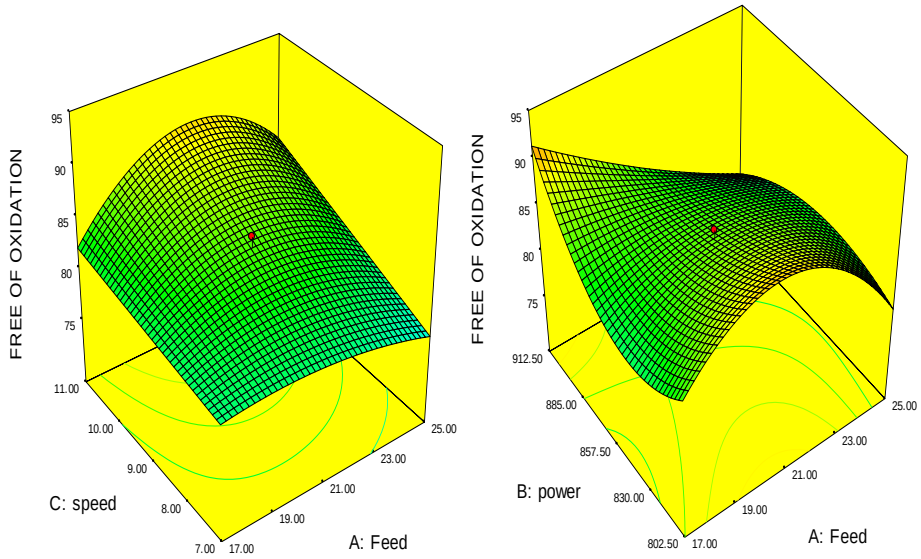

(a) Speed-feed surface graph (b) Power-feed surface graph

Figure 6-20 Response surface graphs for surface chemistry integrity model

6.3.6 Cross weld tensile strength model

The NGLW technique is a multi-pass method; this is difficult to implement in practical applications due to the narrow width of the required welding gap and the resulting tight accuracy constraints. Moreover, the quality of each welding bead is strongly influenced by the quality of the previous one, as defects can accumulate; consequently, achieving a homogeneous and high tensile-strength joint is challenging. The strength of the joint is an important response in the evaluation of joint quality. Despite the importance of the joint strength evaluation in the application of NGLW, it has not been reported as an evaluation variable in previous NGLW studies. A new sub-model will be included in the statistical model, which investigates and optimizes the strength behaviour of the NGLW technique. The quality of the welding will be evaluated according to the strength of the weld joint with respect to welding parameters.

6.3.6.1 ANOVA investigation for tensile strength model

The analysis of variance shows that the result of the tensile strength model is significant, and that 'the lack of fit' is not significant, as shown in Table 6-9. The wire feed rate *A*, welding speed *C*, and interactions *AB*, B^2, C^2 are significant model terms. Validation measures for the model are given as R^2 = 90.8% , Adjusted R^2 = 86.2%,

Adeq. Precision = 14.6. These results indicate that the model can represent the strength data point in the design space with a good accuracy and minimal impact of the noise.

Table 6-9 ANNOVA table for weld tensile strength model

Source	Sum of Squares	df	Mean Square	F Value	p-value Prob > F	
Block	1682.542017	1	1682.54			
Model	45514.61989	5	9102.92	19.87	< 0.0001	significant
A-Feed	22472	1	22472	49.07	< 0.0001	
C-speed	6498	1	6498	14.18	0.0037	
AB	10153.125	1	10153.12	22.17	0.0008	
B^2	5136.41084	1	5136.41	11.21	0.0074	
C^2	2073.572183	1	2073.57	4.521	0.0592	
Residual	4579.308681	10	457.93			
Lack of	3329.308681	9	369.9237	0.29593	0.9008	not significant
Pure	1250	1	1250			
Cor Total	51776.47059	16				

6.3.6.2 Model validation

The strength model has been validated through the scatter diagram as shown in Figure 6-21a - the predicted and actual results values are following 45º diagonal. This result indicates that the model represents a near-perfect fit to the real data points. The output significant response surface is shown in Figure 6-21b. The tensile strength is increased by increasing the power and decreasing the wire feed rate

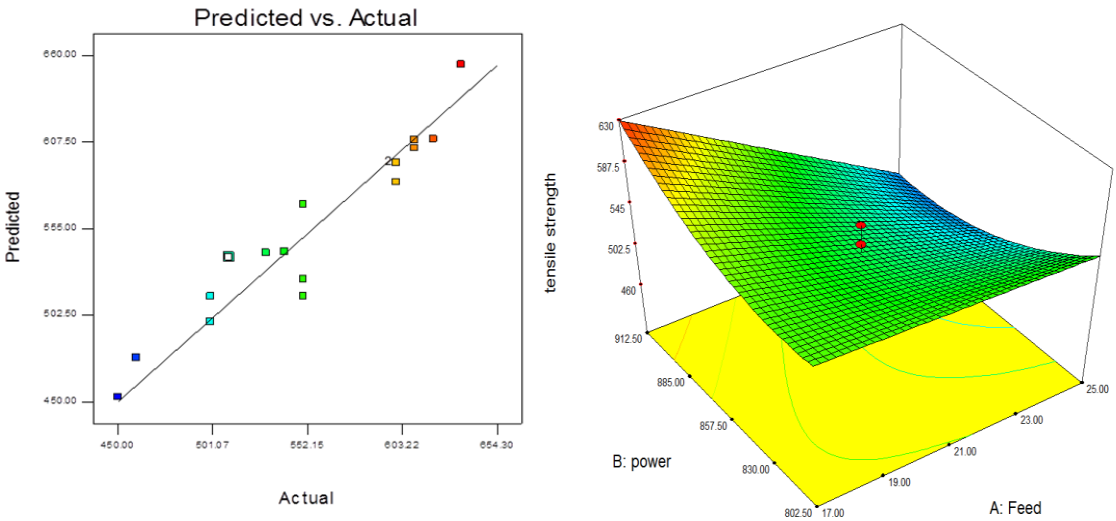

(a) (b)

Figure 6-21 Tensile strength model validation and response surface

6.3.7 Model governing equations and multiple objective optimisation

6.3.7.1 Statistical models

The statistical models developed in this work are shown in equations (6.5) – (6.10) in coded factors form. The governing equations for the models include individual and interaction control factors. The empirical equations given below can be used to predict the process-parameter interactions, and their influences on the process quality responses.

$$\text{Weld width} = 1716.3 + 83.32 * A + 55.12 * B - 125.24 * C - 66.63 * A * C + 36.10 * B^2 + 47.43 * C^2 \quad (6.5)$$

$$\text{Integrity of welding bead} = 84.39 + 8.33 * C - 2.50 * A * C + 2.50 * B * C - 5.83 * A^2 * C - 2.84 * A^3 \quad (6.6)$$

$$\text{Overlap shape factor} = 92.03 + 34.48 * A - 9.8 * B - 62 * C + 15.63 * A * B - 28.13 * A * C + 39.45 * A^2 + 31.45 * C^2 \quad (6.7)$$

$$\text{Number of filling passes} = 5.27 + 0.36 * C - 0.38 * A * C - 0.37 * A * B * C + 0.38 * A^2 * B - 0.32 * A^3 \quad (6.8)$$

$$\text{Surface chemistry integrity (free of oxidation) \%} = 84.71 - 3.33 * B + 5 * C - 2.5 * A * B + 1.25 * A * C - 3.79 * A^2 + 1.77 * B^2 + 1.25 * A * B * C + 4.58 * A^2 * B - 2.50 * A^2 * C - 5 * A * B^2 \quad (6.9)$$

$$\text{Tensile strength} = + 526.85 - 42.40 * A + 22.80 * C - 35.63 * A * B - 24.38 * B^2 + 15.49 * C^2 \quad (6.10)$$

6.3.8 Multi-objective Optimization

According to the results of the models, improving one response may cause another to deteriorate; for example, increasing the welding speed will improve the weld bead integrity, the surface chemistry integrity and the overlap shape factor, but it will also increase the number of passes required to complete the weld. This conflict can be resolved using a multi-objective optimization process, the objective of which is to find values for the factors that simultaneously achieve the specified optimization criteria for all of the responses. Statistical optimization is achieved through a dimensionless objective function, called desirability. The desirability function approach involves

transforming each response, Y_i, into a dimensionless value, d_i, between 0 and 1. It can be calculated according to optimization constraints as follows:

For maximizing constraints;

$d_i = 0$ if response < lower limit.

$d_i = 0$ if response > upper limit.

$0 < d_i < 1$ as response varies from low to upper limit. It is calculated using:

$$\boldsymbol{d_i} = \frac{\boldsymbol{Actual\ response\ value}}{\boldsymbol{Response\ limit\ according\ to\ optimizing\ constraints}} \tag{6.11}$$

A higher d_i value indicates that the response value is more desirable, the goal of optimization is to find a good set of conditions that will meet all of the goals [167]. Each criterion (maximization or minimization) has a specific importance factor according to its direct influences on the final weld bead quality [156]. This value is specified for each optimization criterion. The weld bead integrity model is given the highest importance due to its importance on the final quality of the weld bead, while the number of filling passes is given a lower importance level, because the main objective is to improve weld quality. The strategy for optimization was to start at a random point, and proceed up through the steepest slope to reach the peak point (maximum or minimum) according to the optimization criteria. In order to satisfy the multi-objective optimization requirements, the overall desirability is defined by the geometric mean of all individual desirabilities. It ranges from '0' for the least desirable settings and '1' for the most desirable process. Equation (6-12) represents the overall desirability function, where: ξ is the total desirability using the geometric mean of individual desirability, n is the number of responses, and d_i is the i^{th} response desirability value [156].

$$\xi = \prod_{i=1}^{n} \boldsymbol{d_i} \tag{6.12}$$

6.3.9 Optimization criteria and results

The goal of the optimization process is to maximize lateral fusion (weld gap bridgability), maximize the integrity of the weld bead (minimize porosity), minimize the overlap shape factor, minimize the number of filling passes, maximize the surface

chemistry integrity (% free of oxidation), and maximize the weld joint strength. The desirability shape function is shown in Figure 6-22. It is improved by increasing the laser power and decreasing the wire feed rate. The desirability has two peak regions, but the maximum value is limited to a small range at laser power = 912.5 W, welding speed = 9.5 mm/s and wire feed rate = 18.01 mm/s.

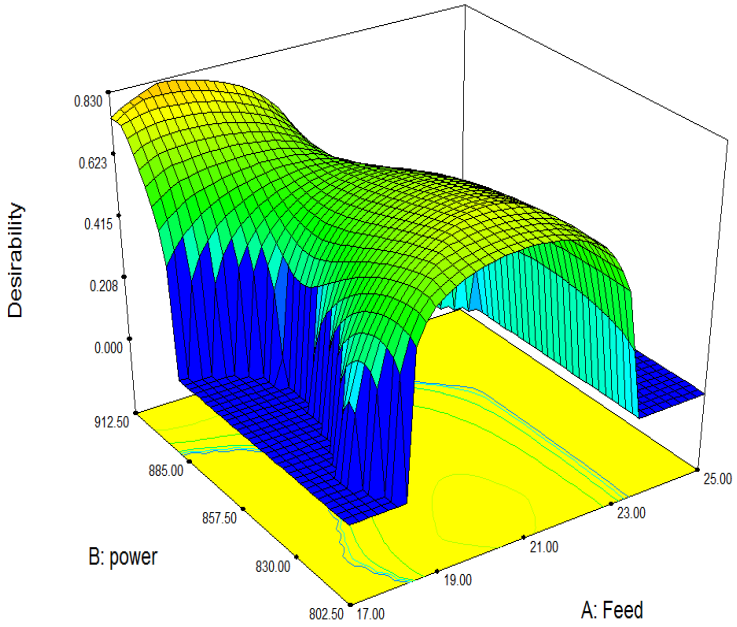

Figure 6-22 Desirability shape function

According to the optimization results the value achieved for the total desirability is 85 %. The weld bead integrity and the surface chemistry integrity are 90 %, and the average lateral fusion value is 1698 μm. The overlap shape factor is 60.4 μm. Details of the maximum desirable solution and the response values are represented in Table 6-10 .

Table 6-10 Multi-objective optimization results

Wire Feed [mm/s]	Power [W]	Speed [mm/s]	Width [mm]	Bead integrity %	Surface chemistry integrity %	Number of passes	Overlap shape factor[μm]	Strength [MPa]	Desirability %
18.01	912.5	9.5	1698	90	90	6	60.4	623.5	85

6.3.9.1 Graphical optimization – an operating window development

Graphical optimization can define regions where the process parameters simultaneously meet the different optimization criteria. The critical responses can be overlayed on a single contour plot, and such a plot is referred to as an overlay plot. The graphical optimization displays the area of feasible response values in the factor space [156]. The limits for the optimization constraints are specified according to the numerical optimization results. Figure 6-23 shows the overlay plot for all of the models according to the optimization constraints. The yellow area highlights the optimum conditions, for which all criteria are satisfied simultaneously. This region corresponds to the following optimization limits; integrity of the weld bead ≥ 85%, surface chemistry integrity (free of oxidation) ≥ 85%, overlap shape factor ≤ 75 µm, bead width ≥ 1700µm, number of filling passes ≤ 5, and tensile strength ≥ 550MPa . According to the graphs, a high laser power and a low wire feed rate provide the optimum condition for each individual constraint. The intersection area for all constraints is consistent with the numerical optimization results shown in Figure 6-22.

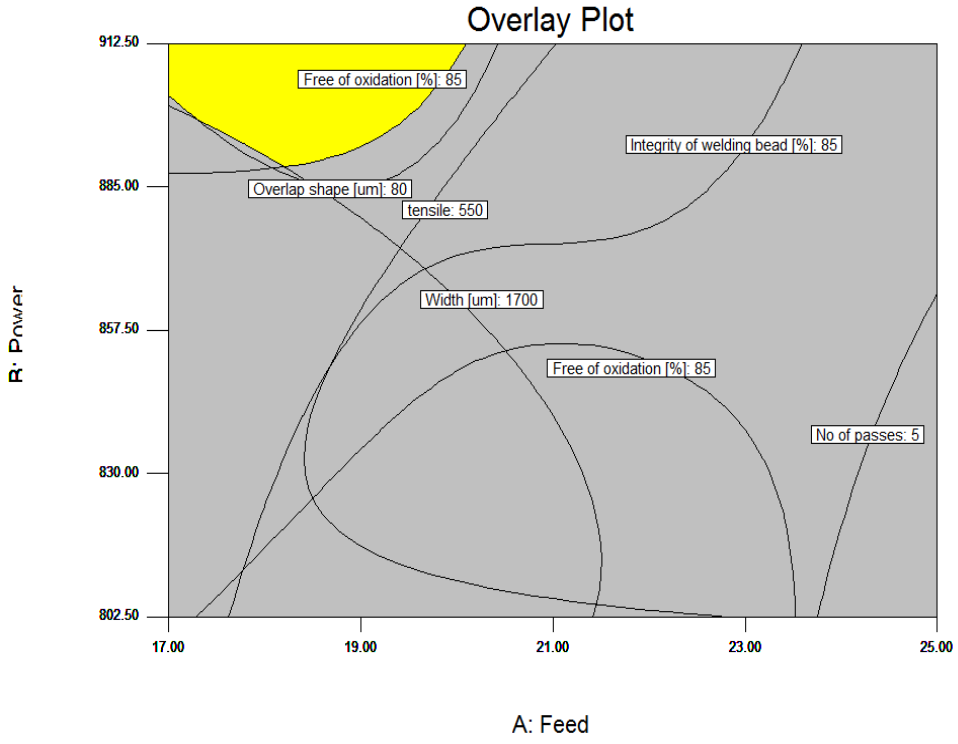

Figure 6-23 optimum overlay plot considering all constraints

6.4 Verification experiment for the model results

The reliability of the modelling was evaluated through new sets of welding experiments, using the optimum welding parameters related to maximum desirability solution as shown in Table 6-10. The weld bead shape related to the optimum welding parameters is shown in Figure 6-24. The output responses were compared to the predicted values by the models for the same conditions to validate the model results. The width of the weld bead was measured at five positions in order to measure the average lateral fusion.

Average lateral fusion = [(1747) + (1780) + (1708) + (1693) + (1648)]/5=1715 μm

Average overlap shape factor =

[(1700- 1596)/2 + (1556-1460)/2+(1880-1675)/2+(1712- 1581)/2]/4 = 67.4 μm

The integrity percent can be calculated by calculating the area of voids or 'miss–integrity' in the total weld bead area; The area of the miss-integrity ~ 0.3mm^2 , the total welding bead area~12 mm^2, and the percentage of miss-integrity = 2.5%. Consequently, the output of the optimum integrity percent is 97.5%. The number of passes required for filling the gap was six, as shown in Figure 6-23.

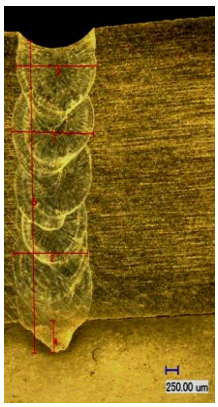

Figure 6-24 Optimum bead cross section

The surface color was golden yellow as shown in Figure 6-25. According to the surface oxidation colour chart, the corresponding surface chemistry integrity is 95%.

Figure 6-25 Optimum condition surface bead colour

A stress-strain curve was developed to evaluate the weld joint relative to the optimum welding parameters for a standard tensile samples with gauge length = 30 mm. The results were compared to base material and another welded joint with different welding parameters as follows: wire feed rate = 17 mm/s, power = 802.5 W, and traverse speed=7mm/s, and to. The actual ultimate tensile strength for the welded joint produced with optimum parameters was 625 MPa, and the failure occurred in the base metal, as shown in the stress-strain curve in Figure 6-26.

A sample welded in non-optimum conditions was produced, and failed in the weld region with an ultimate tensile strength of 555 MPa. The predicted value of strength under non-optimum welding parameters was 551 MPa, due to the lower value of predicted weld bead integrity, 83%. Mechanical behaviour of the welded joint will be investigated in details in the next chapter.

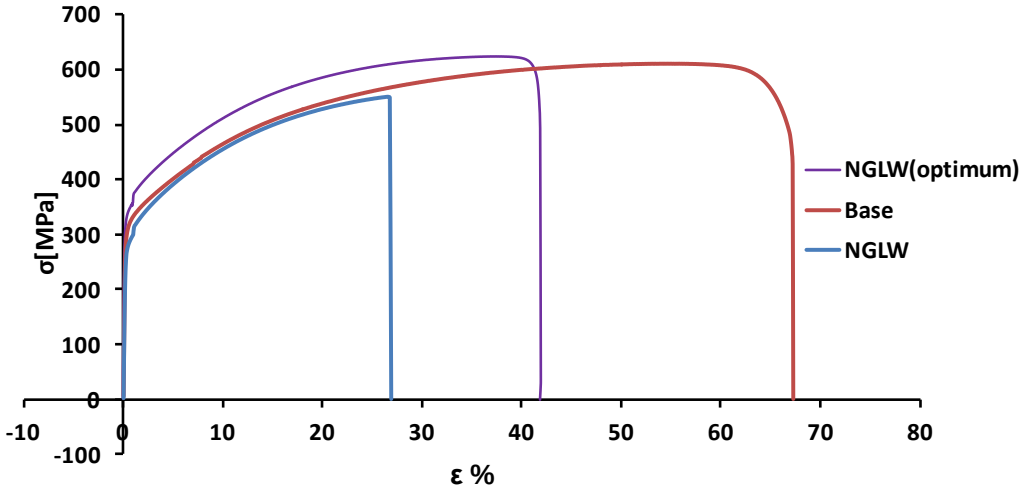

Figure 6-26 Stress strain behavior of different welding conditions

The values predicted by the model for each response, and the experimental values, are compared in Table 6-11 in order to evaluate the reliability of the modelling. The model achieved an average accuracy of more than 96%.

Table 6-11 Comparison of measured and predicted responses

Responses	Width average [µm]	Bead integrity%	Surface oxidation%	Number of passes	Overlap shape factor[µm]	Strength [MPa]	
						optimized	Non
Predicted values	1698	90	90	6	63.3	623.5	551
Experimental	1715	97.5	95	6	67.4	625	555
Model accuracy %	99	92	94.7	100	94	99	99
Average accuracy	96.8						

6.4.1 Model verification with different thicknesses

The verification test for the optimum results was extended to the welding of thicker sections. The optimum parameters from the model were used for welding 10 mm and 20 mm thick AISI grade 316L stainless steel plates with a gap width of 1.5 mm. Figure 6-27a shows the resulting weld cross-section for the 10 mm thick weld - ten passes were required to fill the gap. There was no evidence of a lack of fusion, or oxidation between weld passes, the average overlap shape factor was 85 µm, with the average lateral fusion value being 2 mm. Figure 6-27b shows the resulting weld cross section for the 20 mm thick weld. Twenty two passes were required to fill the gap. The average overlap shape factor was 57 µm, with the average lateral fusion value being 2 mm. All results have been validated against ISO 13919-1 for laser welding.

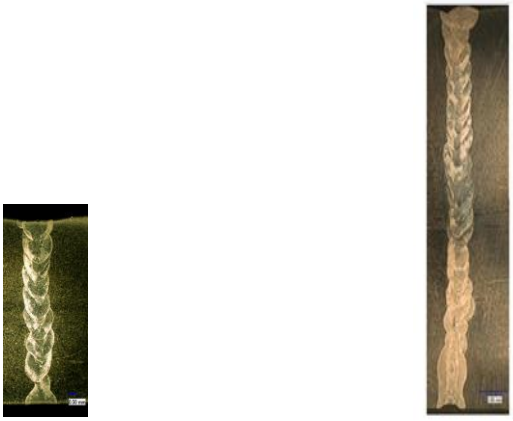

a - 10 mm cross section b- 20 mm cross section

Figure 6-27 Narrow gap welding of thick sections

6.5 Statistical modelling for autogenous laser welding

The experiments described previously were developed to weld without a back plate, as shown in Figure 6-27. The shape and detailed dimensions for the developed welding cross section of the NGLW technique is shown in Figure 5-13. The NGLW welding process consists of two welding techniques; the first pass is an autogenous laser welding pass (without wire feeding), to create the gap as shown in Figure 6-28a; this is followed with a multi-pass filler wire welding technique. Figure 6-28b shows the welding after 2 filling passes.

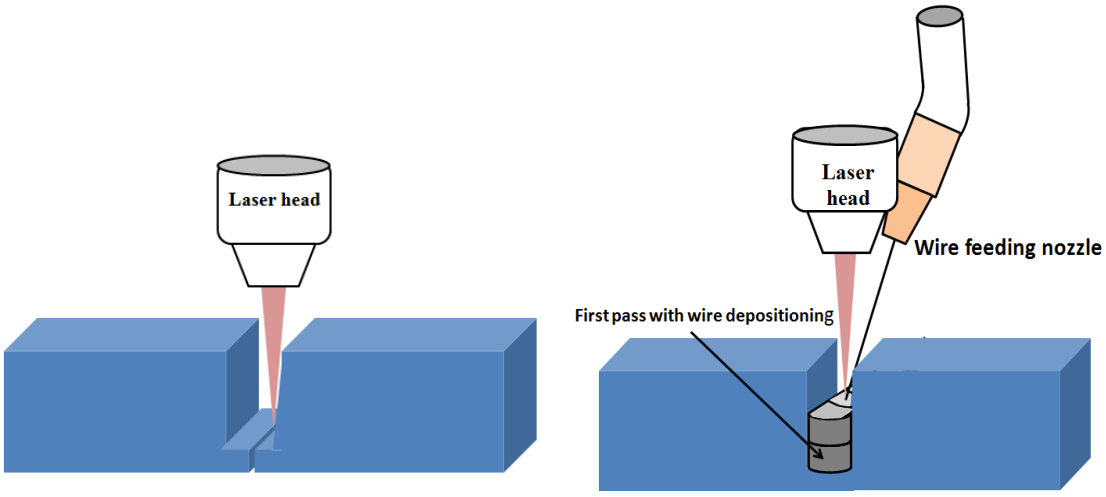

a) First pass autogenous laser welding b) multi filling pass with wire

Figure 6-28 Narrow gap laser welding configuration

Another statistical model experimental set was implemented for optimizing the autogenous laser welding pass parameters, and bead on plate. The optimization responses were: weld bead homogeneity, penetration depth of the welding, and surface cleaning against oxidation. The control parameters were: power, welding speed, gas flow rate, and focus position.

6.5.1 Levels of variables

Table 6-12 Factor levels

Variable	Level 1 (-α)	Level 2 (-1)	Level 3 (0)	Level 4 (1)	Level 5 (α)
Focus position[mm]	-1	0	5	10	11
Power[w]	565	600	775	950	985
Speed[mm/s]	3.5	5	12.5	20	21.5
GFR [l/min]	3.5	5	12.5	20	21.5

Due to the number of factors involved, the number of axial design points was 8, and the factorial design points were 16, and an additional centre design point. Two runs were applied at each point, except for the central point where four runs were applied in order to produce better confirmation; the total number of experimental runs was 52. All of the constructed models follow the same procedures as discussed in detail previously for the NGLW statistical model.

6.5.2 Criteria for optimization and results

The optimization targets were based on three criteria according to the previously discussed models: maximize the penetration depth, maximize the weld bead integrity (percentage free of porosity), and maximize the surface cleaning.
According to the optimization criteria Table 6-10 , shows the first solution for the optimum parameters related to maximum desirability.

Table 6-13 Optimization results

Parameter / Response	Focus [mm]	Power [W]	speed [mm/s]	GFR [l/min]	Width µm	Depth [µm]	bead integrity %	Surface cleaning %	Desirability %
Value	0.00	950	30	15	1423	2120.8	88.9	83.21	0.87

Figure 6-29 a shows the desirability function shape; the desirability is improved at focus distances near to zero, and at high power in order to get the maximum power intensity. The improvement range was limited due to increased optimization criteria, and in particular this highlights the importance of the depth, and weld bead homogeneity criteria.

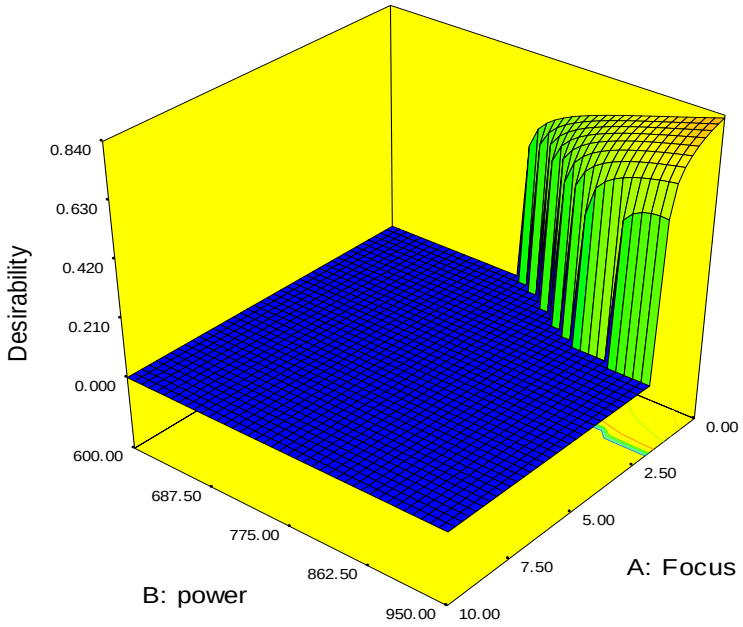

Figure 6-29 Desirability shape function

The result of the optimum parameters for bead on plate welding is shown in Figure 6-30a, and for autogenous laser welding is shown in Figure 6-30 b. Both results show more than 2 mm penetration depth with approximately no porosity. Figure 6-27 shows the final results for the combined welding without back plate and with optimum parameters. The root pass is fully penetrating 1.5 mm depth with no evidence of porosity or lack of fusion for 10 mm and 20 mm thick samples.

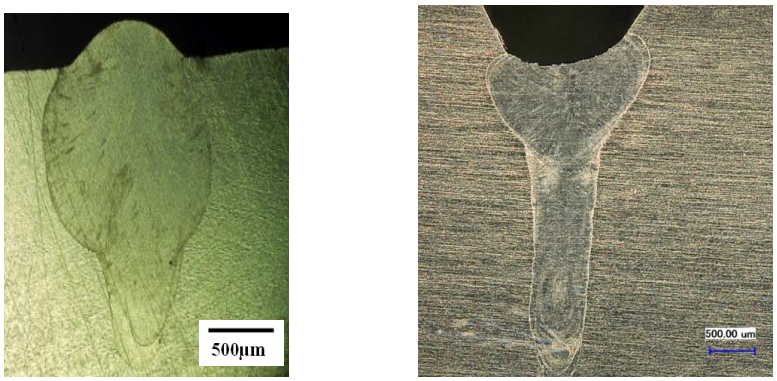

a) Bead on plate b) Autogenous laser butt weld

Figure 6-30 Bead shape for optimized welding without wire

6.6 Summary

This chapter described the development of a statistical model for the control and optimisation of welding parameters for the NGLW technique for different thicknesses.

The over-all weld bead quality is evaluated through predefined responses.

The model demonstrated the significance of the welding control factors (power, wire feed rate, and welding speed), on the quality evaluation responses such as; number of filling passes, overlap shape factor, weld joint strength, weld bead integrity, surface chemistry integrity, and weld bead width.

The results of the multi objective optimization show that, increasing the power and decreasing the wire feed rate at high speed will improve the overall desirability function. The optimization results have been validated by graphical optimization. The results of both methods show a very good correlation.

The optimization results of the model have been verified with different thickness plates 5, 10, 20 mm. The present investigation has clearly demonstrated that significant improvements in weld quality can be achieved through the use of statistical modelling and multi-variable optimization.

Finally, a statistical model was developed to control and optimize autogenous laser welding for the root pass. The optimization results show that, increasing the power at high welding speed will satisfy a required penetration for root pass with no evidence of porosity or lack of fusion.

CHAPTER 7. COMPARISON OF MICROSTRUCTURES AND PRODUCTIVITY OF NGLW, GTAW, COMBINED AND AUTOGENOUS LASER WELDS

7.1 Introduction

In this chapter the developed macrostructures and microstructures for the different welding techniques considered are presented, with special attention being paid to the multi-pass GTAW and multi-pass NGLW techniques. The heat input was calculated for each welding technique in order to understand the relationship between the heat input and welding parameters of the welded joint, and the developed microstructure. The productivity of each welding technique is discussed. The influence of welding parameters and developed microstructure on the mechanical properties of each welded joint was investigated. The influence of welding strategy (one side welding, and two sides welding) on the productivity of welding technique is introduced.

7.2 Welding techniques

In this chapter, four different welding techniques will be considered:

1- Autogenous laser welding will be applied for thicknesses of (3, 10, 20) mm.

2- NGLW will be applied for thicknesses of 3, 5, 10 and 20 mm.

3- GTAW will be applied for thicknesses of 3, 10 and 20 mm.

4- Combined laser and arc welding of 10 mm

7.2.1 Welding of 3 mm thick plates

7.2.1.1 Autogenous laser welding of 3mm thick plates

An optimization process for autogenous laser welding parameters was reported in Chapter 6. The optimization criteria were to improve the weld homogeneity and to maximize the penetration depth. The optimum parameters (results of optimization) was used for the welding of 3 mm-thick plates with a 1 kW fibre laser as shown in Table 7-1.

Table 7-1 welding parameters

Welding variables	
Power [w]	1000
Speed [mm/s]	30
GFR [l/min]	15
Focus [mm]	On surface

The joint preparation is shown in Figure 7-1 a. The welding bead is shown in Figure 7-1 b. The average bead width was 522 μm at the surface and 316 μm at the root; two passes were used. The weld was seen to be homogeneous with no porosity.

The energy transfer efficiency (ETE) is the ratio of power absorbed by the weld joint, to the total laser power. The recommended ratio for low-speed laser welding is 0.15 for conduction mode, and 0.5-0.65 for keyhole mode [168, 169] % .

$$\text{Total Heat input} = \textit{Number of passes} \times \text{Energy Transfer Efficiencies} \times \frac{\textit{Power}}{\textit{Welding speed}} \text{ [J/mm]} \quad (7.1)$$

If the weld was performed with a single welding technique, the heat input per each pass can be calculated as following:

$$\text{Heat input per pass} = \frac{\textit{Total heat input}}{\textit{Number of passes}} \quad (7.2)$$

Consequently:

Total heat input for autogenous laser welding technique for welding 3 mm thickness (two laser passes) = (2 x 0.5 x 1000/30) = 33.33 J/mm.

Heat input per pass = $\frac{33.33}{2}$ = 16.66 J/mm

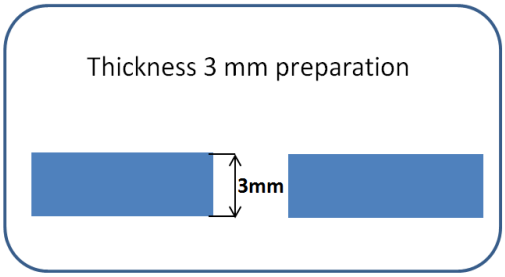

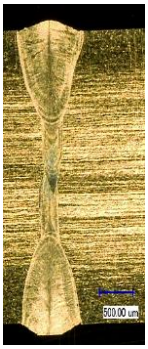

a) Joint prepare (flat face) b) Weld bead shape

Figure 7-1 Optimum welding cross section (Autogenous laser welding 1 kW power)

7.2.1.2 NGLW of 3 mm thick 316L plates

Three passes were required for filling the gap using this technique; the first pass was the root pass, using the autogenous laser welding condition, followed by two filling passes with the filler wire.

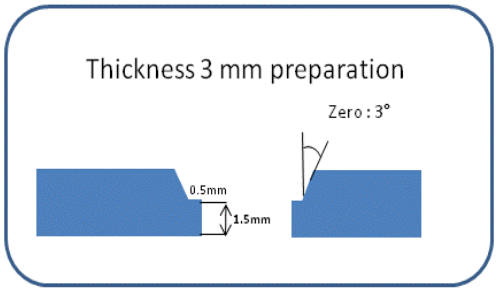

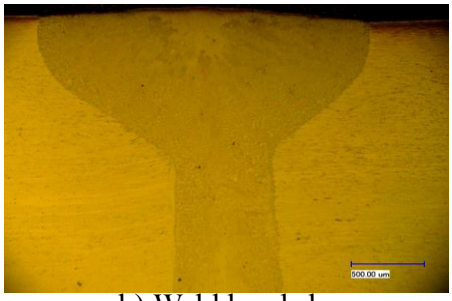

a) Joint preparation b) Weld bead shape

Figure 7-2 NGLW of 3 mm thick 316L stainless steel

The parameters used for the root and filling passes were selected from the optimized results for autogenous laser welding and filling passes models defined in the previous chapter. Figure 7-2 shows the weld joint preparation and weld bead shape. The welding results show no weld defects (porosity or lack of side fusion). The heat input during the welding process is calculated as follows:

NGLW heat input = 0.5* [(1000/30) +2 (912/9.5)]= 109 J/mm

Table 7-2 Welding parameters

Root pass autogenous welding variables	
Power [w]	1000
Speed [mm/s]	30
GFR [l/min]	15
Focus [mm]	On surface
Standoff distance[mm]	8
Filling passes NGLW variables	
Power [w]	912
Speed [mm/s]	9.5
GFR [l/min]	30
Wire Feed [mm/s]	18
Standoff distance [mm]	8

7.2.1.3 GTA welding of 3 mm thick 316L plates

The preparation for the GTA welded joint is shown in Figure 7-3. Two welding passes were required for filling the prepared gap. Figure 7-3 shows the welding bead results, with weld bead sizes ranging from 3168 μm at the root to 4440 μm on the upper surface.

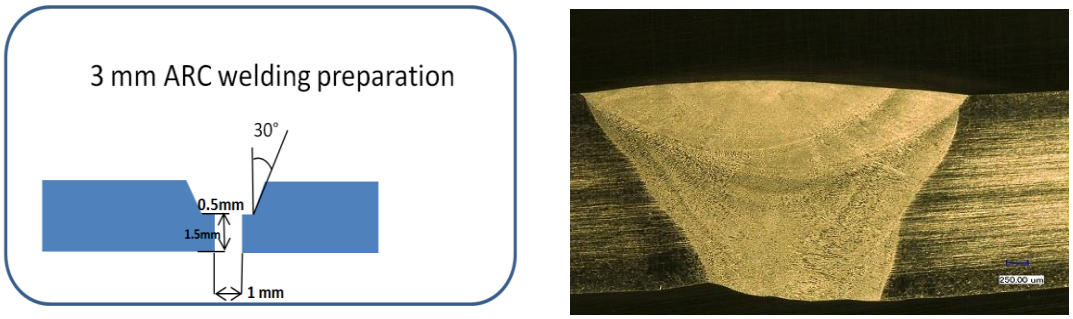

Figure 7-3 Joint preparation and bead shape for GTA welding

The GTA welding parameters are shown in Table 7-3. Average value for energy transfer efficiency (ETE) of GTA welding is 75% [170].

Heat input to the GTA welding = $0.75[\ \frac{8.5*77}{1.86} + \frac{9.1*84}{2.1}\ ] = 0.75[351.88 + 364] = 536.9$ J/mm.

Table 7-3 GTA Welding variables

Volt	Current [A]	Wire feed[mm/s]	traverse speed [mm/s]	Gas flow rate [l/min]
8.5	77	3.1	1.86	12
9.1	84	2.84	2.1	12

7.2.2 10 mm thick 316L plates welds

GTA welding, NGLW and autogenous laser welding techniques were carried out on a sheet thickness of 10 mm. Two strategies were investigated; single side welding and welding from two sides.

7.2.2.1 Welding strategy from one side

Figure 7-4 a shows a schematic drawing of the weld joint preparation of NGLW technique, and Figure 7-4 b shows the joints preparation for the GTA welding technique. The autogenous laser welding was a face-to-face butt weld.

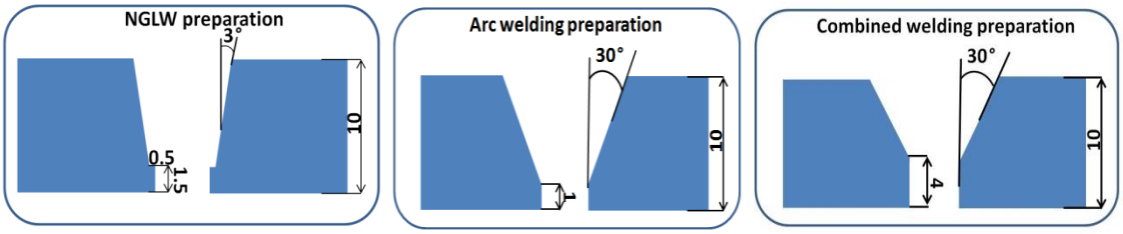

(a) NGLW (b) Arc welding (c) Combined welding

Figure 7-4 Joint preparation for welding 10 mm thick plates

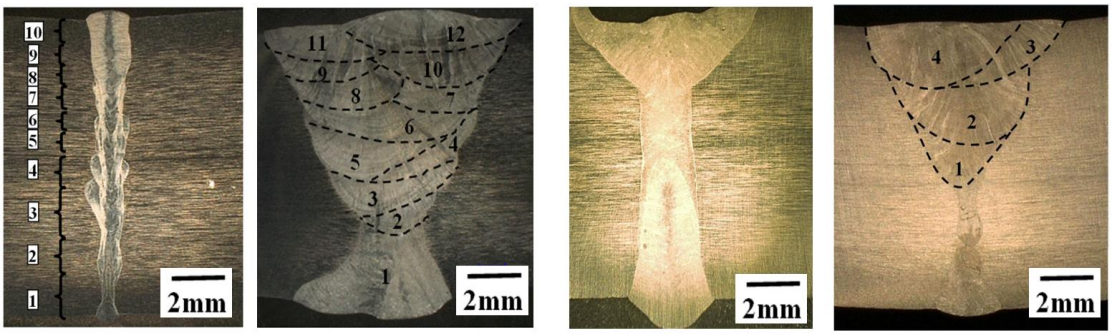

a- NGLW b - GTA welding c-Autogenous d- Combined laser- GTA

Figure 7-5 Bead cross section of 10 mm thickness welding 1 side

Figure 7-5 a shows the weld bead cross section for the NGLW optimum condition, which is discussed in detail in chapter 6. Figure 7-5 b shows the GTA welding bead. Twelve passes were required for the GTA welding technique to fill the gap with the following parameters: average voltage 11 - 11.5 V, current 120 - 140 (A), wire feed rate 260 mm/min, average traverse speed 128 mm/min, and gas flow rate 10 l/min. Figure 7-5 c shows the weld cross section for the autogenous high power laser welding

(HPLW) technique. The weld was completed in one pass with a power 7.5 kW fibre laser and a speed of 8.5 mm/s. Combined laser-arc welding technique is a new welding technique. The objective of the study was to improve the productivity using limited laser power for welding root passes and decrease the number of GTA welding filling passes. 4 passes only were required to complete the combined welding gap plus 2 laser welding passes for the root as shown in Figure 7-5 d. Developed stress, productivity, heat input, and distortion behaviour of this technique will be evaluated and compared to other welding techniques in the following chapters. Table 7-4 shows the heat input to the weld bead for the four techniques.

Table 7-4 Heat input for 10 mm welding techniques

Welding technique	No of pass	Heat Input to weld joint [J/mm]/pass	
GTAW	12	604	
NGLW	(1 root + 9 filling)	47	
Autogenous HPLW	1	450	
Combined laser arc	2 passes(laser) + 4 filling passes (GTAW)	Laser	GTAW
		17	415

7.2.2.2 Welding strategy from both sides

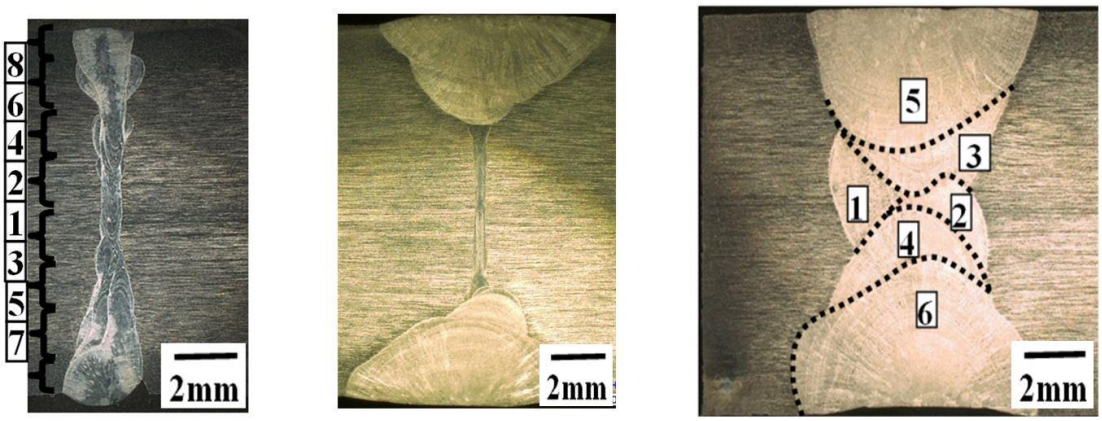

a – NGLW b- combined laser and arc welding c - GTA welding

Figure 7-6 Bead cross section of 10 mm thickness welding from 2 sides

Three different welding techniques were investigated for welding the 10 mm-thick plates from both sides; the methods were NGLW, combined arc and laser welding, and GTA welding, as shown in Figure 7-6. Joint preparation for the welding processes was similar to the previous single-sided strategy shown in Figure 7-4. However, the root

shape for the two-sided process was in the middle of the joint, and gap machining was also from both sides.

The weld joint required three passes from each side, plus the root pass, for completion using the NGLW technique, whilst it needed three passes from each side for the GTA welding technique, and two passes from each side for the combined laser-arc welding technique. The heat input for each welding technique is mentioned in Table 7-5.

Table 7-5 Heat input for 10 mm thickness plates

Welding technique	No. Of passes	Heat Input to weld joint	
GTAW	6	511	
NGLW	6	51	
Combined laser arc welding	2 laser root passes + 2 filling GTAW	18 laser	361 GTAW

7.2.3 20 mm thickness welding evaluation study

Five different welding techniques were evaluated for a plate thickness of 20 mm. Figure 7-7 a and b show GTA and NGLW welded samples respectively, which were produced with the two-sided welding strategy and Figure 7-7 c and d show samples welded with GTA welding and NGLW, respectively, produced with the one-sided welding strategy. Finally, a 2-sided HPLW sample is shown in Figure 7-7e.

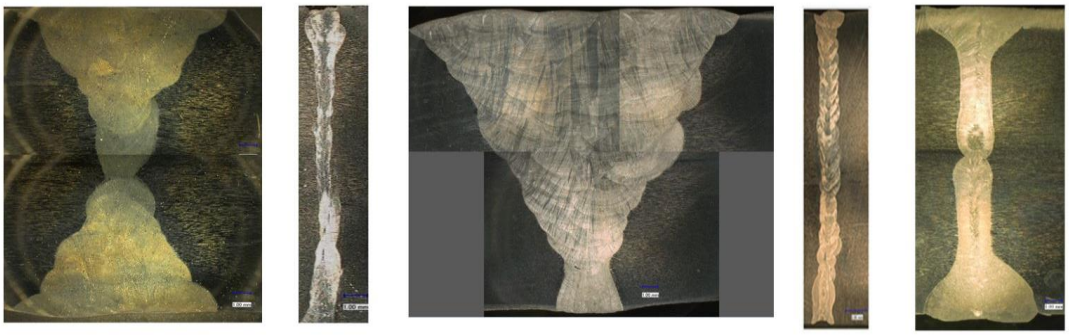

Figure 7-7 Welding techniques for 20 mm thick plates

(a) Two sided GTA welding, (b) Two sided NGLW, (c) one side GTA welding, (d) one side NGLW (e) Two sided autogenous laser welding

The results are shown in Table 7-6. The welding parameters for NGLW technique following the optimization results as mentioned in chapter 6. HPLW parameters similar to 10 mm thick plates welding as mentioned in section 7.2.2.1. The average welding parameters for arc welding process were: average voltage 10 – 10.4 V, current 110 – 120 (A), wire feed rate 260 mm/min, average traverse speed 130-140 mm/min, and gas flow rate 10 l/min.

Table 7-6 Heat input for 20 mm thickness plates

Welding technique	Number of passes	Average heat input/ pass[J/mm]
GTA (2 sides)	34	305
NGLW (2 sides)	20	42
GTA (1 side)	52	388
NGLW (1 side)	23	48
HPLW (2 sides)	2	450

7.3 Microstructure

Figure 7-8 shows the microstructure of samples welded with GTA welding, NGLW, autogenous high power laser welding, and autogenous low power laser welding. There is a visible difference in the microstructure and dendrite spacing for each welding technique. The developed microstructures are dependent on alloying elements, solidification behaviour, and thermal cycles in different welding processes. The solidification and microstructure have a direct influence on the mechanical properties, corrosion behaviour and hot cracking behaviour of the weld bead, as will be disused in detail in the following section.

The laser weld fusion zones, NGLW~ 2 mm and autogenous laser welding 1-5 mm are significantly narrower than those for the GTAW fusion zone (10-50 mm). These different widths and fusion areas are attributed to the different welding speeds and heat inputs in the different welding methods, and different requirement for joint preparation (width and slope of the gap).

Columnar dendrites extend from the fusion boundary to the weld centre, with different dendritic spacing, as shown in Figure 7-8. The equiaxed dendrite region is developed in

the centre of the fusion zone, with different sizes according to heat input and cooling rate.

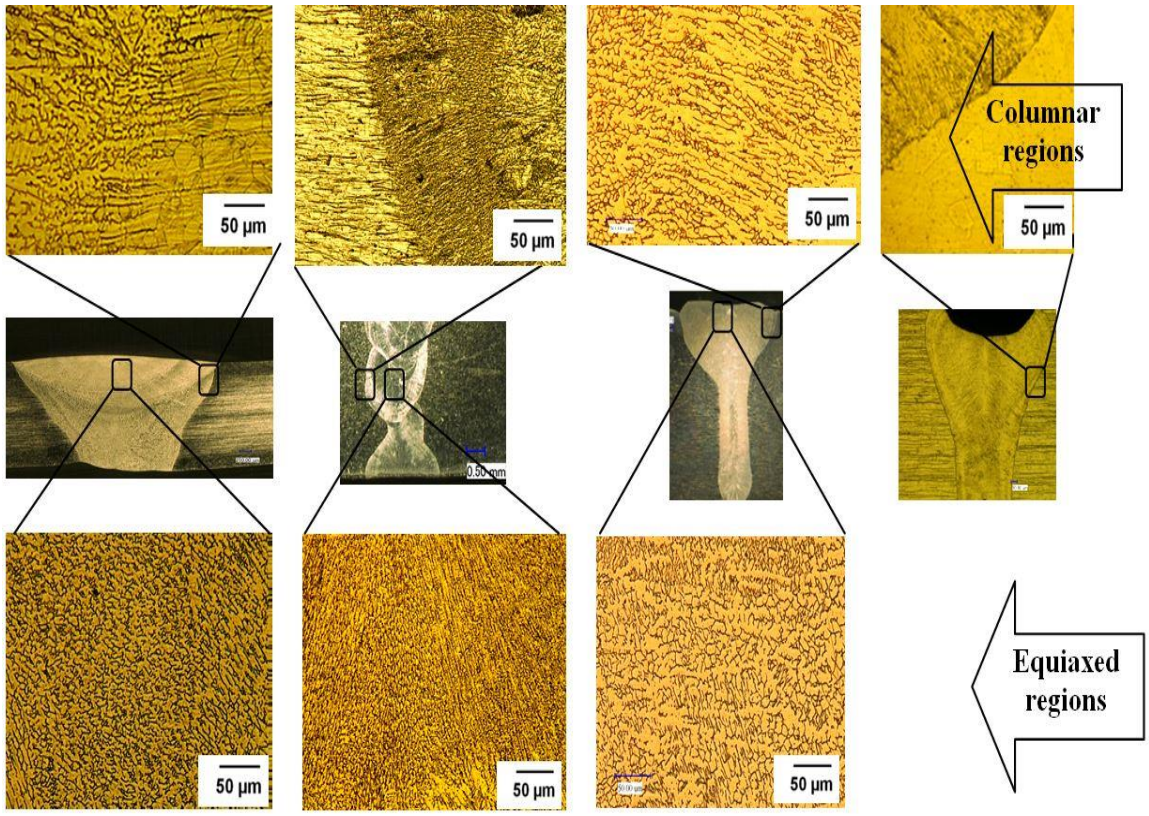

Figure 7-8 Optical micrographs of different welding techniques

(a)GTA (b) NGLW (c) 7.5kW laser welding (d) 1kW autogenous laser welding

The microstructure of the autogenous HPLW sample has the highest directionality of the columnar region at weld bead boundary, around the axis of the laser beam, as shown in Figure 7-8c. This is due to solidification of the weld metal at higher cooling rates, compared to that of conventional GTA welding [80]. The NGLW technique exhibits a special directionality in the columnar region of the weld bead at the centre of each bead, and an equiaxed structure region is developed in the weld bead centre, with a finer dendritic spacing with respect to GTA, as shown in Figure 7-8b.

Low power, high speed autogenous laser welding shows a high directionality of the columnar region around the axis of the laser beam with the finest microstructure and very narrow equiaxed region in the weld centreline as shown in Figure 7-8 d.

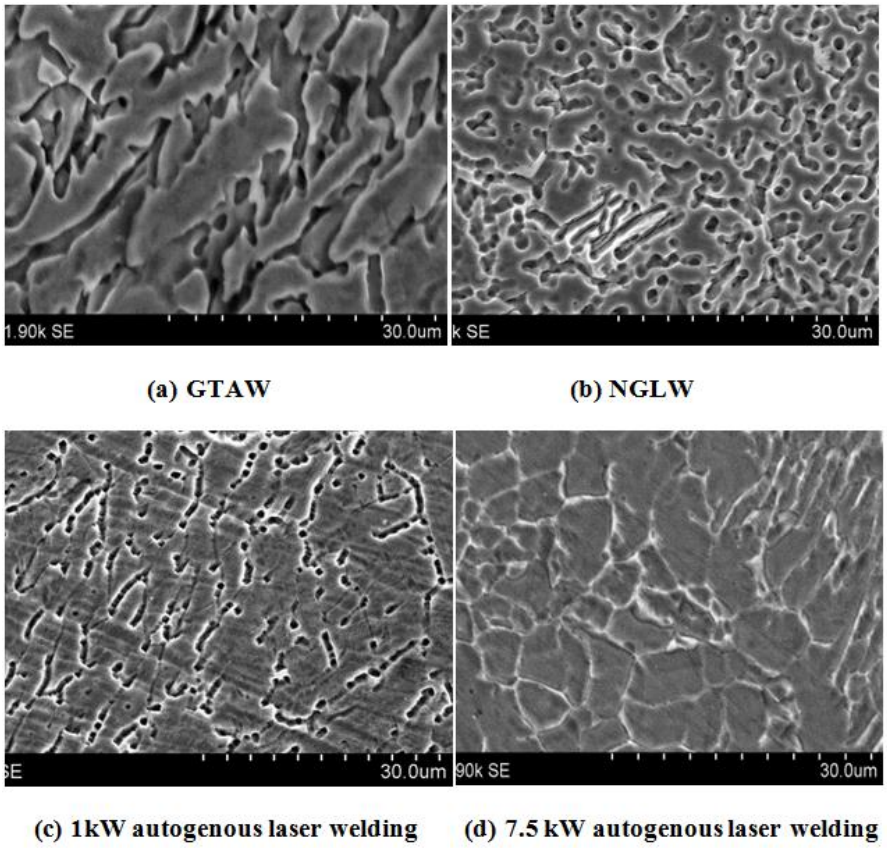

Figure 7-9 SEM micrographs for different welding processes

Figure 7-9 shows a SEM-magnified microstructure for different welding techniques.

The average dendrite spacing in GTA welding is equal to 10-15 µm, as shown in Figure 7-9 a.

The sample prepared with NGLW has a slight change in the dendrite arm spacing. The finest arm spacing is seen in the root passes. The dendrite spacing gradually increases (becoming coarser) towards the upper surface weld bead, due to different cooling rates between the initial passes at the root, and the final passes near to the weld top surface. Generally, the average dendrite spacing range is 3-8 µm, which is larger than the value for autogenous laser welding, as shown in Figure 7-9 b.

The welding speed and power of laser welding have a significant influence on the dendritic structure of autogenous laser welding [171]. Figure 7-8 c and d show autogenous laser welding with a power of 7.5 kW and a speed of 8.33 mm/s, and at a power of 1 kW with a speed 30 mm/s, respectively. The measured secondary dendrite arm spacing is very fine and was estimated to be 2–4 µm, as shown Figure 7-9c, while

for the 1 kW power laser welding the dendrite spacing increased to 4-10 µm as shown in Figure 7-9 d.

7.3.1 Heat Affected Zone (HAZ)

There is no apparent transition zone and HAZ near to the fusion boundaries in autogenous laser welding and NGLW. Due to high welding speed and low heat input to the weld joint, as shown in Figure 7-10, the cooling rate is increased; the grains in the HAZ region have no time to grow. Therefore the HAZ is very narrow. On the other hand, the HAZ in GTA welding is very large as shown in Figure 7-10 b, due to lower welding speed and high heat input, and low cooling rate. This leads to an increase in the size of the grains near to the welding bead, which leads to the formation of the HAZ; the HAZ width in GTA welding is 150-450 µm, depending on the welding parameters and sequence of welding passes.

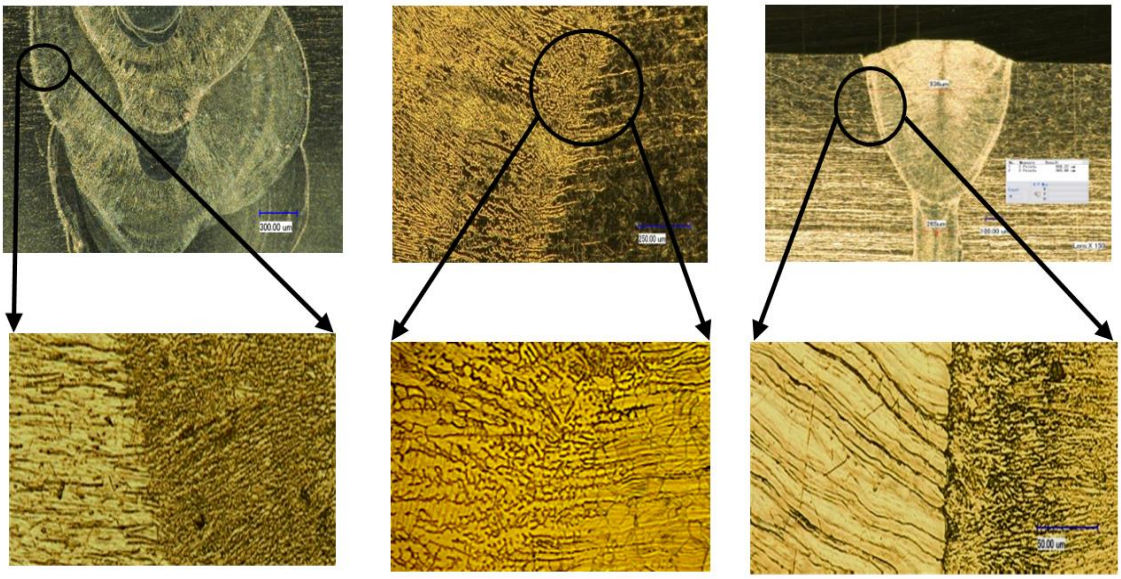

(a) NGLW (b) GTA welding (c) Autogenous laser welding

Figure 7-10 HAZ of different welding processes

7.4 Cost and productivity of different welding techniques

Welding productivity is the measure of efficiency of the welding process. The general definition of the welding process productivity or efficiency is the output divided by the input to the process. The output could be the number of products, profit. The input

could be the time of the process, and the cost of the process which includes the man hour required for operation, labour wage and consumables and welding joint preparation (simple or complex). The most common definition of the productivity is the number of output products per unit time.

The labour and overhead portion of the actual cost of welding is generally between 60 to 70 percent of the total cost [172]. Consequently decreasing the processing (welding) time and joint preparation time will improve the productivity of the process.

The 10 mm thick plates welding were evaluated for different welding processes productivity in terms of productivity and cost. In order to calculate the welding time for 10 mm thick sample for each welding technique the welding speed and length of welding pass have to be defined. The sample dimensions are the same for all welding techniques as shown in Figure 7-11.

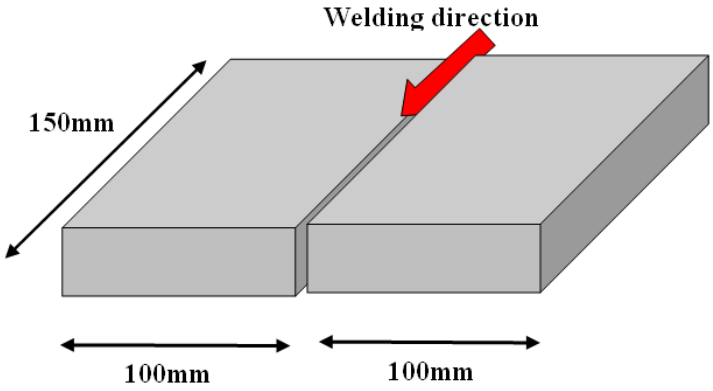

Figure 7-11 Welding specimen dimensions

The welding time was calculated for the autogenous HPLW, NGLW, combined arc laser welding, and GTAW welding techniques according to next equation.

Welding time = (length of welding pass / speed) * number of passes

The following section will investigate a case study for evaluating the productivity of different welding techniques in terms of processing (welding) time.

7.4.1 Productivity of one sides welding strategy

(Case study for welding 10 mm thick plate)

a) Autogenous HPLW

The welding for 10 mm plate thickness with high power laser welding technique was done in one pass, as shown in Figure 7-5, using the following parameters:

Welding speed = (8.33 mm/s), number of passes is one pass.

Welding time = (150 / 8.33) = 18 (s/item).

b) NGLW

Root pass parameters - welding speed = 30 mm/s, number of passes =1.

Filling passes parameters - welding speed = 9.5 mm/s, number of passes 9.

Total welding time = ((150 / 9.5) x 9) + ((150/30) x 1) = 147 s/item.

c) Combined laser-arc welding

The welding bead shape is shown in Figure 7-5 d.

Two root laser welding passes with welding speed = 30 mm/s.

4 GTA welding filling passes with welding average speed = 1.9 mm/s.

Total welding time per item = (150 / 1.9) * 4 + (150/30) * 2 = 325 s/item.

d) GTAW

Welding speed = 2.1(mm/s), number of passes is 12 passes.

Welding time = (150 / 2.1) * 12 = 857.142 (s/item).

Joint preparation for HPLW is considered as the most simple amongst the techniques considered; both GTAW and NGLW need special preparation for the joint, as shown in Figure 7-4. Consequently the shortest total welding times will be for HPLW, then NGLW and finally GTAW. Alignment of the workpiece for HPLW may require more time, but it is insignificant in comparison with much shorter preparation time; a better alignment fixture could be designed to decrease or eliminate this time, especially for mass-production.

7.4.2 Productivity of two sides welding strategy

a) NGLW

The weld needed two root passes with autogenous parameters, and 3 filling passes from each side, as shown in Figure 7-6a. The filling pass parameters were: welding speed = 9.5 mm/s and number of passes = 6. The root pass had a welding speed = 30 mm/s, number of passes = 2.

Total welding time per item = ((150 / 9.5) x 6) + ((150 / 30) x 2) = 104.73 s/item

b) GTAW

The weld joint needed 3 filling passes from each side, as shown in Figure 7-6 b, with the following parameters:

Average welding speed = 2.05 mm/s, number of passes = 63.

Total welding time per item = (150 / 2.05) x 6 = 439 s/item.

c) Combined laser-arc welding

The weld joint is shown in Figure 7-6 c. The welding passes were performed with two root laser welding passes with welding speed = 30mm/s, and 4 filling passes were performed with welding speed = 2.55 mm/s.

Total welding time per item = ((150 / 2.55) x 4) + ((150/30) x 2) = 245 s/item.

Combined laser-arc welding represents an improvement in the welding time with respect to GTAW, due to the use of laser welding for a high-speed root pass. The main advantage for the technique is improved productivity without need for a very high power laser. The two-sided strategy generally shows an improved welding time, and consequently improved productivity with respect to the single-sided strategy. The time reduction for two-sided NGLW is 29% with respect to one side strategy and 49% for both two-sided GTAW, and 24% for combined laser arc welding, as shown in Table 7-7.

Table 7-7 Welding time evaluation for different welding strategies

Process	NGLW		GTAW		Combined Laser-arc welding	
	1 side strategy	2 sides strategy	1 side strategy	2 sides strategy	1 side strategy	2 sides strategy
Welding time / s	147	104.7	857.1	439	325	245
Time reduction of 2-sided strategy compared to one side	29 %		49 %		24 %	

7.5 Summary

This chapter includes a microstructure evaluation for NGLW, GTAW, autogenous laser welding, and base material. It also investigates the productivity of each welding technique in terms of welding time, and the influence of the welding strategy on the productivity.

The results show that, autogenous laser welding shows the finest dendritic micro structure with respect to other welding technique.

Both NGLW and autogenous laser welding show a very small heat affected zone with respect to GTAW.

The productivity of autogenous laser welding is the highest with respect to other welding technique.

NGLW productivity is higher than productivity of GTAW for all welding strategies.

Productivity of two sided welding strategy has a better productivity with respect to one side strategy.

CHAPTER 8. MECHANICAL ASSESSMENT OF NARROW GAP LASER WELDING OF 316L STAINLESS STEELS

8.1 Introduction

Austenitic stainless steel alloys are widely used materials in both high and low temperature industrial applications, due to their superior corrosion resistance and mechanical properties [77, 173]. These alloys are also used extensively in heat-resistant structural components in power generating and chemical industries, as a result of their metallurgical stability, excellent corrosion resistance, and good creep and ductility properties at elevated temperatures. AISI type 300 series stainless steels are the most widely-used structural alloys for cryogenic applications because they also exhibit excellent mechanical properties such as high strength, ductility, and fracture toughness, as well as low magnetic permeability[18].

The welding process has a very significant influence on the material properties. The metallurgical influences of cold working and thermal aging during the welding process can degrade mechanical properties such as ductility, strength, fracture resistance, hardness. The cooling rate during the welding process influences the ferrite percentage at the weld bead region, which has a significant effect on the mechanical characteristics of the base material [18, 78]. Some previous studies have investigated the influence of GTAW on the mechanical behaviour of the austenitic stainless steel [77]. However the detailed mechanical properties of NGLW technique have not been previously investigated in much detail.

This chapter presents a study on the influence of welding parameters and procedures on the mechanical properties for 316L steel welds. A comparison was made with the base material properties, in order to investigate the advantages and disadvantages of each welding technique. The NGLW properties were also compared to the results for material joined with GTAW. The mechanical evaluation includes tensile strength, bending strengths, toughness, fatigue, and hardness measurements, of the different welds and the base material.

The welding parameters were derived from the optimization results of the statistical model as discussed in detail in the previous chapter. Specimens for tensile strength, fatigue, bending, and Charpy tests were extracted from the welded workpiece, according to relevant ASTM standards. Figure 8-1 shows the position of different testing samples with respect to the weld bead.

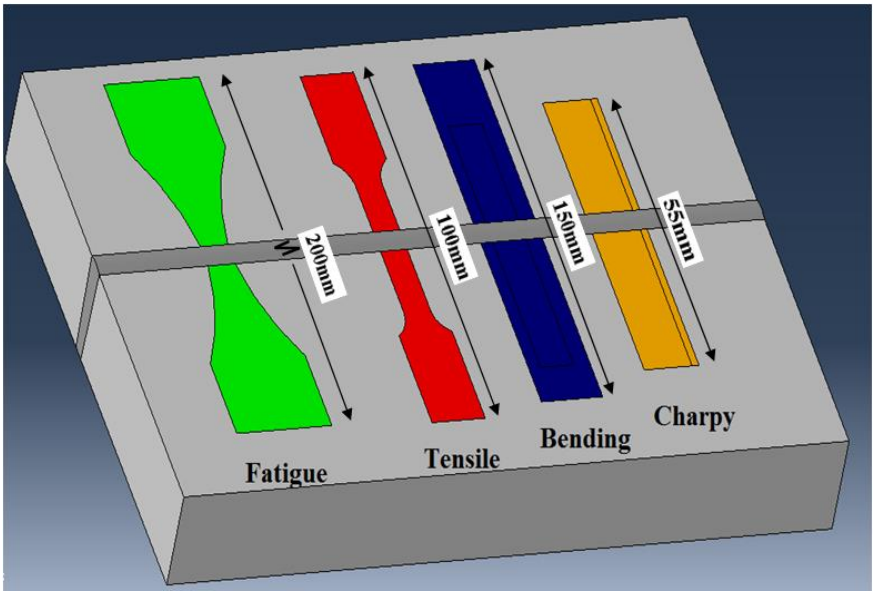

Figure 8-1 Position of testing samples with respect to weld bead

8.2 Stress strain performance of different welding techniques (Tensile testing)

Tensile testing samples were prepared for the base material, and also for the different welding techniques. The welded parameters are according to optimum conditions [14], discussed in details in the previous chapter. Three separate tensile test specimens were prepared for each welding technique in order to minimize errors and improve the reliability of the results. The samples were prepared according to ASTM E8M-04 guidelines [174] as shown in Figure 8-2. The samples thicknesses were 3 mm, and the strain rate was 0.02 mm/s.

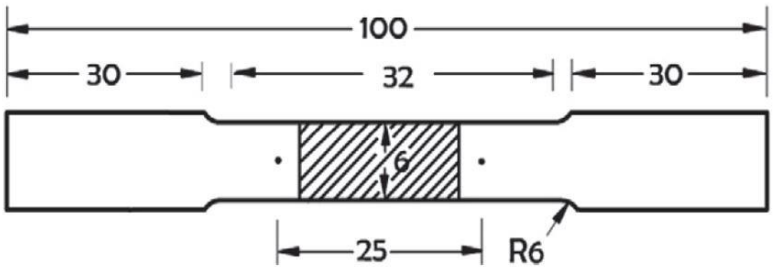

Figure 8-2 Dimensions of sub-size tensile specimen, all dimensions are in 'mm'

The results of tensile tests of all NGLW samples showed failure in the base metal, not in the weld itself. This result is related to the optimum welding parameters for the NGLW technique according to previous statistical model results. The failure of the GTA welding technique was also in the base material.

Figure 8-3 Tensile testing samples for NGLW technique

Figure 8-4 shows a decrease in the strain for NGLW and GTAW compared with that of the base material. The failure strains were 41%, 44%, and 43% for autogenous laser welding, NGLW, and GTAW respectively, while the base material shows a total strain 70% at failure as shown in Figure 8-4.

The values of the ultimate strength for both welding techniques were higher in comparison with the strength of the base metal.

The values of the weld strength for the GTAW technique were investigated previously for AISI 316L stainless steel; the average tensile strength results were 582-640 MPa [175]. The results of the ultimate tensile strength for base metal, GTAW, autogenous laser welding, and NGLW are 607, 632, 621, 670 MPa respectively, as shown in Table 8-1.

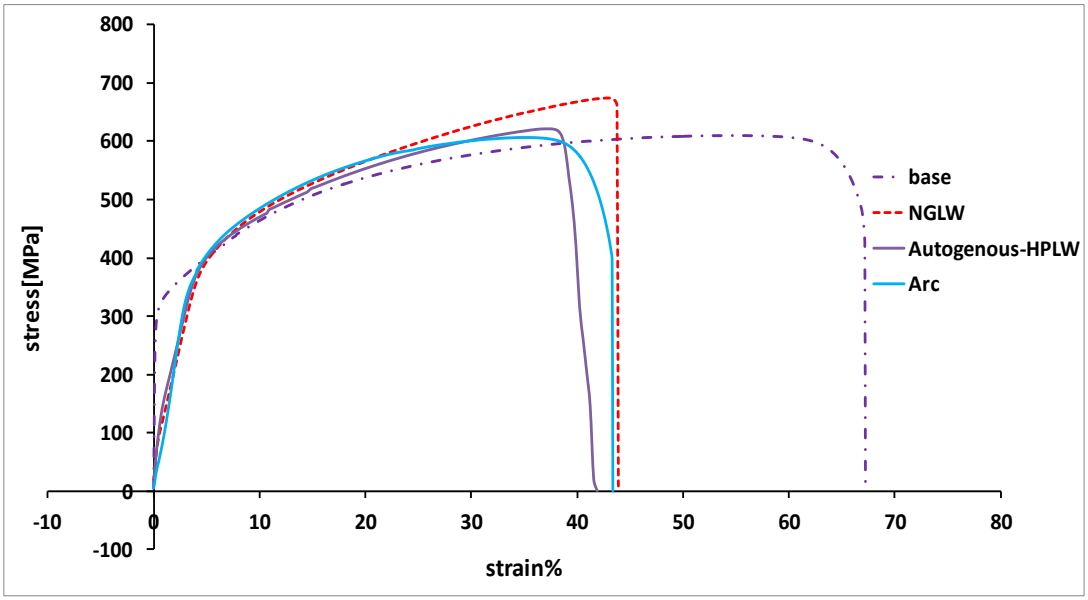

Figure 8-4 Cross-weld stress strain curve for different welding techniques

Different welding thermal cycles lead to phase transformation i.e. a change of the ferrite to austenite ratio. Improving the power density in laser welding leads to an increase in the welding speed, consequently decreasing the heat input to the weld joint. A higher laser welding speed lead to a finer grain size in the welded region compared to that of GTAW.

X-ray diffraction (XRD) analysis was used for investigation of the ferrite percentage in the weld beads. The results show that the average ferrite percentage was 3.64% for the GTA welding bead, and 1.5 % for NGLW, and in autogenous laser welding it was less than 1%. A previous study investigated the influence of delta ferrite on the weld joint strength [176]; the results indicated that the influence of small delta ferrite content variation in the specimens of the different welding techniques had a little impact on the joint strength, due to the smaller difference in delta ferrite percentage.

The grain size refinement in laser welding was found to have a more significant effect on the stress-strain behaviour than the delta ferrite percentage, as shown in Figure 8-4.

Grain boundaries are considered as pinning points impeding further dislocation propagation. The lattice structure of any adjacent grains has a different orientation. It requires more energy for a dislocation to change directions from grain to the adjacent one. Decreasing the grain size will increase the number of direction change and consequently impede any progress of any dislocation.

Table 8-1 Tensile testing results

Materials	**Filler materials**	**Welding methods**	**Ultimate Tensile strength, σ_u, (MPa)**	**Yield strength, σ_Y, (MPa)**	**% elongation**
316L	ER 316L	NGLW	670	385	44
		Autogenous laser weld	621	382	41
		GTAW	632	375	43
Base (316L)			607	302	67

8.3 Bending test

The bending test is a destructive test to measure the weld quality and ductility of the weld region; the test is performed in accordance with ASTM E190-92. The testing instrument was an Instron compression tester with a capacity of 2000N, as shown in Figure 8-5. The span distance was 40mm, the plunger diameter was 10mm with a compression rate of 2mm/min, and the bending angle was 180º. The bending test at room temperature showed no cracks or defects for all joints made with NGLW and GTAW. Two further samples were polished with 2500 grit sandpaper before performing the bending test, in order to show clearly any defects which may have been initiated in the weld region during the testing, as shown in Figure 8-5. These results indicate that the two samples prepared using NGLW and GTAW were free of defects and had reasonable ductility.

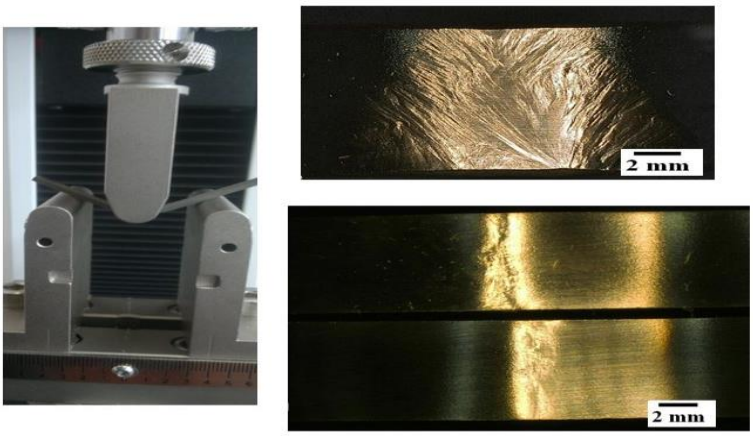

(a) (b)

Figure 8-5 Bending test

a) Instron compressing tester b) GTAW-NGLW bending samples

Figure 8-6 shows the bending test results for the different welding techniques; side-bending test and face-bending test results for NGLW of 10mm-thick plates are shown in Figure 8-6a. Results for autogenous laser welding, GTAW and NGLW for 3mm-thick samples are shown in Figure 8-6 b, c, d respectively. All of the welded samples had a 180^{o} bending angle. The optical microscope monitoring of the samples show no defects or cracking appeared, which implies that they represent a sound weld with very good ductility behaviour.

Figure 8-6 Bending test results for different weld samples

(a)Face –side bend of 10 mm NGLW thick plates (b) Autogenous laser weld of 3 mm thick plates (c) GTAW of 3 mm thick plates (d) NGLW 3 mm thick plates

8.4 Fatigue test results

The influence of NGLW and GTAW on high-cycle fatigue behaviour was studied, and the results were compared to base material properties. The influence of delta ferrite on the fatigue properties was investigated also at cryogenic temperatures, in order to evaluate the long-term reliability of each welding technique, for use in the manufacture of power generation plant.

Fatigue tests were conducted according to the guidelines given in ASTM E 466; the test specimen is shown in Figure 8-7. The thickness of the sample was 3 mm. All testing was done with a 100 kN capacity servo-hydraulic tester, an MTS Instron, model 4507. Testing was performed with a sinusoidal cyclic load at a frequency of 10 Hz. The load ratio *R*, that of minimum to maximum load was 0.2. The equivalent fatigue strength specified for AISI 316L stainless steel, in the rolling direction = 430 MPa. The experimental results for base material were very similar to previously investigated results [19]. The average measurable fatigue life in the present study was restricted to $1.5x10^6$ cycles due to limitations related to long-term testing.

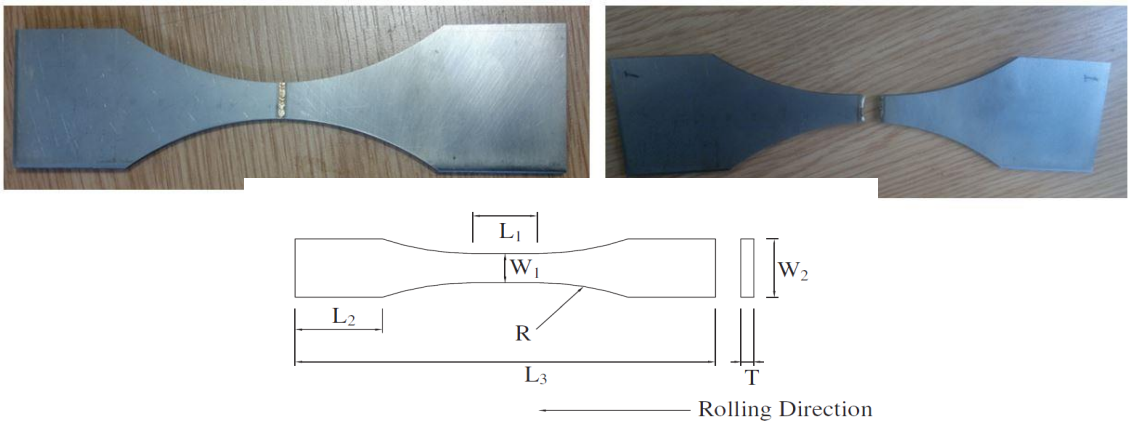

Designations	T (mm)	W_1 (mm)	L_1 (mm)	W_2 (mm)	L_2 (mm)	L_3 (mm)	R (mm)	$\frac{W_1}{T}$	$\frac{L_1}{W_1}$	$\frac{W_2}{W_1}$	$\frac{R}{W_1}$	Reduced cross section area ($T \times W_1$)
Large (Standard specimen)	5	10	30	30	40	190	85	2	3	3	8.5	50 mm^2
Subsize specimen	2.6	5.2	10.4	10.4	14	67	41.6	2	2	2	8	13.52 mm^2
ASTM E466 specifications	≧2.54 (as possible as)							2～6	2～3	> 1.5	≧8	19.4 mm^2～645 mm^2 (preferable)

Figure 8-7 NGLW fatigue specimens

All the samples welded with both the NGLW and GTAW techniques generally showed a high resistance to fatigue stress - the fatigue specimens failed at the weld bead. This failure may be due to micro-defects in the weld, or deterioration of the weld region strength. The results show a slight shift of S-N curve of the base material as compared to previous investigations for 316L [177] toward lower levels of cycles for all investigated welding techniques, however this shift is considered insignificant. The endurance limit for the NGLW technique was 422 MPa, and for GTAW it was 415 MPa, and 403 MPa for autogenous high power laser welding as shown in Figure 8-8.

HPLW represents the lowest endurance limit due to presence of micro-voids, which act as stress concentration sites in fatigue tests and cause lower fatigue resistance. The fatigue crack initiation sites could be at very small blowholes or defects, which may be very difficult to detect [19].

The presence of micro-voids on the results was minimized by the use of an ultrasonic detector for evaluating the welding defects. Moreover, the welding parameters of the NGLW technique were optimized according to the statistical model results in [14], to decrease the influence of voids on the results .

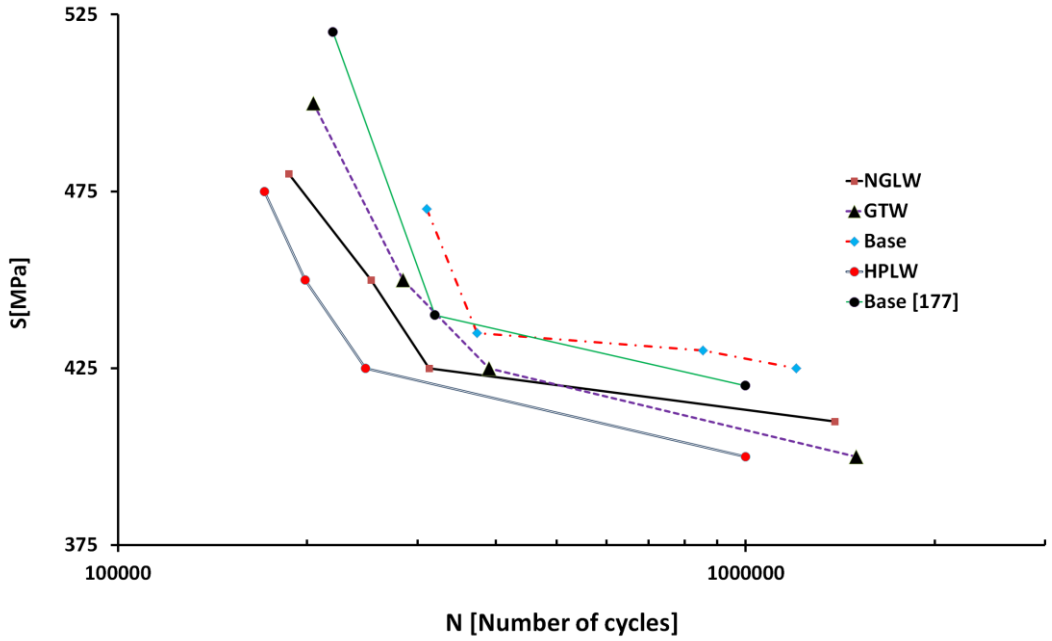

Figure 8-8 Fatigue behaviour for different welding techniques

A previous study for AISI 316L stainless steel indicates that the weld-pass interfaces are the most critical place for crack initiation, but the influence of δ delta ferrite on the

high-cycle fatigue properties was not clear [177]. The results of NGLW experiments show that most of the delta ferrite phases are concentrated at the weld-pass interface boundaries, as shown in Figure 8-9. Change in delta ferrite concentration is believed to be another reason for crack initiation, due to decreased toughness and a low ductile- to-brittle transformation temperature.

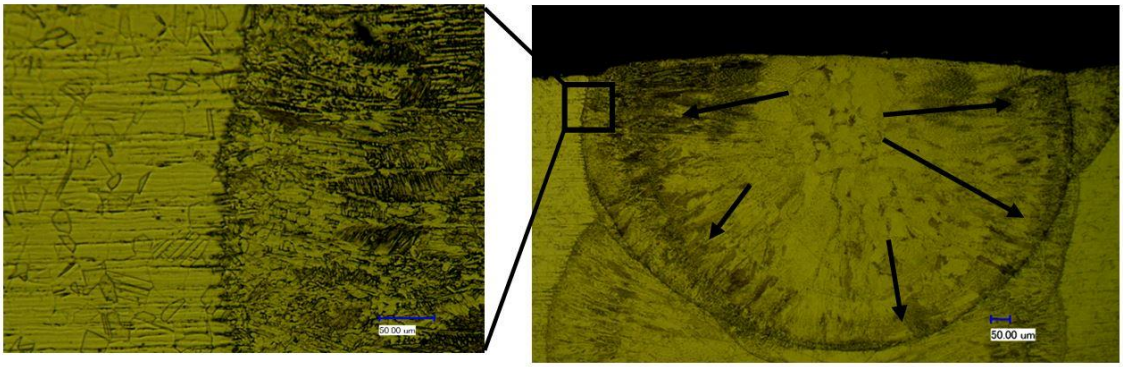

Figure 8-9 Delta ferrite phase concentration areas in welding bead pass

8.4.1 Surface fracture behaviour of welding techniques–base material

Figure 8-10 shows the fracture surface results for NGLW, GTAW, HPLW, and base material. None of the tested specimens for different welding techniques or base material showed any evidence of brittle behaviour; no flat or smooth polygonal grain facets ("rock candy") are detected on the surface of the tested samples. This indicates that all of the fracture surfaces of the different samples exhibited ductile behaviour, with different extents.

Room temperature fracture tests for three different samples were observed under SEM; this revealed failures for the base material and GTAW samples in familiar ductile 'dimples' due to the close proximity of voids, which merge with the fracture surface [178, 179]. The fracture surface for base material samples showed a more complicated fracture surface, with many small inter-granular facets and very fine and small dimples; the GTAW samples also showed the same behaviour, but with slightly coarser dimples. Consequently, both samples exhibited ductile fracture by coalescence of micro voids, and a fracture micro-mechanism of ductile dimpled [179]. The fractures in the autogenous HPLW samples had relatively coarse dimples, and ductile tear ridges. This fracture behaviour indicates a reduced ductility with respect to the base material and GTAW techniques. The results of the fracture surfaces confirm the previous results for

the reduced ductility of welded samples with respect to base material, which has been discussed in tensile testing section as shown in Table 8-1.

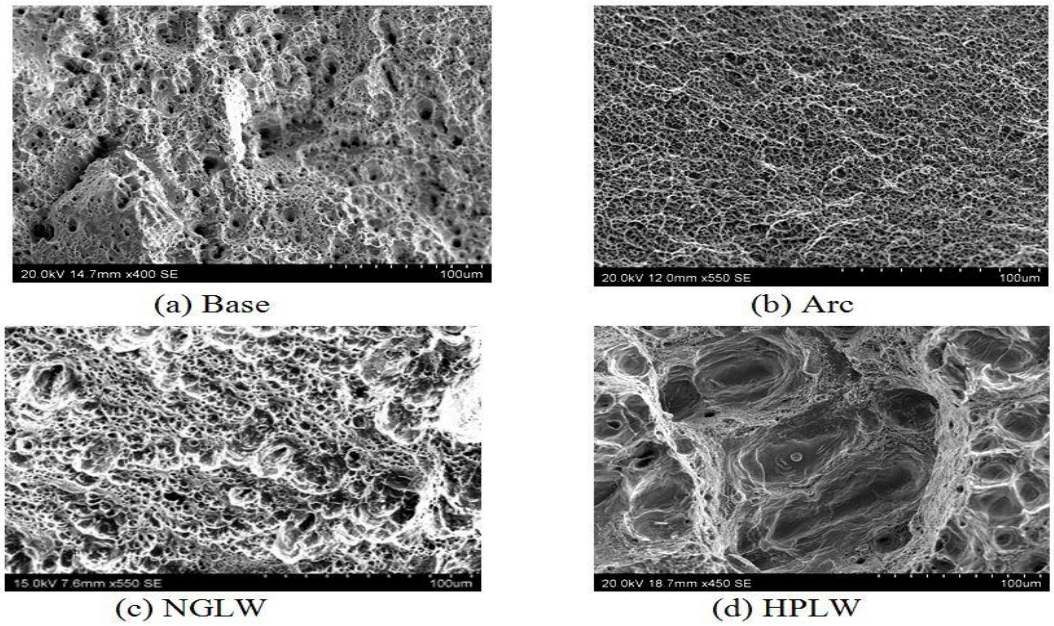

Figure 8-10 Fracture surface results

8.5 Hardness evaluation

The influence of NGLW, autogenous laser welding, and GTA welding on the hardness distribution across the weld joint is investigated. The cyclic hardening of material during welding process will be compared with these techniques. The extent of any work-hardening has a significant influence on the susceptibility of the welded joint to stress corrosion cracking [180]. The hardness of the welded specimens was determined using a Vickers micro-hardness tester. The load applied was 300g, and the loading time was 10 s. The hardness distributions are shown in Figure 8-11. The welding parameters for the three welding techniques are discussed previously in Chapter 7. The hardness of the NGLW sample had two peak values of ≈ 210 HV; the position of these peaks was approximately 1-2 mm from the welding centre line. The value of the hardness sharply decreased down to a steady value. The total hardened width was 10 mm. The hardness of the GTA–welded sample had a peak value of 264 HV, and a total hardened width of 80 mm.

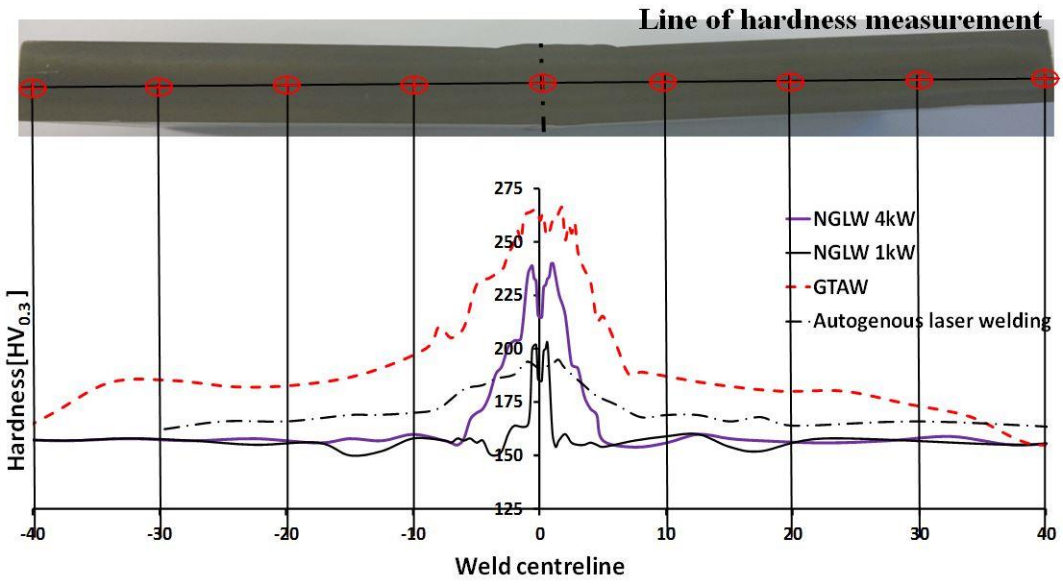

Figure 8-11 Hardness profile across different welding processes

Autogenous laser welding with low laser power, and high speed has the most broad hardness distribution in comparison to the other welding techniques; the peak hardness value was 185 HV. This was mainly due to the high welding speed of 0.5 m/min consequently it had no accumulated plastic strain due to multi-pass welding processes.

There are two main reasons for increased hardness in the GTAW weld fusion zone. An increased delta ferrite phase percentage in the GTA weld bead, compared to that of NGLW[83]. The second reason is the accumulated plastic strain due to multi-pass thermo-mechanical influence [181].

In order to investigate the influence of the power and number of passes on the hardening behaviour of the NGLW technique, the hardness measurement was repeated for a NGLW specimen of 10 mm thickness with higher power 4 kW, welding speed 12 mm/s and filling passes 4 passes. Figure 8-12 shows the NGLW beads for different parameters. The average width of the weld beads was ~ 1 mm for low power higher number of passes, however it was ~ 1.75 mm for high power lower number of passes.

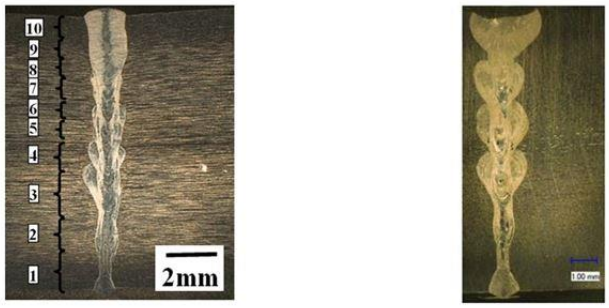

(a) Power = 1kW, speed = 9.5 mm/s (b) Power = 4kW, speed = 12 mm/s

Figure 8-12 NGLW 10 mm thick plates with different parameters

The peak value of the hardness was increased to 225 HV, and the hardened width region increased to 20 mm as shown in Figure 8-11. The results show that the power of the NGLW technique has a more significant influence on the width and magnitude of the hardened region than the number of filling passes.

8.5.1 Micro-hardness characteristics of two-sided welds

The distribution of hardness was investigated for the two-sided welding strategy. The results show M-shaped distributions for hardness in all cases (10 and 20 mm thick samples made with NGLW and GTAW processes) as shown in Figure 8-13. The welding parameters and number of filling passes were mentioned in detail in Chapter 7. The peak hardness values for the GTA welds in the 10 and 20 mm thick samples were approximately 255 and 260 HV respectively. The location at which the peak hardness arises is closer to the weld centreline for the 10 mm thick sample, being approximately 5 mm away in comparison to an offset of approximately 8 mm for the 20 mm thick sample.

The peak value of the hardness for the 10 mm thick NGLW sample with optimum welding parameters (according to results of optimization in chapter 6) was approximately 195 HV, while it is approximately 220 HV for the 20 mm thick NGLW sample. The peak hardness was offset from the centreline by approximately 2 mm at both thicknesses, as can be seen in Figure 8-13.

The hardening peak of the two sided welding strategy for the 10 mm, 20 mm thick plates is lower than the peak of the one side welding strategy for both welding

techniques. The overall hardening behaviour for NGLW shows a lower peak, and width of hardening region with respect to GTAW.

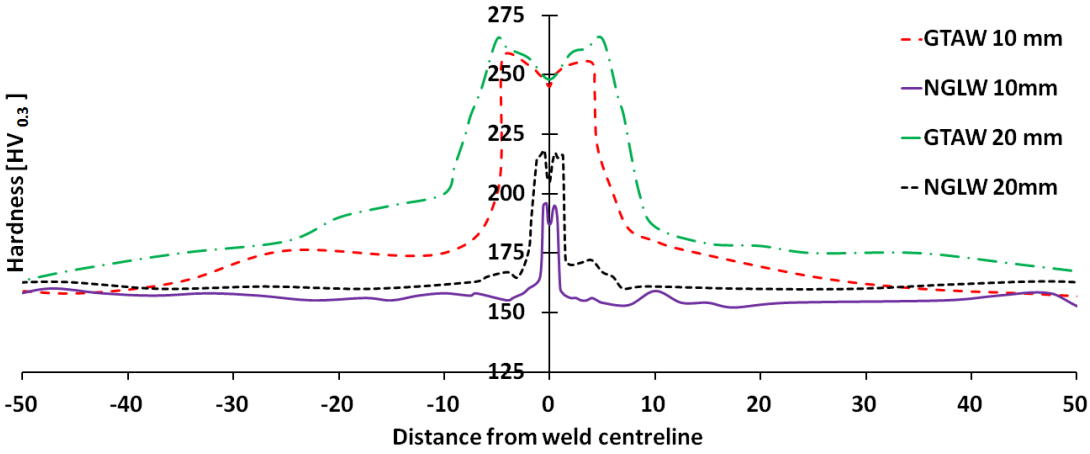

Figure 8-13 Hardness distributions for 10 and 20 mm thick two-sided NGLW and GTAW samples.

8.6 Estimation of Cumulative Plastic Strains in 10 mm Thick Welds

The thermo-mechanical cycling that occurs during multi-pass NGLW and GTA welding is sufficient to produce plastic strain [182]. This could lead to the rupture of the protective oxide film and, if a crack is initiated, a sustained tensile stress at the crack tip is likely to lead to crack propagation [183]. Plastic deformation has a significant influence on the susceptibility to SCC for "L grade" austenitic stainless steels [182]. Consequently, an investigation into the influence of plastic strain upon the hardness was carried out in order to assist in estimating the cumulative plastic strains across the welded joints. A set of tensile tests was carried out on coupons extracted from the parent material, with the tests being terminated at progressively increasing levels of plastic strain (1%, 3%, 5%, 9%, 15%, 30%, 70 % point of failure). The hardness values across the samples were recorded. The results reveal a similar trend to that reported by Katayama et al. [182]. Figure 8-14 shows the plastic strain – hardness relationship in the stainless steel parent material. Each point on this graph was obtained by taking the average value of hardness, as measured on three separate tensile test specimens, for each value of strain. The plotted relationship was then used to relate the hardness that was measured at each point across the welded joint to an estimate for the cumulative plastic strain at that location.

In Figure 8-11 the maximum value across the 10 mm thick NGLW one side strategy was 210 HV. This value would correspond to an estimated cumulative plastic strain of 8 % according to the data shown in Figure 8-14. The maximum value across the 10 mm thick GTAW sample was 260 HV. This value would equate to an estimated cumulative plastic strain of 19%. These results would suggest that the accumulated plastic deformation (or cold work) for the GTA welding process is higher than that in the NGLW. It could be inferred, therefore, that the GTA welding technique produces joints that will be more susceptible to SCC than the NGLW technique. This inference can be drawn from the combination of the higher residual stresses and the higher apparent level of plastic strain in the GTA weld. The double-sided welding strategy was also investigated using the same approach. According to the peak values of hardness shown in Figure 8-13, the accumulated values for plastic strain were lower for two-sided welding. For the 10 mm thick specimens the estimate for the accumulated plastic strain was 5% for NGLW while it was 15% for GTA welding.

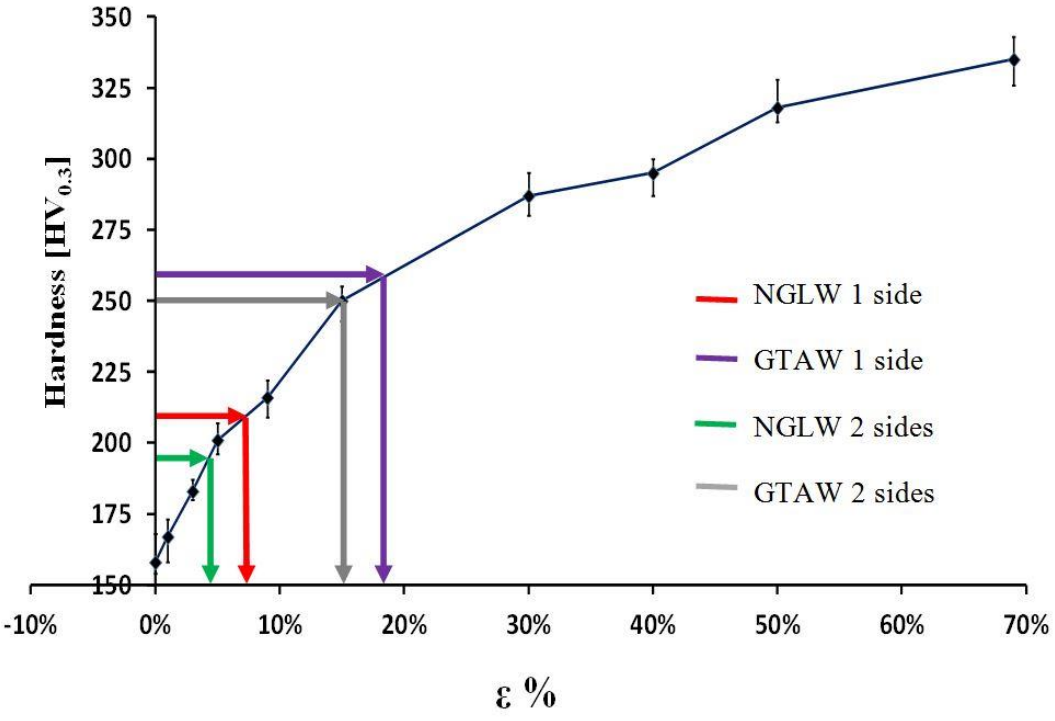

Figure 8-14 Variation in Vickers Hardness ($HV_{0.3}$) with homogeneous strain in tensile coupons extracted from AISI grade 316L base material. The peak hardness values for the 10 mm thick single-sided, double sided NGLW and GTA welding techniques are highlighted to give an indication of the accumulated cold work.

These results suggest that a double-sided welding strategy will lead to lower levels of accumulated plastic strain. Clearly, there are limitations associated with the above analysis. For example, the plastic strain - hardness relationship in Figure 8-14 was established based on the results of uni-axial tension tests, which had been carried out on coupons that were machined from material that was nominally homogeneous. In contrast, welded joints are heterogeneous and they are often associated with highly tri-axial stress states. Nevertheless, this analysis provides a useful qualitative comparison of the extent to which plastic strain is induced with each welding technique.

8.7 Fracture toughness test

Toughness is defined as the ability of a metal to deform plastically and to absorb energy in the process before fracture; in considering this definition, emphasis should be placed on the material's ability to absorb energy before fracture. Charpy V-notch impact toughness tests were conducted for the base material, NGLW and GTAW samples, according to ASTM E23 procedures. The dimensions of the samples were 55x10x10 mm, with notch depth of 2 mm, and the specimen length was oriented perpendicular to the length of the weld, with the notch at the weld centre line, as shown in Figure 8-15.

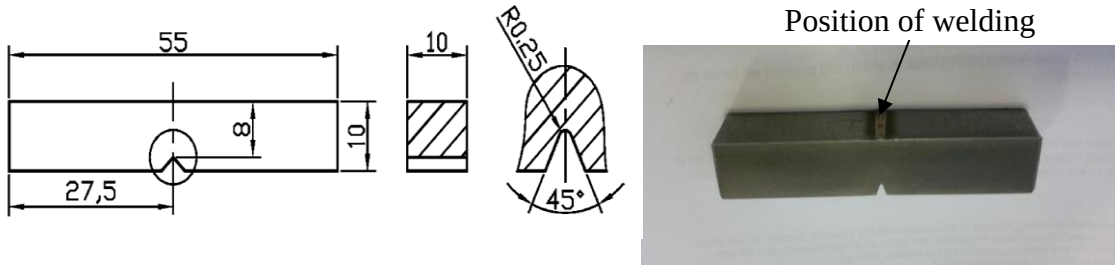

a standard dimension b) position of testing section

Figure 8-15 Charpy V-notch impact samples

The results of the Charpy impact test for different welding techniques are shown in Table 8-2. The average toughness of the optimum condition NGLW sample was 141.33J. This toughness value is very close to the base material toughness value. The GTAW sample represents slight lower toughness behaviour with respect to both NGLW and base material samples - the average GTAW toughness value was 134.3J. Decreased

ductility of the welded joints is considered the main reason of the decreased toughness behaviour for both GTA welding, and NGLW joints.

Table 8-2 Results of the impact test for the different welding techniques.

Sample ID	Consumed energy [Joule]	Notch toughness [J/cm^2]
Base(1)	147	183.75
Base(2)	142	177.5
Base(3)	145	181.25
Average Base	144.6	180.3
GTAW(1)	138	160
GTAW(2)	132	165
GTAW(3)	135	168
Average GTAW	134.3	164
NGLW(1)	136	170
NGLW(2)	145	181.25
NGLW(3)	143	178.75
Average NGLW	141.3	176.6

8.7.1 Fractography

The test specimen was sectioned in the direction of the crack extension, and the crack extension path was examined with a scanning electron microscope (SEM). Figure 8-16 displays the fractograph surfaces for impact tested specimens of the base material, GTAW, and NGLW joints. The fractographs invariably show dimples; these results indicate that all the test specimens failed in a ductile manner, as fracture by dimples and coalescence of micro voids and the fracture micro mechanism is indicative of ductile fracture. Finer dimples were observed in the base material joints and for the GTA welding technique, compared with the NGLW technique, which shows that the failure mode has a higher ductility behaviour in the base material than for GTAW [179], and even higher than for NGLW. The main reason for this is cold working which affect the ductility behaviour of the weld joint, and cause the precipitous decrease in tearing resistance[18]. These results are consistent with the previous fracture surface results of tensile testing for the different welding techniques.

The laser welding technique represents marginally improved toughness for the weld region, compared to GTAW. This is probably associated with the increased strength of

the laser weld due to the rapid cooling rates refined microstructure, and the ferrite content and its morphology, as will be discussed in the next section.

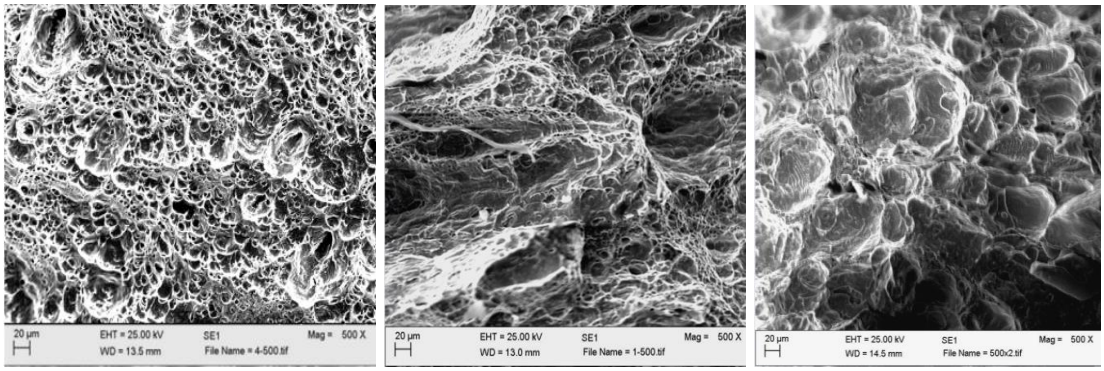

(a) Base material (b) GTAW (c) NGLW

Figure 8-16 Fractography of impact Charpy impact test

8.7.1.1 Influence of ferrite on the toughness

The delta ferrite content of a material, and its morphology, has a significant influence on weld toughness, especially at low temperatures [176]. Delta ferrite has a body-centred-cubic structure in the ferromagnetic phase; it is found in some of the most commonly used stainless steels in the 300-series, such as 316 and 308; its content depends on the alloy composition and the welding technique used. A small delta ferrite percentage in the welding bead often tends to reduce hot-cracking, which mainly occurs in some austenitic stainless steel weld metals. A small delta ferrite percentage has also been suspected of decreasing low-temperature weld toughness because of the low temperature brittleness of body-centred-cubic materials; the atomic structure provides a decreased ductility due to fewer planes for flow of dislocations. According to the XRD analysis for the percentage of the ferrite in the weld beads, GTA weld bead region has 3.64 %, and NGLW has 1.5% as will be mentioned in detail in Chapter 11.

The ferrite morphology is of interest for toughness behaviour [176]. The isolated patches of ferrite morphology as a result of laser welding may have a less harmful influence toughness than the semi-continuous network morphology found in GTAW, which offers a path for crack propagation as shown in Figure 8-17.

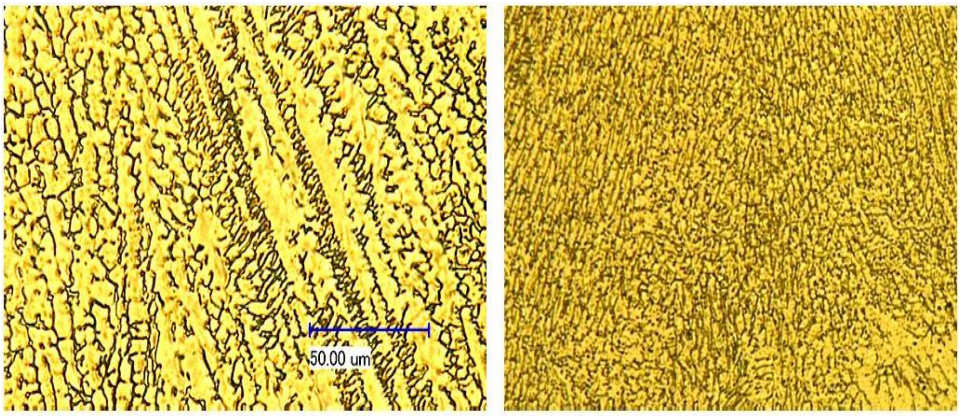

a) Semi continuous network GTAW b) isolated fine patches of ferrite NGLW

Figure 8-17 Delta ferrite morphology for welding techniques

8.8 Summary

This chapter includes a comparative study of the mechanical behaviour of NGLW, GTAW and autogenous laser welding. The results show that there are no absolutely favourable welding techniques, however laser welding offers some advantages compared with conventional GTA welding for thick cross section welding, due to the narrower weld fusion zone, narrow HAZ, and potential improved strength with respect to the base material. Tensile test results show a decreased failure strain for all welded joints; however the ductility and ultimate strength of the NGLW joint are higher than for the GTAW joint. Face and side bending tests were conducted to evaluate the weld bead soundness and ductility. All welded joints show a slight reduction in the fatigue performance with respect to base material. The accumulation of plastic strain due to thermo-mechanical cycling in GTA welding was higher than for NGLW, and a double-sided welding strategy led to lower levels of hardening in comparison to a one-sided welding strategy, for both welding processes. Charpy testing showed decreased toughness of the laser and GTA welded samples, with respect to the base material.

CHAPTER 9. MEASUREMENT OF RESIDUAL STRESSES IN MULTI-PASS WELDS

9.1 Introduction

Fusion welding processes generally involve material melting, phase transformations, and multiple thermal cycles. In the welding of thick components, localised heating or cooling cycles can lead to large thermal gradients. The non-uniform expansion and contraction of the material, when coupled with the material constraint in the bulk of a component, introduces misfit strains into the parts being welded. If these misfit strains are modest, they can be accommodated by the elasticity of the material; however if the misfit strains become too large to be elastically absorbed, localised plastic deformation is induced, which leads to the development of residual stresses. Significant residual stresses may therefore reside in the vicinity of the weld region after the component has reached thermal equilibrium [184].

Residual stresses can play a significant role in accelerating or delaying many failure processes [185, 186]. Residual stresses in welded joints are usually tensile in the fusion zone and heat-affected zone. Tensile residual stresses are of particular concern because they can contribute to fatigue crack development in a structure even under compressive cyclic loading [187]; they are also considered to be the main reason for the initiation and propagation of stress corrosion cracks (SCC) in austenitic weldments [180]; in addition, the kinetics of defect growth can be affected by residual stresses. Therefore, significant research effort has been directed to understanding the development of residual stresses in power plant welds [188].

The safe operation of a nuclear power plant is strongly dependent upon the application of robust structural integrity assessment procedures. The residual stresses arising due to welding operations can be critical in affecting the structural integrity of a power plant. Tensile residual stress in engineering structures generally has an undesirable effect on structure life time; it may be combined with the operating load of the component, or become in itself a source of crack initiation, especially for thick sections [10].

There are significant technical challenges associated with measuring residual stresses in thick-section welds [62]; without an accurate knowledge of the welding residual stresses, it is likely that conservative or incorrect assumptions will be made, which can ultimately limit the economical lifespan of power plants.

AISI 316L stainless steels are frequently employed in nuclear power plants, because they have a high resistance to SCC. The development of plastic strain and cold working in the vicinity of a welded joint can have a significant influence on the resistance to degradation by SCC in stainless steels [182]. Indeed, time-temperature-sensitization curves tend toward shorter times with increasing levels of cold working [189]. Thus, while the control and minimisation of residual stresses in welded joints is critical in designing against failure, and in improving the lifetime of engineering structures [181], residual stress mitigation techniques, such as shot peening, laser shock peening, and low-plasticity burnishing [190], can be difficult to apply to large components, and they will lead to increased cold working at the surface of the material.

Laser welding is an effective, low-distortion joining process, due to its combination of high welding speeds and low heat input to the weld joint. The development of residual stresses in autogenous laser welds has been investigated previously [67, 191]. However, multi-pass NGLW can also be an efficient process for the welding of thick-section components; Zhang *et al.*[60], and Starling *et al.* [150] demonstrated thick-section welding using a NGLW approach, and Zhang et al. [16] studied the feasibility of applying this technique to the welding of 50mm thick stainless steels using an 8kW laser. In another study, Salminen *et al.* studied the interaction of filler wire with the laser beam in a narrow-gap laser welding process *** [153, 154]. Despite NGLW being a very promising technique for thick-section welding, detailed through-the-depth residual stress investigations have not been reported in previous studies, although Zhang *et al.* [60] have investigated surface residual stresses by using the X-ray diffraction technique.

The aim of this chapter is to investigate the development of through-thickness residual stresses in NGLW of AISI 316L stainless steel. Three different measurement techniques are used for residual stress evaluation; contour method, X-ray diffraction, and neutron diffraction were carried out on the same specimens for the purpose of validation. In this study, the use of the NGLW technique for thicknesses up to 20mm were investigated,

and the results were compared with the residual stresses in conventional GTA welds for the same thickness. The influence of the welding strategy on the induced residual stress and the distortions associated with each technique were also compared. The influence of the power and number of passes on the induced residual stress are examined.

9.2 Contour method

The contour method is a stress-relaxation based technique for 2-D, cross-sectional residual stress evaluation; this technique is derived from Bueckner's superposition principles [192, 193]. Figure 9-1 presents an illustration of the main principles; they state that internal stresses are, in part, equal to the load required to revert the material to its original state. This superposition principle assumes that the material behaves elastically during the relaxation of residual stress.

Where

Residual stress distribution (A) = Stress relieved half (B) + Force required to return deformed surface to original values (C).

$$\sigma_{(A)}(x,y,z) = \sigma_{(B)}(x,y,z) + \sigma_{(C)}(x,y,z) \qquad (9.1)$$

However, the created surface due to cutting is stress free $\sigma_{(B)}$ (x,y,z) = zero [193]. Consequently, the stress inside the sample will equal to force required to return it back to original value.

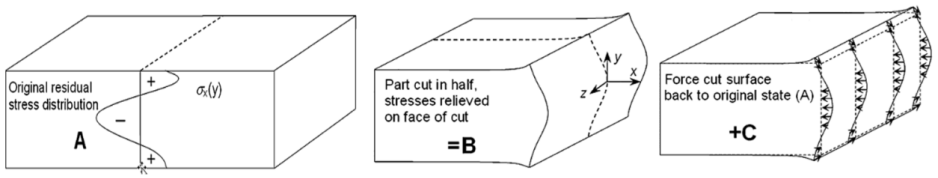

Figure 9-1 Bueckner's principles [71, 193].

The contour method involves measuring the deformations that occur, due to the relaxation of stresses, when a component is cut in order to evaluate the residual stresses that existed within the component before the cut has been done. This method allows to measure the component of residual stress that acts in a direction normal to the plane of the cut, over the expanse of the cut surface – i.e. it provides a two-dimensional map of

residual stresses. The potential of the contour method was demonstrated on a 12-pass GTA weld, where complex stress variations were captured across the weld cross-section [194]. The results obtained with the contour method were in acceptable quantitative agreement with the outcome of non-destructive measurements based on X-ray diffraction. Many researchers, including Kartal *et al.* [195], Withers *et al.* [196] and Edwards et al. [5], have used this technique successfully for the evaluation of the residual stresses in various welds. Although the contour method is destructive, it has the potential to measure a full cross-sectional profile of residual stresses in a relatively cheap and time-efficient manner [192].

It can determine an arbitrary cross-sectional area map of residual stress directly from cut profiles without the need for time-consuming inversion techniques. A limitation of the original contour method is that only one residual stress component can be determined, however there are recent studies that expand the contour method application to include measurement of multi-components of residual stresses [193, 197].

9.3 Contour method Procedures

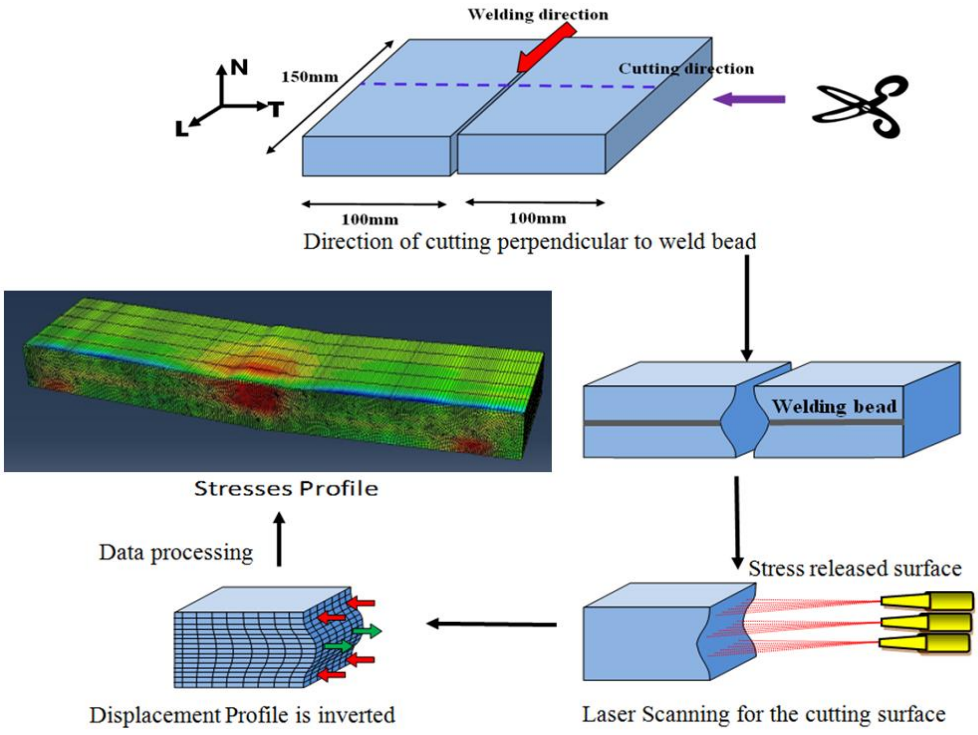

Figure 9-2 An overview of the steps in the contour method for residual stress measurement

There are three main steps used to evaluate residual stress using the contour method [198] as shown in Figure 9-2. The first stage involves cutting the workpiece under study in to two parts at the plane of interest for residual stress measurement. The cutting process is mainly by using a skim cut with electric discharge machining (EDM), as the technique must not apply additional stresses during the cutting process [192] - EDM represents the best technique to create the free-surface cut.

The second step is surface profile scanning to determine the deformation due to stress relaxation. The contours of the two opposing surfaces created by cutting are measured by using contouring measuring machine (CMM) or non-contact laser scanner.

The third step is to pass the data to a finite element model for processing the scanned surface data (cleaning noise, smoothing the scanned surfaces and averaging data). Once this is completed, the data is ready to be used to calculate the residual stress values in the opposite sign to the surface scanning, as will be discussed later in more detail.

9.4 Experimental procedures for the contour method measurements

9.4.1 EDM skim cutting

In order to carry out contour method measurements, the stresses that are introduced to the surface during cutting should be minimised. The material removal process must not introduce stresses of sufficient magnitude to affect the measured displacements, and must make a precisely straight cut without removing any further material, and without causing plastic deformation. The EDM method is the closest to ideal [192].

Figure 9-3 EDM wire cutting machine

Quality of the EDM cut made has a significant and direct influence on both accuracy and resolution of the contour method [198]. The cutting of the samples examined here was done by using a GF Agie Charmilles “F1 440 ccs” wire EDM, as shown in Figure 9-3 a 250 μm diameter pure brass wire was used as a cutting tool, and “Skim cut” settings were applied (minimum applied voltage with minimum cutting speed) to ensure minimum stresses were introduced to the surface during the cutting process, and to ensure the minimum possible recast layer [199].

9.4.2 Laser scanning of the cut surface

Figure 9-4 Nano laser scanner for relaxed surface scanning

A laser scanner with a non-contact laser head was used for scanning the EDM cut surfaces. The profile of each surface was scanned with scanning pitch of ±10 μm space by using a nano laser scanner head, as shown in Figure 9-4. The scanned profiles showed small deformations due to the relaxation of residual stresses; for example, the dashed line in Figure 9-5 represents the edge of the work piece before distortion due to the welding process. The induced distortion is clear in Figure 9-5 , which shows that the sample has “butterfly” distortion. The contour data for all points on the surface were scanned and saved in the form of $z = f(x, y)$. The scanning was then repeated on the other half of the work piece, before the data were input to a stress analysis module in ABAQUS 6.12-2, in order to calculate the residual stresses.

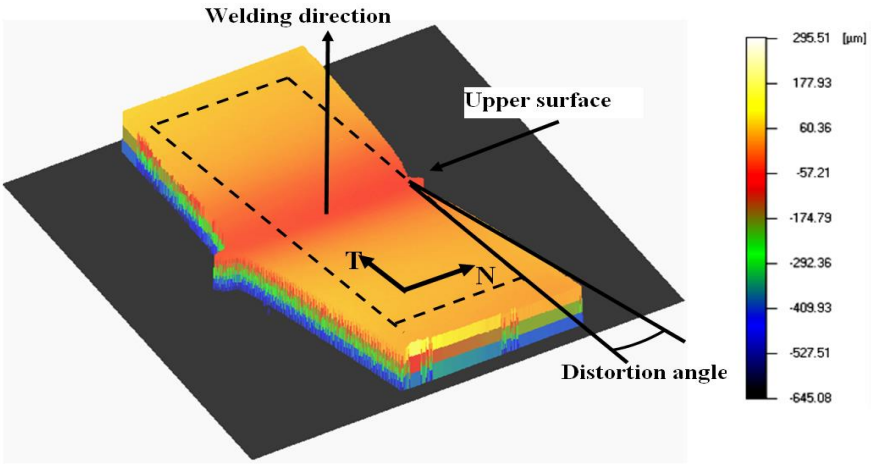

Figure 9-5 A scanned surface profile for a GTA weld.

9.4.3 Data processing

The raw displacement data for the two halves of the cut were averaged, in order to remove any sources of anti-symmetric error sources as will be discussed in detail in next section.

The next step was to smooth the data, through the creation of a least-squares spline curve fit, to improve the sensitivity of final results of residual stress, and eliminate errors associated with cutting stresses, and from the measurement conditions. This step is crucial if an accurate evaluation of stresses is to be achieved with the contour method [72]. Figure 9-6 shows examples of both rough and smoothed scanned surfaces.

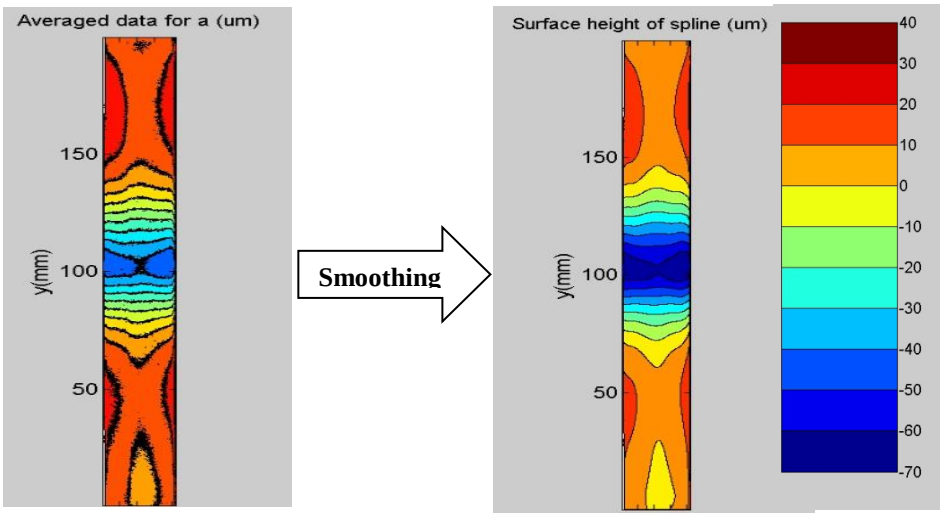

Figure 9-6 Contour maps of (a) rough surface contour (b) smoothed spline fit.

Stress analysis is the final step. The smoothed spline surface was input to a finite element (FE) model to create displacement boundary conditions. The material is assumed to have isotropic elastic properties. An arbitrary plane was defined, which represented the initial cut surface, and this was assumed to be perfectly flat. The stress field on the cut surface was calculated as a function of the deformation distance (with the opposite sign), using appropriate material properties for AISI 316L stainless steel. The Young's modulus of the material was assumed to be 193 GPa, with a Poisson ratio of 0.3. The mechanical boundary conditions (restraint) were imposed to avoid motion of rigid body. The FE model was developed using ABAQUS 6.1-CAE.

9.4.4 Challenges and error sources in the contour measurement process

Cutting of a stressed body into two halves can result in asymmetric surfaces, which consists of symmetric and anti-symmetric contour portions [198] as shown in Figure 9-7. There are several reasons for developing anti-symmetric surfaces such as, shear stress in the cut body, a crooked cut, movement of the cut plane due to stress relaxation and asymmetric restraint during the cutting operation (eg. clamping one half of the component during EDM cutting process) [71, 198]. The influence of the anti-symmetric surfaces can be reduced or removed by averaging the two mating cut surfaces. Clamping on both sides during cutting has a significant influence on decreasing the source of most anti-symmetric errors helping to ensure a straight pass of the cutting direction [71, 200].

The sources of symmetric surface contour features are: local cutting irregularities (wire over burn), wire vibration, and stress induced due to the cutting process. These errors could be avoided by using proper parameters for EDM cutting process. Cutting tip plasticity is violating the assumption of elastic stress relaxation. Bulge error is mainly due to tip cut deformation and stress relaxation, which affects the width of the cut. An FEM study showed that both plasticity and bulge errors are generally small when clamping the specimen during cutting [201].

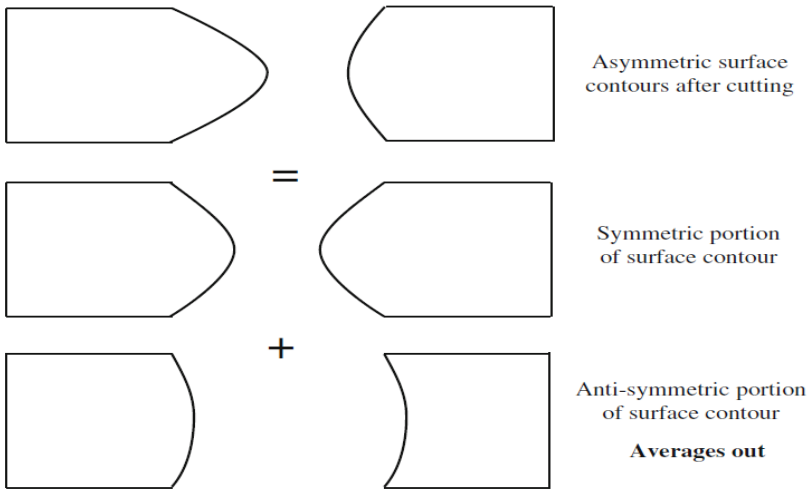

Figure 9-7 Asymmetric surface contour (symmetric and anti-symmetric) portions [71]

A rigid fixture has been designed with a suitable longitudinal through-groove for clamping the workpiece during the EDM wire cutting process to prevent misalignment of the cutting pass, due to stress release, as shown in Figure 9-8.

Any sources of symmetric or non-symmetric deformation, which could not be recovered partially or totally by optimizing EDM cutting conditions or the averaging process or by using a rigid clamp will contribute directly to uncertainties in the residual stress measurement by the contour method [198]. There are disturbances of the cut width near to the cutting edges. The EDM cut width may flare out at the wire entry and wire exit interfaces [71]. This can be considered a source of uncertainty for the contour method near to the edges of the cut.

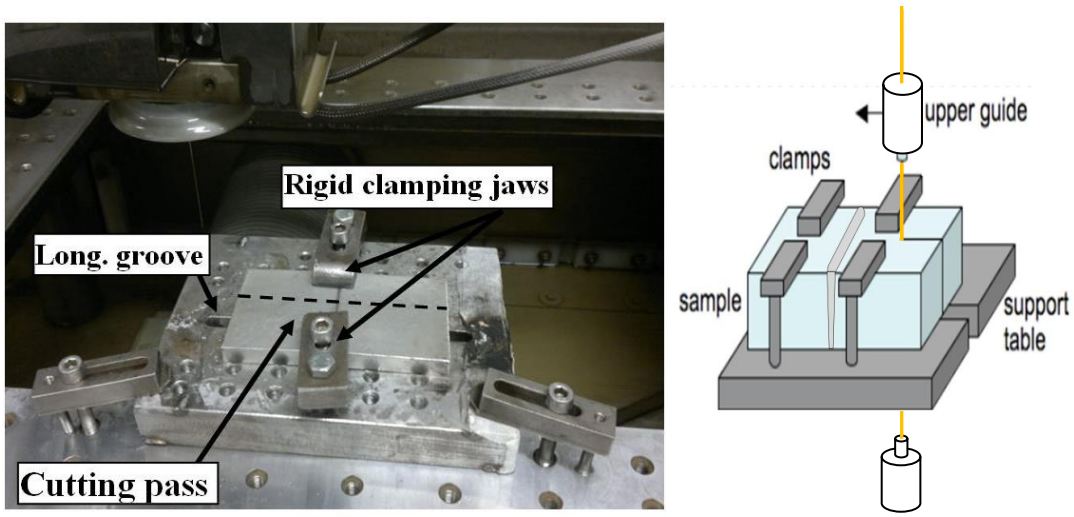

Figure 9-8 Rigid clamping fixture during EDM cutting

9.5 Results and Discussions

The 2D residual stress profiles through the thickness of the welds were compared in order to understand the influence of the different thermal cycles on the residual stresses. The investigation will include different thicknesses 3, 10, and 20 mm. The influence of the welding strategy (i.e. one-sided or two-sided welding) and the degree of constraint were also investigated. The influence of the power and number of filling passes for NGLW technique is also investigated.

9.5.1 Residual stress investigation for 10 mm thick samples

9.5.1.1 Residual stress in 10 mm thick single-sided GTA weld

Figure 9-9 shows the distribution of longitudinal residual stresses for the single-sided GTA weld. The residual stress distribution is approximately symmetrical about the weld centreline. The stresses in the vicinity of the weld centreline are highly tensile, with the peak tensile stress being close to 500 MPa in magnitude. The peak stresses occur at a location 2 mm below the top surface of the weld, and the stresses decay gradually with increasing distance from the weld centreline. It is not surprising that the peak tensile stresses occur closer to the upper surface of the specimen, since this is the side of the specimen from which heat was applied during welding. Twelve weld passes were required to fill the weld groove, as can be seen in Figure 7-5 b. The width of the area with a tensile residual stress is approximately 75 mm, and the butterfly distortion angle was 3.9 º as shown in Figure 9-9.

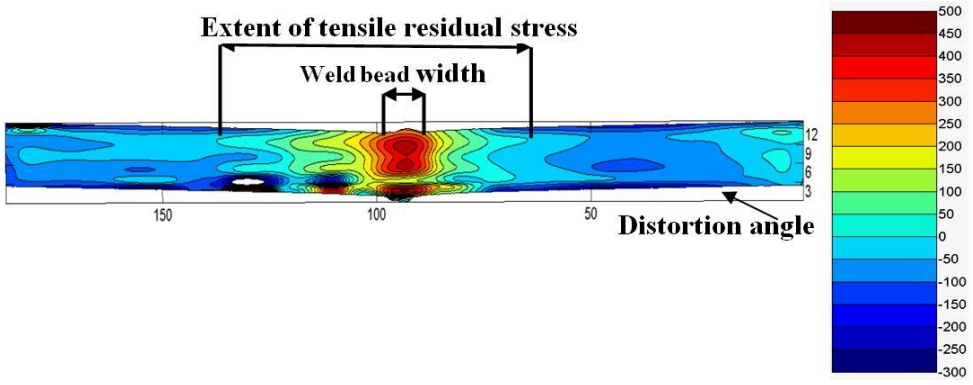

Figure 9-9 Residual stress distribution for 10 mm thick single-sided GTA weld (in MPa)

9.5.1.2 Residual stresses in 10 mm thick NGLW

Figure 9-10 shows the distribution of longitudinal residual stresses for the single-sided NGLW sample. It can be seen that the residual stresses for the NGLW are lower than those for the single-sided GTA weld, and the residual stress distribution is approximately symmetrical about the weld centreline. The stresses in the vicinity of the weld centreline are tensile, but the peak tensile stresses are closer to 300 or 350 MPa in magnitude, and they occur approximately 3 mm below the upper surface of the specimen on the weld centreline. Four passes were required to fill the lower half of the groove, while six passes were required to fill the upper half, as can be seen in Figure 7-5 a. The tensile stresses decreased rapidly with distance from the weld centreline, and compressive stresses were measured over significant areas of the measurement plane. There are three reasons for the decrease in the magnitude of residual stresses in the plate joined using NGLW. Firstly, the laser is a high power-density heat source with a very small spot diameter (the spot size was approximately 70 μm). Secondly, the welding speed (590 mm/min) was very high compared with that for the GTA weld (130 mm/min), and finally the average width of the weld groove was very small (~ 1.5 mm) as can be seen in Figure 7-4 a. As such, the volume of filler metal required to fill the groove with laser welding is lower than for GTA welding. Consequently, the number of passes and the cumulative heat input to the weld were lower for laser welding than for GTA welding. The width of the tensile region was approximately 15 mm for the NGLW technique, and it decreased towards the upper surface as shown in Figure 9-10. The magnitude of the stresses was close to zero toward both edges of the specimen, and the butterfly distortion angle was 1.8º. A detailed comparison of the results for each welding process is presented in the next section.

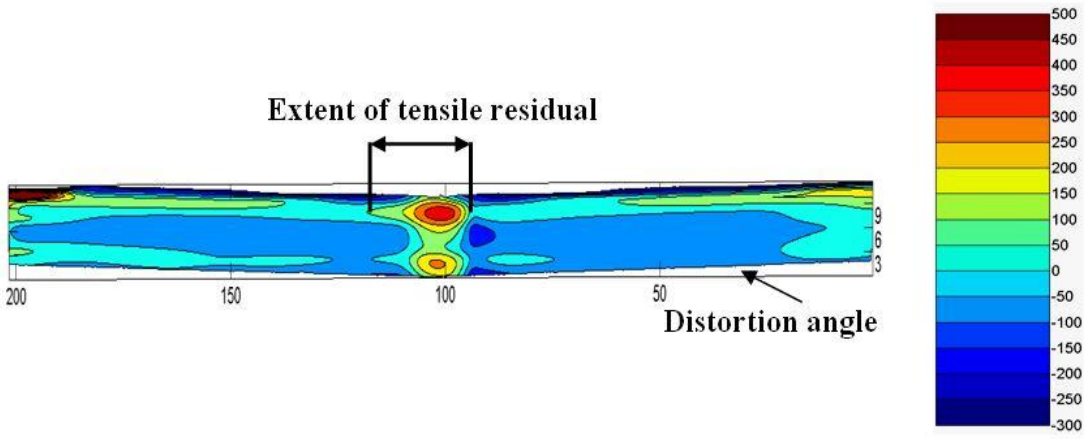

Figure 9-10 Residual stress distribution (MPa) for a single-sided NGLW joint.

9.5.1.3 Residual stresses 2 mm below the top surface for 10 mm thick GTA weld and NGLW

Figure 9-11 shows a comparison of the residual stress profiles for the NGLW and GTA welding processes, measured along a line 2 mm below the upper surface with the contour method. The results suggest that the NGLW technique induces lower residual stresses over the entire width of the specimen. The maximum tensile stress for the NGLW was 310 MPa. The tensile stresses for this process decayed sharply with distance from the weld centreline, to a value close to zero, at a distance of approximately 10 mm from the weld centreline.

The peak tensile residual stress for the GTA weld was 520 MPa, and the width of the tensile region was approximately 60 mm. The tensile stresses at the weld centreline were approximately 40 % lower for the NGLW sample than for the GTAW sample. Figure 9-11 shows that the distribution of residual stresses is approximately symmetrical about the weld centreline for both processes, with peak stresses occurring at the weld centreline, and with the stresses gradually decreasing until they become compressive further from the weld centreline, which is in agreement with results of previous studies of GTA welding [186].

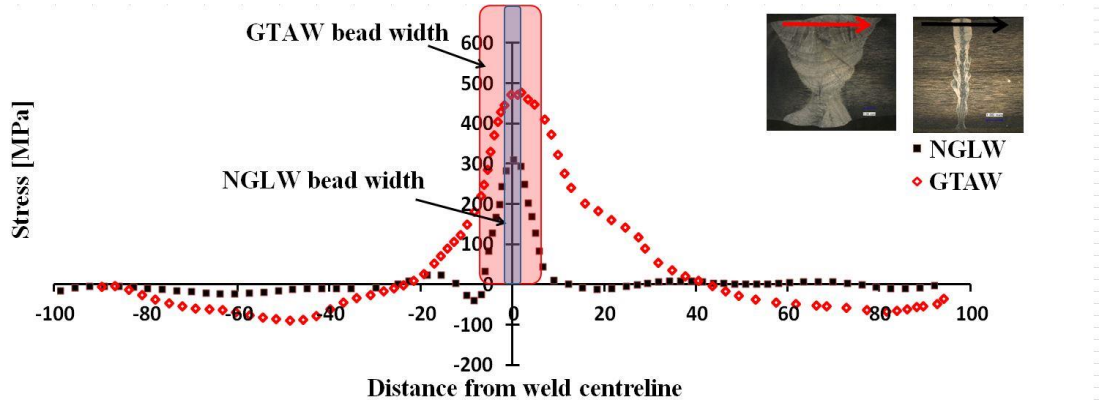

Figure 9-11. Residual stress distributions 2 mm below the top surface of the 10 mm thick specimens for the NGLW and GTA welding processes

The analysis of the residual stress distribution in the mid-section, for both techniques, shows the NGLW technique also exhibits a lower stress distribution as shown in Figure 9-12. The tensile stresses at the weld centreline were approximately 70% lower for the NGLW sample than for the GTAW sample. The peak value for GTA welding is 450 MPa, whereas it is 150 MPa for NGLW. The width of the tensile region is 60 mm for GTA welding, whereas it is only 20 mm for NGLW.

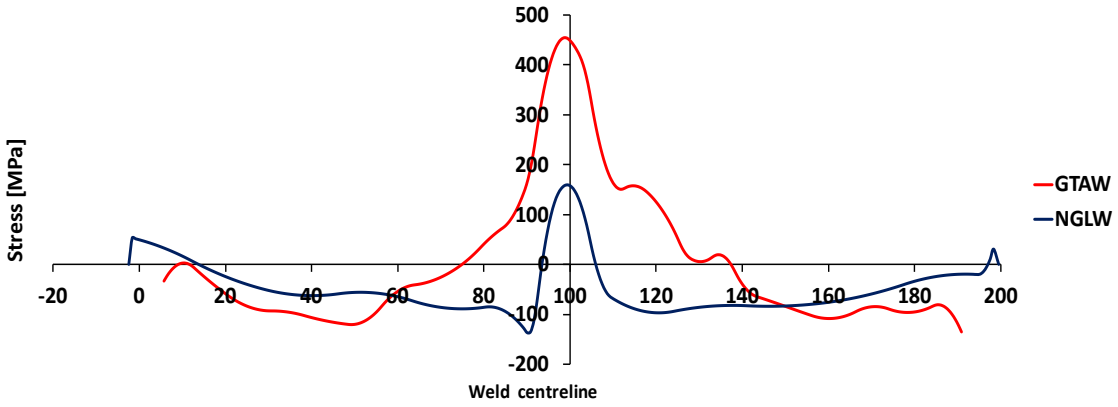

Figure 9-12 Residual stress distribution at mid-depth for NGLW, and arc welding

9.5.1.4 Residual stress distribution on the weld centreline

The variation in residual stress values along the weld centreline, as measured with the contour method, was investigated as shown in Figure 9-13. The red and blue arrows highlight the locations of the measurement lines, and the direction corresponding to an increase in the distance parameter on the horizontal axis, for the GTA and NGLW

samples respectively; there are similar features in the residual stress distributions for each sample. Starting from the lower surface of each sample, the residual stress increases up to an initial peak value, which is approximately 550 MPa for the GTA weld and 250 MPa for the NGLW. With increasing distance from the bottom surface, the stress decreases to approximately 100 MPa for NGLW, and 150 MPa for the GTA weld, at mid-section. In both samples, the stresses then increase again to the second peak, which is approximately 500 MPa for the GTA weld and approximately 400 MPa for the NGLW. Finally, the stresses decrease in both samples towards the top surface, having values of approximately 330 MPa for the GTA weld and 125 MPa for the NGLW. Overall, the average residual stress values are significantly lower in the NGLW.

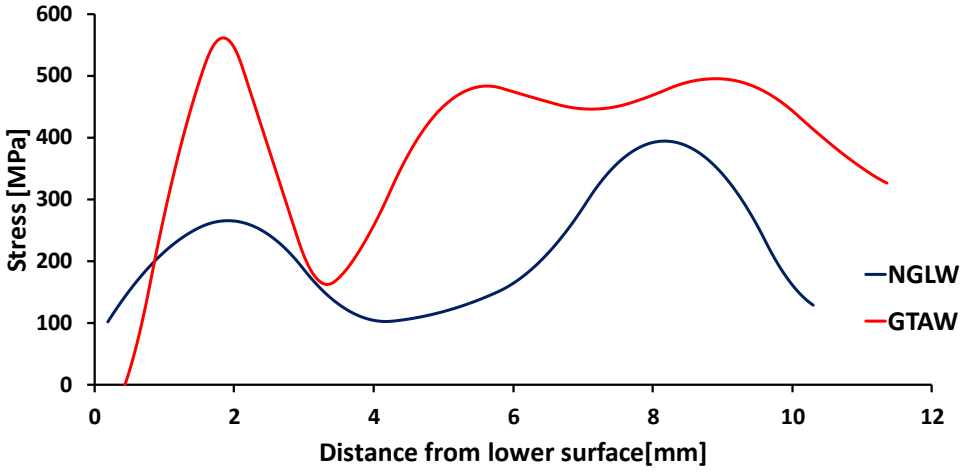

Figure 9-13 Variation in residual stresses along the weld centreline for the NGLW and GTAW samples

9.5.2 Stress validation using X-Ray diffraction

Residual stress evaluation of welded joints is a complicated process, due to the severe thermal cycles involved, coupled with welding restraint, which can cause the workpiece to have multi-axis strain components; in addition, phase transformation during solidification can cause further complexity. Consequently it is very important to validate the results of the stress distribution analysis across the welded joint. Despite X-ray diffraction being an efficient technique for residual stress evaluation [202], limited penetration is considered a significant limitation when used with thick

samples [62, 73]. X-ray diffraction will be used for measuring the residual stress distribution of the NGLW technique at the surface only. The results will be compared to the contour method of residual stress distribution for the NGLW technique, in order to validate the results of the technique.

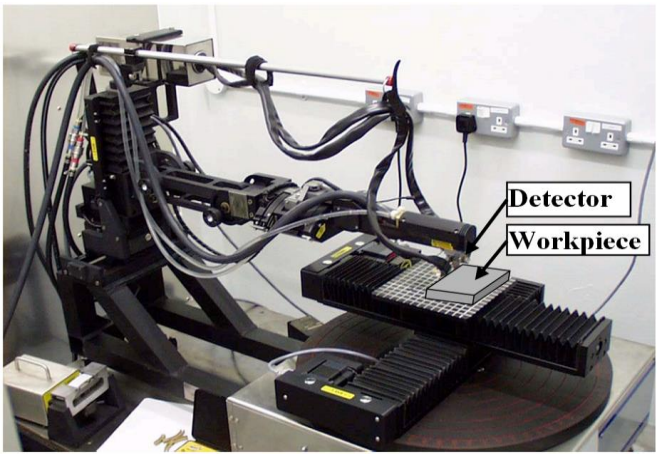

Figure 9-14 Proto-I XRD, residual stress instrument

The Proto i XRD residual stress instrument was used for residual stress evaluation on the surface of the welded samples as shown in Figure 9-14. The longitudinal residual stresses on the upper surface of the NGLW specimen, as measured by the contour method and XRD, are depicted in Figure 9-15 - the highest value of tensile stress at the upper surface was 190MPa.

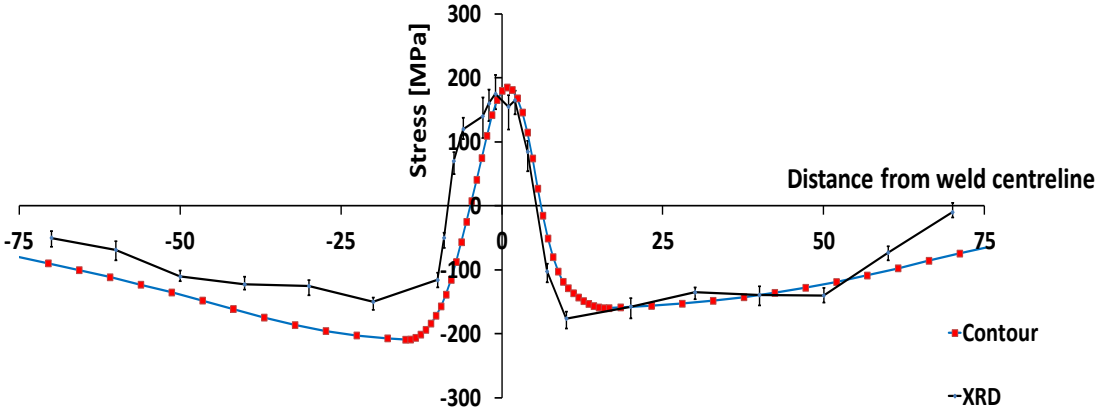

Figure 9-15 Comparison of residual stress profiles at top surface of 10 mm thick NGLW plate, as measured with the contour method and X-ray diffraction.

Figure 9-15 shows that there is good agreement between the stresses measured with the two measurement techniques. It is evident that both techniques capture similar distributions for the longitudinal stresses, with the maximum tensile stresses coinciding with the weld centreline. The stresses quickly become compressive with increasing distance from the weld centreline, and then decay towards the far edges of the specimen. There are small discrepancies in the stress values on the left hand side of the plot. These discrepancies may have arisen, in part, due to the distortion of the welded specimen, which may have affected the accuracy of the XRD measurement on this side of the sample, however, the results achieve acceptable agreement across the welded joint.

9.5.3 Influence of welding strategy on the induced residual stress

The results that have been discussed thus far were all based on welding from a single side. When welding was performed from both sides as shown in Figure 7-6 the NGLW technique needed 4 passes from each side to fill the gap, with the same parameters that were used for the single side welding, and the GTA welding needed 4 passes from each side to fill the gap. The combined welding needed 2 root passes with autogenous laser welding and 2 filling passes with GTAW from each side.

The joint preparation for the welded joints was similar to the single-sided weld preparations. The results for the three welding techniques show approximately symmetrical residual stress profiles with respect to weld centreline. The magnitude of the residual stresses is noticeably lower for the NGLW technique, the tensile region is very narrow, with a width < 5mm, and there are two peaks of tensile residual stress on the weld centreline. The peak value for NGLW is 300-350MPa, as shown in Figure 9-16 a. The residual stress distributions for the GTA weld reveal highly tensile peaks, with a magnitude of 500MPa, as shown in Figure 9-16 b. In contrast, the width of the tensile region for GTAW is approximately 50mm.

Combined laser GTA welding demonstrates a lower stress distribution in comparison with GTAW. The peak value is 450MPa, and covers a very small area, outside of this area, the stress is decreased to zero, and then becomes highly compressive in a very small width - especially in the mid-section - due to low heat input in the mid-section, as shown in Figure 9-16 c.

The two-sided welding strategy resulted in a decrease in the number of passes required to fill the gap for all welding techniques; on the other hand it, requires accessibility to both

sides of the weld joint. This strategy has a significant influence on reducing the magnitude of the residual stresses for the NGLW method, but the influence was insignificant for the GTA welding technique. Finally, it can be seen that using the two- sided welding strategy leads to a reduction of the distortion angle to almost zero for both welding techniques.

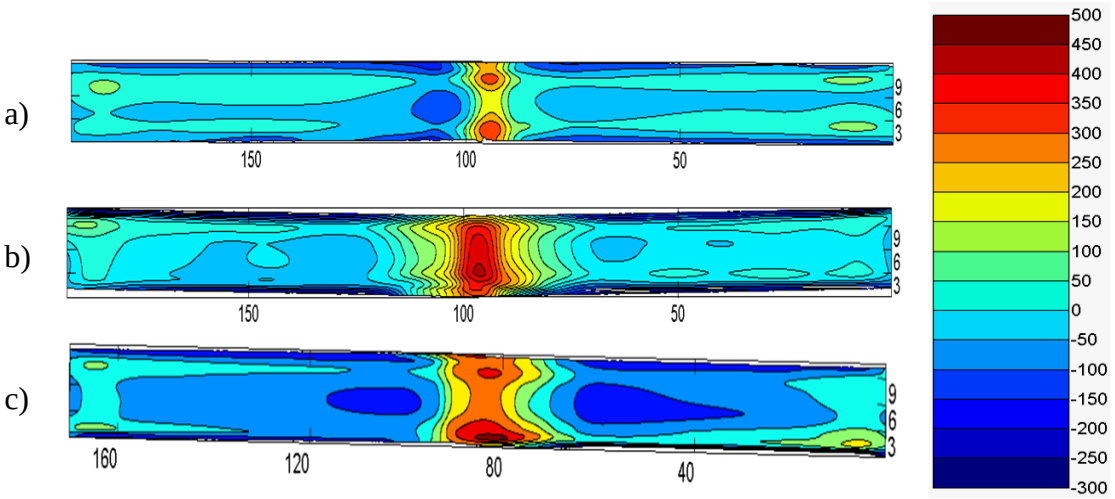

a- NGLW b- GTA welding c- Combined laser-GTA welding

Figure 9-16 Residual stress distributions in 10 mm thick plates for two-sided welding strategy (MPa)

9.5.4 Influence of restraint on induced residual stresses

This part of the study investigates the influence of the degree of restraint on the nature of the longitudinal residual stresses in the weld joints. Figure 9-17 shows the residual stress distributions for unrestrained NGLW and GTA welds made from one side. These results show approximately symmetrical residual stress distributions with respect to the weld centreline. The NGLW residual stress distribution is shown in Figure 9-17 a. The peak residual stress value is 450 MPa. The distortion angle is 9.5 º and the width of the tensile residual stress region on the weld surface is very narrow, around 10 mm. The GTA welding residual stress distribution is shown in Figure 9-17 b. The peak residual stress value is ~ 550 MPa, and the distortion increased dramatically to 37.2 º. The combined laser arc welding technique shows a lower stress peak and lower distortion. The peak value is 450-550 in a very limited region, while the distortion angle is decreased to 13 º as shown in Figure 9-17 b.

The overall influence of the restraint is not significant for the peak value of the longitudinal component of residual stress for both NGLW, and GTAW. The average increase of the stress is ~ 50 MPa compared to restrained conditions. The significant influence is expected in the transverse component of residual stress, and is expected to be more significant in GTAW due to the dramatic increase in distortion angle found for the unrestrained cases as shown in Figure 9-17. Although decreasing the level of restraint results in an increase in the residual stress peaks, the NGLW technique still leads to a significantly lower peak, and smaller tensile regions compared to those produced by GTA and combined welding.

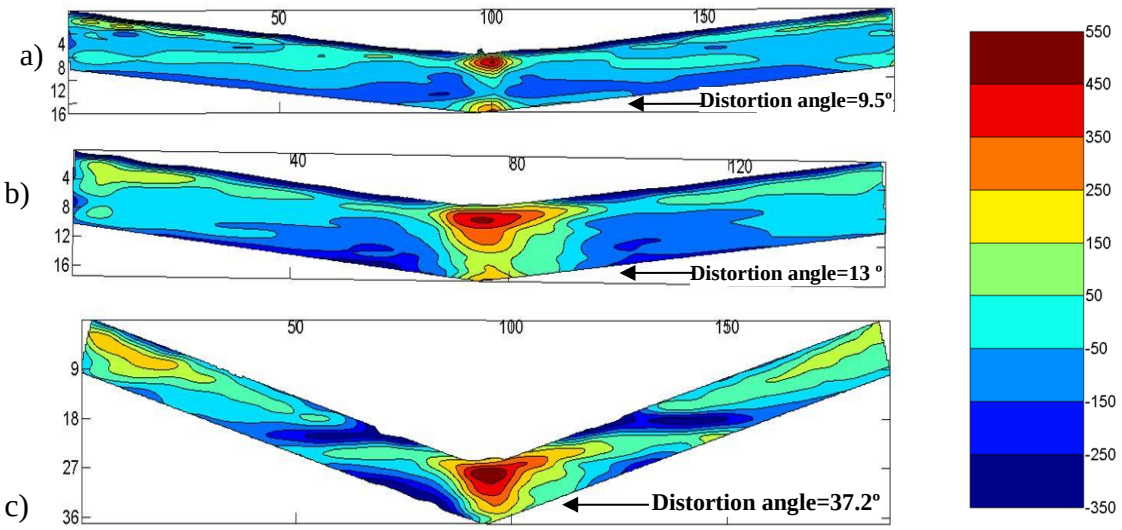

a) NGLW b) combined laser GTA welding c) GTA welding

Figure 9-17 Residual stress profiles for 10 mm thick unrestrained plates

9.5.5 High power autogenous laser welding

One pass high power autogenous laser welding was performed on 10 mm-thick plates. The residual stresses were evaluated for the weld cross-section, using the contour method. The welding parameters were: power = 7.5 kW, welding speed = 10 mm/s. The results show a high tensile peak of around 650 MPa at the weld bead region, as shown in Figure 9-18. High- power input with relatively low speed, and the high thermal expansion coefficient of the stainless steel is the main reason for the increased stress associated with this technique. The residual stress behaviour by using contour method has sources of uncertainties for the results near to the edges, however it is believed to

have an acceptable accuracy for the general behaviour of the stress distribution across the welding joint on the basis of quality evaluation with respect to other welding techniques. Moreover the stress distribution across the weld sample will be validated by using a neutron diffraction technique in the next sections.

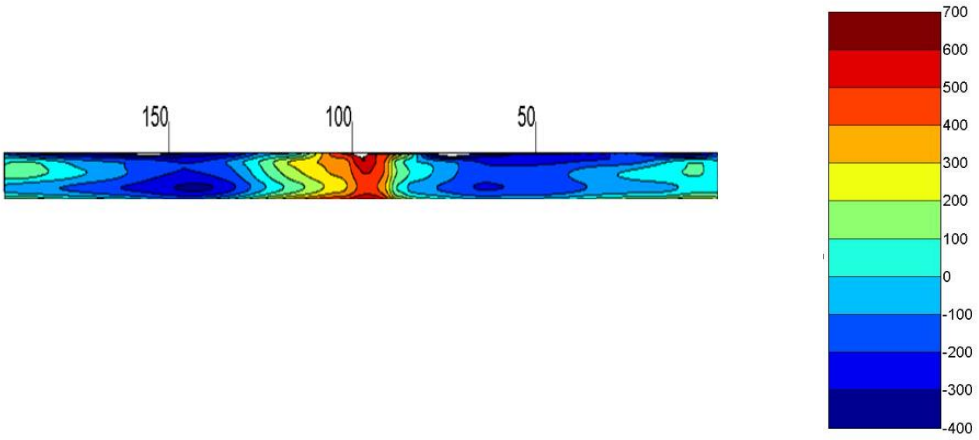

Figure 9-18 Stress profile for one pass autogenous laser welding for 10 mm thick plate

9.5.5.1 Influence of the welding parameters on the residual stress distribution of autogenous high power laser welding

The influence of the power and speed has been investigated for the residual stress distribution of the high power autogenous laser welding for 10 mm thick plates. The welding parameters changed as following; power has been decreased to 5 kW, and welding speed has been increased to 16 mm/s. According to experimental investigations these parameters were sufficient to satisfy a full penetration of 10 mm thick plates. The longitudinal stress distribution across the weld specimen has been evaluated. The results show that both the peak stress value and width of the tensile region have been decreased as shown in Figure 9-19 .

A comparison between residual stress distributions for the two welding parameters at 2 mm below the top surface is shown in Figure 9-20. The results show that the peak stress value for high power, low speed was ~ 625 MPa and the width of the tensile region was ~ 50 mm. These values decreased to ~ 420 MPa peak stress, and 40 mm tensile region width at lower power 5 kW, and higher welding speed = 16 mm/s as shown in Figure 9-20. The results show that the welding power and the welding speed has a more

significant influence on the stress peak as it decreased by 33% however the width of the tensile region decreased by 20%.

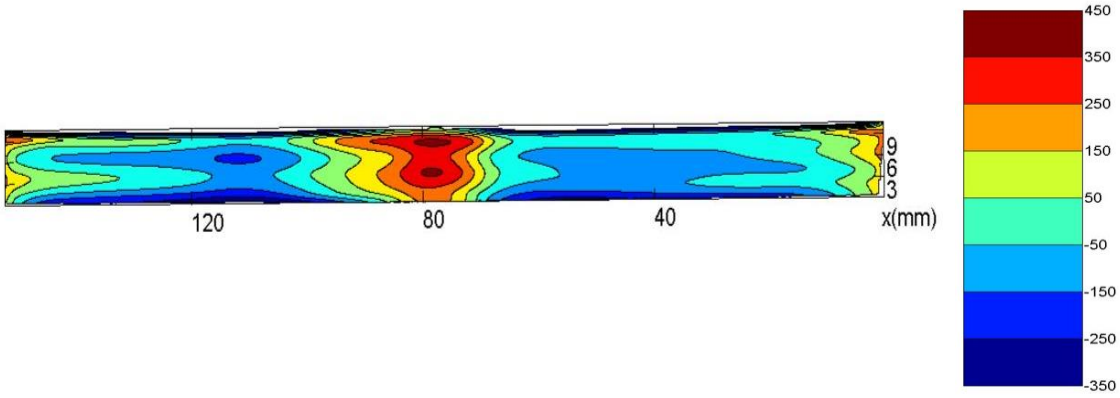

Figure 9-19 Stress profile for one pass autogenous laser welding for 10 mm thick plate low power – high speed

Consequently it is recommended, in terms of induced residual stress, for autogenous laser welding to use lower laser power with high speed sufficient to satisfy a full penetration.

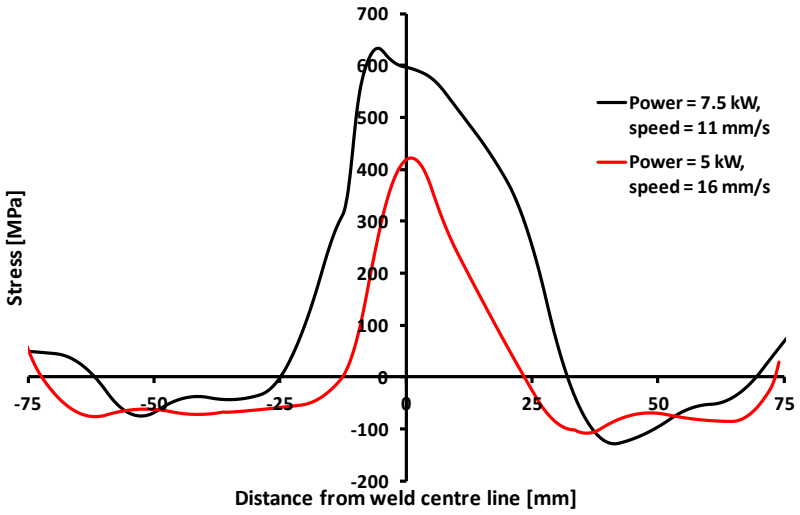

Figure 9-20 Residual stress profile at 2 mm below the top surface of different welding parameters for autogenous high power laser welding technique

9.5.6 Investigation of residual stress for 3mm thick sheet

Welding 3 mm thickness sheets has been carried out using NGLW, autogenous laser welding, and GTA welding. Details of welding parameters for each technique are

mentioned previously in chapter 7. There are limitations for the quality of the results of contour method for thin cross-sections, however it will be used for comparative evaluation between different welding processes. Figure 9-21a shows a profile of the residual stress across a GTAW bead. Figure 9-21 b, c show residual stress values across NGLW and autogenous laser welded samples. The results show peak residual stress value (≈ 300 MPa) along the upper surface of the weld joint for both NGLW, and autogenous laser welding cases. The peak value of GTAW is ~ 350 MPa and on the surface of the welding joint. Distortion of both laser welding techniques samples is approximately equal to zero, however the distortion angle for the GTA welding sample is 4 º as shown in Figure 9-21 a.

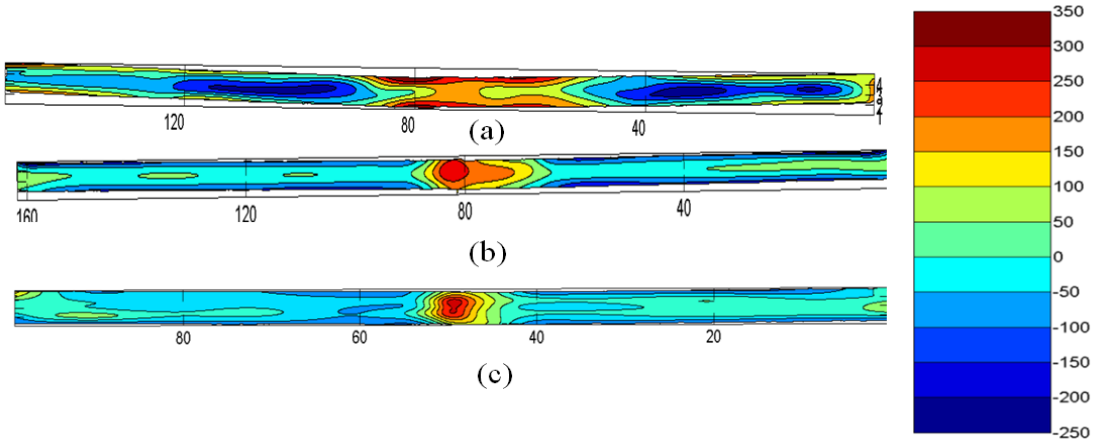

(a) GTAW (b) NGLW (c) Autogenous laser welding

Figure 9-21 Residual stress profile of 3 mm thick sheet

Figure 9-22 shows a comparison between the stress profiles for the three welding techniques 1 mm below the top surface. The width of the tensile region was ~ 10 mm for autogenous laser welding, and ~ 20 mm for NGLW, and ~ 40 mm for GTAW. It is very clear from the three profiles that the three techniques have approximately the same peak; however the width of the tensile region is greater in GTAW as shown in Figure 9-22. Generally the autogenous laser welding technique represents the narrowest tensile region with respect to other welding techniques. That is mainly due to high traverse speed during the welding process.

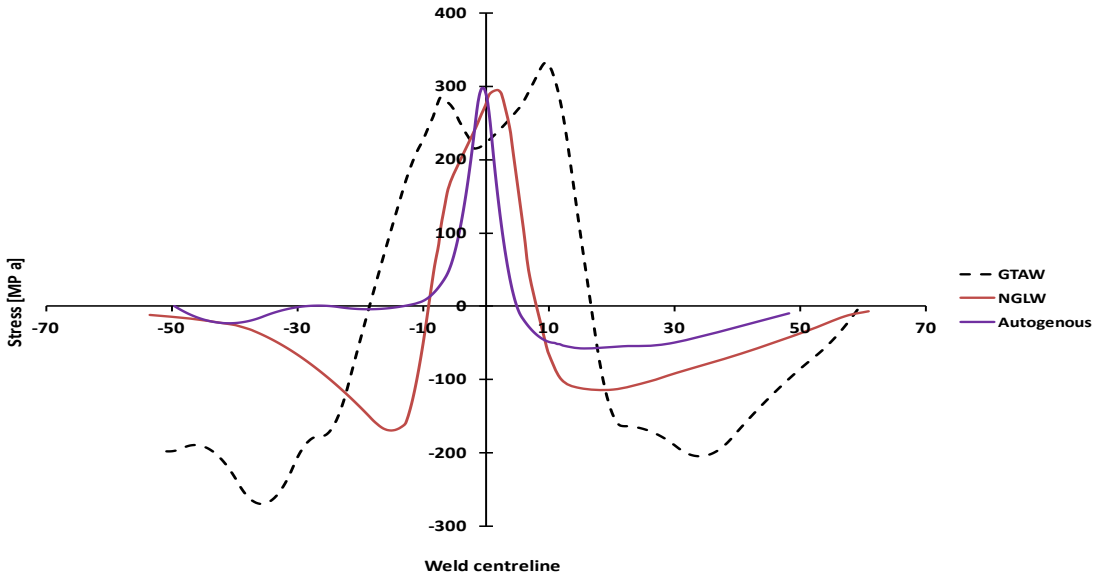

Figure 9-22 Residual stress distribution at 1 mm below the top surface for 3 mm thick sheet

9.5.7 Investigation of residual stress for 20 mm thick samples

9.5.7.1 Welding strategy from one side

Contour method steps were repeated for evaluating 20mm-thickness singled-sided plate welds, with 23 passes required to fill the welding gap as discusses in detail in section 6.4.1, while 52 passes were required to fill the GTA weld gap, as shown in Figure 7-7. The residual stress distribution is shown in Figure 9-23.

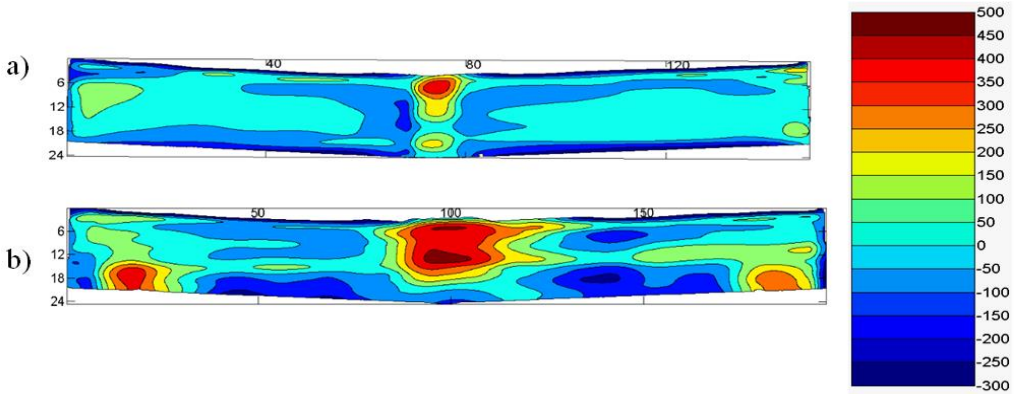

(a) NGLW (b) GTAW

Figure 9-23 Residual stress profiles for 20 mm thick- 1 side welding strategy

9.5.7.2 Welding strategy from two sides

Figure 9-24 shows the residual stress map across the 20mm thickness samples welded using NGLW, GTA welding and HPLW techniques. The NGLW technique needed 9 passes from each side to fill the prepared gap, while the GTA welding needed 17 passes from each side to fill the gap, and HPLW need 1 pass from each side to weld the joint.

The colour maps clearly show that the results for both HPLW and NGLW techniques exhibit lower stress behaviour in terms of peak value and width of tensile region with respect to GTA welding. The peak stresses arise in the light red coloured areas, which indicate stresses in the range from 300-400MPa, as shown in Figure 9-24 a.

The peak value of stress for GTA welding is in the dark red colour, which is equivalent to 400-500MPa, as shown in Figure 9-24b. The peak value of HPLW is almost 300:400MPa except a very small region has increased stress over 400 MPa at the side of second welding pass as shown in Figure 9-24 c. Distortion is almost zero since the welding followed the two side welding strategy. The stress map of each welding technique is very close to the map corresponding to the two-sided technique for the 10 mm thick samples. This indicates that the welding strategy (one-sided versus two-sided) has a more significant effect on the induced residual stresses than the thickness of the samples.

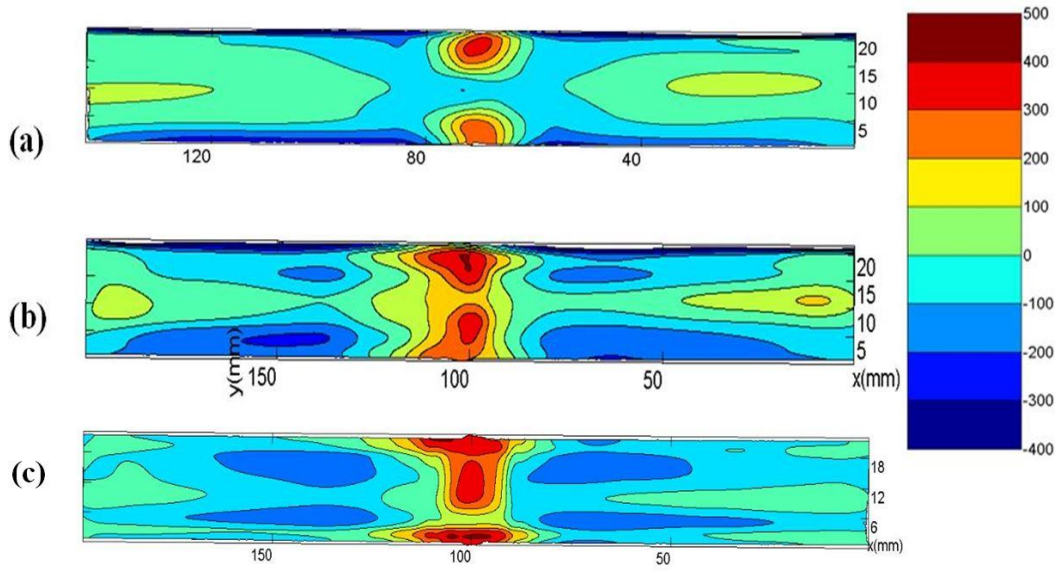

a- NGLW stress profile b- GTA welding stress profile c - HPLW

Figure 9-24 Residual stress profiles for 20 mm thick double-sided welds

9.5.8 Influence of the laser power and number of filling passes of NGLW on the induced residual stress across the weld joint

In order to investigate the influence of the power and the number of passes on the induced residual stress of a welded joint, another experimental work has been done with 4 kW fibre laser, and 1.2 mm wire diameter. The welding parameters were; power = 4 kW, welding speed = 12 mm/s, standoff distance = 108 mm. The specimen needs 4 filling passes. The longitudinal stress has been evaluated. Figure 9-25 shows the stress profile. The peak stress value is ~ 600 MPa, and the distortion angle = 2.4 º. The stress behaviour shows a more aggressive behaviour with respect to low power, high number of passes as discussed previously in section 8.5.1.2

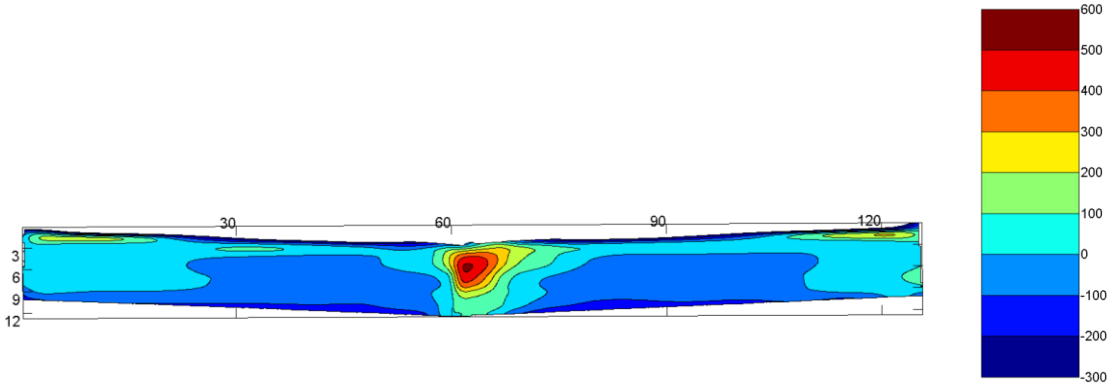

Figure 9-25 Longitudinal residual stress profile for NGLW of 10 mm thick plate- power = 4000 kW, speed = 12 mm/s

The stress distribution of NGLW 10 mm thick plates with high power 4 kW, low number of passes 4 passes is compared to the stress distribution of 10 mm thick plates with low power = 1 kW, and 10 filling passes.

Figure 9-26 shows the stress distribution at 2 mm depth from the top surface for both welding conditions. The peak stresses position is at the weld bead centreline with approximately symmetric behaviour. The peak value for 4 passes welding parameters ~ 300 MPa. The stress value was increased to 600 MPa for high power laser welding as shown in Figure 9-26. There is no significant influence of the laser power increase on the width of the tensile region.

The results show that the residual stress distribution for NGLW is more sensitive to laser power than number of welding passes. Laser power has a high significant

influence on the peak value of the developed residual stress; however it has less significant influence for the width of the tensile region as shown in

In terms of the residual stress behaviour of welding, it is recommended to use low welding power with a higher number of passes. However it will lead to an increase in the number of passes required to fill the welding gap. The influence of the power and number of passes on the developed hardness is investigated in detail in chapter 7.

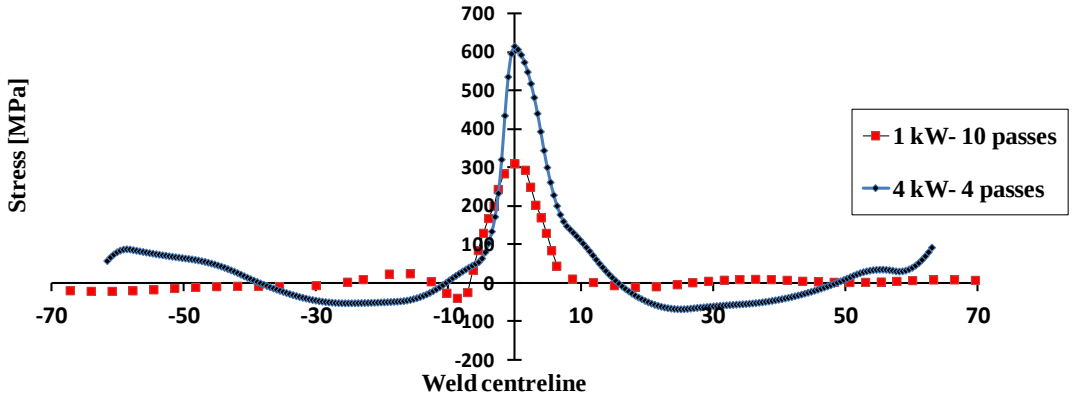

Figure 9-26 Residual stress distribution for NGLW 10 mm thick plates using different power- number of filling passes

9.6 Neutron diffraction investigations

Despite X-ray diffraction being an efficient technique for residual stress analysis, its small penetration depth is considered as a significant limitation for using this technique for thick sample evaluation - the penetration depth of X-rays for metallic components is < 10μm [73]. The penetration capability of a neutron beam is higher than that of X-rays in most metallic components [74]; consequently it will be used for the measurement of lattice spacing, strain, and residual stress validation in thick welded cross-sections. Residual stresses will be determined in terms of lattice parameter measurements made by neutron diffraction in three orthogonal directions.

Experiments were done at the Strain Analyser for Large and Small scale engineering Applications (SALSA), ILL, Grenoble, France. The overall schematic design of the instrument is shown in Figure 9-27, and the real experimental setup is shown in Figure 9-27 b. The system uses a monochromatic neutron beam having a wavelength of 1.7Å to

perform strain measurements. In the strain scanning setup, a position sensitive detector (PSD) is fitted, which records a single diffraction peak.

Elastic strains in the specimen cause changes in lattice spacing, and result in changes of scattering angle; by measuring these small changes in the scattering (Bragg) angle, it is possible to obtain the elastic strain in the lattice by using Bragg law, and hence the bulk strain in three orthogonal directions [203].

The investigations of residual stress in polycrystalline austenitic stainless steel alloys is in the 3,1,1 plane [203] , with a peak average angle of 99.8º. Bragg reflections are considered as the optimum choice in this plane because the reflections exhibit an approximately linear response to lattice strain as plasticity starts to occur. This means that they give a good representation of the macroscopic elastic strain, with minimal sensitivity to inter-granular and inter-phase stresses.

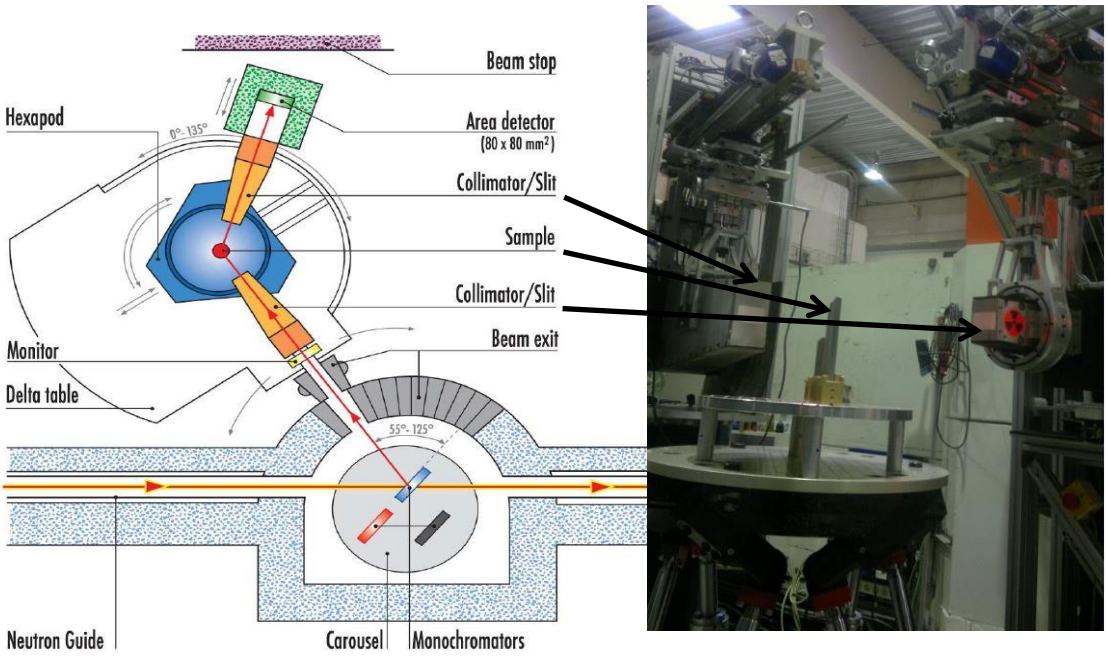

(a) (b)

Figure 9-27 Overview of SALSA design

9.6.1 Preparation for measurement

The incident and diffracted neutron beams are defined by slits or collimators as shown in Figure 9-28 . The gauge volume is defined by the intersection of the incident and diffracted beams, which defines the region used to calculate the average stress.

There were two different gauge volumes employed for experiments, the first is 2x2x2 mm gauge volume, which is used for analysis of GTA welding samples, and samples thickness 20mm. The other size is 1x1x1 mm, which was used for laser-welded joints in samples of 10mm thickness.

In order to obtain a stress value, it is usually necessary to measure strains in a three different sample orientations (longitudinal-transverse-normal), as shown in Figure 9-28. The slits can be increased in the direction in which the strain values are not very sensitive to the position, in order to decrease the measurement time without affecting the accuracy.

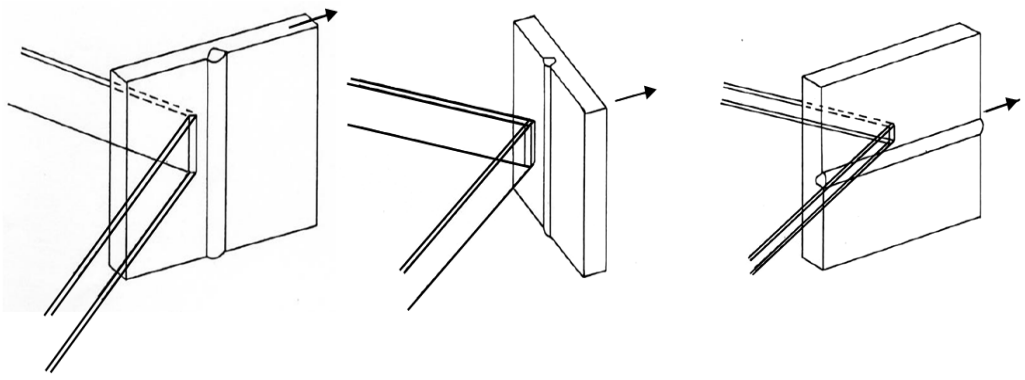

(a) Transverse (b) Normal (c) Longitudinal

Figure 9-28 Strain measurement directions

9.6.1.1 Sample preparation and measurement positions

Elastic strain and stress evaluations were performed at the mid-length position of the weld. The locations of the measurements for each sample are shown in Figure 9-29.

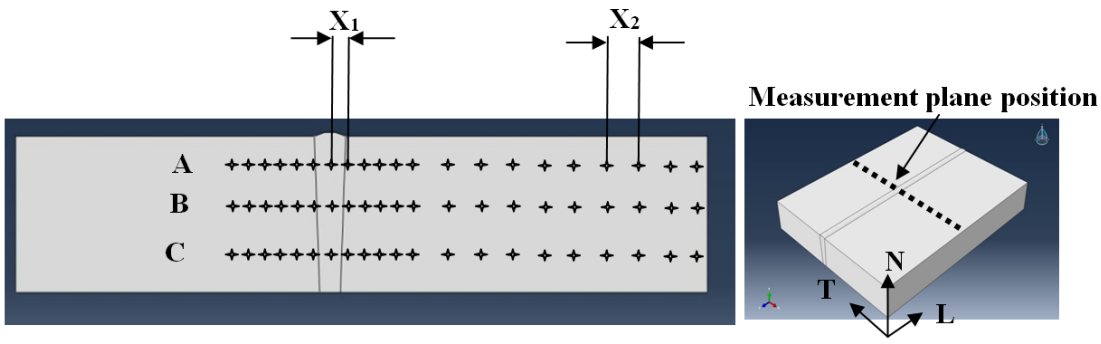

Figure 9-29 Locations of neutron diffraction measurements

The distance between measurements was very small near to the weld bead, such that X_1 = 1 mm for the NGLW sample, over a width of 20 mm (20 measurements per level). These measurement positions were repeated at three different levels, A, B and C; levels A, and C were 2 mm down each face of the weld joint, and level B was at exactly at the mid-section point. The horizontal distance between two successive measurements in the same level was increased toward the weld edge, due to decrease in the sharpness of the stress change. Distance X_2 is 5 mm for the rest of the workpiece.

The measurement distances were slightly different for the GTA-welded sample, due to the use of a higher gauge volume and a wider stress region; the depth of levels A and C was 2-3 mm from each side of the workpiece, and the distance between measurement locations, X_1, was 5 mm, over a 40 mm width, rising to X_2=20 mm in the outer section of the samples.

Once the lattice spacing of the welded samples has been calculated at each measurement location, the strain in the same direction can be calculated by using the engineering strain equation,

$$\boldsymbol{\varepsilon_{L(x,y)}} = \frac{\boldsymbol{d_{L(x,y)} - d_{ref\,(x,y)}}}{\boldsymbol{d_{ref(x,y)}}} \qquad (9.2)$$

where $\varepsilon_{L(x,y)}$ is the calculated strain at point (x, y), $d_{L(x,\,y)}$ is the lattice spacing measured in longitudinal orientation at point (x, y) as shown in Figure 9-28, and $d_{ref(x,y)}$ is the stress-free lattice spacing at point (x, y). Figure 9-29 shows the longitudinal (L), transverse (T) and normal (N) directions with respect to the weld joint,

In order to calculate the stress-free lattice space, $d_{ref(x,y)}$, comb-shaped strain-free reference (d_{ref}) specimens were prepared; the specimens were required so that stress-free lattice parameters across the weld can be determined. The samples were prepared by using an electric discharge machining (EDM) wire cut with skim cutting conditions to minimize any additional stresses due to the cutting operation. The configuration of the comb-shaped specimens is shown in Figure 9-30. The samples were sliced from the weld joint with a thickness 3.6mm, and then the comb teeth were opened using EDM, such that the dimensions of each comb tooth was 3.6 x 3.6 mm. Each comb tooth represents a stress- free region used to measure $d_{ref(x,y)}$ [204], where Y_i is the depth of each tooth, which was 8mm in the 10mm-thick samples, and 16mm in the 20mm-thick samples. The dimensions of each comb tooth had been calculated and cut precisely to ensure that the gauge volume was completely immersed within an individual comb tooth, to avoid errors associated with incomplete gauge filling [205].

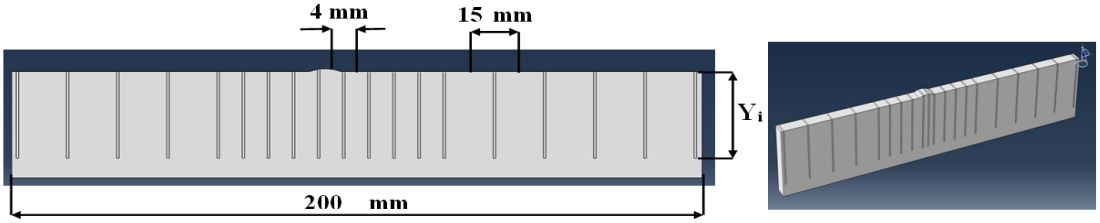

Figure 9-30 Schematic drawing for the location and orientation of the strain-free reference (d_0) combs

Similarly the strain in the normal ε_N and transverse ε_T direction is calculated. The stress acting in the longitudinal orientation, at a point (x, y) in the measurement plane, can then be calculated using a generalised version of Hooke's law, according to the following equation:

$$\boldsymbol{\sigma_{L(x,y)}} = \frac{\boldsymbol{E_{3,1,1}}}{\boldsymbol{1+\nu_{3,1,1}}}\left[\boldsymbol{\varepsilon_{L(x,y)}} + \frac{\boldsymbol{\nu_{3,1,1}}}{\boldsymbol{1-2\nu_{3,1,1}}}\left(\boldsymbol{\varepsilon_{L(x,y)}} + \boldsymbol{\varepsilon_{T(x,y)}} + \boldsymbol{\varepsilon_{N(x,y)}}\right)\right] \qquad (9.3)$$

Where $E_{3,1,1}$ and $\nu_{3,1,1}$ are the plane specific values of the elastic modulus and Poisson's ratio respectively, determined from in-situ tensile diffraction data. The values of $E_{3,1,1}$ and $\nu_{3,1,1}$ were taken to be 193 GPa and 0.28 respectively, and these steps were repeated to calculate the normal and transverse components of the stresses.

9.6.2 Results

9.6.2.1 NGLW of 10 mm-thick plates

Figure 9-31 shows the results for the longitudinal residual stress component for NGLW of 10mm-thick plates; the results show a normal residual stress distribution, with a narrow tensile region, especially at the middle position. The peak value of the stress is 400MPa at 2 mm below the top surface, and the stress rapidly decreases towards the edge of the sample. The results show a very good stress distribution for the NGLW samples, except at a distance 4mm from the weld centreline, where there is a small deviation from the regular behaviour of the stress. This could be due to a small error in the measurement position and depth of the (d_o) free lattice parameters in the stress-free sample, with respect to the corresponding position of the stressed sample.

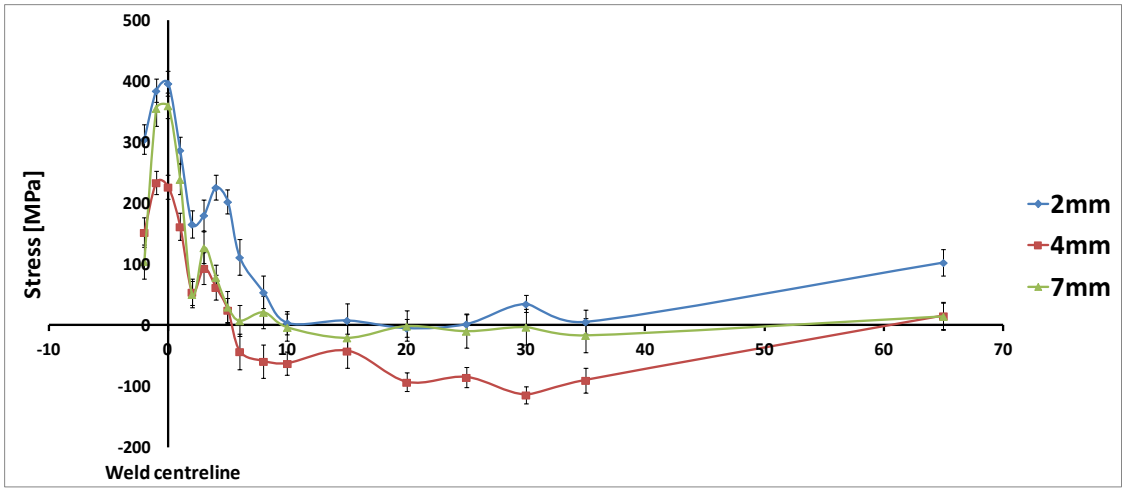

Figure 9-31 Longitudinal stresses measured by neutron diffraction at different depths for NGLW 10 mm thick plates

Figure 9-32 shows a comparison between the three residual stress components at 2 mm below the top surface of the NGLW sample; the results show a similar behaviour for the three components, but with a different peak value and width of the significant tensile stress region. The highest peak value is for the longitudinal component, then the transverse, and finally the normal value, as expected. The peak of each component is double that of the value of the other component; the longitudinal is 400MPa, the transverse is 200MPa, and the normal component is 100MPa.

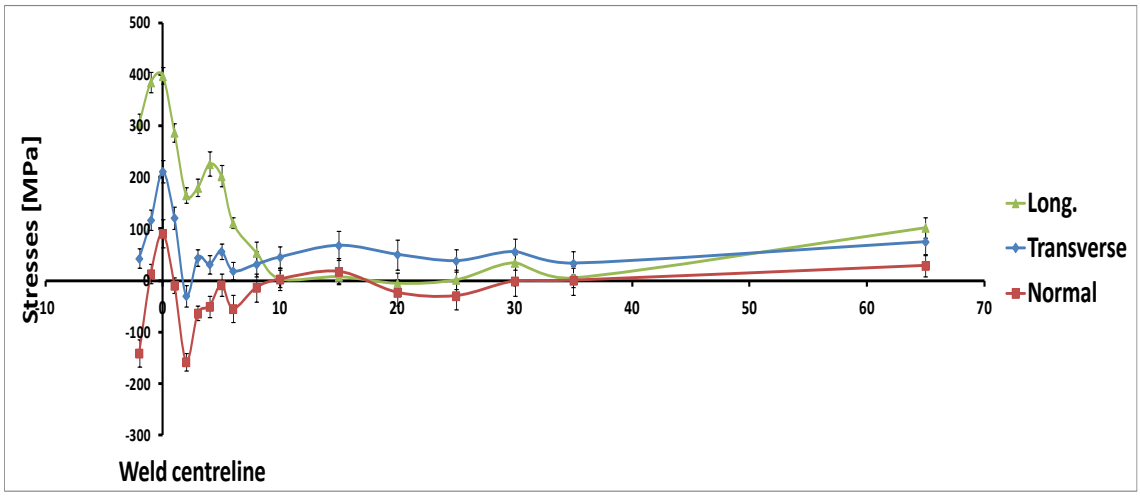

Figure 9-32 Longitudinal, transverse, and normal stress at 2 mm below the top surface for NGLW 10 mm thick plate

9.6.2.2 Validation with contour method results

This section discusses the validation of the neutron diffraction results with the results of the contour method for NGLW at the same position. The results are validated at 2 mm below the top surface as shown in Figure 9-33 a, and at mid-section as shown in Figure 9-33 b. There is a slight difference between the stress distributions for each measuring technique; however the overall behaviour generally exhibits a very good correlation between the techniques at both positions. The peak value is 400 MPa, at 2 mm below the top surface, and in the mid- section the value of the peak decreased to 250 MPa for both measuring techniques. The width of tensile region of both techniques is approximately 20 mm at 2 mm below the top surface, while it is decreased to less than 10 mm at mid-section.

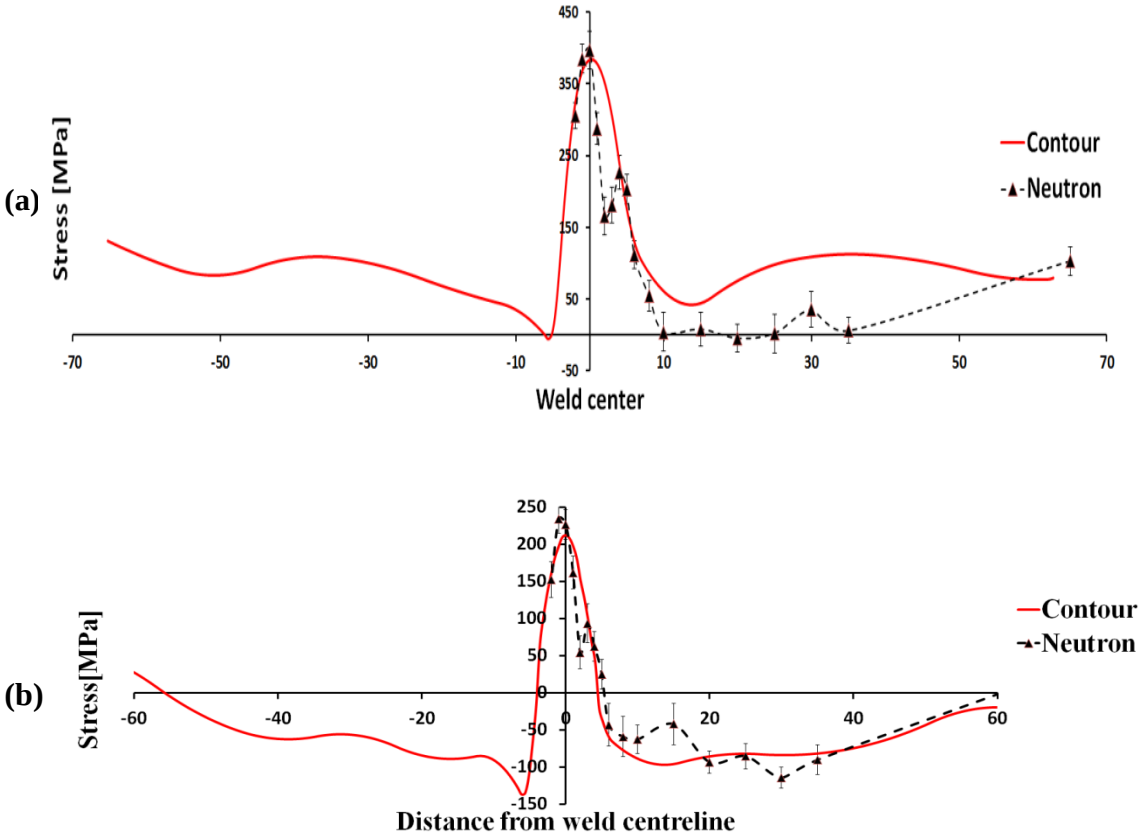

(a) 2 mm below top surface (b) Mid-depth

Figure 9-33 Comparison of longitudinal residual stress as measured by neutron diffraction and contour method for NGLW

9.6.2.3 GTA welding of 10 mm thick plates

The results of the neutron diffraction measurements are compared with those of the contour method, for the single-sided fully-restrained GTA welding process for 10mm-thick plates. The results show a similar stress behaviour of the two measurement techniques at 2 mm below the top surface. The peak value is 500MPa, and the width of the tensile region is 50mm, as shown in Figure 9-34.

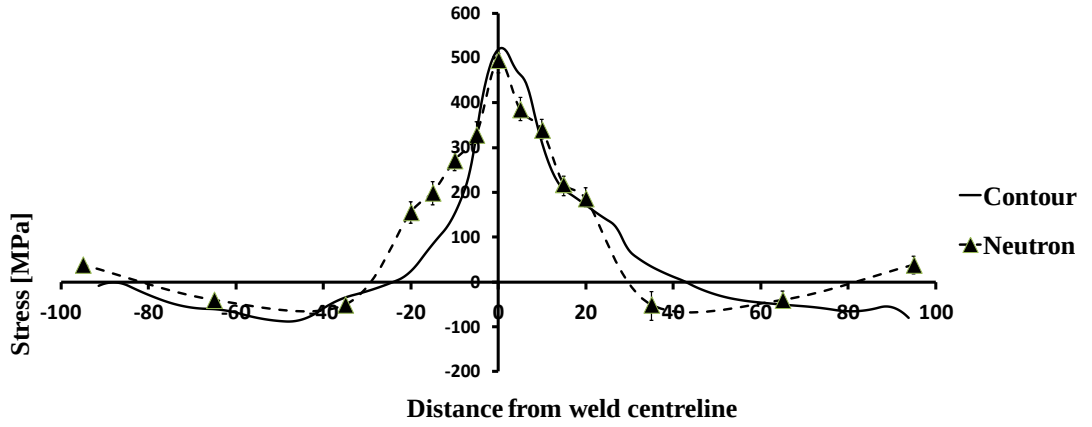

Figure 9-34 Residual stress distribution 2 mm below the top surface for GTA welding of 10 mm thick plate as measured by neutron diffraction, and contour method

The results of the contour method are validated for GTA welding at the mid-depth of the welded sample - a comparison between the two techniques is shown in Figure 9-35. The correlation between the two methods is good; however there is a small deviation at 5mm distance from the welding centreline. this mainly be due to a small deviation in the position of the calculation of the stress-free lattice parameters d_o, with respect to the position in the stressed sample as mentioned previously.

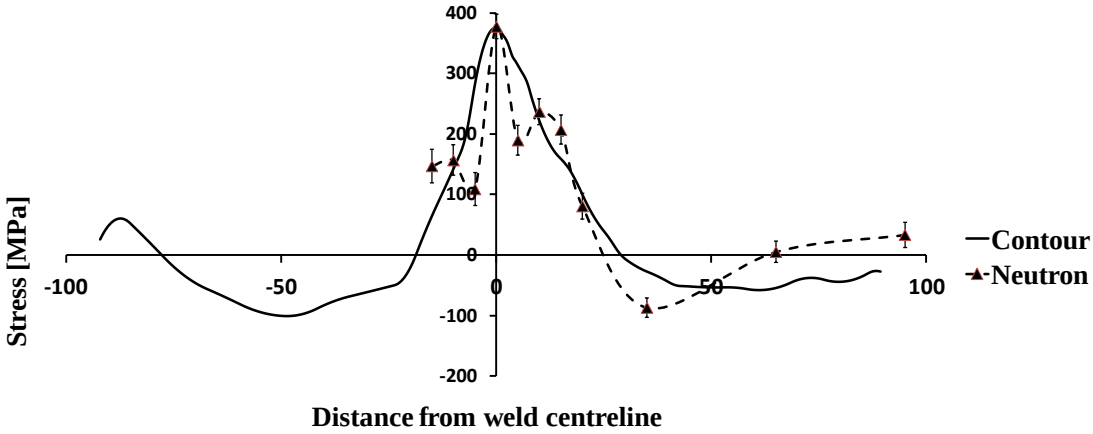

Figure 9-35 Residual stress distribution at mid-depth for 10 mm GTA welding as measured by neutron diffraction, and contour method

9.6.2.4 Autogenous HPLW of 10 mm thick plates

The stress behaviour for high power laser welding of 10mm-thick fully restrained plates will be evaluated. The welding parameters were discussed in detail in section 7.2.2.1. The results show a high peak tensile stress of ~ 650 MPa in the welding centreline (2 mm down the upper surface), as shown in Figure 9-36 . The width of the tensile region is constant for the three stress components with value 40mm as shown in Figure 9-36, the transverse stress component has its peak value of 560MPa at the centreline, and the transverse component also has other stress components which represent homogeneity with the longitudinal component.

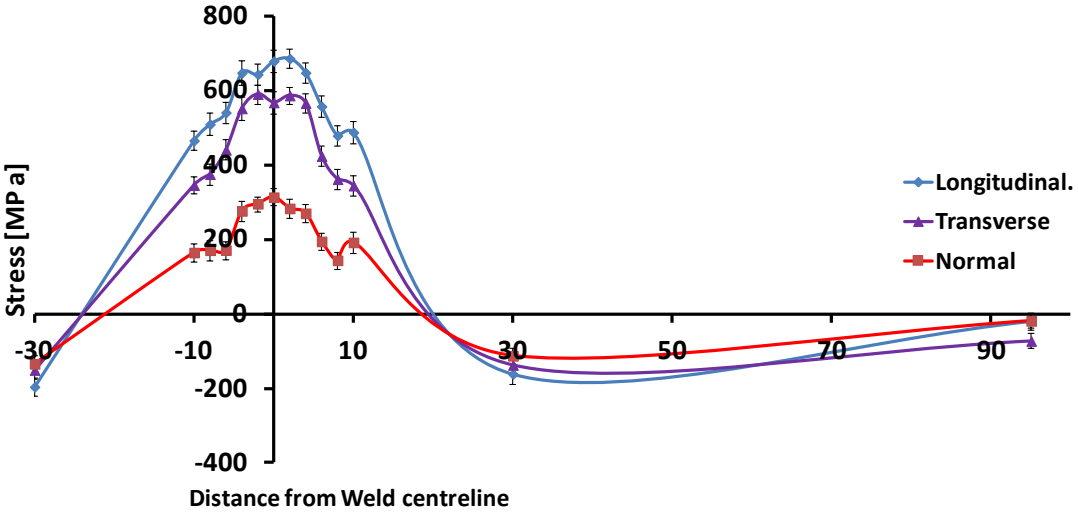

Figure 9-36 Longitudinal, transverse, normal stress of autogenous HPLW 10 mm thick plate

The results of neutron diffraction at different depths for 10mm thick-plates welded with HPLW are shown in Figure 9-37. The results show that there are two peaks of the tensile stress region at the weld centreline, with a value of 650MPa - these are at 2, 8 mm below the top surfaces. The stress does not exhibit a large change in value across the thickness. HPLW technique involves single pass-welding with high power in keyhole mode, so there is no gradient in temperature field in depth direction, and no stress-relaxation behaviour like that seen with multi-pass welding processes, just a slight relaxation of the stress at the mid depth of the welding joint to 550MPa. These results represent a very good correlation with the contour method results for the same welding technique using the same parameters as shown previously in Figure 9-18. The

width of tensile region is approximately the same at all depths with a value of 45 mm as shown in Figure 9-37.

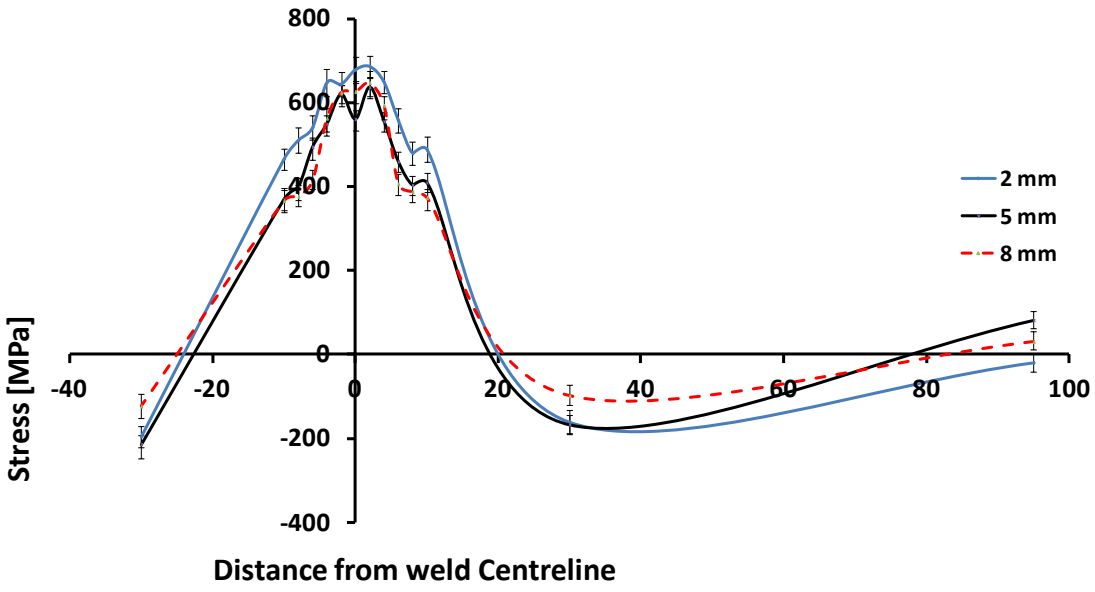

Figure 9-37 Longitudinal stresses measured by neutron diffraction at different depths for autogenous HPLW of 10 mm thick plates

9.6.2.5 GTA welding of 20 mm- thick plates

Figure 9-38 shows the stress distribution of GTA welded 20mm-thick plates, with a 2-sided strategy. The peak stress value is 500MPa, at 2 mm below the top surface, which has the final welding pass. The stress also has another peak with a smaller value, at 18 mm below the top surface, while the value in the mid-depth of the sample represents a more relaxed stress distribution. Despite these results showing a small deviation from the results of the contour method for the same sample, the overall peak value and behaviour sre acceptably close to the contour method results, as shown in Figure 9-24. The width of the tensile region is 40 mm, and the width of the tensile region and tensile peak values for the GTA welding are higher than for the NGLW values, as shown previously in Figure 9-24 a, b.

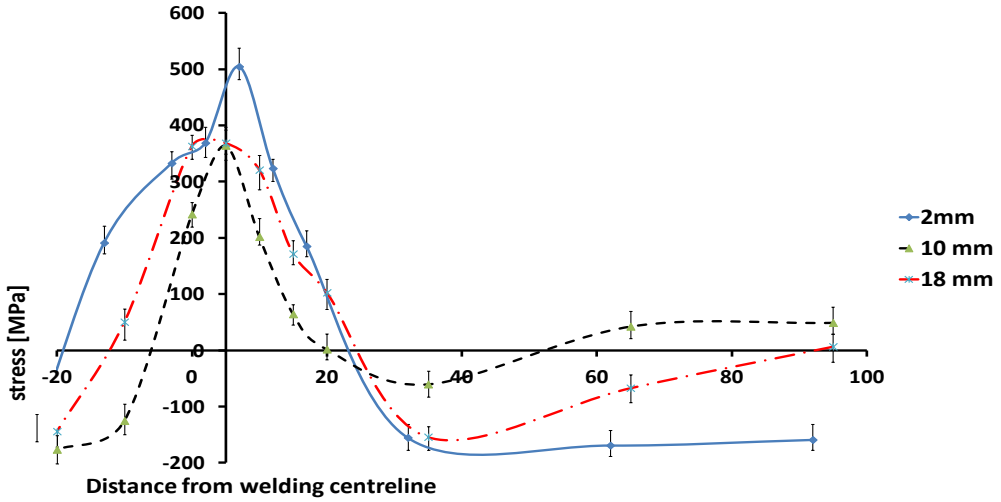

Figure 9-38 Longitudinal stresses measured by neutron diffraction at different depths for 20 mm thick plates with GTA welding

Figure 9-39 shows the three components of the induced residual stress across the 20 mm-thick GTA-welded sample; such that σ_L is Longitudinal stress component, σ_t is transverse stress component, and $-\sigma_n$ is normal stress component. The results show that the stress peak is higher in the longitudinal direction with a value ~ 500 MPa, then the traverse component with a value ~ 400 MPa, and finally the normal component with a value ~ 200 MPa.

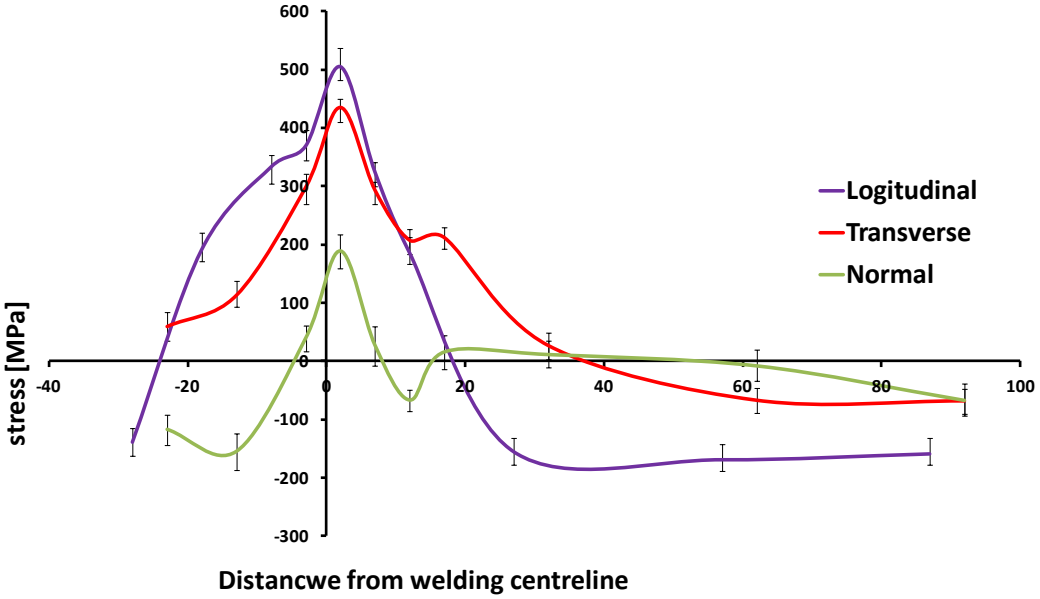

Figure 9-39 Longitudinal, transverse, normal stress for GTA welding of 20 mm thick plates, at 2 mm below the top surface

9.6.2.6 Autogenous high power laser welding of 20 mm thick plates

Autogenous HPLW of 20 mm thick plates needed 2 passes with a 7.5 kW fibre laser from both sides; the details of the welding parameters were discussed in Chapter 7. The results of the contour method for the weld joint were shown in Figure 9-24 c. The neutron diffraction results show a similar behaviour to the contouring method results - the highest peak value of the stress is at 2 mm below the top surface of the last welding pass, with a value of 500 MPa. At 18 mm below the top surface there is another peak with a lower value of 460 MPa, and the stress is slightly decreased in the mid-depth, with a peak value of 400 MPa. This welding technique represents the highest homogeneous distribution of stress across the weld joint at any position; the stress does not exhibit a large change in value across the thickness.

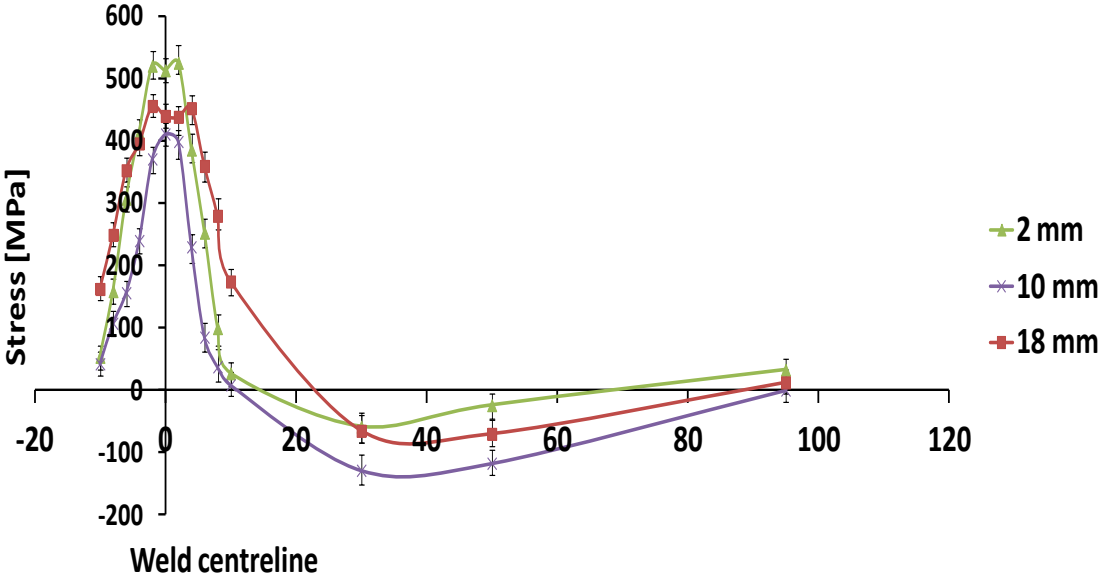

Figure 9-40 Longitudinal stresses measured by neutron diffraction at different depths for 20 mm thick plates with autogenous HPLW

Figure 9-40 represents the three components of the induced residual stress in the autogenous HPLW joint for the 20mm-thick plates. The results show low transverse and normal stress component behaviour; the peak value of transverse stress is 200MPa, and normal stress is 100MPa, with a small tensile-region width.

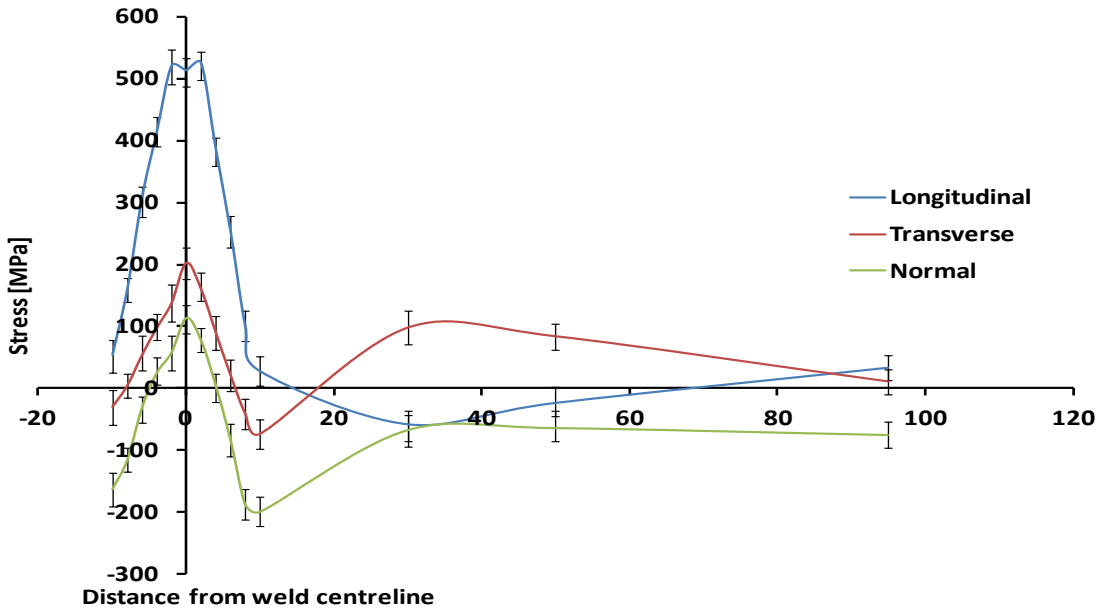

Figure 9-41 Stress components for autogenous HPLW of 20 mm thick plates

9.6.3 Summary

- The results obtained in this study indicate that NGLW may offer significant advantages for the structural integrity of components in cases where tensile residual stresses.
- The residual stresses were generally 30-40% lower in magnitude for the narrow gap laser welds in comparison to those for GTA welding. For the restrained 10 mm thick welds, the peak tensile stress was ~ 520 MPa for the GTA process and ~ 310 MPa in the case of NGLW. Furthermore, the NGLW technique resulted in a very narrow tensile stress region close to the upper surface of the welded plates, with the expanse of the tensile stress region being less than 5 mm to either side of the weld centreline.
- The butterfly distortion angle for the GTA welds was approximately 3 times higher than for NGLW.
- The welding strategy (single side welding or double side welding) had a significant influence on the induced residual stresses, especially for the NGLW technique, while it had a less significant influence for the GTA welding technique.

- The thickness of the welded samples had a less significant influence on the induced residual stresses than the choice of welding process.
- Power has more significant influence on the peak value of the residual stress with respect to width of the tensile region.
- Neutron diffraction measurement shows a very good agreement with the contour method results for all experimental welded joints.

Table 9-1 Summary of longitudinal residual stress performance of different welding techniques for 10 mm thickness

Welding technique	Welding strategy	Average longitudinal residual stress [MPa]
NGLW	One side	≈ 350 MPa
	Two sided	≈ 300 MPa
GTAW	One side	≈ 500 MPa
	Two sided	≈ 450 MPa
Combined (laser-arc) welding	One side	≈ 450 MPa
	Two sided	≈ 450 MPa
Autogenous HPLW	One side	≈ 600 MPa

CHAPTER 10. FINITE ELEMENT MODELLING OF RESIDUAL STRESSES IN MULTI-PASS NARROW GAP LASER AND ARC WELDS

10.1 Introduction

Residual stress in welds has a complex dependency on many interacting variables, including geometry, welding parameters, process constrains (boundary conditions), and material properties.

The ability to predict the residual stresses allows engineers to select welding parameters and procedures which can reduce the probability of in-service failure.

The requirement for increasing the service lives of new nuclear power plants has increased the interest in developing better understanding of induced residual stresses in welded joints. Residual stresses have a direct influence on the structural integrity and stress corrosion cracking [5]. Although multi-pass laser welding has shown less residual stresses compared to conventional GTA welding, the influence of the welding parameters on the developed stress is still not well understood.

Welding simulation is a complicated and time-consuming process. Geometric features, temperature dependent material properties, thermal, structural boundary and mechanical responses of the structure have to be simulated [10]. Furthermore, in order to understand residual stress and microstructure formation, it is necessary to understand the thermal history developed in laser and arc welds. This study will employ finite element (FE) modelling technique to analyse the thermal history and residual stresses in narrow gap laser welding compared with arc welds validated by experiments. The ABAQUS Welding Interface (AWI) is used.

10.2 AWI modelling

The ABAQUS Welding Interface (AWI) module is a newly developed module for modelling a multi-pass welding process, based on an element birth and death technique to simulate a moving heat source and weld filler deposition as a function of time in each single pass. This welding module provides the capability to improve two and three-

dimensional numerical welding simulations by automating most of the tasks associated with building a welding finite element model.

Many FE models have been developed previously to understand and simulate the conventional GTA welding process [206, 207] and autogenous laser welding process [208]; however, there is little knowledge about the evolution of residual stress in NGLW and understanding the contribution of each weld parameter on the final stress distribution. Hodgson et al. [209] used a 2D weld AWI on ABAQUS for modelling 8 passes conventional arc welding process with default heat source.

In the present investigation, the AWI module was used to simulate the residual stress distribution in NGLW joints. The influence of inter-pass time on the developed residual stress was investigated. The influence of the welding parameters (speed, power) on the developed stress was investigated in order to optimise the welding procedures. The applied heat source in AWI was modified to simulate the actual thermal profile across the welding bead for both NGLW, and GTAW welding techniques as discussed in detail in next sections.

On the other hand there are two limitations for this module. AWI modelling analysis cannot capture the influence of the phase transformation on the induced residual stress; however, during this study it was found that phase transformation during welding process is very limited. It is 3% in GTA welding, and 1% in laser welding. AWI has another limitation concerning the heat source definition. In this investigation laser heat source modelling was carried out.

10.2.1 Analysis procedure using AWI

AWI is a modelling approach used for multi-pass welding process, based on standard ABAQUS. AWI uses a sequentially-coupled thermal and stress analysis, where the temperature profile is extracted using a thermal analysis and then are applied to the mechanical model to calculate residual stress development.

The procedures for implementing a full weld model, and to complete heat and stress analysis, are divided into two main tasks; the first is weld joint generation through the ABAQUS CAE modules (create part, identify properties, assemblies, mesh), and the

second task is to create the weld model through weld definition and welding pass setup by using the AWI module.

10.2.1.1 Weld joint geometry and meshing

The weld joint geometry creation was modelled in the following procedure.

a) Welded joint geometry generation according to real dimensions. Modelling of the welded samples is based on actual samples dimensions 150 x 200 mm, with various thicknesses.

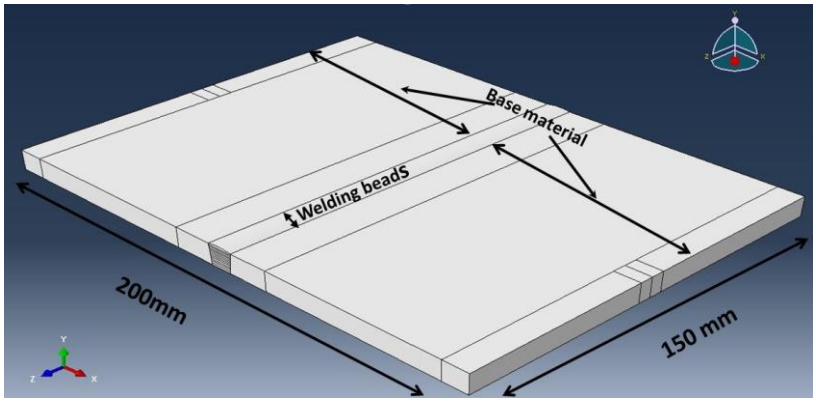

Figure 10-1 Model dimension and definition according to real weld case

b) Partitioning of the part to represent base material and individual beads according to actual weld bead geometry (lumping of beads handled in AWI). Figure 10-1 shows modelled joint, weld beads, and bead cross-section for NGLW 10 mm-thick plates.

c) Material properties (thermal and mechanical): Material properties (thermo physical, and thermo mechanical) are very important inputs to the model in order to obtain accurate and reliable responses of the developed model. For this investigation the properties of 316 L were as listed in Table 10-1.

Table 10-1 Material properties of stainless steel 316 L at different temperatures [210]

Temperature	Density [Kg / m³]	Film coefficient [W/mm²°C]	Conductivity [Wm / ° C]	Specific heat [KJ/Kg °C]	Thermal expansion coeff. [mm/mm °C]	Young Modulus [GPa]	Poisson's Ratio	Yield strength (0.2% proof) [MPa]	Yield(1% plastic strain) [MPa]
20	7979	0.012	13.31	0.47	15.24	195	0.267	278	325
100	7937	0.0135	14.68	0.487	15.8	191	0.273	233	272
500	7760	0.0333	20.96	0.571	17.85	164	0.313	146	171
1000	7535	0.0892	27.53	0.676	19.38	100	0.229	35	40
1200	7430	0.126	29.76	0.719	19.95	59.5	0.223	12	15
1400	7320	0.174	31.95	0.765	20.6	2 *	0.223	3	3.3
1500	7320	0.202	320 *	0.765	20.7	2 *	0.223	3	3.3

* Extreme values change of material properties due to high temperature (>melting temperature) [210]

d) External surface, and interfaces definitions: This step includes the definition of all external surfaces for the weld joint (upper surface, front, back, front, and sides), and interfaces between beads and base material for thermal boundary conditions, like convection, radiation boundary conditions (BC), and to apply heat transfer equations to the model change requirements for weld bead deposition.

The generalised differential equation, which represents heat conduction in solid body in AWI is:

$$\frac{\partial}{\partial x}\left(k_x \frac{\partial T}{\partial x}\right) + \frac{\partial}{\partial y}\left(k_y \frac{\partial T}{\partial x}\right) + \frac{\partial}{\partial z}\left(k_z \frac{\partial T}{\partial x}\right) + Q = \rho C \frac{\partial T}{\partial t} \qquad (10.1)$$

Where k_x, k_y, k_z are the thermal conductivity coefficients in the x, y and z directions respectively. T is the current temperature, Q is the rate of internal heat generation, ρ is the density, C is the specific heat and t is the time. The general solution is obtained by applying initial and boundary conditions as following:

Boundary conditions are:

Initial condition $T(x, y, z, 0) = T_0(x, y, z)$

Convection $Q_c = h_c A (T - T_\infty)$

Radiation $Q_r = \sigma \varepsilon A (T^4 - T_\infty^4)$

Where h_c is convective heat-transfer coefficient, A is surface area subjected to convection, radiation, s is the Stefan-Boltzmann constant (5.7x10-8 W/m^2K^4) and ε is the body emissivity. T_∞ is the ambient temperature.

$$Q_t = Q_c + Q_r = \sigma \varepsilon A (T^4 - T_\infty^4) + h_c A (T - T_\infty)$$

$$= \sigma \varepsilon A (T^2 + T_\infty^2)(T- T_\infty)(T+ T_\infty) + h_c A (T - T_\infty)$$

$$= A (T - T_\infty) [\sigma \varepsilon (T^2 + T_\infty^2)(T+ T_\infty) + h_c]$$

The equation could be written in the form of:

$$Q_t = h_t A (T - T_\infty) \qquad (10.2)$$

Q_t is total heat due to convection and radiation, h_t is total heat transfer coefficient or film coefficient.

Such that, $$h_t = \sigma \varepsilon (T^2 + T_\infty^2)(T+ T_\infty) + h_c \qquad (10.3)$$

e) Mesh creation: This task involves the meshing of all the components of the model (plate and weld joints) with suitable mesh density according to welding process and expected heat gradient for each region, as shown in Figure 10-2. Meshing of the model was performed with different densities according to heat gradient and stress variation across the welded joint. A high-density mesh was used near to the weld bead (10mm width in NGLW model), as shown in Figure 10-2. For the ten - passes NGLW model, the number of elements in the x direction n_x = 60 elements, number of elements in y direction n_y = 100 elements, and number of elements in z direction n_z = 10 elements. Elements used for heat transfer analysis are linear DC3D8, and for stress analysis are C3D8. Both elements are 8 noded linear brick elements as shown in Figure 10-2.

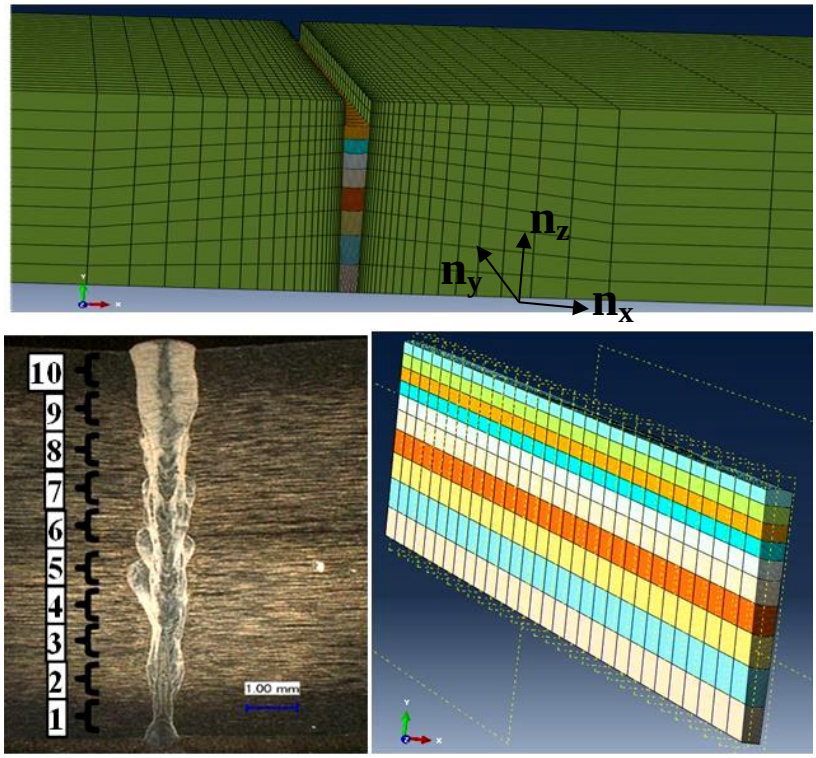

Figure 10-2 Modelled, and real weld bead cross section for NGLW 10 mm thick plates

10.2.1.2 Weld model creation (definitions and welding pass setup)

Weld model creation was realised by submitting the meshed part to the weld modeller generator to create the 2D or 3D weld model.

The modeller imports a basic meshed part (a meshed part with no boundary conditions, loads or interactions). The materials and sections were defined and allowed the user to create the weld beads.

a) Weld beads geometry definition

The weld beads have to be defined for the model in sequence to create the weld passes according to the weld bead order. Figure 10-3 shows the pass order for a 3 mm thick sample based on the bead selection sequence.

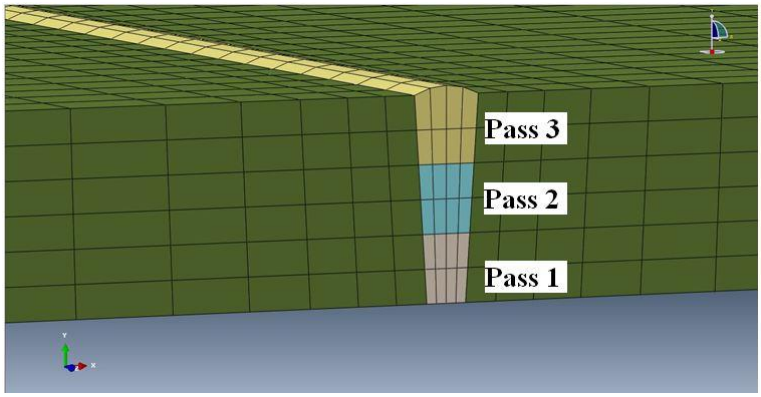

Figure 10-3 Pass sequence for 3 mm thick samples

The model could include more than one weld to control the welding parameters for each pass. AWI automates the creation of weld passes based on the defined structure and sequence of the weld beads by introducing element birth and death. Weld could consist of single or multi-beads.

A weld pass is divided into basic unit called chunk, which is defined as the birth unit. Then number of elements per chunk has to be defined. If the number is 1 that means the birth unit (chunk) will consist of one element. One element will be deposited on the plate once the heat source approaches, and if the number is 2 the birth unit will consist of two elements. More elements per chunk would decrease the calculation time for the model but can cause numerical instability. Decreasing the chunk size is desirable to simulate a continuous and homogeneous welding process, but it will increase the required processing capacity. On the other hand if the aspect ratio of the chunk is high it could affect the accuracy of the model and it could crash.

b) Weld pass control

Pass control is a very important step in the FE weld modeller. It includes the definition of the time of each step in the pass. Steps include heating up (applying the torch) or cooling down. The speed of the heat source can be controlled through specifying the time period (the time required to apply the heat source to one element). The time for a step is specified by the user according to real welding parameters. In this study for the NGLW technique, the real welding pass length is 150 mm, and the number of elements in that direction is 100 elements. The element length is 1.5 mm, and the time period was

0.15 s per element. It is related to the welding speed of 9.5 mm/s. The cool down step time between successive passes was 30 min.

Surface film and radiation heat transfer properties were applied automatically to the defined outer surfaces and intersection surfaces. This was used for the thermal analysis calculations for each pass. This automation speeds up the process significantly.

c) Weld model creation and submitting the job for analysis

This involves the creation of the welding job with predefined welding conditions. Two jobs were created (thermal and structural jobs). The thermal model was then submitted for the analysis. The model was then validated through experiments.

d) Apply welding restraint and submit structural analysis

This involves the definition of boundary conditions during the welding process such constrained surfaces and degree of constrains (translation or rotation and axes of constrains). Use results of the thermal analysis with defined boundary conditions to submit the structural model for stress analysis. Mechanical boundary conditions should also represent the reality.

10.2.2 Thermal model

This study simulates weld thermal cycles for 10 passes NGLW of 10 mm thickness stainless steel 316L as shown in Figure 10-2. In the thermal analysis, a total of 200 load steps were used to complete the first heating cycle.

10.2.2.1 Modelling the heat source across the weld bead

The heat source for the AWI model was applied as a temperature profile. AWI assumes a prescribed temperature during the bead generation to represent the heat source. A critical limitation of the AWI is that temperature profile is uniform (top hat) across the weld bead; Figure 10-4 shows the thermal profile for a laser heat source with different speeds at peak temperature 2500 ºC. Having a constant temperature profile across weld bead is the default case in AWI model generation which obviously needs modification.

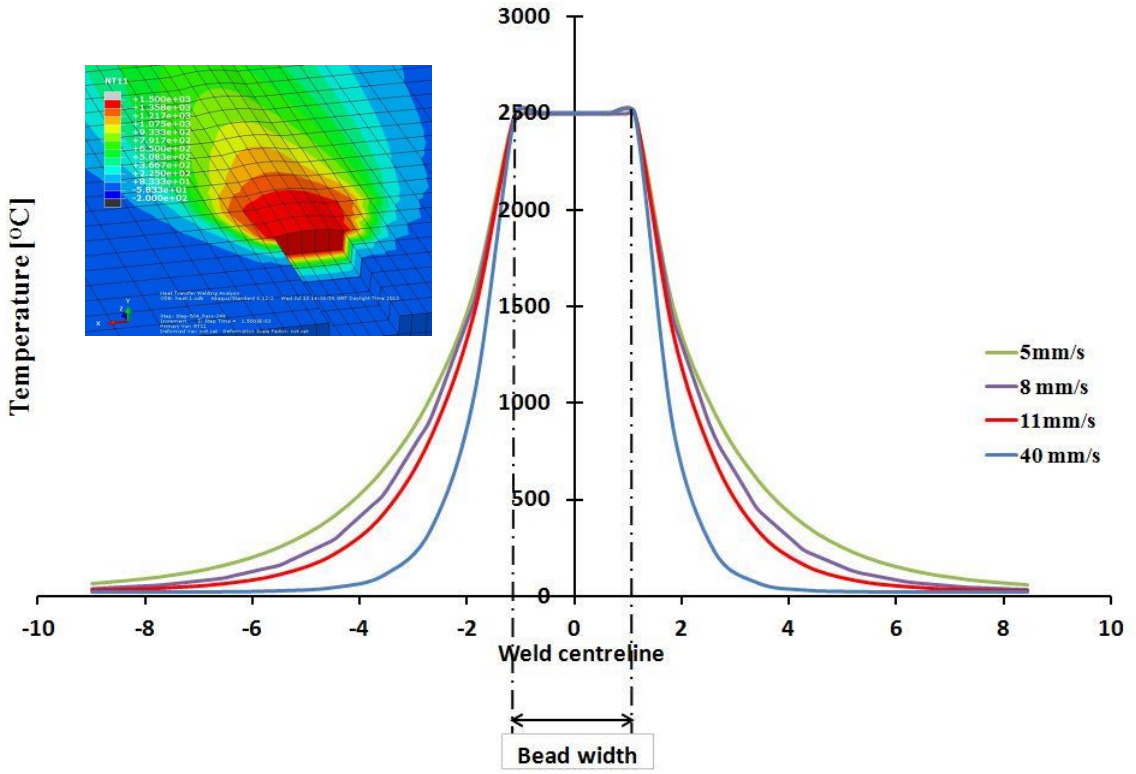

Figure 10-4 Thermal profile for the heat source for NGLW with different speeds

Laser welding numerical simulation has been investigated previously aiming at establishing a reliable heat source for simulating the laser welding processes. Most of the previous work used a Gaussian heat source profile [211, 212]. Shanmugam *et al.*[211] developed a model for laser welding process. They implemented a temperature profile for different ranges of laser powers as shown in Figure 10-5a. They suggested that a parabolic profile is the best fitting for the temperature distribution in laser welding. In the present work, both Gaussian and parabolic functions are examined for the temperature profile across the laser weld bead, as the experimental work was based on a single mode 1 kW fibre laser that has a Gaussian beam profile. The used peak temperature of the weld bead related to power 1 kW laser was 3000 ° C [211] as shown in the red dash line in Figure 10-5, and the bead-gap edge interface temperature at 0.5 mm from the bead centreline (average width of the actual weld bead) is 1500 ° C as shown in black dash line in Figure 10-5b.

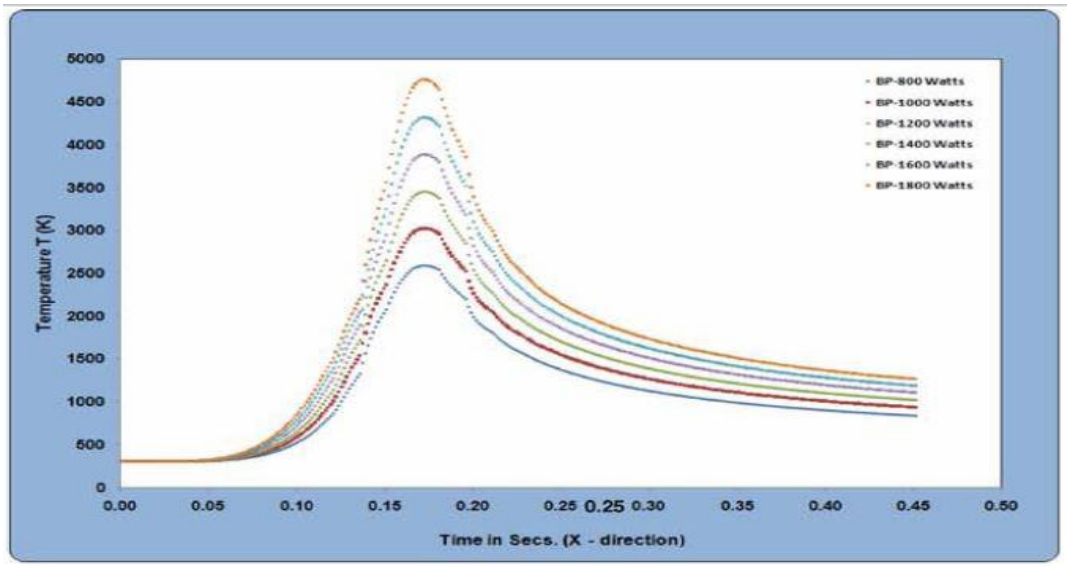

(a)

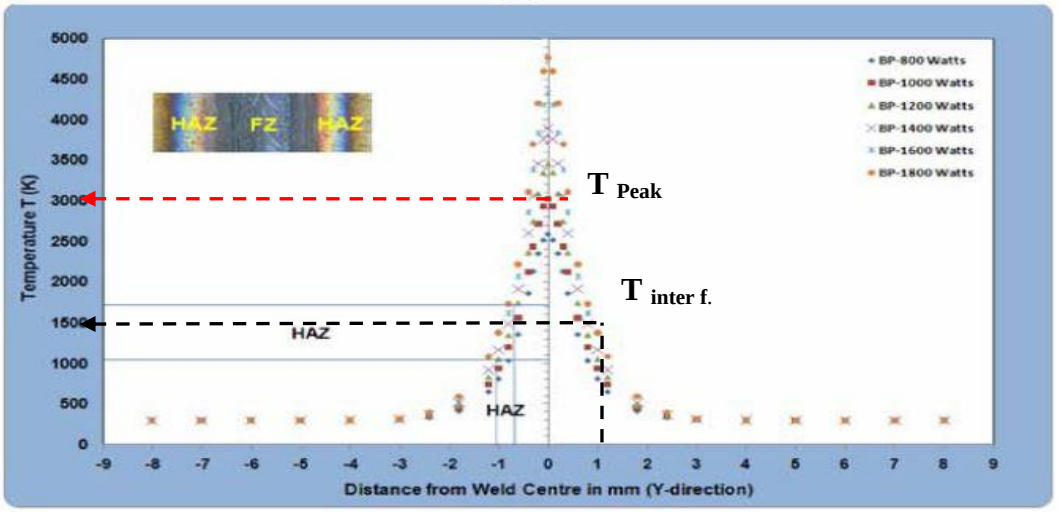

(b)

(a) Temperature - time profile (b) Temperature profile with respect to weld centreline

Figure 10-5 Temperature profile across laser welding of austenitic stainless steel [211]

Chandrasekhar et al. [213] used an infra-red (IR) camera during GTA welding of 316LN austenitic stainless steel, to build a temperature profile across the weld bead. The following parameters were used for the welding process; current 150 –170 A, welding speed 120 (mm/min), electrode diameter 3.2 mm, the shielding gas was argon, and the gas flow rate was 10 l/min, and the electrode tip angle was 45º. A Gaussian distribution was used for data fitting - this represents a very good fit to the temperature profile, as shown in Figure 10-6. The peak temperature was 1550ºC, as shown in Figure

10-6- these values were used during modelling of the GTA welding process in the present study for comparison.

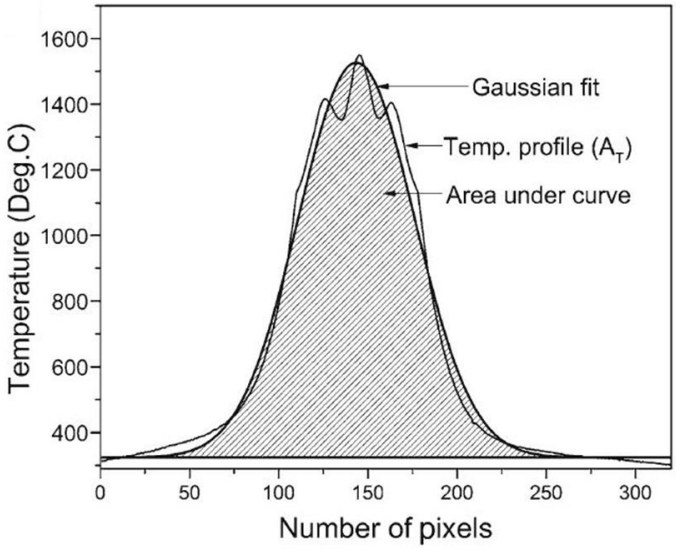

Figure 10-6 Gaussian fitting for temperature profile across GTA welding of 316L [213]

The assumed 2D Gaussian distribution for the bead temperature profile will be as follows;

$$T(x,y) = [T_{peak} - T_{interface}]e^{-[\frac{(x^2+y^2)}{(x^2+y^2)-R^2}]} + T_{interface} \quad (10.4)$$

The assumed parabolic distribution for the bead temperature will be as follows;

$$T(x,y) = [T_{peak} - T_{interface}][1 - \frac{x^2+y^2}{R^2}] + T_{interface} \quad (10.5)$$

where T_{peak} is the peak temperature at the weld bead centre; $T_{interface}$ is the temperature at the weld bead interface with the base material; x, y are the Cartesian position of the measured point with respect to weld bead centre and R is radius of the weld bead. The results of the thermal analysis, for both parabolic and Gaussian thermal distribution, were validated with the experimental measurement of the temperature. The result which is closer to the actual thermal history of the welding process was used for residual stress evaluation.

10.2.2.2 Experimental measurement of temperature

A set of four K-type thermocouples were attached to the weld joint during the NGLW process. The thermocouples are attached at different distances of 0.5 mm, 1 mm, 1.5 mm, and 2 mm from the weld bead edge.

Figure 10-7 shows the results of the experimental measurement of the temperature distribution for the NGLW process at different locations. The results show that the measured peak temperature was 1450ºC at 0.5mm from the weld bead edge. The measured temperature decreases to 1150 ºC at 1 mm from the middle, and to 800 ºC at 1.55 mm, and finally to 250 ºC at 2 mm. These values will be used for validating of the thermal analysis results.

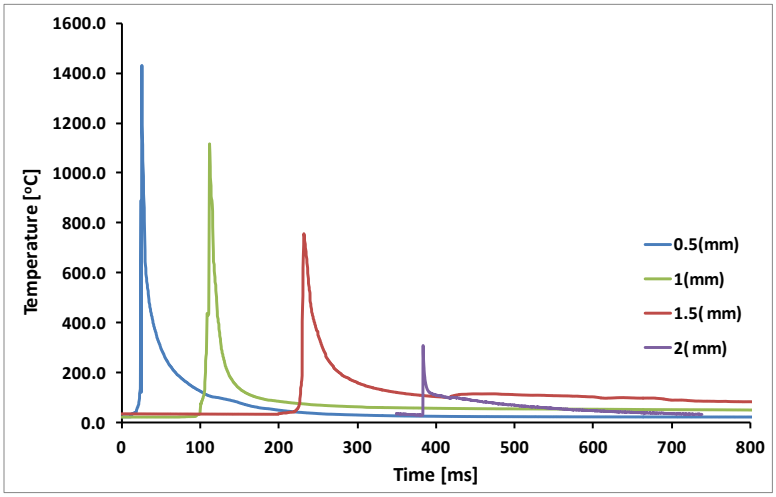

Figure 10-7 Experimental measurement of the temperature profile for NGLW

10.2.2.3 Thermal analysis validation

In this section results of the FE simulations for both modified heat sources (Gaussian, parabolic) are compared to the experimental measured values.

Figure 10-8 shows the calculated temperature profiles for both the Gaussian distribution of temperature across the welding bead and the parabolic distribution. The results show a close agreement between experimental measurements and theoretical model predictions of temperature profiles for both distributions. The weld bead temperature profile is shown in the Figure 10-8 as a sample output of the thermal analysis. The influence of the interface temperature is also investigated for the data fitting. The

modelling was repeated with a different interface temperature of 1700 ºC. The results showed that interface temperature has more significant influence on the accuracy of temperature as shown in Figure 10-8. Consequently the gaussian profile for the temperature distribution will be used during this work with an interface temperature = 1500 ºC.

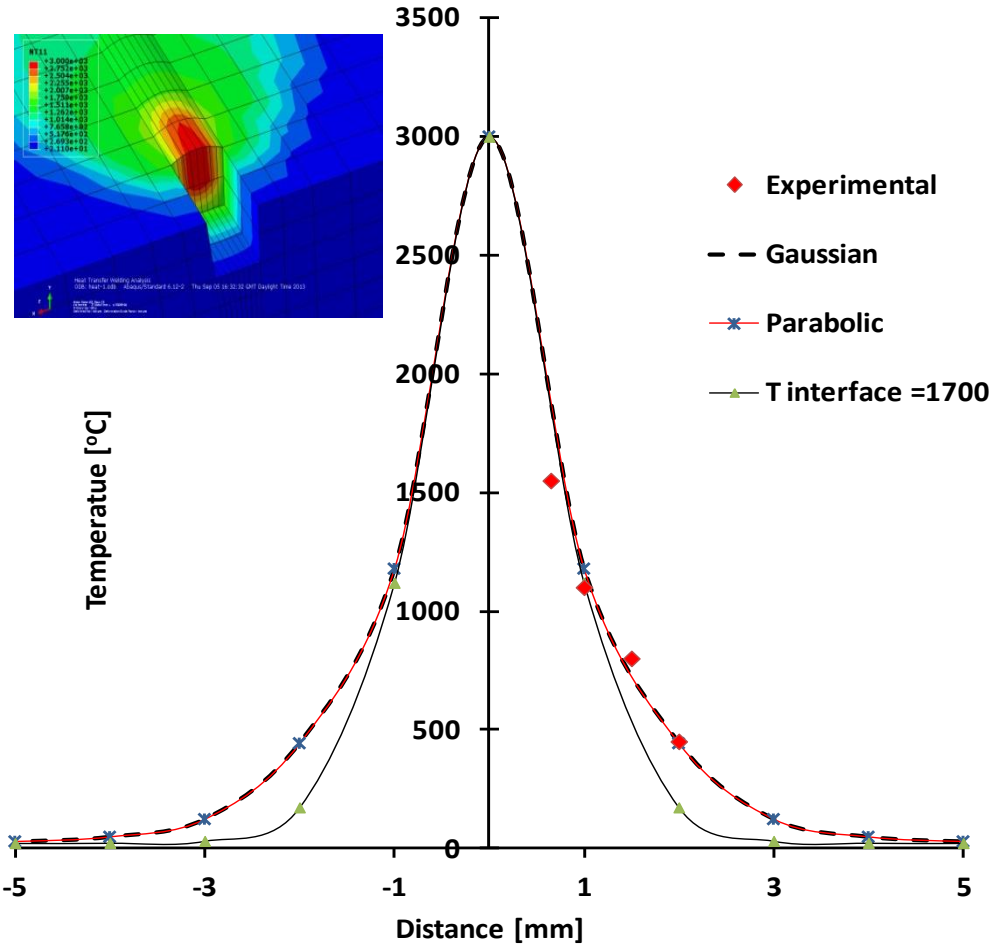

Figure 10-8 NGLW thermal analysis validation of NGLW

10.2.3 Mechanical model

The input for the mechanical analysis is the temperature history (thermal loading) obtained from the thermal analysis. The thermal strains and stresses can be calculated at each time increment. The final state of residual stresses will be accumulated by the thermal strains and stresses for all previous passes. During each weld pass, stresses are calculated from the temperature distributions determined by the thermal model.

The thermo-elastic–plastic constitutive equations based on the Von Mises yield criterion and the isotropic strain hardening rule, are utilized in the AWI model in the mechanical part of the simulation. Phase transformation effects were not considered in the current analysis due to lower influence on the final residual stress.

10.2.3.1 Restraint conditions of workpiece

Rigid jaws were used for restraint of the workpiece during the welding process. The area of contact between the jaws and the workpiece was approximately 20 x 20 mm at the mid-position of the outer edge of each welded plate. The boundary conditions during the welding process were modelled to represent the real case, as shown in Figure 10-9. The mechanical restraint applied during the modelling were on the area marked with the black circle as shown in Figure 10-9a. Displacement and rotation in three directions for the constrained surfaces are zero as shown in Figure 10-9b.

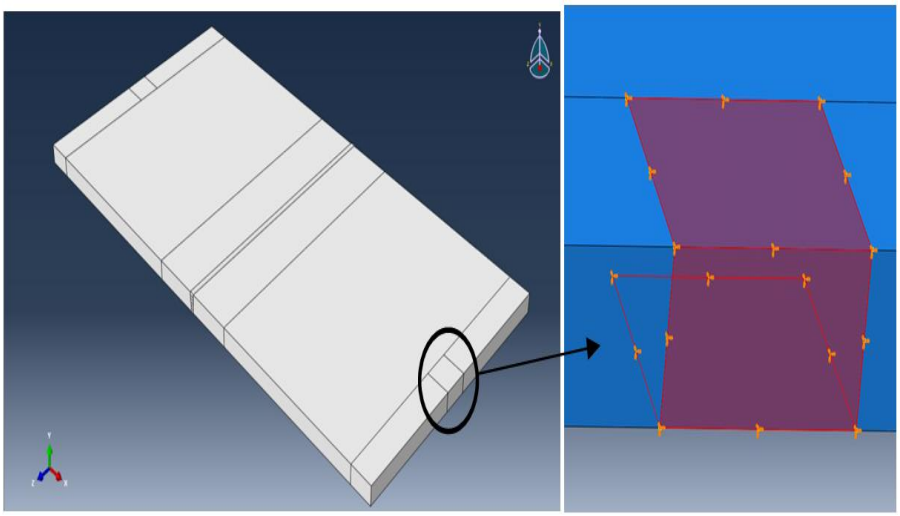

Figure 10-9 Boundary conditions during welding process

10.2.3.2 Mechanical modelling results

Figure 10-10 shows the modelling results of the welding of a 10 mm-thick plate with optimum welding parameters, using 10 filling passes. The result shows a tensile residual stress at a narrow region surrounding the welding pass with peak surface value 400 MPa. The stress is relaxed to zero within 10 mm from each side of the weld bead center, then compression stress arises at both sides with, values up to -150 MPa, and finally stress is relaxed again to the outer end of each weld plate.

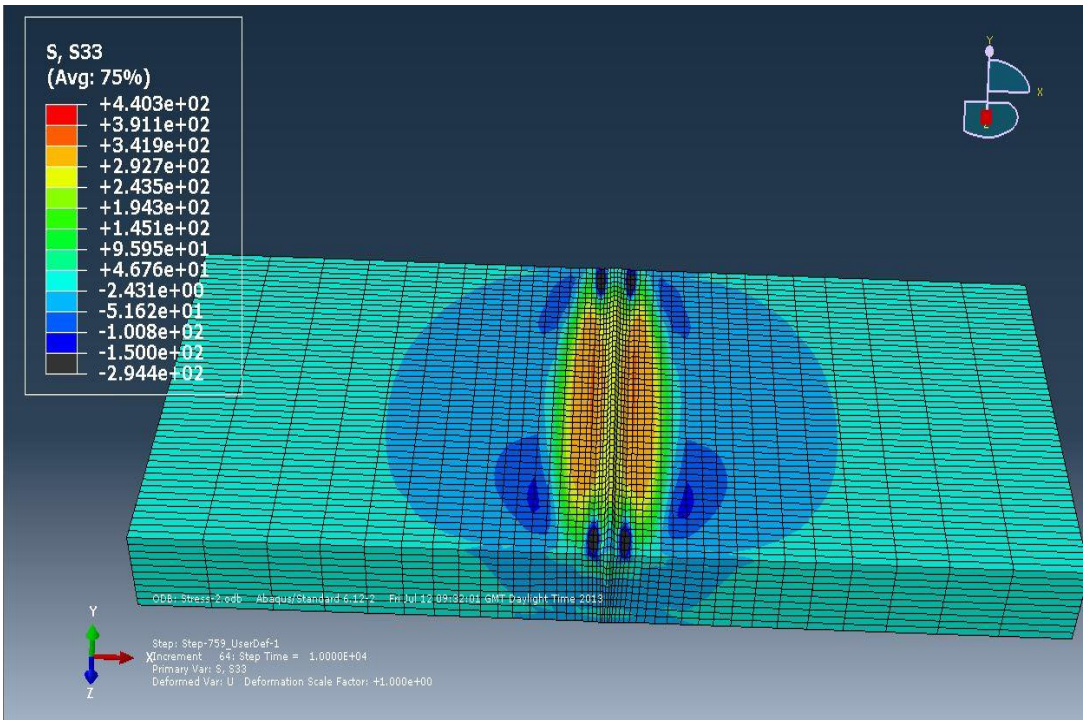

Figure 10-10 Residual stress results for 10mm thickness NGLW modelling

The first validation for the modelling results was made against the contouring residual stress measurement results. Most of the details of the stress distribution for the contour method were captured with a very good correlation in the model results as shown in Figure 10-11. The peak stress value is 450 MPa, and 2 mm below the upper surface for both contour and modelling results. The width of the tensile region on the surface and across the depth of the sample is very close for both results with a value ~ 20 mm. The lower peak in the contour method results is not captured clearly in the model results, however this peak is very shallow, and by increasing the resolution of scale it is captured as shown in Figure 10-11. The slight difference between the model results and contour results is mainly due to the phase transformation (austenite to ferrite) FCC to BCC which was not considered during the modelling [209, 214], and approximation of the applied of the heat source, but the overall behaviour of the stress distribution is satisfactory.

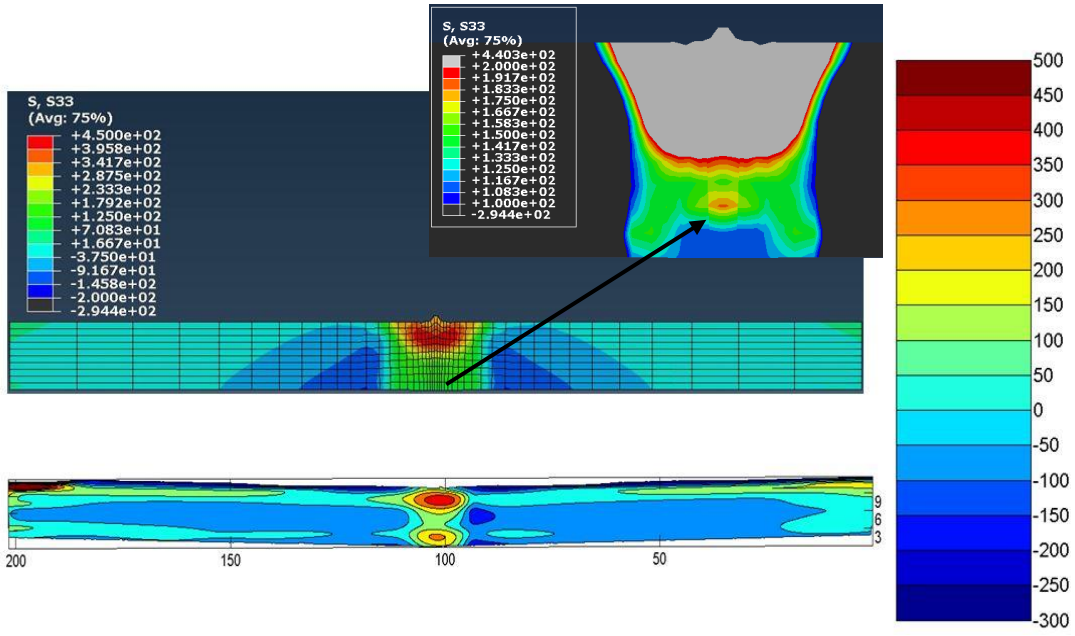

Figure 10-11 Residual stresses modelling vs. contour method results for NGLW 10 mm thick

10.2.4 Validation of model results against contour and neutron diffraction

Figure 10-12 shows the results of the model for NGLW process for 10 mm-thick plates. The longitudinal stresses were evaluated at a depth of 2 mm from the upper surface. The direction of measurement was perpendicular to the welding direction, as shown in Figure 10-12. The modelled results are compared with the results for both contour and neutron diffraction. The comparison shows a very good correlation between the three evaluation methods for the residual stress. The centreline peak value is 400 MPa, and it sharply relaxes to zero stress at 10mm from the weld centreline.

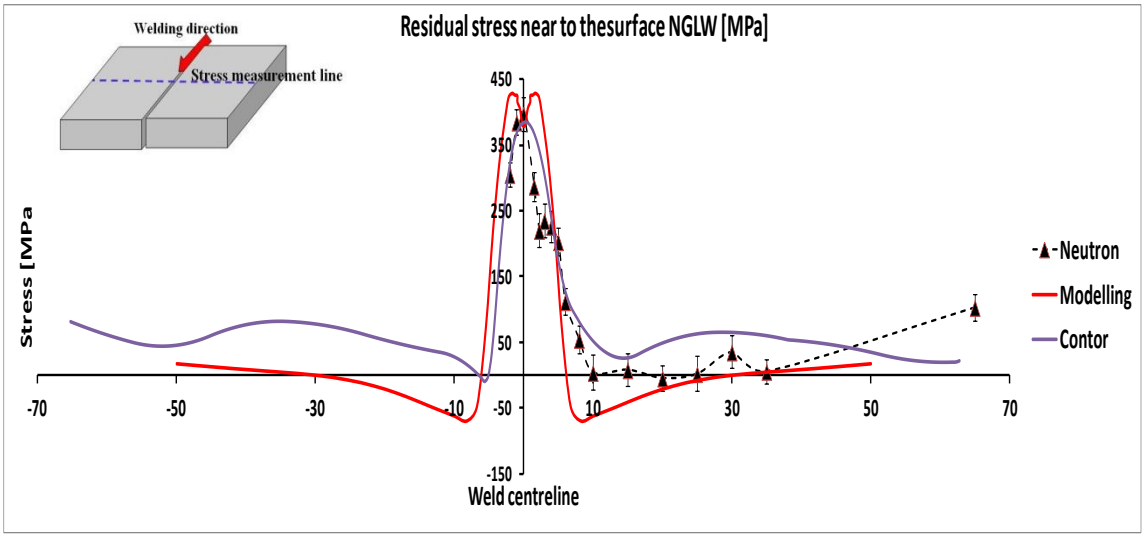

Figure 10-12 Comparison of predicted longitudinal residual stresses against contour and neutron diffraction measurements for NGLW

The error between the model results and experimental results is calculated at 10 positions with different spacing to the weld centreline as shown in Table 10-2. The average error between the model and the neutron method results was 28 MPa. It represents 6 % of the stress peak value. The average error between the model and the contour method results was 49 MPa. It represents 10 % of the stress peak value.

Table 10-2 Error between model and experimental results

Distance from weld centreline [mm]	0	2	4	6	8	10	20	30	40	50	Average error [MPa]	Average error %
Model results [MPa]	400	450	270	0	-70	-60	-20	0	10	20	--	
Error between model and neutron	0	100	0	20	50	25	25	15	20	25	28	6
Error between model and contour	0	70	0	100	100	60	70	50	30	10	49	10

10.3 Modelling results for the 3 mm-thick plate welds

Figure 10-13 shows the results of the stress analysis for the 3 mm thick plate NGLW process. The number of elements used was n_x = 42 elements, n_y = 50 elements, n_z = 6 elements. n_x, n_y, n_z are defined in Figure 10-2. The total number of elements is 12600 elements. The welding parameters used are related to the optimum welding parameters presented in Chapter 6. The gap needed 3 passes to complete welding. The result represents a tensile residual stress at a narrow region surrounding the welding pass, with a peak value of 320 MPa. The stress relaxed quickly to zero within 8 mm on each side of the weld centreline, then compressive stress arises on both sides, with values up to -150 MPa, and finally the stress is relaxed again towards the outer edge of the welded plates.

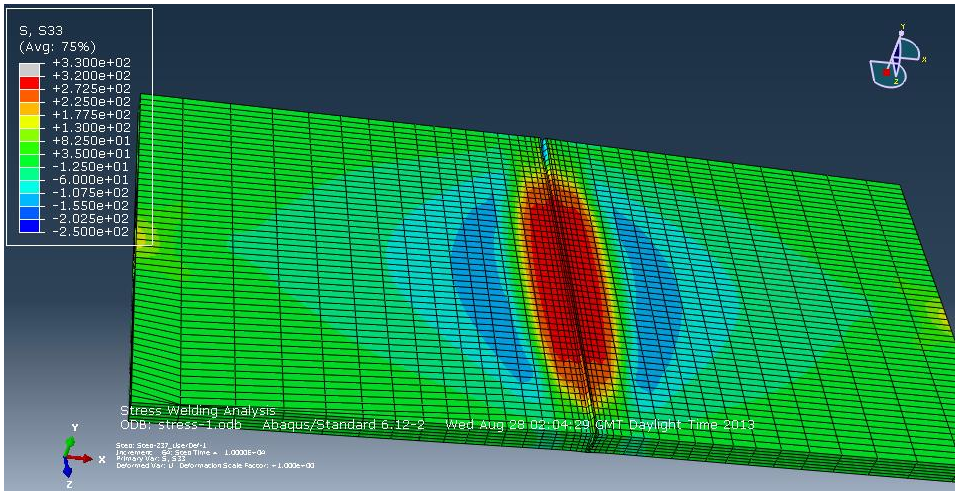

Figure 10-13 Modelling results for 3mm thickness NGLW modelling

10.3.1 Validation for the 3 mm thick plate weld model

The modelled results are validated with the contour method for the same thickness and welding parameters. Both show a very narrow tensile region with width ~ 10 mm, and peak tensile stress 350 as shown in Figure 10-14. The overall stress distribution shows a good agreement between the results of modelling and contouring technique.

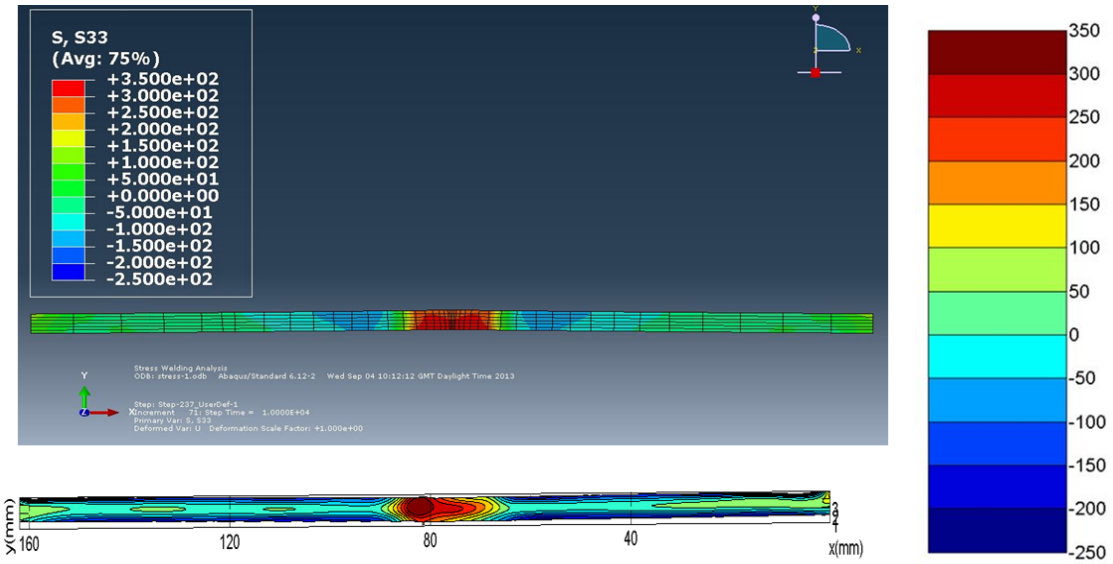

Figure 10-14 Residual stress modelling - contour method results for NGLW 3 mm thick plates

Figure 10-15 shows the stress distribution at depth 2 mm from the upper surface for the NGLW model results, compared with the experimental contour method results. There is a slight difference between the model results and the experimental results; however, the overall behaviour is similar specially near the weld bead region (high stress region). The peak stress value is ~ 300 MPa at the weld centreline, and the width of the tensile region is ~ 20m for both contour and finite element model results as shown in Figure 10-15. The average error is calculated similar to 10 mm NGLW specimen in section 10.2.4. The results shows an average error = 41 MPa. It represents 13 % of the stress peak value. The reason the difference in the results between the model and contour method is mainly due small deviation between the model measuring plane and the contour method measuring plane. The contour method is following a horizontal direction of measurement whatever the distortion angle, however the model is following the surface with distortion angle.

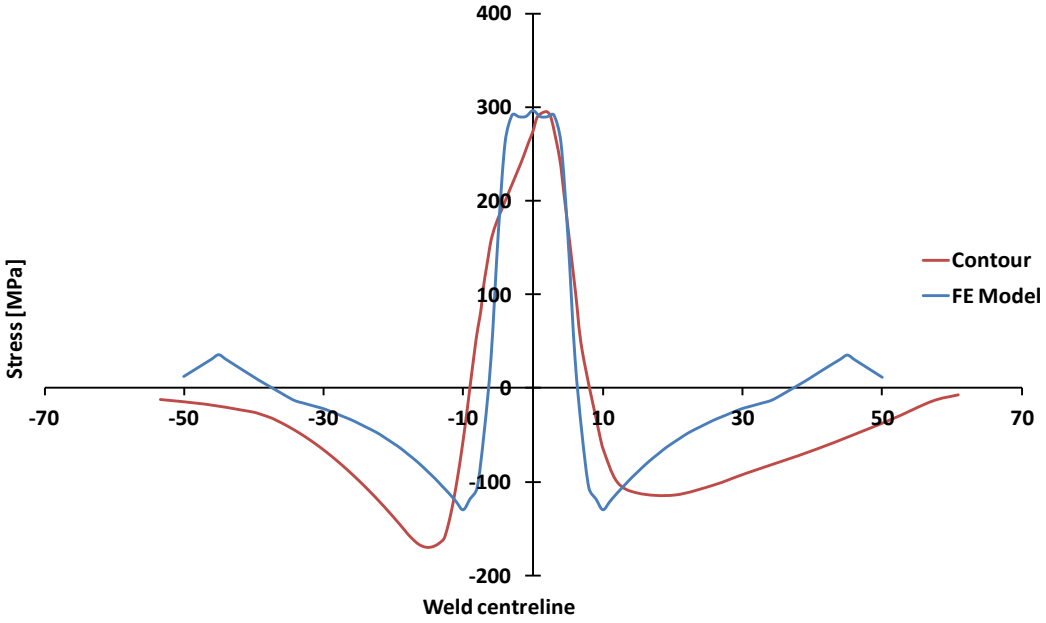

Figure 10-15 Residual stress distribution at depth 2 mm from the upper surface

10.4 Model convergence verification

The size of the finite element mesh has a significant influence on the accuracy of the model results and processing requirement [207]. The implemented model was checked for convergence in order to examine the adequacy of the element size.

The implemented of the FE model for the 3 mm thick sample was re-meshed again with finer meshing. The new model with refined meshes consists of nx = 60 elements, ny = 100 elements nz = 12 elements. The total number of elements was 72000 elements.

Figure 10-16 displays the distributions of the longitudinal residual stress with original mesh and fine mesh densities. There is a very slight difference in the results between these two different mesh models, and the main characteristics of the residual stress distribution from the different meshes are almost the same. Therefore, the original FEM model with a rough mesh is sufficient for reliable results with no divergence influence for the results.

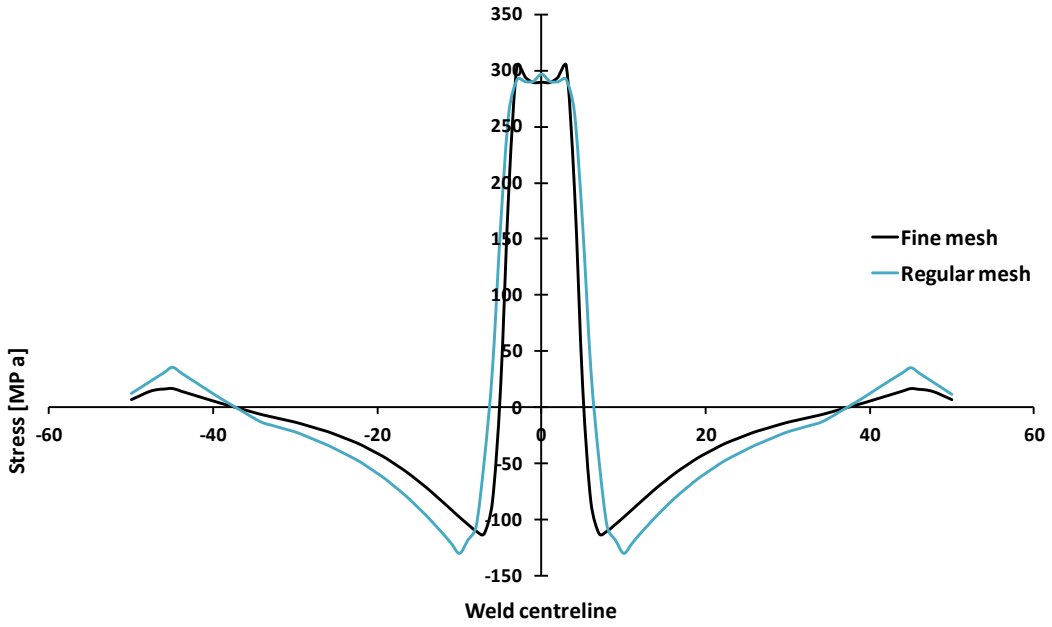

Figure 10-16 Longitudinal residual stress distribution for different mesh densities

10.5 Investigations of stress development for NGLW technique

10.5.1 Power-speed influences on the developed residual stress

This section will present the influence of the power and the welding speed on the induced residual stress for NGLW technique.

Figure 10-17 a shows the longitudinal residual stress profile for 3 mm thick samples. The welding parameters are; power = 1000 W speed = 9.5 mm/s. The experiment was carried out at a lower power = 750 W to study the influence of laser power on the induced residual stress. Figure 10-17 b shows the residual stress profile. The colour profile of the stress distribution shows a similar behaviour as the higher power stress, but with much smaller stress values.

Figure 10-17 c shows a comparison of the stress distribution at depth 2 mm from the upper surface for both set of welding parameters. The results show similar stress behaviour across the welded sample, but with a lower peak stress value of 200 MPa for the 750 W laser power. The width of the tensile region is slightly narrower at 750 W power. The significant influence of laser power is on the stress peak value as shown in Figure 10-17 c.

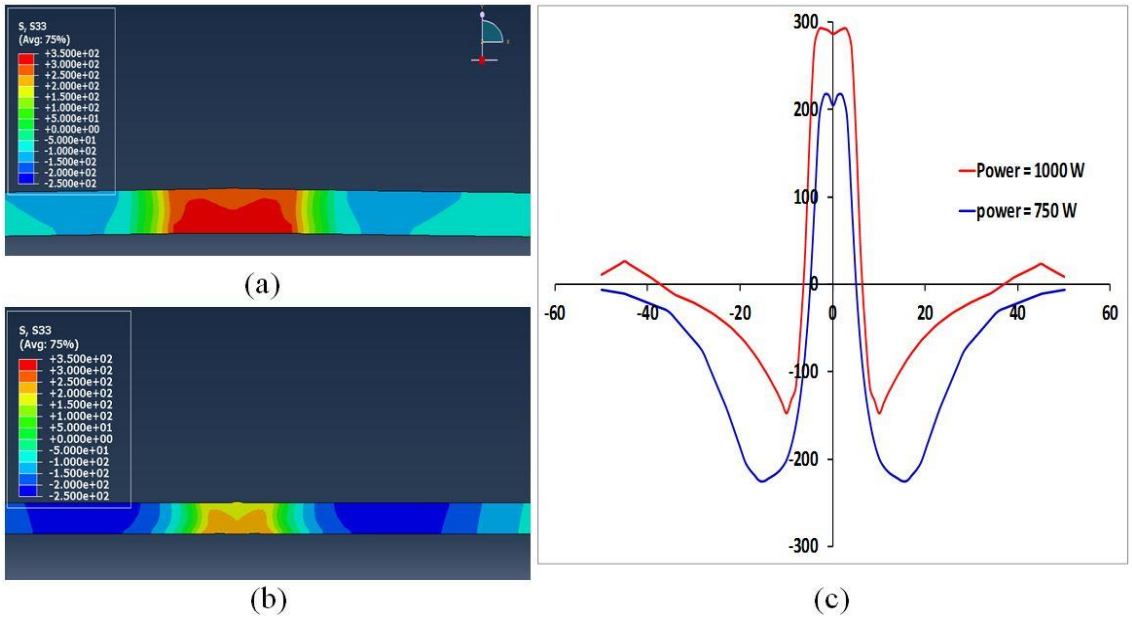

Figure 10-17 influence of power on the developed residual stress

The influence of the welding speed on the induced residual stress was investigated. The results are shown in Figure 10-18. The results show that decreasing the welding speed will lead to wider tensile stress region. The width of the tensile region for welding speed 5 mm/s is 22 mm, while it is 15 mm at the welding speed of 9.5 mm/s at the same power. On the other hand it is found that the influence of the welding speed on the stress peak value is non-significant.

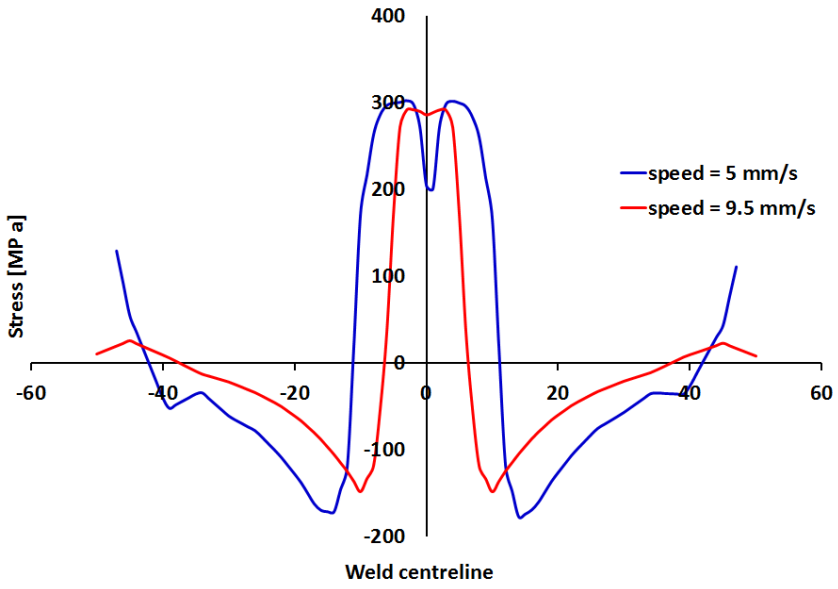

Figure 10-18 Speed influence on the induced residual stress

To summarise it was found that the laser power has a significant influence on the peak value of the induced residual stress across the welding sample, while the welding speed has significant influence on the width of the tensile region rather than the peak value of the stresses.

The thermal history for the influence of the welding power and speed on the temperature distribution are shown in Figure 10-19. The power increase shows a significant increase in the peak temperature across the welding bead as shown in Figure 10-19a. On the other hand the welding speed shows a significant influence on the width of the temperature developed region as shown in Figure 10-19b. Consequently a wider region will be subjected to localized thermal strain, which will increase the width of the tensile residual stress region.

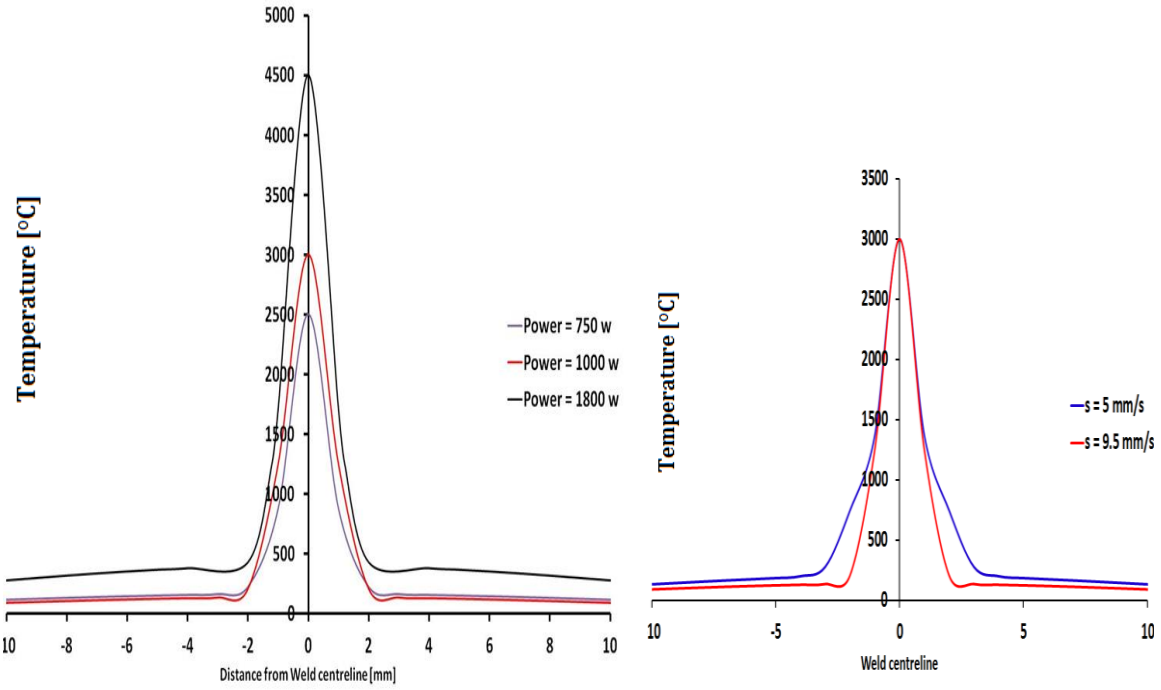

Figure 10-19 Temperature distribution of different welding parameters

Figure 10-20 shows the combined influence of the power and speed on the developed residual stress distribution. The results show that increase the power from to 1800W and decrease the speed to 5 mm/s will lead to increase both the peak and width of the tensile region as shown in Figure 10-20.

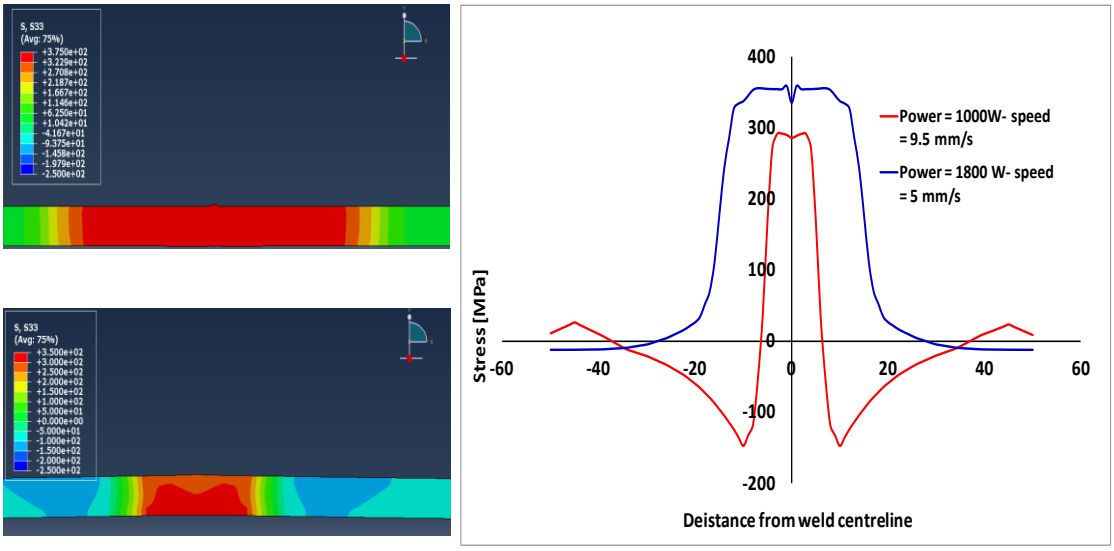

Figure 10-20 Combined influence of power and speed on the induced residual stress

10.5.2 Residual stress evolution during multi pass NGLW 10 mm thick plates

This section investigates the evolution of the residual stress across the NGLW bead region during the multi-pass welding process for 10 mm-thick sheet with 10 passes. The stresses were evaluated during the welding process after each pass. Figure 10-21 a, b, c shows the development of the residual stress distribution during the multi-pass welding process. The scale is similar to scale of the whole cross section as shown in Figure 10-11. The peak value of stresses at the first pass is less than 300 MPa, and the position of the peak is 2 mm above the lower face, as shown in the Figure 10-21. The width of the tensile region is still very narrow and affects the lower part of the weld bead cross section only. The peak stress value increases and moves up during the intermediate passes. The peak value increases to 400 MPa, and its position moves to the mid height of the cross section as shown in Figure 10-21 b. The width of the tensile region also increases; it covers the whole thickness of the weld joint.

The last set of passes is shown in Figure 10-21 c. The welding peak increases slightly in these passes, and is still moving towards the upper surface. The value of the peak is 450MPa and slightly down the upper surface with 2 mm. The width of the tensile region does not increase significantly during this set of passes.

(a)

(b)

(c)

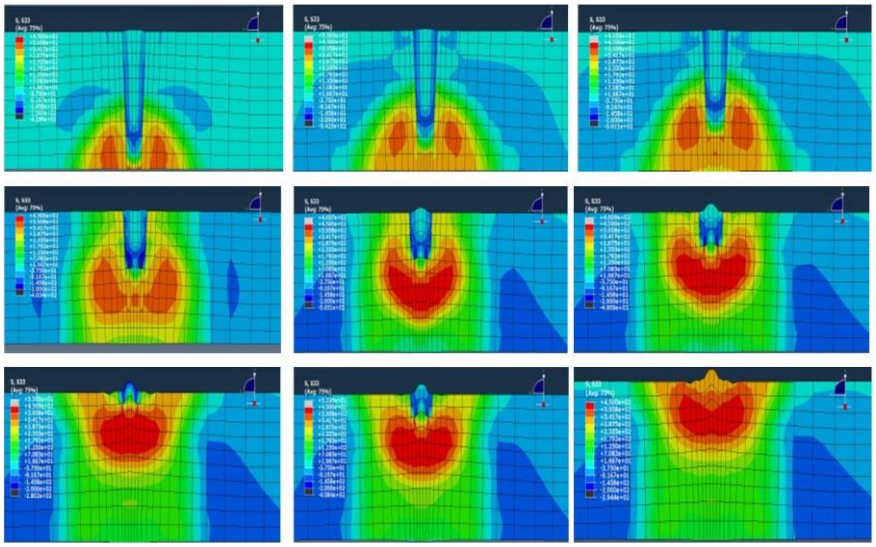

(a)First passes (b) Intermediate passes (c)Upper passes

Figure 10-21 Long. residual stress evolution in multi pass welding process 10 mm thick

The results show a significant influence of the position of the heat source on the stress peak position. The first three passes shows the stress peak is developing at the sides of the welding beads as shown in Figure 10-21 a. The stress in each bead is accumulated to the stress in the previous beads after cooling down time. The stress is developed for each new pass at the sides of the weld beads then it is developed slowly to the weld centreline after applying the next passes, consequently the peak shape profile has a heart shape (peaks at the both sides of the present bead, and the centre of the previous bead). The stress peak value is approximately 450 MPa. This value is affecting the specimen after the pass number 5 and then it changes its position only due to the position of the heat source during depositioning the new passes. The main reason is the preheat influence of the weld specimen due to previous passes. This improves the investigation of preheating influence on the stress distribution of NGLW samples.

10.5.3 Residual stress evolution during multi pass NGLW 3 mm thick plates

Figure 10-22 shows the stress evolution during multi pass welding process of 3 mm thick plates. The welding parameters are; power = 1000 W, speed = 9.5 mm/s with 3 filling passes. The longitudinal stress distribution showed similar behaviour to the 10 mm sample. The stress peak position at the first pass is located at the sides of the weld

bead centreline, forming the heart shape as shown in Figure 10-22. The peak value of the stress is approximately constant after the first pass with value 350 MPa as shown in Figure 10-22.

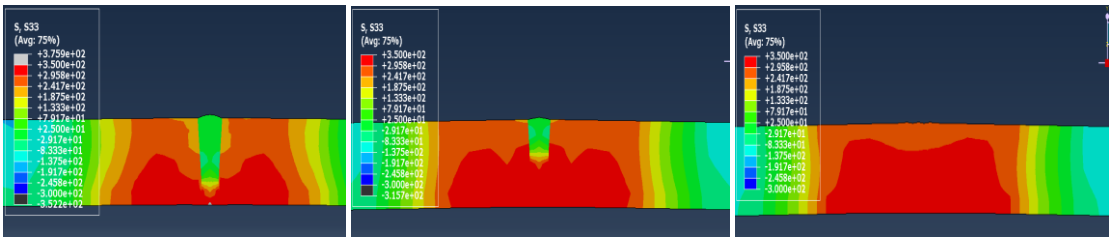

(a) First pass (b) Second pass (c) Last pass

Figure 10-22 Long. residual stress evolution in multi pass welding process 3 mm thick

10.5.4 Influence of the inter-pass time on the induced residual stress

The influence of the inter-pass time on the developed residual stress across the welding bead has been investigated. The welding parameters are; power = 750 W speed = 9.5 mm/s 3 passes for welding 3 mm thick plate. Figure 10-23 a shows the stress distribution for inter-pass time = 10 s, while Figure 10-23 b shows the stress distribution for inter- pass time = 30 min. The results show an approximately similar peak value of the residual stress across the weld bead for the two welding conditions, however it is shifted to the upper surface for decreased inter- pass time. The main reason for this behaviour of the residual stress distribution is that the developed stresses in the intermediate passes are approximately zero due to a small time, which is not sufficient for developing significant stresses. The stress which developed is mainly due to the final pass, which causes the shift of the stress peak location to the upper surface as shown in Figure 10-23 b.

a)

b)

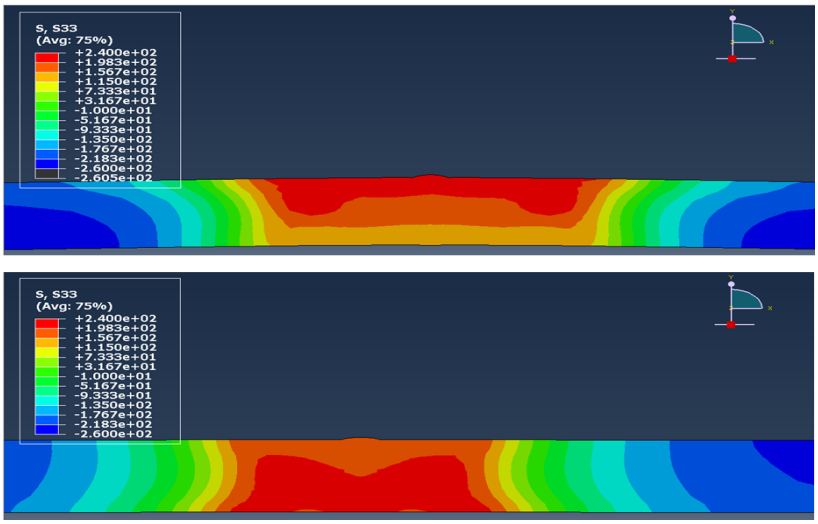

Figure 10-23 Influence of the inter-pass time on the induced residual stress

(a) Zero inter-pass time (b) 30 min inter-pass time

10.6 Modelling results of GTA welding process

10.6.1 Experimental thermal study

Figure 10-24 shows the results of the experimental measurement of the temperature distribution for the GTAW process at different locations from the weld. The peak temperature is 1150 ^{o}C at 11 mm from the weld centre-line; it then decreases to 800^{o}C at a distance of 13 mm, to 440 ^{o}C at 15 mm, and finally to 265 ^{o}C at 17 mm. The measurement values were then used for the validation of the thermal analysis results of the developed model.

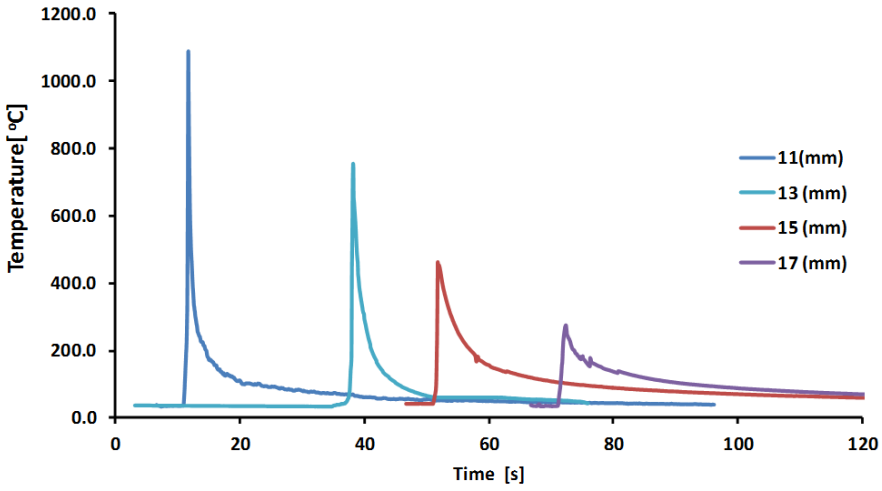

Figure 10-24 Experimental measurement of temperature profile for TIG arc welding

10.6.2 Validation for the implemented model

The results of the temperature profile of the model perpendicular to welding bead were compared with experimental measurements of the temperature at different locations. Figure 10-25 shows the temperature profile across the weld bead for both the model and experimental measurement values. The welding parameters for 10 mm thick plates with 12 filling passes were discussed in details in chapter 7. The heat source is according to the GTAW heat source profile, which was discussed in section 9.2.2.1.

The results show a minimum deviation between the model results and the measured temperatures. The heat distribution profile across the weld bead is shown in Figure 10-25

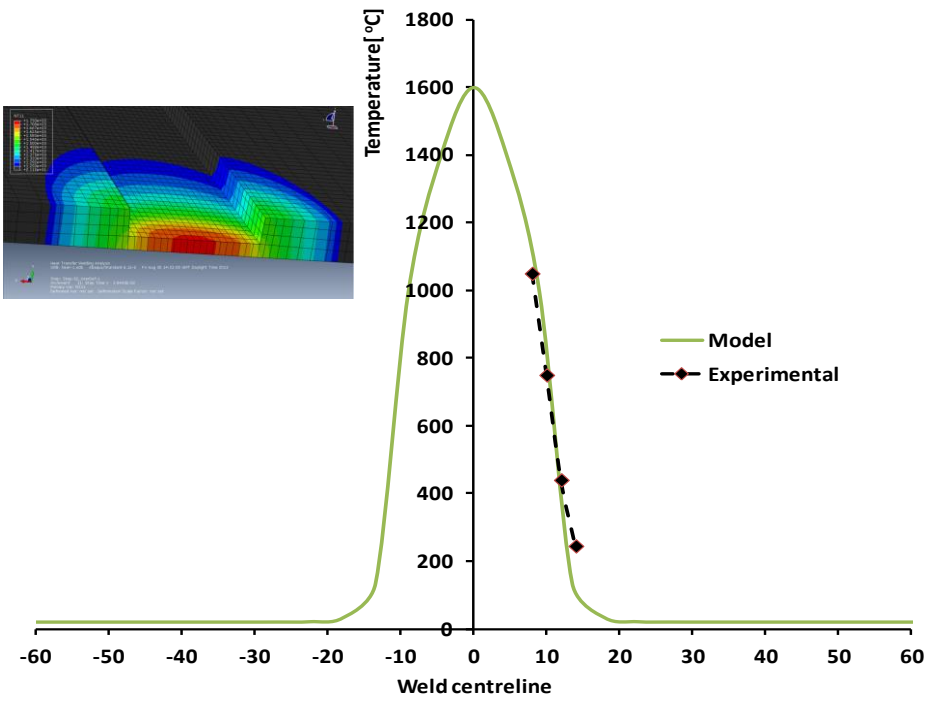

Figure 10-25 Thermal analysis validation for GTA welding

10.6.3 Model result of GTAW process

FE structural analysis was carried out for GTA welding of 10 mm thick samples. The model results are shown in Figure 10-26. The results show that absolute weld joint peak position is below the upper surface. The peak stress value on the upper surface is ~ 400 MPa.

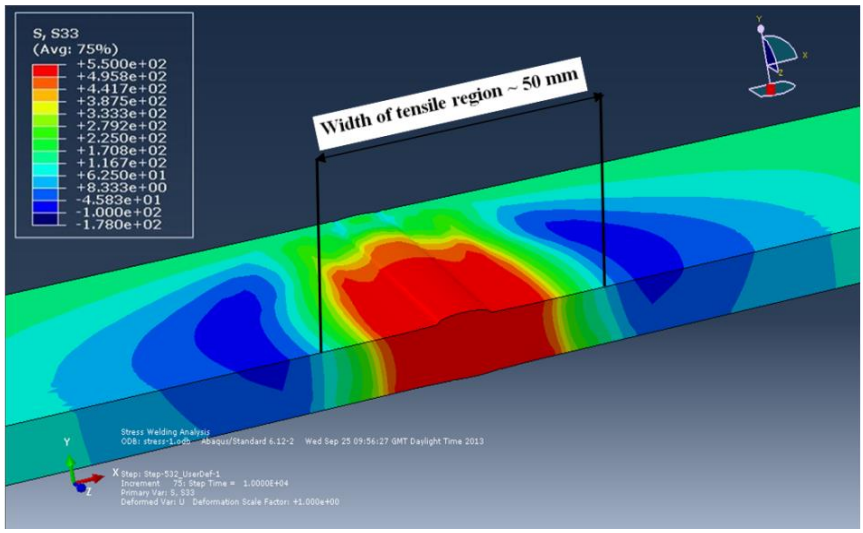

Figure 10-26 Results of structural model for GTA welding 10 mm thickness

The model results are compared to both the contour results and neutron diffraction for validation 2 mm below the top surface of weld joint. There is a very good correlation between the model results and the experimental measurement by neutron diffraction technique, and also by the contour method. The tensile region width is much wider in comparison with NGLW; the average tensile width is 50 mm, as shown in Figure 10-27.The peak value for GTAW near to the surface has an average value 500 MPa.

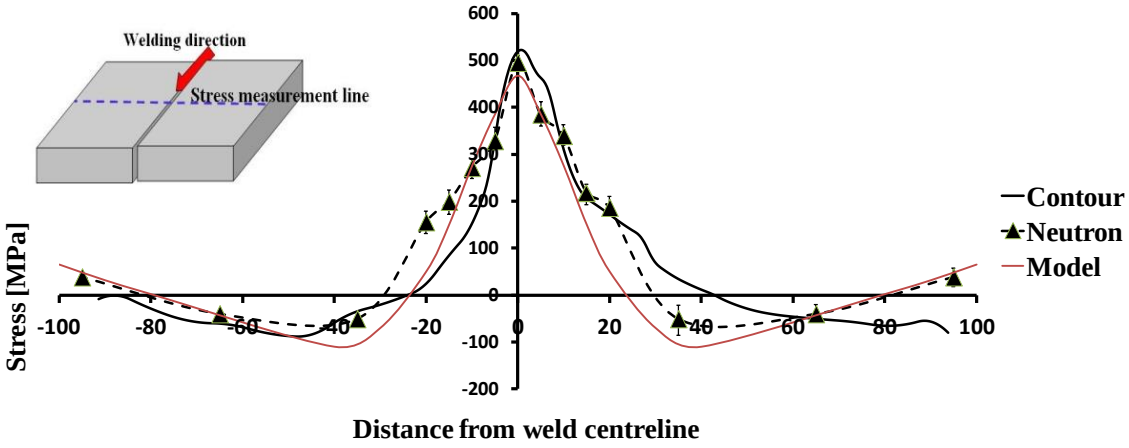

Figure 10-27 Comparison of predicted longitudinal residual stresses against contour and neutron diffraction measurements for GTA

10.7 Summary

- The AWI weld module in ABAQUS provides an efficient tool for simulating the multipass welding process.
- A heat source model has been developed successfully to simulate the real case across the welding beads for both GTAW and NGLW. The results were validated with the experimental results and show a very good agreement.
- AWI shows a development of stress during multi-pass NGLW process efficiently, and predict the stress behaviour for different welding scenarios successfully.

- The size of the finite element mesh has been examined for model convergence. The results show a good correlation between the used mesh and fine mesh densities.
- Modelling results show that the tensile peak of the developed longitudinal residual stress of GTAW welding is higher than NGLW for the same thicknesses, and the width of the tensile region is approximately doubled.
- The results of the NGLW model shows that laser power has a significant influence on the peak value of the induced residual stress across the welding sample. However, the welding speed has little influence over the peak stress values but has a significant influence on the width on the tensile region.

CHAPTER 11. Corrosion and Stress Corrosion Cracking Characteristics of NGLW Joints

11.1 Introduction

Austenitic stainless steels are considered as one of the most weldable alloys amongest stainless steels. In addition, 316L austenitic stainless steel is highly resistant to atmospheric and other mild types of corrosion. Due to their excellent mechanical properties and corrosion resistance, stainless steels are used in many industrial and power generation industries. However, stainless steel corrosion resistance is strongly affected by severe welding thermal cycles, resulting in the degradation of mechanical properties and corrosion resistance [215] - localized attack may occur in many forms, such as pitting or stress corrosion cracking (SCC) [36]. Segregation of some important alloying elements during solidification leads to the depletion of dendrite (or cell) cores from some important elements like Cr and Mo, relative to the parent steel - the result is a loss of pitting resistance [216].

Austenitic stainless steel welded joints are more susceptible to different types of corrosion, such as pitting corrosion and environmental corrosion, but the most significant is SCC, especially in aggressive conditions such the presence of halide ions [215]. In particular, 316L stainless steel tends to be susceptible to the precipitation of chromium carbides in grain boundaries, especially when operated in the sensitization temperature range (427 to 816°C) for long time periods, as previously discussed in detail in the literature review chapter of this thesis.

SCC is considered as a significant challenge in welding stainless steel when the welded material operates in nuclear power generation environments. There are many reasons for the occurrence of SCC, including susceptiblity of material, material properties degradation, exposure to a corrosive environment, and tensile stresses above a threshold (for example due to induced residual stress in weld region) [36]. Control of any one of these factors contributing to SCC can help in the elimination or delay of SCC initiation [217].

The international organization for corrosion control in industry, NACE, state that, chloride stress corrosion is one of the most important causes of failures found in the nuclear industry [218]. The maintenance costs in the nuclear industry due to SCC have been estimated at more than 10 billion dollars for the U.S alone in the last thirty years. Moreover, SCC can drastically shorten the design life of a facility, and may be a cause of sudden catastrophic failure with no warning.

Annealing welded components can be used as a stress-relief method to control SCC, but the process is not suitable for large componets. Surface enhancement techniques such as shot peening, cavitation peening, and Low Plasticity Burnishing (LPB) have been proposed as methods to impede SCC and improve the fatigue life [219]. These processes induce compressive residual stresses into the surface of materials. However, the depth of compression achieved is typically shallow, and SCC often still occurs. These operations also cause a considerable amount of cold working, which can exceed 50%; high levels of cold work further increase the risk of SCC initiation, and produce a thermally unstable residual stress state. It is difficult to apply these operations on massive size components. Retention of beneficial residual compression is critical in power generation applications at the operating temperatures found in boiling water reactors, steam turbines and pressurized water reactor systems [217].

There are four important considerations for weld joints inside power plants, in order to improve their lifetime, as follows: avoidance of solidification cracking, preservation of corrosion resistance of the weld and heat-affected zones, minimizing the heat entering the weld joint, and minimizing the residual stresses induced in the weld joint.

The objectives of the investigation reported in this chapter are:

1- To study the influence of the different welding techniques (GTAW, autogenous laser welding, NGLW) on the material composition in the weld bead region, and the impact of these changes on the corrosion resistance behaviour of different welding techniques in aggressive environments.

2- To examine the influence of the welding techniques on the environmental corrosion resistance behaviour in highly aggressive conditions such as halide presence at high temperature and humidity.

3- To investigate the pitting corrosion behaviour of the welding techniques using polarization curves.

4- To investigate the tendency for solidification cracking across welding beads.

5- To investigate the tendency of GTAW and NGLW techniques to SCC in a high-pressure reactor working environment.

11.2 Chemical composition changes in welded zones

The chemical compositions of the welded zones were investigated for three different welding techniques: autogenous laser welding, NGLW, and GTAW.

11.2.1 Element analysis of base material

Energy Dispersive Spectroscopy EDS was used for the element analysis of the base material - the average results are shown in Table 11-1. These results show good correlation with the values for 316L defined in ASTM A240 and ASME SA-240.

Table 11-1 Material composition of stainless steel 316L

Element	C	Mn	Cr	Ni	Mo	N	S
Percentage by	0.027	2.02	16.68	9.9	2.03	0.05	0.02

11.2.2 EDS investigations for welding beads

Element analysis of the weld bead composition was carried out for an NGLW bead using EDS. More than one scanning process was performed inside the weld bead in order to improve the reliability of the results, as shown in Figure 11-1. The results of the EDS scanning are shown in Table 11-2.

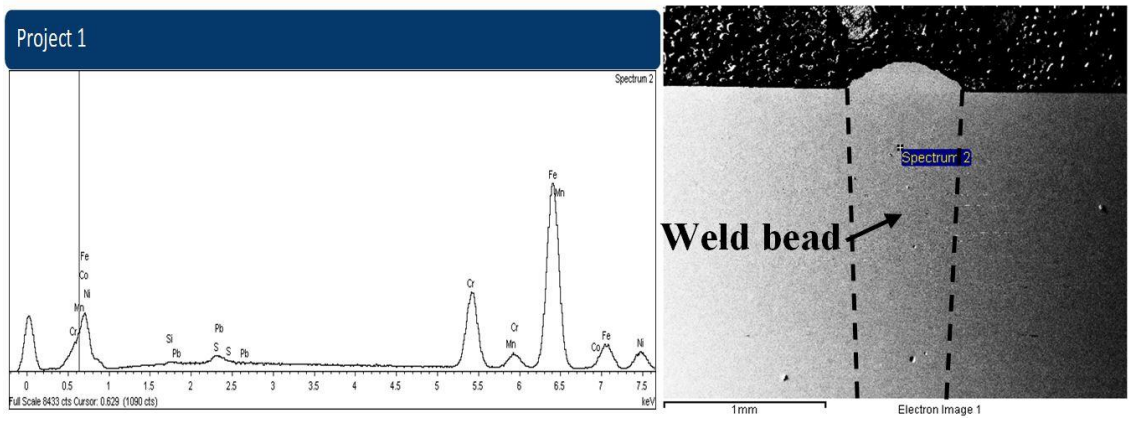

Figure 11-1 EDS results for NGLW bead analysis

These measurements were repeated for GTAW and autogenous laser weld beads. The results tests for the different welding techniques, and for the base material for multi measurements, are shown in Table 11-2. These results will be used as a reference for the comparison of corrosion behaviour between different welding techniques.

Table 11-2 Compositional analysis for different welding beads (in percent)

Element	Base AR			Autogenous		GTA Welding		NGLW	
	(a)	(b)	(c)	(a)	(b)	(a)	(b)	(a)	(b)
Cr	16.68	16.58	16.70	16.65	16.52	16.11	16.2	16.56	16.44
Mn	1.63	1.64	1.53	1.63	1.53	1.37	1.69	1.72	1.68
Mo	2.54	2.4	2.58	2.49	2.37	2.12	2.16	2.29	2.44
Ni	9.86	9.82	9.94	9.86	9.60	10.63	10.46	10.87	10.47
Fe	68.41	68.27	68.50	68.39	68.50	67.22	66.52	67.47	67.45
N	0.04	0.05	0.05	0.04	0.05	0.02	0.02	0.04	0.03
Totals	100	100	100	100	100	100	100	100	100

The element analysis shows slight changes in the Cr content across different welded beads, in comparison to the base material. Generally, the average content of Cr is higher in the autogenous laser weld zones, compared to GTAW; this could improve the passivation of the laser-welded area against corrosion, and this will be investigated in detail in the following sections. The other important result is a slight change in the molybdenum content between different weld beads and the base material, as shown in Table 11-2 . The average molybdenum content in the base material was 2.5%, this was decreased to 2.1% in the case of GTAW, while in the autogenous laser welding bead it was 2.4%. The decrease in molybdenum percentage values will influence the corrosion resistance, and decrease the hot strength by about 40%, especially at temperatures above 760°C [35].

11.3 Pitting Resistance Equivalent Numbers

The pitting Resistance Equivalent Number (PREN) allows comparison of the pitting corrosion resistance of various types of stainless steels, based on their chemical composition according to following equation [220].

$$PREN = \%Cr + 3.3(\%Mo) + 30(\%N) \quad (11.1)$$

The PREN are useful for ranking and comparing the different alloys and grades; they will be used primarily for the evaluation of the GTAW and laser weld beads, and of the base material. The average values from the content analysis will be used to calculate the pitting resistance equivalent for each method.

$$PREN_{Base} = 16.65 + 3.3 * 2.46 + 30\ (0.05) = 26.268$$

$$PREN_{Laser} = 16.58 + 3.3 * 2.43 + 30(0.05) = 26.1$$

$$PREN_{NGLW} = 16.60 + 3.3 * 2.42 + 30(.04) = 25.786$$

$$PREN_{GTAW} = 16.15 + 3.3 * 2.14 + 30(.02) = 24.112$$

The PREN values show that both laser welding and NGLW give results closer to the base material PREN; the level of segregation of important elements is greatly decreased due to the high welding speed and low heat input to the weld joint. The GTAW PREN value decreased to 24.1, indicating that the laser welding technique conserves the material passivity against pitting corrosion better than GTAW, due to the decreased amount of heat entering the weld joint during laser welding. The welding speed of the laser method is much higher than that of GTAW.

v_{laser}=30 mm/s, v_{NGLW} = 9.5 mm/s, and average v_{GTAW} = 1.5 mm/s. This results in a decreased amount of micro segregation, especially for molybdenum, and decreased chromium depletion, as will be discussed in detail in Section 11.6.

11.4 Inter-granular corrosion characteristics of welds

Chloride ions are the most common and important atmospheric corrosive agent for ferrous metals; chloride anions combine with ferrous cations produced in the anodic reaction, resulting in the stimulation of corrosive attack [221] - this is considered a major mechanism for corrosion in power plants. Austenitic stainless steel is susceptible to SCC by an anodic active-path mechanism, especially when used in aqueous chloride solution environments. Immersion granular corrosion tests were carried out for three weld joints with high concentrations of $MgCl_2$. The shape of the weld beads and position of the corrosive droplets are shown in Figure 11-2.

The test conditions were: concentration of $MgCl_2$ 1 mole/L, droplet volume 0.5 μL, temperature 80°C, and relative humidity 30% during the experimental period. The

immersion corrosion was investigated at intervals of 240 hours, 360 hours, 480 hours and 500 hours.

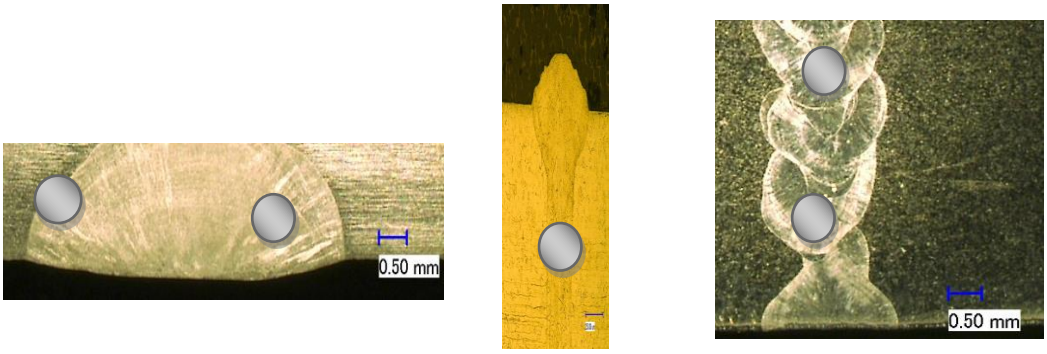

a- GTA b- Laser c - NGLW

Figure 11-2 Droplet position on the welded samples

11.4.1 Results of Inter-granular corrosion testing

The results are shown in Table 11-3. The green colour indicates no evidence of corrosion, and the red colour indicates observation of corrosion; the final column represents the corrosion behaviour of the weld beads after 500 hours of testing.

Table 11-3 Corrosion behaviour against different welding techniques

duration	240 hours	360 hours	480 hours	500 hours	SEM for surface corrosion behaviour
Base	No corrosion	No corrosion	No Corrosion	Corrosion	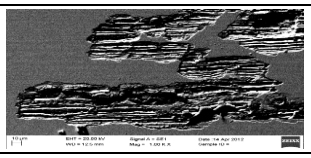
Laser	No corrosion	No corrosion	No corrosion	Corrosion	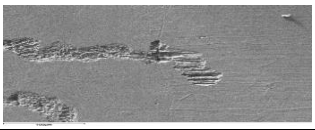
GTAW	No corrosion	Corrosion	Corrosion	Corrosion	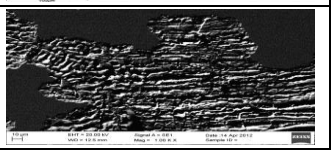
NGLW	No corrosion	No corrosion	Corrosion	Corrosion	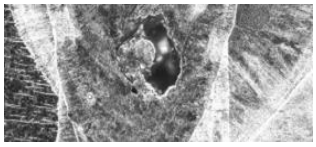

The SEM images show different corrosion behaviours for different welding techniques, and for the base material. The corrosion started after 360 hours in the GTAW bead, as shown in Table 11-3; the corrosion is aggressive and the propagation rate is high, as will be discussed in detail later in this section. Corrosion of the NGLW weld bead was observed after 480 h, followed by the corrosion of the autogenous laser weld bead and the base material, approximately at the same time - the corrosion started after 500 h, and the propagation rate was very low.

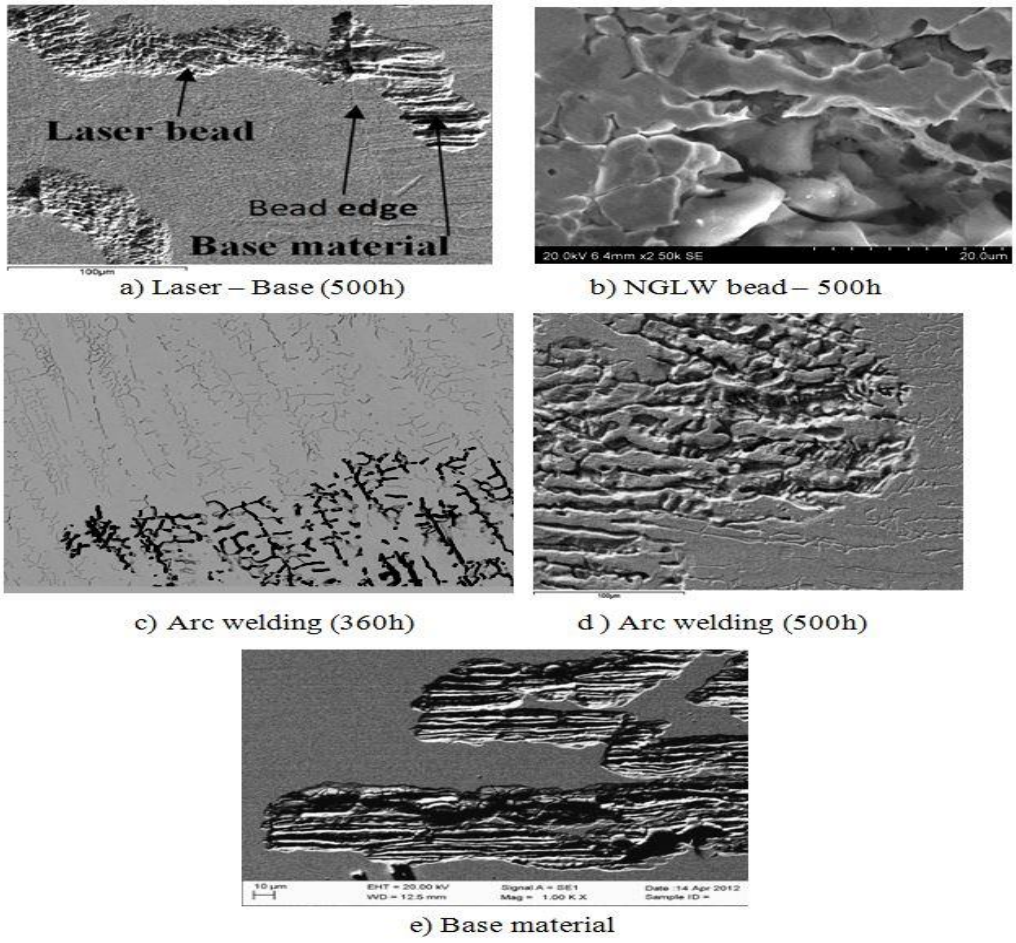

Figure 11-3 Corrosion behaviour against different welding techniques

The corrosion initiation and propagation path were different in the four cases. In GTAW, the corrosion started in the dendrite core, as shown in Figure 11-3c, and then propagated laterally between the dendrite arms, as shown in Figure 11-3d. The corrosion in the base material followed the rolling lines, starting in approximately straight lines in the rolling direction and propagating across these lines, as shown in Figure 11-3a,e. Autogenous laser welding has no specific path for corrosion initiation

and propagation, but the corroded regions show a very fine microstructure, as shown in Figure 11-3a. NGLW corrosion is similar to that of GTAW; the corrosion initiates in the dendrite core, as shown in Figure 11-3b, and propagates in the transverse direction but with a slow rate. The corrosion behaviour for both laser welding and NGLW beads has a late start and slow propagation rate with respect to GTAW. The improved corrosion resistance of laser welding and NGLW, relative to GTAW, is possible due to the low heat input to the weld joint during the welding process reducing micro-segregation of important element like Mo, Cr, Mn and chromium depletion.

11.4.2 Morphological characteristics

A quantitative study was carried out on the corrosion of the different weld beads; the target was to evaluate each weld bead in terms of the total corroded area and the maximum penetration depth, in order to evaluate the propagation of corrosion in the lateral and transversal (depth) directions, for the three welding techniques, compared to that of the base material. The examination of the morphology was applied to the samples after 500 h in the test conditions.

A Digital Keyence microscope, model VHX-500, was used to construct 3D images of the corroded surfaces, as shown in Figure 11-4. These images were used for the evaluation of the corrosion of different weld beads, by the precise measurement of the corroded area. In addition, the profile of the surface was used to measure the depth of the corrosion pits across the weld beads.

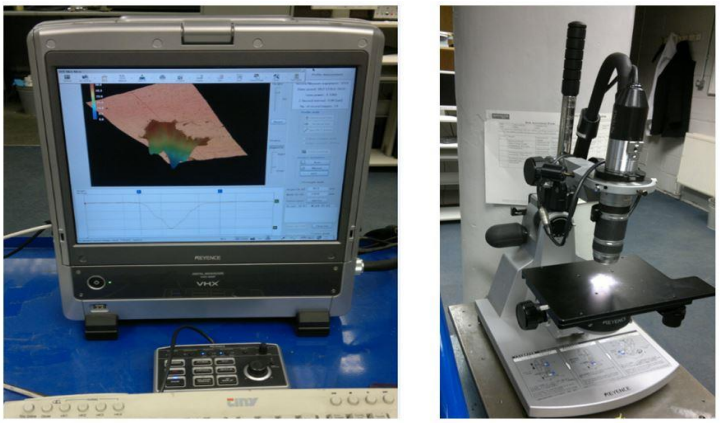

Figure 11-4 3D image microscope

11.4.2.1 Corrosion behaviour in base metal

Figure 11-5 shows the corrosion profile of the base material. The corroded area and the maximum corrosion depth were evaluated; the total corroded area was approximately 154,910 μm^2, with a maximum depth of 63 μm, according to length of AB as marked with a red rectangle in Figure 11-5.

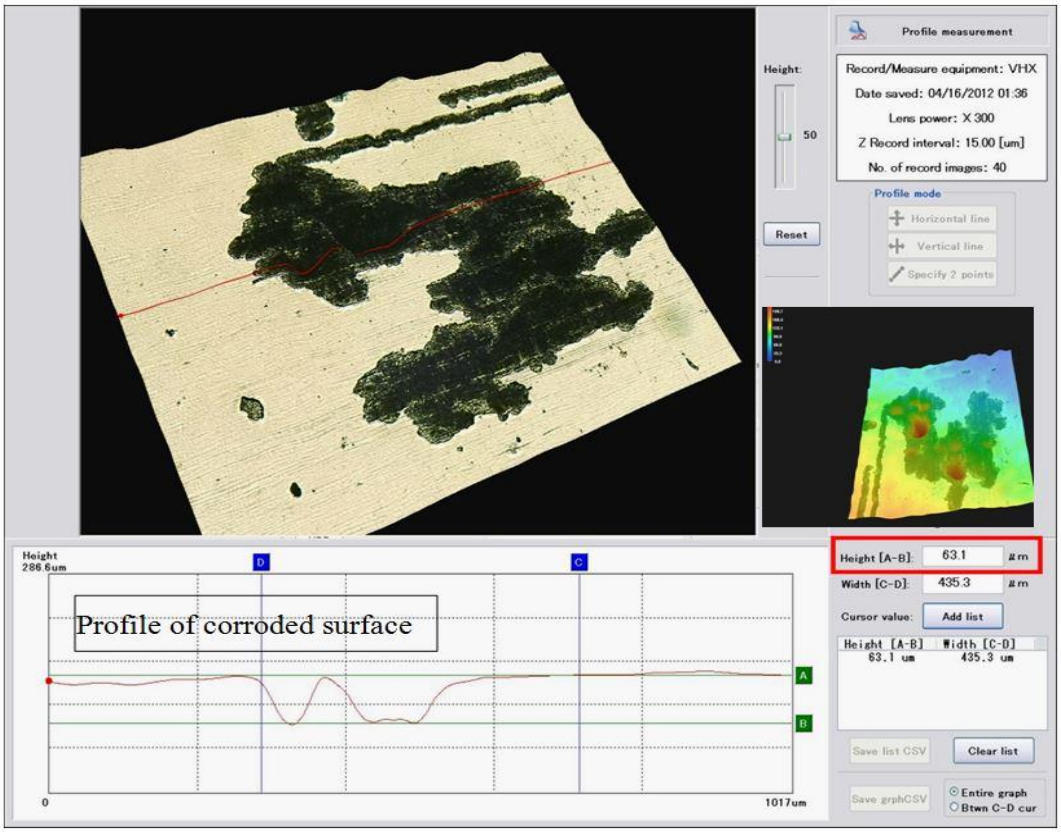

Figure 11-5 Corrosion profile in Base material

11.4.2.2 Corrosion behaviour in GTA weld fusion zone

The corrosion profile in the GTA weld bead is shown in Figure 11-6; the 3D image clearly shows that corrosion is very aggressive in the GTA bead. Both the corrosion area and pit depth are very high in comparison to the base material. The measured values are as follows;

Total corroded area approximately = 1,123,857 μm^2, maximum pit depth = 170 μm.

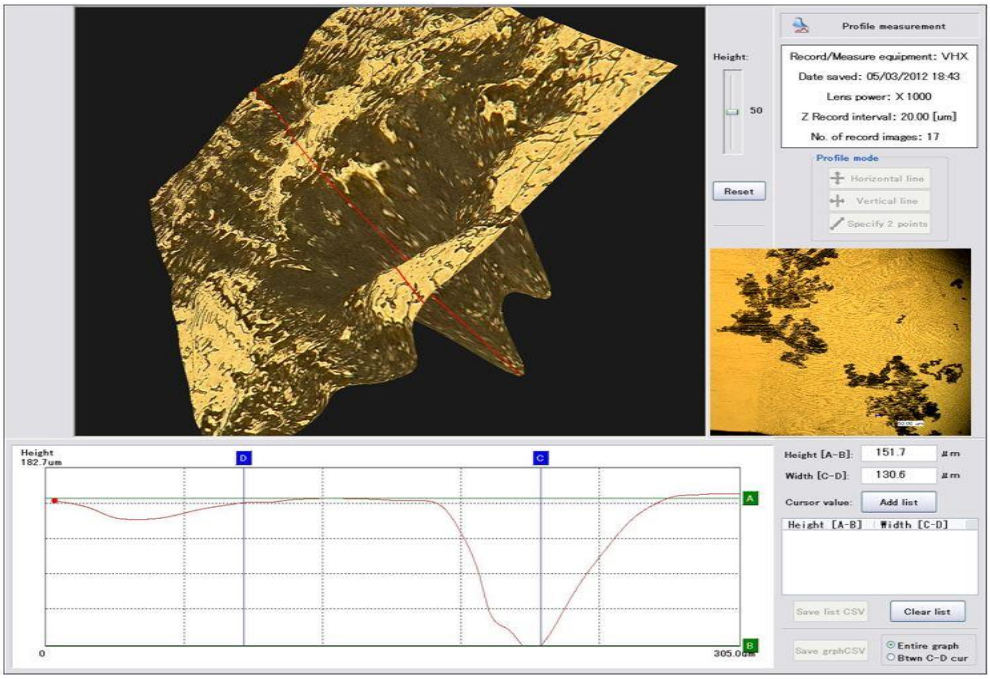

Figure 11-6 Corrosion profile in GTA welding bead

11.4.2.3 Corrosion behaviour in autogenous laser weld fusion zone

The laser weld bead was evaluated for corrosion. The result shows a low propagation rate for the corrosion in both directions compared to GTA welding, Corrosion area approximately = 125,526 µm2, and maximum depth = 48 µm as shown in Figure 11-7.

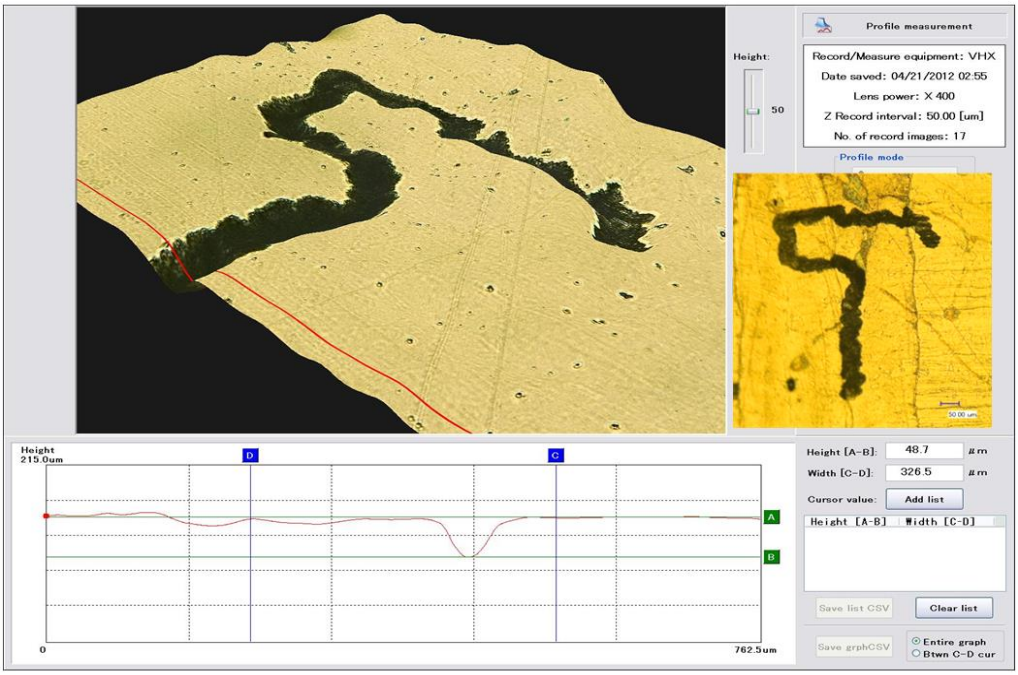

Figure 11-7 Corrosion profile in laser welding bead

11.4.2.4 Corrosion behaviour in NGLW fusion zone

The NGLW bead was tested for corrosion behaviour using the same test condition. The corroded area was approximately 254,029 μm^2, and the maximum pit depth 55 μm, as shown in Figure 11-8.

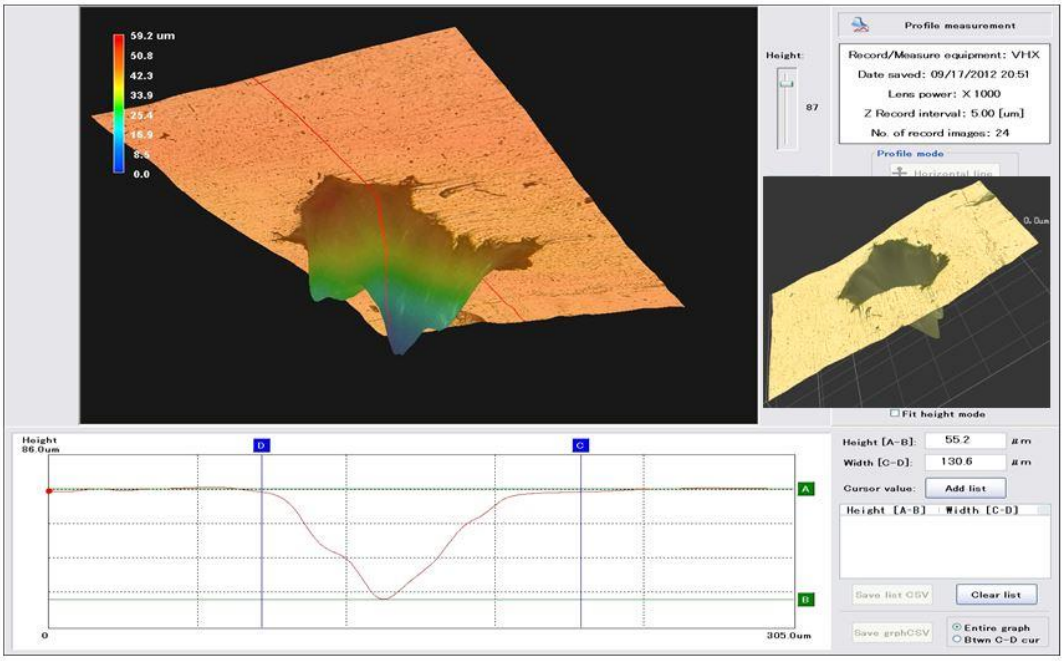

Figure 11-8 Corrosion profile in NGLW bead

Table 11-4 shows the morphological characteristics of different welding beads with respect to base material. As a conclusion of the quantitative evaluation, the GTA welding has the lowest passivation against the corrosion; the corrosion aggressivety (propagation rate) in both the lateral and transverse directions is higher in the GTA weld bead than for the other methods. Autogenous laser welding represents the highest passivity against the corrosion. Although NGLW has lower passivity than autogenous laser welding, it is considered very corrosion resistant with respect to GTAW. The next sections will include detailed discussion of the reasons for the corrosion behaviour in the different weld beads.

Table 11-4 Corrosion morphological characteristics of welding beads with respect to base material

Welding	Corroded area [μm^2]	Maximum bit depth [μm]
Autogenous laser welding	125,526	48
NGLW	254,029	55
GTAW	1,123,857	170
Base	154,910	63

11.5 Sensitization phenomenon

The concentration of chromium plays the dominant role in the passivity of ferrous alloys. The pitting potential was correspondingly found to increase dramatically as the Cr content increased above the critical 13% value needed to create stainless steel. Cr depletion is reported as the main reason for decreases in stainless steel passivation and high rate metal dissolution [222]. In addition, Mo percent in stainless steel is very critical for corrosion resistance, and segregation will lead to a decrease in the corrosion resistance [223].

Sensitization is considered as a main reason for the decay in the pitting corrosion of stainless steel owing to welding. Sensitization is caused by the formation of chromium carbide along grain boundaries, resulting in the depletion of chromium in the region adjacent to the grain boundary. This chromium depletion produces localized galvanic cells, due to the potential difference between the chromium depletion zone and the precipitation zone, as shown in Figure 11-9.

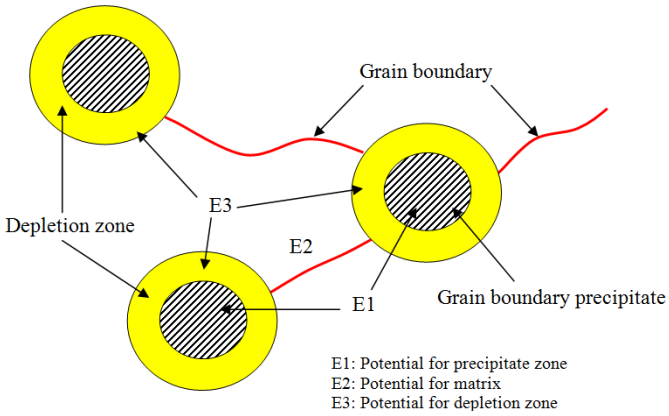

Figure 11-9 Depleted region adjacent to precipitate

If this depletion reduces the chromium content sufficiently, the region will become sensitized to corrosion, resulting in inter-granular attack. This type of corrosion most often occurs in the weld bead region, especially near to the HAZ.

The formation of chromium carbide is the main cause of sensitization; it can be described by the C-shaped carbide nucleation curves on the continuous cooling diagram shown in Figure 11-10. The susceptibility to sensitization is a function of temperature, time, and carbon content. If the cooling rate is sufficiently high as shown in (Figure 11-10 curve A), the cooling curve will not intersect the given C-shaped curve for chromium carbide and the stainless steel will not be sensitized; by decreasing the cooling rate, the cooling curve (curve B) eventually intersects the C-shape. At very low cooling rates, the formation of chromium carbide occurs at higher temperature and allows for more nucleation and growth, resulting in a more extensive chromium-depleted region. Laser welding is advantageous, since both the welding speed and cooling rate with this technique are higher, in the order of 10^6 °C/s [171], which help to avoid sensitization .

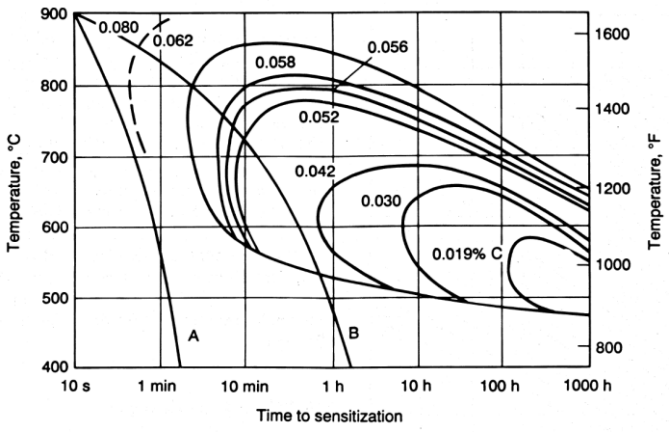

Figure 11-10 Carbide nucleation curve [35]

11.6 Weld bead investigation using EDS element analysis

In order to understand the difference in the corrosion performance of each weld bead, material analysis was performed across the dendrite of each welding bead. The aim of this work was to trace the change in the material composition, and the depletion of some elements across the dendrite in the weld bead region, in order to understand the different corrosion behaviours. The evaluation took the form of point spectrum measurements for

a number of points inside and outside the dendrite arms. Line spectrum measurement was performed across the dendrite region, for three different samples for each welding techniques in order to improve the reliability of the captured data from the point spectrum analysis.

11.6.1 Element analysis of GTA weld bead

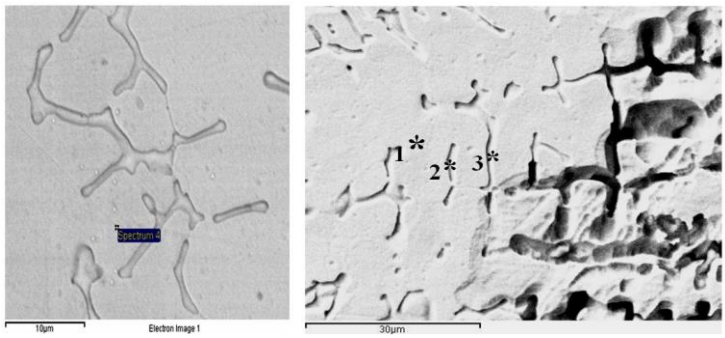

a - point spectrum b- point spectrum close to corrosion region

Figure 11-11 Point spectrum analysis GTAW bead

Figure 11-11 shows the spectrum analysis of the GTAW bead carried out at different points across the dendrite arms in the weld bead. The analysis was repeated in the welded region, and close to the corrosion starting region, as shown in Figure 11-11 a, b. The results of the spectrum analysis at these points are shown in Table 11-5, and show a significant variation in the element distribution across the weld bead.

Table 11-5 Result of spectrum for GTA welding bead

Weight%	Spectrum 1	Spectrum 2	Spectrum 3	Spectrum 4
Cr	16.13	15.90	27.67	21.22
Mn	1.81	0.87	0.63	1.31
Fe	68.30	65.87	61.45	65.51
Ni	11.19	10.24	9.93	10.27
Mo	1.58	1.84	2.32	1.86

Line spectrum measurement was carried out on the weld bead to confirm the point spectrum measurement for the element distribution. The position and direction of the scanning is shown in Figure 11-12; the scan line passed through three dendrite arms at positions A, B, C to measure the material composition changes across these dendrites.

The composition values at positions A, B, C will be compared with values at other positions to investigate the difference in the material composition along the line-pass.

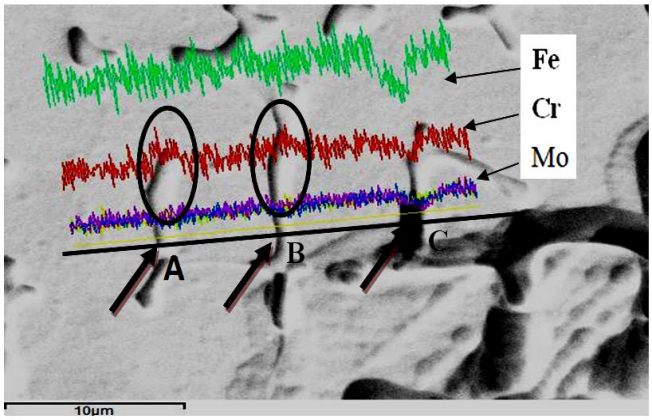

Figure 11-12 Line spectrum analysis of GTAW bead near to corrosion

The elements distribution is shown in Figure 11-12. There is disturbance of the chromium contents across the dendrites at positions A and B. These results correlate well with the point spectrum analysis of chromium depletion in some regions, and enrichment in other region, due to sensitization phenomena. At point C, a decrease in all the detected elements percentage was noticed; the reason for this is the corrosion of the surface starts at this point, and consequently the distance between the detector and detected surface is increased, therefore the reflected data from the surface was weaker.

Further scanning was carried out in two welding beads, which were welded with different speeds. Figure 11-13 shows the scanning result for GTAW sample with an average welding speed 95 mm/min. The fluctuation is very clear for both Cr and Mo due to lower welding speed and increased Cr depletion, which is considered the main reason for aggressive corrosion. Decrease of the welding speed led to prolonged exposure to the sensitization temperature (427 to 826°C), which is very harmful for the corrosion resistance of the welded region. Mo shows a disturbance in the distribution, which is considered another reason for decreasing the resistance to pitting corrosion.

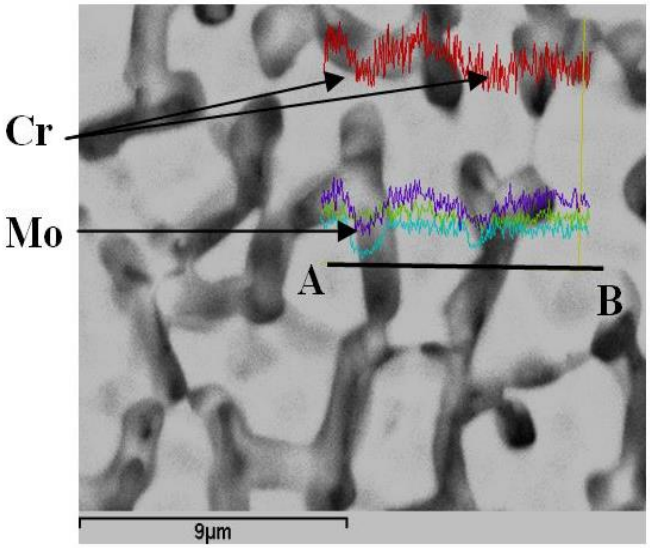

Figure 11-13 Line spectrum analysis across dendrite arm

11.6.2 Element analysis of autogenous laser weld cross section

Scanning has been repeated across the laser dendrite arms in the autogenous laser welding beads. High speed welding results in a very fine dendritic structure. The analysis has to be carried out on a high magnification scale to measure the elemental composition across the dendrite structure of the laser bead. The dendrite arm spacing is in the order of 2 µm [171] as shown in Figure 11-14. The output results for the material analysis are shown in Table 11-6.

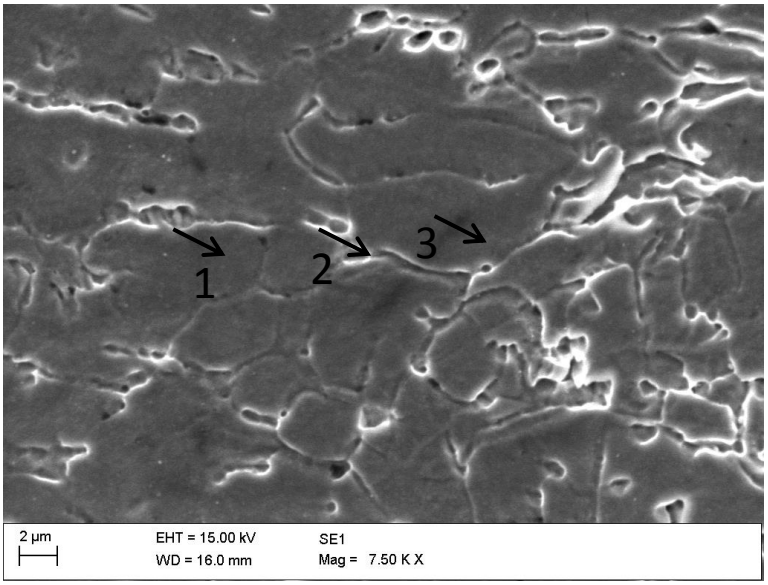

Figure 11-14 Point Spectrum for Laser bead

Table 11-6 Point spectrum analysis inside laser weld bead

Element	Spectrum	Spectrum	Spectrum
Cr	17.21	16.46	16.89
Mn	1.28	1.16	1.12
Fe	65.55	66.67	64.61
Ni	9.24	8.15	8.93
Mo	2.13	2.56	2.95

The amount of the chromium content in the laser welding bead was found to be between 16.46% to 17.21% as shown in Table 11-6, which is a very small depletion percent in comparison to the value found across the GTAW bead dendrite arms, where the corresponding values across the GTAW dendrite ranged from 15.9% to 27.67%, as shown in Table 11-5.

Line scanning across laser welding beads was carried out to investigate the element fluctuation and sensitization percent across the dendrite arms. Two specimens with different welding speeds were scanned across line AB, and the spectrum results are shown in Figure 11-15.

The analysis shows an approximately homogeneous distribution for the elements, with minimal variation in the percentage across the line for welded samples with speed 30 mm/s as shown in Figure 11-15 a. This result indicates a smaller micro- segregation

affect in the weld bead. The process was repeated across dendrite arms of laser welded specimen with speed 20 mm/s. The results also show a very limited fluctuation for the Cr, and Mo as shown in Figure 11-15 b.

The sensitization percentage inside the weld bead is very limited due to high welding speed, and the limited heat input during the welding process, consequently the passivity of the material is conserved.

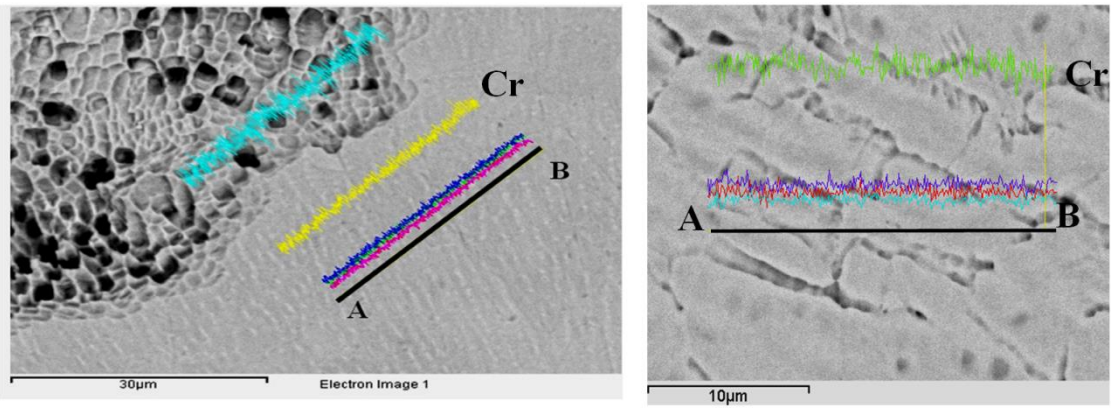

(a)Welding speed 30mm/s (b) Welding speed 20 mm/s

Figure 11-15 Line scanning across dendrite arm

11.6.3 Element analysis of NGLW cross section

Spectrum analysis was applied to the NGLW bead. The results of the SEM scanning show a fine dendrite arm spacing with respect to the GTAW dendrite arms. The average arm spacing was 4 µm. The spectrum measurements were applied at points 1 and 2 inside the dendrite, and points 3 and 4 outside the dendrite, as shown in

Figure 11-16. The chromium content ranged from 17.39% to 21.21%, showing less sensitization of the Cr for this welding technique, as shown in Table 11-7. In addition there was limited segregation of molybdenum; consequently the material still has a significantly higher corrosion resistance than GTA welded material.

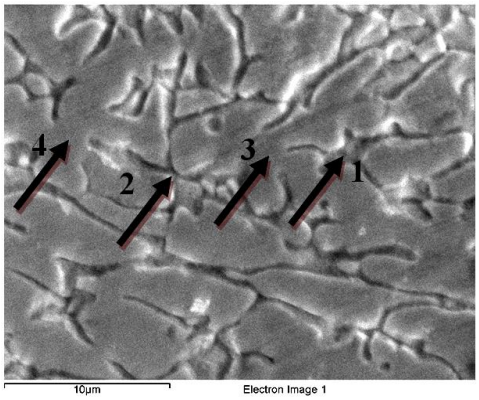

Table 11-7 Material analysis results

	Cr	Fe	Ni	Mo	Mn
Spectrum 1	17.39	69.45	10.76	2.36	1.80
Spectrum 2	17.64	67.45	11.99	2.85	1.87
Spectrum 3	18.59	67.18	11.59	2.91	1.63
Spectrum 4	21.21	66.94	10.96	2.33	1.54

Figure 11-16 Position of spectrum analysis

Line spectrum analysis was carried out across the NGLW bead at two different positions (columnar - equiaxed) dendritic microstructure are shown in Figure 11-17. The results of scanning line AB show a small variation in the element percentage. The Cr distribution is considered homogeneous in comparison to arc welding results, as there were no sharp changes across the dendrites as shown in the yellow colour in Figure 11-17 a for outer region of the weld bead (columnar dendrite region).

The central position of the weld bead (equiaxed dendritic region) is shown in Figure 11-17 b. The sensitization due to Cr depletion inside the welding bead is very small due to relatively limited heat entering the weld bead during the welding process. Moreover, the results show very limited segregation of molybdenum and homogenous element distribution along the scanning direction as shown in purples colour in Figure 11-17 b.

The analysis across the weld bead of the different welding techniques shows that the GTAW bead had the highest variation in the Cr content. This is might be associated with sensitization phenomenon.

Another reason for the aggressive corrosion might be the micro-segregation of the important elements, especially molybdenum. The value of the micro-segregation is at its maximum in the GTAW bead. The NGLW bead appears to have greater passivityto corrosion than the GTAW bead.

(a)

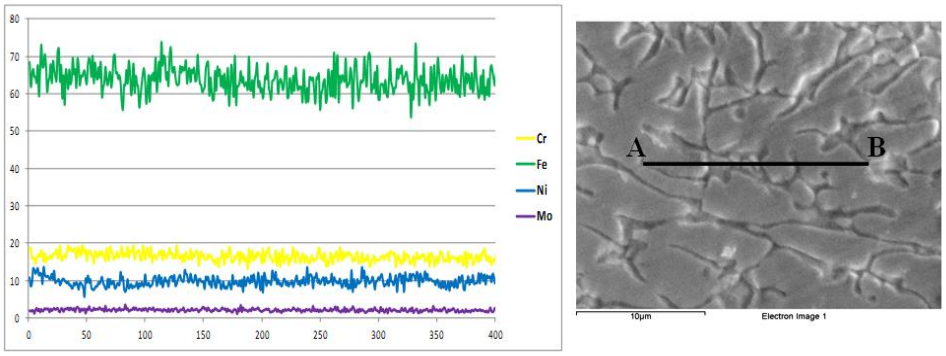

(b)

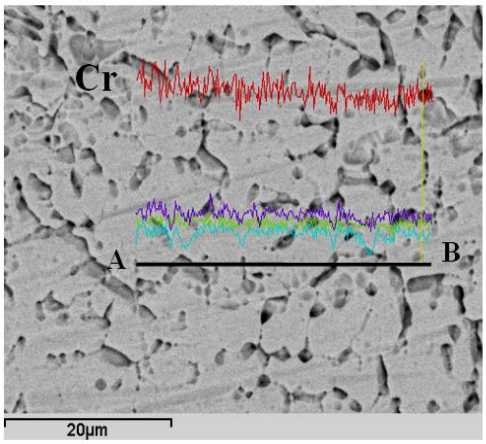

(a) Welding speed 9.5 mm/s (b) Welding speed 12 mm/s

Figure 11-17 Line scanning across NGLW bead

11.7 Solidification cracking and Ferrite contents in the welding bead

The ferrite concentration is very important in austenitic stainless steel weld solidification. Due to the solidification behaviour of austenitic stainless steels, it is necessary for weld deposits to solidify as primary ferrite, if hot cracking is to be minimized [40], as discussed in detail in the literature review. The optimum ferrite content is between 3% and 8% by volume in the weld deposit, in order to maximize the solidification cracking resistance. Ferrite contents above 3% by volume usually guarantees primary ferrite formation, and thus reduces hot cracking susceptibility [50].

X Ray diffraction for ferrite percentage in the weld bead.

X-ray diffraction (XRD) is a powerful non-destructive technique for characterizing crystalline materials. It provides information on structures and phases, and it represents

a fingerprint of periodic atomic arrangements in the material. Weld bead solidification behaviour is very sensitive to the ferrite concentration in the weld bead; the mechanical properties of the weld joint are directly linked to this percentage. XRD analysis was carried out for weld beads produced with GTAW, autogenous laser welding and NGLW.

The results show that the average ferrite phase in the GTAW bead is 3.64%, whereas it is 1.5% and 1 % for NGLW and autogenous laser welding respectively. These results indicate that autogenous laser welding and NGLW solidification are more susceptible to solidification hot cracking due to the lower ferrite percentage compared to GTAW welding [40]. It is critical to control the level of impurities (P phosphorus, S sulphur) in the weld fusion zone, and if necessary change the filler wire used to a higher ferrite concentration, in order to decrease the probability of solidification cracking occurring, especially in the case of high-power density high-speed welding processes.

11.7.1 Primary solidification mode for conventional arc welding bead

The primary phase solidification graph for stainless steel, from the Welding Research Council (WRC-1988), is shown in Figure 11.18. The Cr_{eq} and Ni_{eq} are the chromium and nickel equivalents; they are used to determine the primary solidification phase for the weld bead as shown in the same graph.

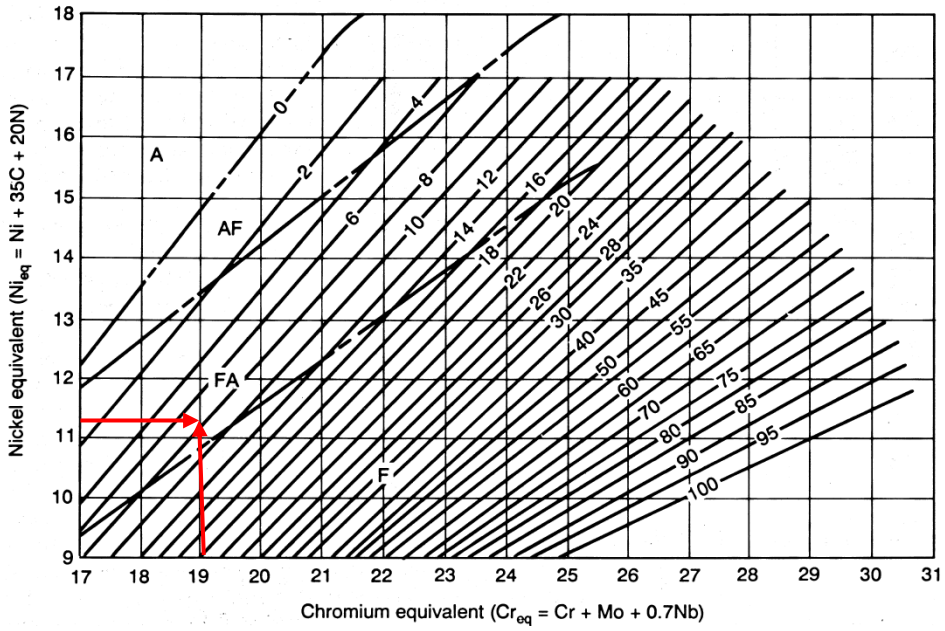

Figure 11-18 Primary solidification graph - Welding Research Council (WRC-1988)

Cr_{eq} = 16.6+2.5+0=19.1

Ni_{eq} = 9.89+(35*0.02) + (20*0.034)= 11.27

The calculated values for the Cr_{eq} and Ni_{eq} indicate that the solidification is a dual-ferrite-austenite mode with primary ferrite, as shown in Figure 11-18. This solidification mode shows that the weld bead is less susceptible to hot cracking during solidification; the welding results for the three methods show no evidence of hot cracking across the welding bead.

11.7.2 Weldability diagram for laser welded austenitic stainless steels

Lippold *et al*. [58] implemented the weldability diagram for laser welded austenitic stainless steels. Solidification behaviour during laser welding is different from that in conventional GTAW, due to the high intensity heat source with a high welding speed leading to low heat input to the weld joint, over a very short time - the solidification rate of laser welding is very high. The limits of the solidification mode for the laser welding process were determined by Lippold *et al.* [58]. These limits define the primary solidification phase and cracking behaviour associated with these regions for laser welding. This diagram is based on the ratio of Cr_{eq}/Ni_{eq} to the phosphorus and sulphur percentage in stainless steel, where the ratio is calculated by the Hammer and Svenson equivalent.

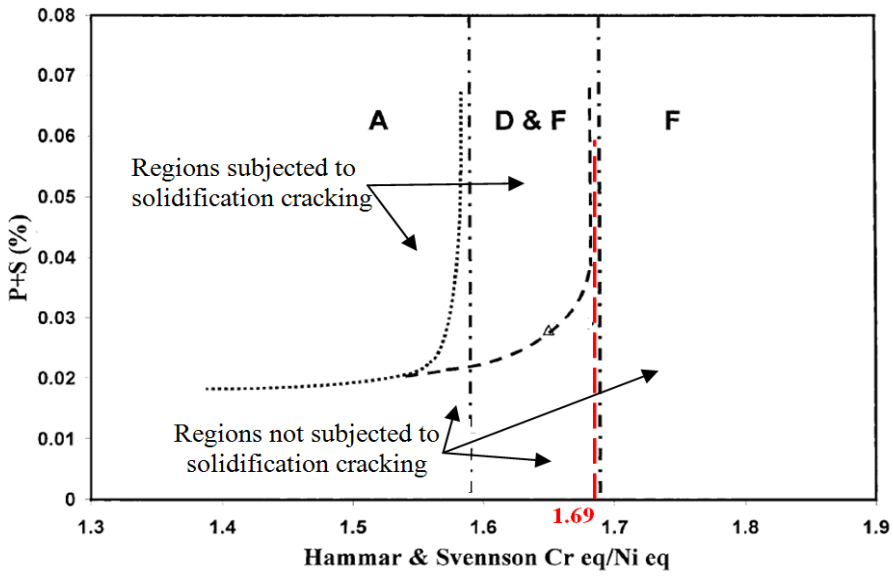

Figure 11-19 Weldability diagram for laser welded austenitic stainless steels

$$Creq = \%Cr + 1{:}37 \times \%\,Mo + 1.5 \times \%Si + 2 \times \%Nb + 3 \times \%Ti \quad (11.2)$$

$$Ni_{eq} = Ni + 0.31 \times \%Mn + 22 \times \%C + 14.2 \times \%N + \%Cu \quad (11.3)$$

According to Lippold *et al.* [58] if $Cr_{eq} / Ni_{eq} < 1.59$, the solidification of the laser weld bead will be primary austenite, which is more susceptible to solidification cracking if the P+S% ≥ 0.02%. The second region is $1.59 < (Cr_{eq} / Ni_{eq}) < 1.69$, so the solidification will be dual-mode primary austenite. This case is less susceptible to solidification cracking only if the P+S % ≥ 0.04%. The limit of tolerable P+S is increasing at the end of this region. In the last region, if $1.69 < (Cr_{eq} / Ni_{eq})$, the solidification of the laser weld bead will be primary ferrite, and in this case the weld bead does not suffer from solidification cracking. All the tested samples showed no cracks, regardless of the impurity levels. The value of Cr_{eq} / Ni_{eq} is calculated for the base material:

$$Cr_{eq} = 16.65 + (1.37*2.5) = 19.075.$$

$$Ni_{eq} = 9.76 + (0.31*\ 1.61) + (22*0.02) + (14.2\ *0.05) = 11.3.$$

$$Cr_{eq} / Ni_{eq} = 1.69.$$

The results are shown in the weldability diagram in

Figure 11-19. The red dashed line marks the Cr_{eq}/Ni_{eq} value for the welded material. The results show that the solidification mode is on the border between the dual mode and the primary ferrite mode - according to the graph. This region is not subjected to solidification cracking. This result is coincident with the experimental results. Figure 11-20 a, b show the GTAW joint of 3 mm and 10 mm thickness, and Figure 11-20 c, d shows the laser welding fusion zone cross-sections of 3 mm and 10 mm thick samples, respectively. There is no evidence of any cracks across any of the weld samples.

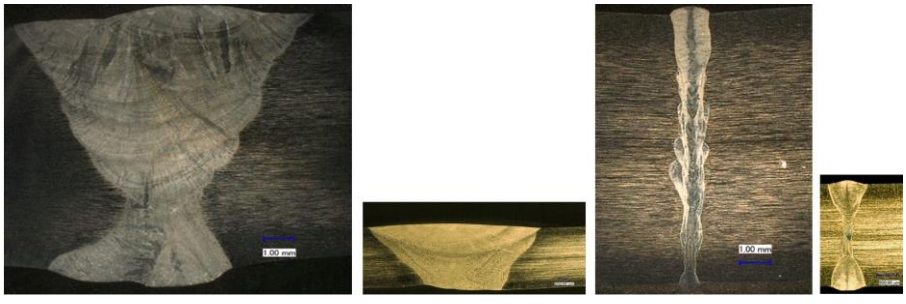

(a) (b) (c) (d)

Figure 11-20 Welding beads of different welding techniques

11.8 Pitting corrosion behaviour

The pitting corrosion behaviour of autogenous laser welding, GTAW and NGLW was investigated along with that of the base material. The polarization curve for each welding technique was examined. The passivation against pitting corrosion is an indication of the stress corrosion cracking (SCC) behaviour of the different welding techniques. Lu *et al.* [215] state that alloys which have better resistance to the pitting are also more resistant to SCC. Polarization scans were carried out for prepared samples using a scan rate of 0.6v/h. The test was performed in 3.56% sodium chloride (Na Cl) aqueous solution at 23°C ± 1°C, according to ASTM G61-86. The pitting corrosion (E_{pit}) is marked and recorded once a rapid increase is observed in the anodic current - at this point the test is finished. A saturated calomel electrode (SCE) was used as the reference electrode. The experimental data was recorded after an initial delay of one hour, to allow the specimen to reach a steady state. The polarization curves for the three welding techniques and the base material are shown in Figure 11-21. The polarization curves all showed similar behaviour in that the open circuit potential (OCP) for all of the curves was ~ 150 mV. However they show different passivation potentials (the extent of the passive zone). The autogenous laser welding passivation potential $E_{pit\text{-}laser}$ was 697 mV as shown in Figure 11-21. The value for the base material $E_{pit\text{-}Base}$ was 517 mV. $E_{pit\text{-}NGLW}$ was 412 mV, and the lowest value was for GTAW; $E_{pit\text{-}GTAW}$ was 325 mV. The critical current was also reduced slightly for the autogenous laser welding. These results indicate that laser weld joints have improved passivation potential with respect to GTAW beads and the base material, due to a homogeneous modified surface with a very fine dendritic structure [171].

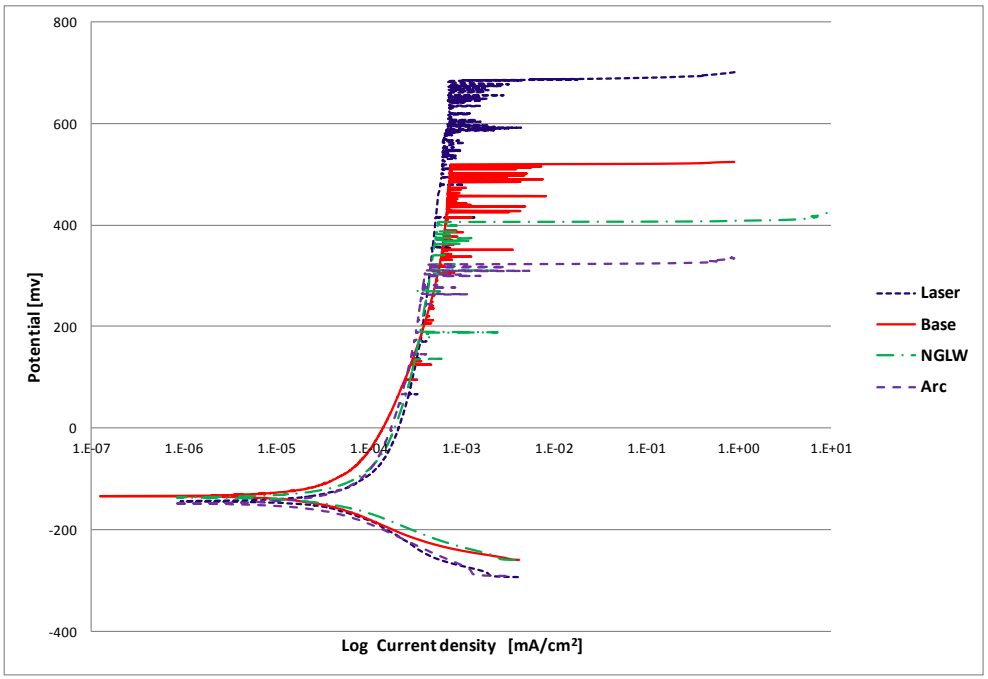

Figure 11-21 Polarization curve for welding techniques

The corrosion rate for each technique was automatically calculated while constructing the polarization curve with the Potentiostat software. The corrosion rate for each constructed curve was calculated according to [224]:

$$\text{Corrosion rate} = \frac{i_o\, N}{\rho\, n\, F} \qquad \textbf{(11.4)}$$

Where, N is the atomic mass = 55.847 g/mole, ρ is the density = 7.90 g/cm^3 , n is the number of free electrons per atom, F is Faraday's constant = 96,487 coulomb/mol, and i_o is the corrosion current calculated according as

$$i_o = \frac{B}{R_P} \qquad \textbf{(11.5)}$$

Where, B is the Stern–Geary constant = 26 mV, R_P is the polarization resistance (slope of potential vs. current plot for each technique).

Corrosion rate $_{laser}$ = 0.552 mm/year.

Corrosion rate $_{Base}$ = 0.703 mm/year.

Corrosion rate $_{NGLW}$ = 0.778 mm/year.

Corrosion rate $_{GTAW}$= 0.977 mm/year.

Autogenous laser welding produced the lowest corrosion rate of 0.55 mm/year, mainly due to the homogeneous bead with very fine dendrites, and the high welding speed and low heat input to the weld joint, which lead to high polarization resistance and consequently low corrosion current. The corrosion rate of the NGLW bead and the base material were very similar, whereas the GTAW weld bead had the highest corrosion rate, due to the high heat input and segregation of some important elements causing degradation in the weld bead passivity.

11.9 Stress corrosion cracking

Stress corrosion cracking (SCC) is the initiation and growth of cracks in metallic materials, enhanced by both stress and corrosive environments. It is considered to be one of the most critical failure mechanisms for stainless steel weld joints.

High temperature, high pressure recirculating loop with a small oxygen percent simulates the primary water of Pressurized Water Reactors (PWR) and will increase the initiation potential for the SCC [225]. The SCC threshold has a direct relationship with both the cold work and sensitization values of the metal [225, 226]. The effect of cold work in SCC initiation is closely associated with residual stress. According to the residual stress behaviour across the weld bead, SCC is expected to be more aggressive in GTA welding compared to NGLW, for the same material thickness, due to higher level of developed residual stress and sensitization percentage.

11.9.1 Experimental procedures

Slow strain rate test (SSRT) was used for assessing the environmentally assisted cracking (EAC) of metallic materials. EAC is any cracking caused by combined effect of stress, and surrounding environment. It includes more than one type such as; hydrogen embrittlement cracking, sulfide stress cracking, and stress corrosion cracking [227]. The SSRT was used previously for investigating the SCC in different environmental conditions and different industries such as nuclear power, oil drilling, and chemical production industries [228].

This test is a dynamic slow strain for relatively rapid screening or comparative evaluation of environmental, processing variables on metallic components. It depends on variations in the load during testing to maintain the constant slow extension rate.

The test follows the guidelines in the ASTM G129-00 for slow strain testing [227].

The local strain rate for SSRT should be slow enough to allow suitable time for the corrosion process, and hydrogen embrittlement to occur in specimens operating in environments containing hydrogen. If the loading rate is increased, the hydrogen has less time to diffuse to the sample surface and so the influence of hydrogen embrittlement will be insignificant. On the other hand it should be fast enough to produce cracking of the sample. The strain rate range 10^{-4} to 10^{-7} s^{-1} [227].

It is strongly recommended, the SSRT application should be used in combination with other testing techniques especially for new applications, where experience is limited as discussed previously in this chapter for other evaluation tests for the welded samples. SSRT should be conducted in simulated service environment such that, testing results and anticipated in service components have an acceptable correlation [227].

Specimens were tested in an autoclave, which is a testing device that can be used to simulate the nuclear work environment (high temperature, high pressure) during the loading of the samples. The autoclave has very accurate control of the strain rate inside the testing chamber, and also has accurate control of circulating gases with a specific flow rate during testing. The test set-up is shown in Figure 11-22.

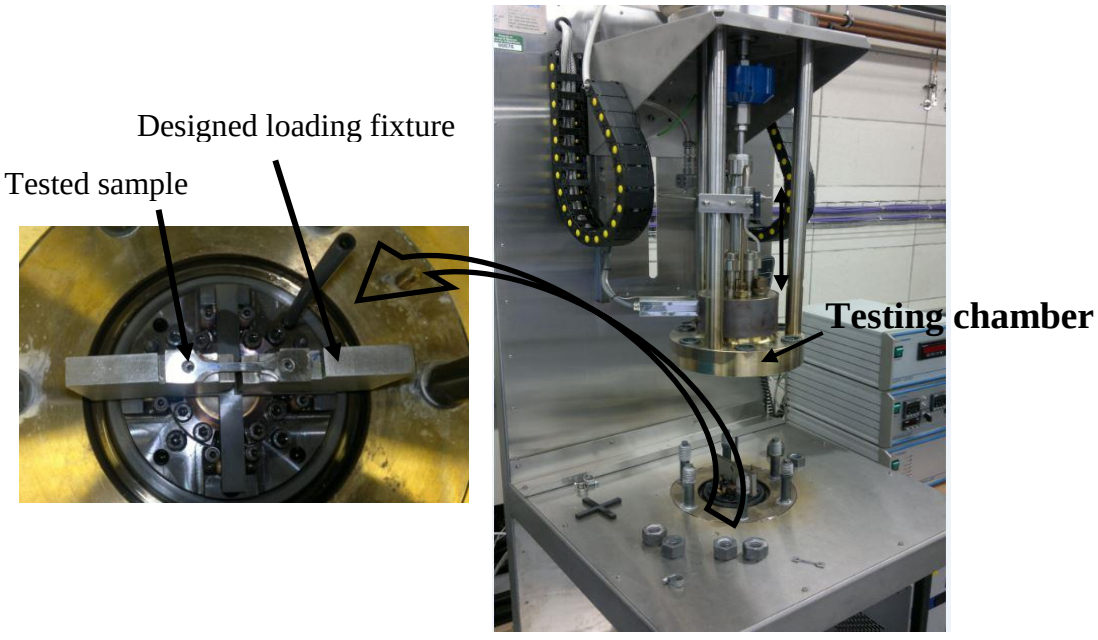

Figure 11-22 Autoclave testing facility

The autoclave loading system depends on a four-point bending load. A special fixture was designed to convert the 4 point bending load in to an axial tensile load. The fixture is shown in Figure 11-23. It consists of two symmetrical parts, which are free to rotate around the main pivot point E. Points A, B, C, and D are the positions of application of the bending load inside the autoclave. By applying the load at these points, the test sample was subjected to tensile loading.

Test samples were cut using wire EDM according to the dimensions shown in Figure 11-23. The surfaces were polished to 4000 grit, and then 1 µm diamond paste was used for fine polishing. The test started by loading the samples with relatively high strain rate of $5.5x10^{-4}$ mm/s, up to the yield of the base material. The strain rate was then decreased to $1.5x10^{-7}$ mm/s. The total testing time was 750 hours. The SSRT samples were analyzed for SCC, and if cracking occurred, characterization of the cracking and its position with respect to the weld bead was performed. The difference in the oxide layer behaviour for each weld bead will be reported in the following section.

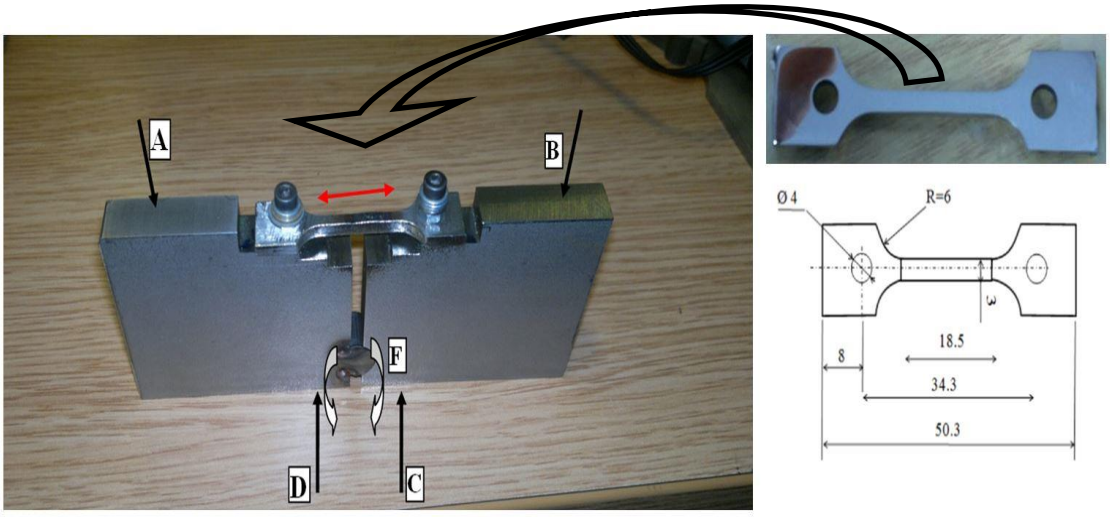

(a) Loading fixture (b) testing sample dimensions

Figure 11-23 Sample preparation – autoclave testing fixture

11.9.2 Testing environment

The tests were performed with simulated PWR primary water, consisting of high-purity water containing 1000 ppm boron, 2 ppm Lithium, and 2 ppm H_2,at a pressure of 200 bar and a temperature of 320 ºC [225]. Chemical analysis of the water was performed during the test in order to measure the element concentrations at different points in the test duration.

11.9.3 Results and discussion

After completion of the test at 750 hours, the total strain in the samples was 4.35%. This strain was not sufficient for crack initiation in the GTAW or NGLW samples. The strain was increased outside the autoclave until it reached to 18 %. Necking then started in both samples. In the NGLW specimen, it developed in the base material at position B, while in the GTAW welding specimen, it developed in the weld bead region at position A, as shown in Figure 11-24. These results indicate that the laser welding method offers better resistance to SCC under high temperature and high pressure conditions, compared to GTAW. These results might be due to the lower residual stress developed in the NGLW sample, and also the lower value of sensitization inside the weld joint with respect to the GTAW joint.

(a)

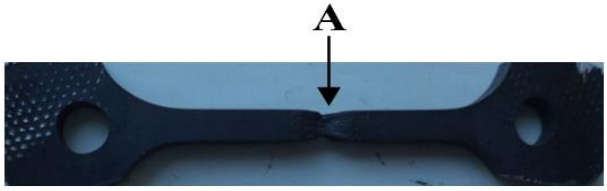

(b)

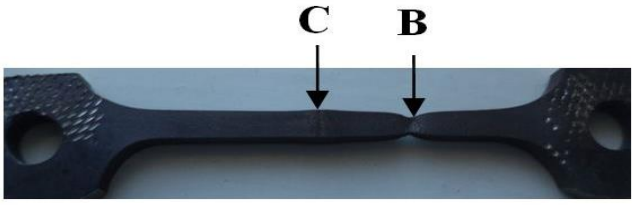

(a) GTA welding (b) NGLW

Figure 11-24 Samples after 750 hours testing inside autoclave

The strain was continued until the sample failed. The value of the strain at failure was 26% for NGLW samples, while it was 22% for GTA welding sample. Figure 11-24 shows the testing specimens for the NGLW and GTAW techniques just before failure. It

is clear that elongation of the laser welding sample is higher than the GTAW sample. Both samples show decreased ductility compared to normal testing conditions as previously discussed in Chapter 8; however GTAW joints are more sensitive to embrittlement compared to NGLW joints.

Stainless steel surfaces are rendered as passive by the formation of a thin surface oxide film that is a "barrier" to corrosion. This passive layer consists primarily of chromium oxides, hydroxides and iron compounds, which form on the outermost surface of the metal phase. The high temperature environment has a significant influence upon the passive film. There is a considerable increase in oxide thickness, with the formation of a double layer, consisting of an internal compact oxide Cr_2O_3 (inner chromium rich spinel), and external, less compact, nickel-rich crystalline oxides [229]. The uniformity and stability of this film will vary depending upon the method of treatment. The passive-layer thickness and stability is critical to weld joint longevity, therefore the thickness of this layer for both samples was investigated in this research.

11.9.4 Glow-Discharge Optical Emission Spectroscopy (GDOES)

Glow Discharge Optical Emission Spectroscopy (GDOES) is a very efficient method for determining chemical composition as a function of depth. It can be used for analyzing the elemental and molecular composition of solids. The depth of penetration has a wide range, from few hundred nm to 50 μm [230]. The method is normally performed in a low pressure cell ~ 10 Torr, with two active electrodes. The cell is filled with neon, and an electric potential is applied between the electrodes such that the specimen becomes the cathode. Positively charged neon atoms are driven to the cathode; when neon ions and atoms strike the sample surface, they knock atoms off the surface, in a process known as sputtering.

Once free of the cathode, atoms move into the bulk of the glow discharge due to the energy they gained from sputtering. The atoms can then be excited by collisions with ions, electrons, or other atoms. Once excited, atoms lose their energy. The wavelength of the released photon can be used to identify the dislodged atom, and by observing the intensity of the emission, the concentration of atoms of that type can be determined.

Both NGLW and GTAW weld bead regions were analyzed across a range of depths, in order to investigate the protective (oxide) layer development, and distribution of important elements. The objective was to understand and compare the influence of each welding thermal cycle on the protective layer development.

(a)

(b)

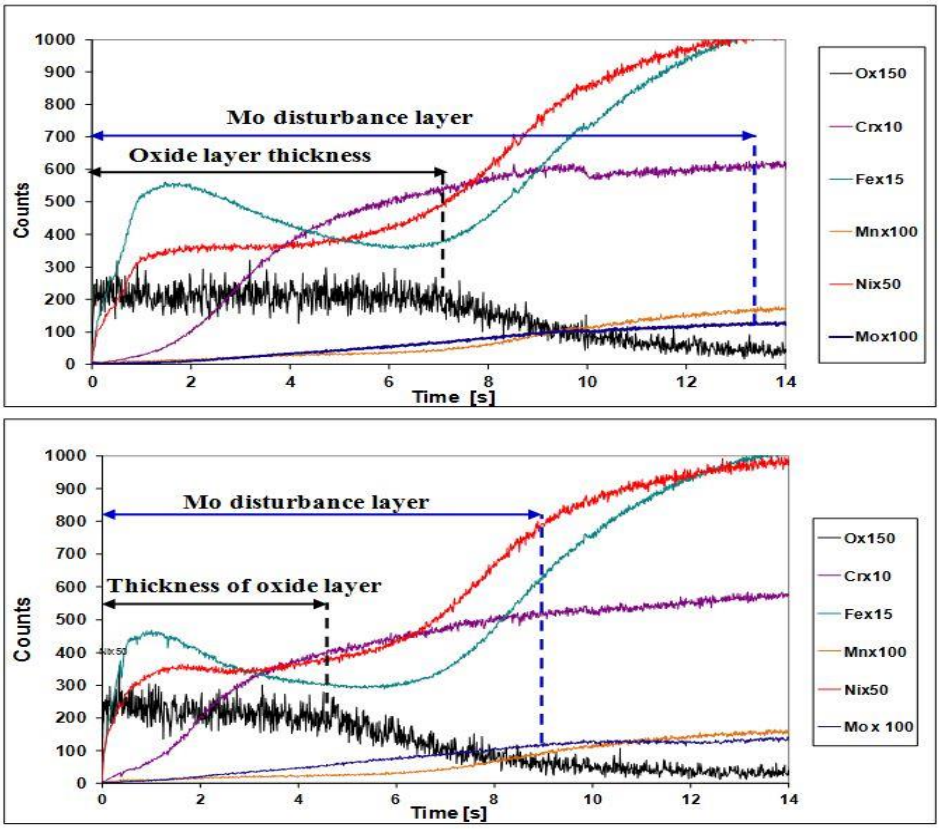

(a) GTA welding (b) NGLW

Figure 11-25 GD OES testing results

The results of the depth analysis of NGLW and GTAW techniques are shown in Figure 11-25 a, b; the values have been magnified with different factors for representation in the same scale. The magnification scale is shown in the developed graph. O x 150 relates to the oxygen concentration magnified by 150 times, and Cr x 10 relates to a chromium magnification factor of 10 times. The results show a similar behaviour for the material distribution in the depth direction for both welding techniques. The oxygen distribution of the GTAW bead shows a longer duration of stable measurement, starting to decrease after a sputtering time of 7 s as shown in Figure 11-25 a, while for the NGLW sample, sputtering began to decrease in after 4.5 s, as shown in Figure 11-25 b.

This difference is mainly due to the thicker oxide layer present in the GTAW sample relative to the material surface.

Although the passive film is thicker in GTAW joint, the stability of this film against attack is heavily dependent on the ferrite content in the microstructure. Coarser-ferrite grains have lower passive film stability [151]. Consequently the thinner passive film of the laser weld bead will be more stable against attack due to finer ferrite grains. The high cooling rate of laser beam welding (LBW) is another reason for improving the laser bead behaviour. It leads to suppression of the segregation of alloying elements. As the alloying elements in the fusion zone are uniformly distributed, micro- segregation was reduced with LBW [220] as shown for molybdenum distribution in blue colour in Figure 11-25. The analysis shows that the thickness of the molybdenum disturbance layer of GTAW technique is more than the thickness of disturbance layer across the NGLW sample. It required more than 13.5 s to reach a stable molybdenum concentration in the arc weld bead sample, while it needs only 9 s to reach stable concentration, in NGLW sample as shown in Figure 11-25.

11.9.5 Crack propagation

The final evaluation of the tested samples involved cleaning the surface of the samples to remove the oxide layer, in order to evaluate the cracking behaviour of the base material. The oxide layer was removed from the surface of the tested specimens by using electrolytic etching of the tested position in a 5% concentration oxalic acid in distilled water for 15s.

Figure 11-26 shows a micrograph of the necking positions for the NGLW and GTAW welding samples at 18% strain rate. It is clear from Figure 11-26 that the crack direction in both cases is approximately perpendicular to the strain direction. As mentioned previously, cracking in the GTAW sample occurred in the weld bead region, while in the NGLW sample it was in the base material. The initiated crack in the GTAW sample is deeper compared with that in the NGLW sample. Figure 11-26 b shows that the crack in the NGLW sample is very shallow - the depth of the crack in the NGLW bead was ~ 3 µm, however in the GTAW samples it was ~ 10-15 µm. The calculated crack growth rate for the GTAW is 5.55×10^{-9} mm/s, while it is 1.85×10^{-9} mm/s for NGLW. These results agree with previous studies using a fracture mechanics approach [228]. Figure

11-26c shows a cross-section perpendicular to the strain direction for GTAW sample - it is clear that crack propagation behaviour is inter-dendritic. For the NGLW sample, the perpendicular cross-section did not show the behaviour of crack propagation clearly, as the crack was very shallow.

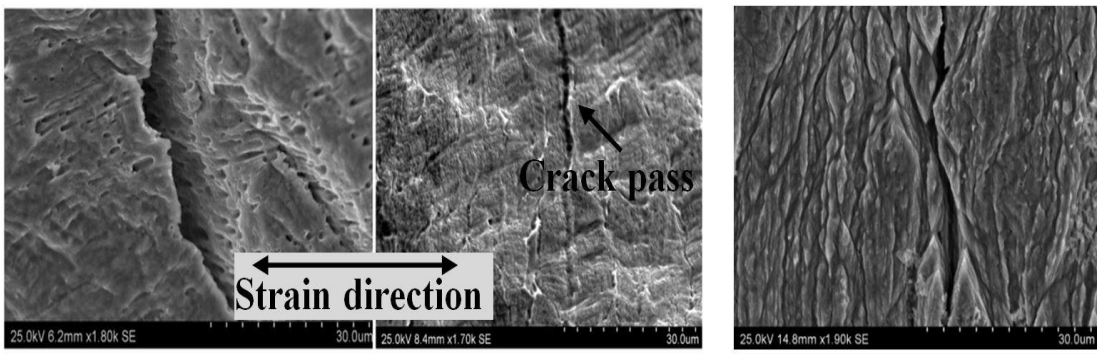

(a) GTA welding bead (b) NLW sample (base material) (c) GTA perpendicular to strain

Figure 11-26 Crack propagation

11.10 Summary

This chapter reports an evaluation for the performance of NGLW against other welding process in various corrosive environments. The results show that the corrosion resistances of the GTAW weld beads are generally poorer than those of the NGLW joints.

A high heat-input and low cooling rate for GTAW is likely to induce the segregation of alloying elements and the formation of Cr-depleted zones, resulting in the degradation of the resistance to localized corrosion.

The impurities are enriched at grain boundaries during the solidification of the fusion zone making the grain boundaries more likely to be an ‘active path’ of SCC, so that the inter-granular cracking mechanism dominates the crack propagation process in the fusion zone. The larger grain boundary area produced by the small grain size in laser welding can dilute the impurities and make the grain boundaries less susceptible to attack [215].

The weldability diagram for both laser-welded and GTAW welded austenitic stainless steels indicates that autogenous laser welding, NGLW, and GTAW are not subject to solidification cracking during welding.

Polarization curves show that the laser weld bead has the highest passivity against pitting corrosion, then base material, then NGLW, and finally GTAW shows the lowest passivation potential in the weld bead.

The preliminary SCC results show that both GTAW and NGLW have a significant influence on hydrogen embrittlement of weld joint due to reduced ductility. Limited evidence shows that the thickness of the oxide layer was higher in the GTAW bead with respect to the NGLW sample, which could affect the SCC resistance.

The molybdenum disturbance layer of GTAW technique is higher than thickness of disturbance layer across NGLW sample.

CHAPTER 12. **CONCLUSIONS AND FURTHER WORK**

12.1 Introduction

This thesis describes a new study of narrow gap laser welding of 316L stainless steel sheets up to 20 mm thick with a 1 kW fibre laser. Design of experiments and statistical modelling were used to optimise the laser welding parameters. Two dimensional residual stress analysis was carried out using the contour method validated by the neutron diffraction and XRD methods for both NGLW joints and arc weld joints. Mechanical properties including fatigue, tensile strength, bending strength and fracture toughness were evaluated for the NGLW joints compared with arc welded joints. Inter-granular corrosion, pitting corrosion and stress corrosion cracking characteristics of NGLW joints were investigated in comparison to those by arc welding. Finally, finite element modelling was carried out to understand the thermal history and their effects on residual stress formation, with experimental validation.

12.2 General conclusions

- NGLW is suitable for application to thick section (> 5 mm) in AISI grade 316L stainless steel due to the following;
- The residual stresses for NGLW are typically 30 - 40 % lower than for GTAW. The region of tensile stress is 50 - 70 % lower (narrower) than for GTAW for all of the investigated thicknesses, different constraints, and different welding strategies.
- GTAW shows higher peak hardness value and width of hardened region with respect to weld centreline.
- Accumulation of plastic strain due to thermo-mechanical cycling in NGLW was lower than for GTAW.
- For NGLW technique, low power with a high number of passes tends to decrease the peak value of the induced residual stress; however it will decrease

the productivity of the process. To decrease the width of the tensile region a high welding speed should be used.

- NGLW shows a higher resistance for inter-granular corrosion, and pitting corrosion in a nuclear operating environment relevant to GTAW; this is probably associated with lower stresses across the NGLW joints, and decreased element segregation and sensitization of chromium, as a consequence of the higher cooling rate.
- For thinner sheets (< 5 mm), autogenous high speed laser welding is a superior welding technique. It represents the highest-productivity technique with the lowest residual stresses in terms of peak and width of tensile region, the finest dendrite structure, with dendrite arm spacing of 2-4 μm, and the highest pitting corrosion resistance weld bead. The method also exhibits the narrowest fusion zone, < 2 mm, due to the low heat input and high welding speed, with a very narrow heat affected zone.

In addition to the general conclusions, there are some specific conclusions related to each field in the study. These will be discussed in the following sections.

12.3 Controlling and optimizing the NGLW technique

- Optimization of NGLW parameters is critical for the production of acceptable results. The study found that the quality and homogeneity of each weld bead is dependent on the homogeneity of the previous passes and a decrease in weld bead integrity is accumulated in the next passes.
- Increasing the welding speed inside a window of acceptance has the most significant influence on improving the overall desirability function for multi-objective optimization of NGLW.

12.4 Productivity of different welding techniques

- NGLW productivity, in terms of processing time, is higher than that of GTAW of the same thickness. The 10 mm thick plate welding case study shows that welding time of NGLW is lower than that of GTAW by 80%

- NGLW double-sided strategy shows improved productivity by 30%, and lower peak of residual stresses by 12%, and a zero distortion angle compared to single side strategy. However, for pipe welding in the nuclear power plants, double sided welding may not be feasible.
- Combined laser – arc welding shows improved productivity, and residual stresses compared to GTAW for one side, and double sided welding strategies.

12.5 Residual stress

- The laser power intensity and the welding speed of NGLW has a significant influence on the induced residual stress compared to the number of filling passes; NGLW of 10 mm-thick plates showed a lower stress distribution with 10 filling passes, at high welding speed and a low power intensity, compared with 4 filling passes at low speed and high power intensity.
- The thickness of the welded samples had a less significant influence on the induced residual stresses compared to welding process. Therefore, it is expected that for thicker sections, the basic process parameter relationships shown in this work would still hold.
- Decreasing the welding speed has a significant influence on the induced residual stress in the key-hole mode welding process.

12.6 Finite element modelling of NGLW

- From the FE modeling, it was found the peak value of the induced residual stress across the welding sample increases with increasing laser power, and width of the tensile region increases with reducing welding speed.
- Inter- pass time or cool down time between passes show a significant influence on the profile of the residual stress (position of stress peak with respect to upper surface). On the other hand, it shows less significant influence on the peak value of the residual stress.
- The model for the applied heat source for both GTAW and NGLW modelling has a significant influence on the accuracy of the modelling results. A Gaussian

profile and parabolic profile were selected and the results of the thermal analysis show a good agreement with those of the experimental measurement.

- Modelling results show that peak of the developed residual stress in GTAW is higher than for NGLW for the same material thicknesses, and the width of the tensile region is approximately doubled - these results shows good agreements with the experimental results.
- Residual stress evolution during multi-pass NGLW shows that the position of the residual stress peak generally follows the heat source position during the welding process. However, the initial welding passes are more significant than the last passes for the peak value and the width of the tensile region.

12.7 Corrosion and stress corrosion behaviour of NGLW joints

- Polarization curves show that the laser weld bead has the highest passivity against pitting corrosion, followed by the base material then NGLW, and finally GTAW shows the lowest passivation potential in the weld bead.
- SSRT in nuclear environment test shows that GTAW sample is more sensitive to reduction of the ductility due to hydrogen embrittlement than NGLW.
- Limited measurement results suggest that, the thickness of the oxide layer of the GTAW specimen is higher than the NGLW sample, and the thickness of the molybdenum disturbance layer of the GTAW technique is higher than that of the NGLW sample.

12.8 Further work

There are several areas in which further research is required. Some of the most important include the following:

12.8.1 Extending the current work to welds at thicker materials

NGLW of thick sections > 40 mm has been discussed previously, in terms of the control of the welding parameters in order to achieve a sound weld bead, and to reduce hot cracking susceptibility. However, detailed and reliable investigations of residual stress and corrosion behaviour have not been reported previously. The influence of induced

residual stress on the SCC susceptibility in comparison with other welding techniques such as GTAW represents a good potential topic for future research.

12.8.2 Further optimisation of NGLW performance

This may include the investigation of the influence of NGLW parameters; joint preparation especially the gap-width and gap-angle, on the weld soundness and distortion of the weld joint, and also the influence of the preheating on the developed residual stress in NGLW technique, and modelling their influence on the developed residual stress is considered as a promising area for research.

12.8.3 Further development of finite element model for thick sections performance

Another promising area of future direction of study is the use of an AWI module to simulate the NGLW process for thicker plates > 40 mm, to predict the developed residual stress for different welding scenarios and constraint, and to model the influence of the joint preparation, and the inter-pass time influence on the induced residual stress for the NGLW technique.

12.8.4 Detailed investigations of combined laser-arc welding

Combined arc-laser welding is a promising welding technique. It can be used to improve welding productivity, and represents improved residual stress behaviour compared to GTAW. The method can decrease the number of filling passes required with GTAW, and can decrease the high laser power laser requirement; however it still needs further investigation of the optimum welding parameters, and the influence of both arc and laser welding parameters on the induced residual stress and corrosion behaviour.

12.8.5 Improving statistical modelling of NGLW technique

Improvement of the statistical model to include the influence laser focus position, and angle between wire and laser beam, in the evaluation of responses will improve the reliability of the induced model. Including the residual stress behaviour in the statistical modelling responses can help to optimize the welding parameters in terms of

minimizing residual stress, and predicting the residual stress at different welding parameters, which will in turn significantly reduce the quantity of experimental work required for residual stress evaluation.

12.8.6 Further SCC evaluation of NGLW against different welding techniques

Study of the influence of different strain rates during SSRT, of the susceptibility of different welding techniques to SCC would be beneficial, as SCC is significantly sensitive to strain rate. Analysis may be conducted into the cracking behaviour for different welding techniques on the basis of the fracture mechanics, by using in-situ observation during SSRT using a CCD camera to understand the cracking propagation behaviour and the strain at which crack initiates and the influence of the strain rate on the crack initiation for different welds.

12.8.7 Transition NGLW application

Finally, the potential application of NGLW to dissimilar metal welds between low alloy steel SA 508-3, and austenitic stainless steel AISI 316L is a challenging area of study, but it offers good potential for future research in order to improve the connections between most of the heavy section components of pressurized water nuclear reactors, which are made of low alloy steel, and the stainless steel main piping. Most of existing connections are very sensitive to fatigue, corrosion, and low toughness regions. Investigation of a new technique such as NGLW is believed to offer residual stress behaviour in the weld region, and consequently the mechanical and corrosion behaviour of the connection.

REFERENCES

[1] **International Energy Agency, "World Energy Outlook (executive summary)," ed: Corlet, France, 2012, Vol 18, p. 7.**

[2] **Adamantiades, A. and Kessides I., "Nuclear power for sustainable development: current status and future prospects," *Energy Policy,* vol. 37, pp. 5149-5166, 2009.**

[3] **R.Price, "Nuclear fuel resources: Enough to last," *NUCLEAR ENERGY AGENCY News* vol. 20.2, p. 13, 2002.**

[4] **IAEA, "International Atomic Energy Agency , Nuclear Power Reactors in the World," vol. 2/31, ed: IAEA,VIENA, 2012, pp. 1-25.**

[5] **Edwards, L., Smith, M.C., Turski, M., Fitzpatrick, M.E., Bouchard, P.J., "Advances in residual stress modeling and measurement for the structural integrity assessment of welded thermal power plant," *Advanced Materials Research,* vol. 41, pp. 391-400, 2008.**

[6] **Steve, M.E.W., Jeffrey. H., "Welding for New Nuclear Power Plants," *Welding Journal,* vol. 88, pp. 40-43, 2009.**

[7] **Saario, T. (2001) Corrosion in Nuclear Power Plants. *Industrial Horizons Magazine*.**

[8] **Material UK energy. (2008). *The mapping of the material supply chains in the UK's power generation sector*. Available: http://www.matuk.co.uk/docs/Mapping_Materials_Supply%20locked.pdf. 10/2012**

[9] **Ioki, K., Daenner,W., Koizumi ,K., Krylov, V., "ITER-FEAT Vacuum Vessel and Blanket Design Features and Implications for the R&D Programme," *Nuclear Fusion,* vol. 41, p. 11, 2001.**

[10] **Bouchard, P.J., "Residual Stresses in Lifetime and Structural Integrity Assessment," in *Encyclopedia of Materials: Science and Technology (Second Edition)*, J. Buschow, W. C. Robert, C. F. Merton, I. Bernard, J. K. Edward, M. Subhash, and V. Patrick, Eds., ed Oxford: Elsevier, 2001, pp. 8134-8142.**

[11] **Webster, G. and Ezeilo A., "Residual stress distributions and their influence on fatigue lifetimes," *International Journal of Fatigue,* vol. 23, pp. 375-383, 2001.**

[12] **Sanderson, A., Punshon C., and Russell J., "Advanced welding processes for fusion reactor fabrication," *Fusion Engineering and Design,* vol. 49, p. 11, 2000.**

[13] **Kim, J.D., Kim, C.Jung C., Chin, M,, "Repair welding of etched tubular components of nuclear power plant by Nd: YAG laser," *Journal of Materials Processing Technology,* vol. 114, pp. 51-56, 2001.**

[14] **Elmesalamy, A.S., Li, L., Francis, J. A. and Sezer, H. K., "Understanding the process parameter interactions in multiple-pass ultra-narrow-gap laser**

welding of thick-section stainless steels," ***International Journal of Advanced Manufacturing Technology,*** **vol. 68, pp. 1-17, 2013/01/01 2013.**

[15] Sun, Z., Salminen, A.S., "Current status of laser welding with wire feed," ***Materials and Manufacturing Processes,*** **vol. 12, pp. 759-777, 1997.**

[16] Zhang, X., Ashida, E., Tarasawa, S., Ashida, E., Tarasawa, S., Anma, Y., Okada, M., Katayama, S., Mizutani, M., "Welding of thick stainless steel plates up to 50 mm with high brightness lasers," ***Journal of Laser Applications,*** **vol. 23, pp. 1-7, 2011.**

[17] Zhang, X., Ashida, E., "Welding of thick stainless steel plates up to 50 mm with high brightness lasers," presented at the ICALIO USA, 2009.

[18] Mills, W., "Fracture toughness of type 304 and 316 stainless steels and their welds," ***International Materials Reviews,*** **vol. 42, pp. 45-82, 1997.**

[19] Huang, J.Y., Jung Y.J., Long J.S.,Ying C.C.,Ching K.R., "High-cycle fatigue behavior of type 316L stainless steel," ***Materials transactions,*** **vol. 47, pp. 409-417, 2006.**

[20] Smart, N.W., RJ. Fennell, PAH. Reddy, B. Rance, AP. Padovani, C, "Waste container durability: monitoring of a stainless steel 4 metre box over 12 years," ***Mineralogical Magazine,*** **vol. 76, pp. 2891-2899, 2012.**

[21] IAEA, "International Status and Prospects for Nuclear Power " presented at the Board of Governors General Conference, GOV/INF/2012/12-GC(56)/INF/6, 2012.

[22] Habjanec, D. (2012), Energy history facts. ***Interesting facts about energy sources, energy news and energy articles.***

[23] Reisch, F., "High Pressure Boiling Water Reactor," ***Nuclear Technology,*** **vol. 172, pp. 101-107, 2010.**

[24] Dann, C. (2009, Nuclear Fusion and Its Future Uses In Spacecraft. Available: http://www.weirdwarp.com/2009/08/nuclear-fusion-and-its-future-uses-in-spacecraft/ 12/2011

[25] Hayes, B., ***Infrastructure: A field guide to the industrial landscape*** **vol. 26: New York, WW Norton & Co. Ltd, 2005.**

[26] Wikipedia. (2013). ***Pressurized water reactor.*** **Available: http://en.wikipedia.org/wiki/Pressurized_water_reactor. 2/2013**

[27] American Nuclear Society. (2012). ***Nuclear power : A sustainable source of energy.*** **Available: http://www2.ans.org/pi/brochures/pdfs/power.pdf. 8/2011**

[28] Canadian Nuclear Association. (2010). ***Nuclear energy exploring possibilities.*** **Available: http://www.cna.ca/curriculum/cna_nuc_tech/nuclear_reactor-eng.asp?bc=How%20a%20Nuclear%20Reactor%20Works&pid=How%20a%20Nuclear%20Reactor%20Works. 7/2011**

[29] Haluzan, N. (2011). ***Nuclear power plants - Advantages and disadvantages*** **Available: http://www.renewables-**

info.com/drawbacks_and_benefits/nuclear power plants - advantages and disadvantages.html. 11/2011

[30] DOE.Nuclear.Energy.Research.Committee.and.the.Generation.IV., I.F., "Technology Roadmap for Generation IV Nuclear Energy System," 2002.

[31] ASME, "Boiler and Pressure Vessel Code-Rules for Construction of Nuclear Facility Components," in *III Division 1 — Subsection NB Class 1 Components*, ed: ASME, 2010, p. 248.

[32] Shankar, V., Gill, T.P.S., Mannan, S.L., Sundaresan, S., "Solidification cracking in austenitic stainless steel welds," *Sadhana*, vol. 28, pp. 359-382, 2003.

[33] Staelhe, R.W., "Ageing Management of Light Water ReactorsAnatomy of proactivity," in *Anatomy of proactivity*, 2007.

[34] R.castro, *welding metallurgy of stainless and heat-resisting steels*: Syndics of cambridge, 1975.

[35] Lippold, J.C. and Kotecki D.J., *Welding metallurgy and weldability of stainless steels*: John wiley & sons, 2005.

[36] Priya, C., Rao, K.B., Anoop, M.B., Lakshmanan, N., Gopika, V., Kushwaha, H.S., Saraf, R.K., "Probabilistic failure analysis of austenitic nuclear pipelines against stress corrosion cracking," *Proceedings of the Institution of Mechanical Engineers, Part C: Journal of Mechanical Engineering Science*, vol. 219, pp. 607-624, 2005.

[37] Tjong, S.Z., SM. Ho, NJ. Ku, JS, "Microstructural characteristics and creep rupture behavior of electron beam and laser welded AISI 316L stainless steel," *Journal of nuclear materials*, vol. 227, pp. 24-31, 1995.

[38] Brooks, J.A., Thompson, A. W. , "Microstructural development and solidification cracking susceptibility of austenitic stainless steel weldsJ.," *International Materials Reviews*, vol. 36, p. 29, 1991.

[39] Sun, Z. and Kuo M., "Bridging the joint gap with wire feed laser welding," *Journal of Materials Processing Technology*, vol. 87, pp. 213-222, 1999.

[40] Lienert, T. and Lippold J., "Improved weldability diagram for pulsed laser welded austenitic stainless steels," *Science and Technology of Welding &# 38; Joining*, vol. 8, pp. 1-9, 2003.

[41] Kell, J.T., JR Higginson, RL Thomson, RC, "Microstructural characterization of autogenous laser welds on 316L stainless steel using EBSD and EDS," *Journal of microscopy*, vol. 217, pp. 167-173, 2005.

[42] D'amato, C., Fenech,M. ,Abela,S., Betts,J., Buhagiar,J., "Autogenous Laser Keyhole Welding of AISI 316LTi," *Materials and Manufacturing Processes*, vol. 25, pp. 1269-1277, 2010.

[43] Dahotre, N.B. and Harimkar S.P., *Laser fabrication and machining of materials*: Springer Verlag, 2008.

[44] Cary, H.B. and Helzer S.C., *Modern welding technology*: Prentice Hall, 2002.

[45] **ASME, "ASME Boiler and Pressure Vessel Code " in *IX Qualification Standard for Welding and Brazing Procedures, Welders, Brazers, and Welding and Brazing Operators*, ed: ASME, 2010, p. 324.**

[46] **McPherson, N., Chi K., and Baker T., "Submerged arc welding of stainless steel and the challenge from the laser welding process," *Journal of Materials Processing Technology*, vol. 134, pp. 174-179, 2003.**

[47] **Wolfgang, J. (2006), Welding on Rotors for Power Plant Turbo Sets State of the Art 13. Available: http://www.energy.siemens.com/us/pool/hq/energy-topics/pdfs/en/steam-turbines-power-plants/2_Welding_on_Rotors.pdf. 6/2011**

[48] **Odette, G.R., Lucas,G.E "Embrittlement of Nuclear Reactor Pressure Vessels," *The Minerals, Metals & Materials Society - JOM* vol. 53, pp. 18-22, 2001.**

[49] **Kou, S., *Welding metallurgy*, second ed.: Wiley-Interscience (2003), (2002).**

[50] **R.L.O'brien, *Welding Processes.*, 8 ed. vol. 2: AWS, 1991.**

[51] **Ltd., T. (2013), The Manual Metal Arc process (MMA Welding). Available: http://www.twi.co.uk/technical-knowledge/job-knowledge/the-manual-metal-arc-process-mma-welding-002/. 7/2011**

[52] **Agency, I.A.E., *Guidebook for the Fabrication of Non-Destructive Testing (NDT)*: IAEA in Austria, 2001.**

[53] **Mitchel, K.C., "The application of flux cored arc welding (FCAW) in UK power plant," *journal of OMMI*, vol. 2, p. 7, april 2003 2003.**

[54] **Carr, R.H., O'Con,R.L., *Welding practices and procedures*: Englewood Cliffs, N.J. : Prentice-Hall 1983.**

[55] **Messler, R.W., *Principles of welding*: John wiley & sons, 1999.**

[56] **Tjong, S., Zhu S., Ho N., and Ku J., "Microstructural characteristics and creep rupture behavior of electron beam and laser welded AISI 316L stainless steel," *Journal of nuclear materials*, vol. 227, pp. 24-31, 1995.**

[57] **Dawes, C., *Laser welding: a practical guide*: Woodhead Publishing, 1992.**

[58] **William.R.Oates, *Materials and applications*, 8 ed. vol. 4: AWS, 1991.**

[59] **Karhu, M. and Kujanpää V., "Experimental test set-up for studying hot cracking in multi pass laser hybrid welding of thick section austenitic stainless steel," in *ICALEO*, USA, 2008, pp. 535-544.**

[60] **Zhang, X., Ashida, E., Tarasawa, S., "Properties of welded joint for narrow gap laser welding of austenitic stainless steels," presented at the Proceeding of 29 th. International Congress on Applciation of Lasers and Electro-Optics (ICALEO), Paper No. 1805, Anhiem , California, USA, 2010.**

[61] **National.Physical.Laboratory. (2000), Stress Corrosion Cracking. Available: http://www.npl.co.uk/upload/pdf/stress.pdf. 2/2012**

[62] **Withers, P.J., Bhadeshia, H.K.D.H., "Residual stress. Part 1–measurement techniques," *Materials Science and technology*, vol. 17, pp. 355-365, 2001.**

[63] **Nyashin, Y., Lokhov V., and Ziegler F., "Decomposition method in linear elastic problems with eigenstrain," *Z. Angew. Math. Mech.*, vol. 85, pp. 557 – 570, 2005 2005.**

[64] **Kou, S., *Welding metallurgy*: John Wiley and Sons, 2003.**

[65] **Leggatt, R., "Residual stresses in welded structures," *International Journal of Pressure Vessels and Piping*, vol. 85, pp. 144-151, 2008.**

[66] **Olabi, A.G., Benyounis, K.Y., Hashmi, M.S., "Application of Response Surface Methodology in Describing the Residual Stress Distribution in CO2 Laser Welding of AISI304," *Strain*, vol. 43, pp. 37-46, 2007.**

[67] **Bang, H.S., Han, S. K., You, C. O., Ik, H., "A study on mechanical and microstructure characteristics of the STS304L butt joints using hybrid CO2 laser-gas metal arc welding," *Materials & Design*, vol. 32, pp. 2328-2333, 2011.**

[68] **Metallurgical Consultants. (2012), Creep and stress rupture. Available: http://www.materialsengineer.com/CA-Creep-Stress-Rupture.htm. 2/2013**

[69] **Smith, D.J., Bouchard, P.J., George, D., "Measurement and prediction of residual stresses in thick-section steel welds," *The Journal of Strain Analysis for Engineering Design*, vol. 35, pp. 287-305, 2000.**

[70] **Hosseinzadeh, F., Mahmoudi,A.H., Truman,C.E., Smith,D.J., "Application of Deep Hole Drilling to the Measurement and Analysis of Residual Stresses in Steel Shrink-Fitted Assemblies " *Journal of Strain* p. 15, 2010.**

[71] **Prime, M.B., Kastengren, A.L., "The contour method cutting assumption: error minimization and correction," in *Experimental and Applied Mechanics, Volume 6*, ed: Springer, 2011, pp. 233-250.**

[72] **Zhang, Y., Ganguly, S., Edwards, L., Fitzpatrick, M.E., "Cross-sectional mapping of residual stresses in a VPPA weld using the contour method," *Journal of Acta materialia*, vol. 52, pp. 5225-5232, 2004.**

[73] **Prevéy, P.S., "Current applications of X-ray diffraction residual stress measurement," *ASM International, Materials Park-Developments in Materials Characterization Technologies*, pp. 103-110, 1996.**

[74] **Clapham, L., Abdullah, K., Jeswiet, J.J., Wild, P.M., Rogge, R., "Neutron diffraction residual stress mapping in same gauge and differential gauge tailor-welded blanks," *Journal of Materials Processing Technology*, vol. 148, pp. 177-185, 2004.**

[75] **Wikipedia. (2013). *Bragg's law*. Available: http://en.wikipedia.org/wiki/Bragg's_law . 3/3013**

[76] **Noyan, I.C., Cohen, J.B., "Residual Stress--Measurement by Diffraction and Interpretation," *Springer-Verlag, Heidelberger Platz 3, D-1000 Berlin 33, FRG, 1987.*, 1987.**

[77] **Yilmaz, R., Uzun, H., "Mechanical properties of austenitic stainless steels welded by GMAW and GTAW," *Journal of Marmara for Pure and Applied Sciences*, vol. 18, pp. 97-113, 2002.**

[78] **Joseph, B.K., Sathiya,D., Murthy,P., Srinivasa,.C.V., "Weld metal characterization of 316L (N) austenitic stainless steel by electron beam welding process," *International Journal of Engineering, Science and Technology,* vol. 4, pp. 169-176, 2012.**

[79] **Lakshminarayanan, A.K., Balasubramanian, V., "An assessment of microstructure, hardness, tensile and impact strength of friction stir welded ferritic stainless steel joints," *Materials & Design,* vol. 31, pp. 4592-4600, 2010.**

[80] **Yan, J., Gao M., and Zeng X., "Study on microstructure and mechanical properties of 304 stainless steel joints by TIG, laser and laser-TIG hybrid welding," *Optics and Lasers in Engineering,* vol. 48, pp. 512-517, 2010.**

[81] **Germanischer, L.S. (2009). *Impact testing*. Available: http://www.gl-group.com/infoServices/rules/pdfs/english/werkstof/teil-1/kap-1/englisch/abschn02.pdf. 1/2013**

[82] **Gordon England. (2007), HARDNESS TESTING. Available: http://www.gordonengland.co.uk/hardness/. 2/2013**

[83] **Kwok, C.T., Fong,S. L.,Cheng, F. T., Man, H. C. , "Pitting and galvanic corrosion behavior of laser-welded stainless steels," *Journal of Materials Processing Technology,* vol. 176, pp. 168-178, 2006.**

[84] **Hafez, K.M. and Seiji K., "Fiber laser welding of AISI 304 stainless steel plates," *The japan welding society,* vol. 27, pp. 69-73, 2009.**

[85] **Koshiishi, M., Fujimori, H., Okada, E. M., Hirano, A., "Hitachi's activities for suppression of stress corrosion cracking," *Hitachi Review,* vol. 58, p. 89, 2009.**

[86] **Nguyen, T.C., Weckman, D.C., Johnson, D.A., Kerr, H.W., "The humping phenomenon during high speed gas metal arc welding," *Science and Technology of Welding &# 38; Joining,* vol. 10, pp. 447-459, 2005.**

[87] **Bauer, B. and Bušić M., "High energy density welding processes," *Encyclopedia of Life Support Systems (EOLSS)*.**

[88] **Sun, Z. and Karppi R., "The application of electron beam welding for the joining of dissimilar metals: an overview," *Journal of Materials Processing Technology,* vol. 59, pp. 257-267, 1996.**

[89] **GuoMing, H., Jian Z., and JianQang L., "Dynamic simulation of the temperature field of stainless steel laser welding," *Materials & Design,* vol. 28, pp. 240-245, 2007.**

[90] **Sun, Z. and Ion J., "Laser welding of dissimilar metal combinations," *Journal of Materials Science,* vol. 30, pp. 4205-4214, 1995.**

[91] **El-Batahgy, A., *Laser Beam Welding of Austenitic Stainless Steels – Similar Butt and Dissimilar Lap Joints*: Janeza Trdine 9, 51000 Rijeka, Croatia, 2012.**

[92] **Department of Energy USA. (2010), Nuclear Energy Enabling Technologies Available: http://www.ne.doe.gov/pdfFiles/Neet_Workshop_07292010.pdf. 9/2011**

[93] **Fan, T., "Laser beam combining for high-power, high-radiance sources," *Selected Topics in Quantum Electronics, IEEE Journal of,* vol. 11, pp. 567-577, 2005.**

[94] **Arieli, R. (1998). *Laser adventure*. *11*. Available: http://perg.phys.ksu.edu/vqm/laserweb/index.htm. 5/2012**

[95] **Jokinen, T., Kujanpää, V., "High power Nd: YAG laser welding in manufacturing of vacuum vessel of fusion reactor," *Fusion Engineering and Design,* vol. 69, pp. 349-353, 2003.**

[96] **Benyounis, K.Y., Olabi, A.G., Hashmi, M.S., "Effect of laser welding parameters on the heat input and weld-bead profile," *Journal of Materials Processing Technology,* vol. 164, pp. 978-985, 2005.**

[97] **Ribolla, A., Damoulis, G.L., Batalha, G.F., "The use of Nd: YAG laser weld for large scale volume assembly of automotive body in white," *Journal of Materials Processing Technology,* vol. 164, pp. 1120-1127, 2005.**

[98] **Lionard, M., *Laser material processing*: Marcel Dekker, 1996.**

[99] **Sibillano, T., Ancona, A., Berardi, V., Schingaro, E., Basile, G., Lugar , P.M., "Optical detection of conduction/keyhole mode transition in laser welding," *Journal of Materials Processing Technology,* vol. 191, pp. 364-367, 2007.**

[100] **Tusek, J. and Suban M., "Hybrid welding with arc and laser beam," *Science and Technology of Welding* vol. 4, pp. 308-311, 1999.**

[101] **Jin, X., Li L., and Zhang Y., "A study on fresnel absorption and reflections in the keyhole in deep penetration laser welding," *Journal of Physics D: Applied Physics,* vol. 35, p. 2304, 2002.**

[102] **Lankalapalli, K.N., Tu, J.F., Gartner, M., "A model for estimating penetration depth of laser welding processes," *Journal of Physics D: Applied Physics,* vol. 29, p. 1831, 1996.**

[103] **Bonollo, F., Tiziani, A., Zamban, A., "Model for CO 2 laser welding of stainless steel, titanium, and nickel: parametric study," *journal of Materials Science and Technology,* vol. 9, pp. 1137-1144, 1993.**

[104] **Carmignani, C., Mares R., and Toselli G., "Transient finite element analysis of deep penetration laser welding process in a singlepass butt-welded thick steel plate," *Computer Methods in Applied Mechanics and Engineering,* vol. 179, pp. 197-214, 1999.**

[105] **Jin, X. and Li L., "An experimental study on the keyhole shapes in laser deep penetration welding," *Optics and Lasers in Engineering,* vol. 41, pp. 779-790, 2004.**

[106] **Milewski, J.O., Sklar, E. , "Narrow gap laser welding," USA Patent, 1998.**

[107] Zhang, Y., Li, L., Zhang, G., "Spectroscopic measurements of plasma inside the keyhole in deep penetration laser welding," *Journal of Physics D: Applied Physics,* vol. 38, p. 703, 2005.

[108] Chung, B.G., Rhee,S. ,Lee,C.H., "The effect of shielding gas types on CO2 laser tailored blank weldability of low carbon automotive galvanized steel," *Materials Science and Engineering A,* vol. 272, pp. 357-362, 1999.

[109] Zhang, X., Chen,W. ,Jiang, P. ,Guo, J. ,Tian, Z., "Modeling and application of plasma charge current in deep penetration laser welding," *Journal of Applied Physics,* vol. 93, pp. 8842-8847, 2009.

[110] Schubert, E., Klassen, M. ,Zerner, I. ,Walz, C. ,Sepold, G., "Light-weight structures produced by laser beam joining for future applications in automobile and aerospace industry," *Journal of Materials Processing Technology,* vol. 115, pp. 2-8, 2001.

[111] Kaplan, A., "A model of deep penetration laser welding based on calculation of the keyhole profile," *Journal of Physics D: Applied Physics,* vol. 27, p. 1805, 1994.

[112] Pecharapa, W. and Kar A., "Effects of phase changes on weld pool shape in laser welding," *Journal of Physics D: Applied Physics,* vol. 30, p. 3322, 1997.

[113] Chen, X. and Wang H.X., "Prediction of the laser-induced plasma characteristics in laser welding: a new modelling approach including a simplified keyhole model," *Journal of Physics D: Applied Physics,* vol. 36, p. 1634, 2003.

[114] Ming, G., Xiaoyan, Z. ,Qianwu, H., "Effects of gas shielding parameters on weld penetration of CO2 laser-TIG hybrid welding," *Journal of Materials Processing Technology,* vol. 184, pp. 177-183, 2007.

[115] Ribic, B., Palmer,T. ,DebRoy,T., "Problems and issues in laser-arc hybrid welding," *International materials reviews,* vol. 54, p. 223, 2009.

[116] Steen, W.M., *Laser material processing*: Springer Verlag, 2010.

[117] El-Batahgy, A.M., "Effect of laser welding parameters on fusion zone shape and solidification structure of austenitic stainless steels," *Materials Letters,* vol. 32, pp. 155-163, 1997.

[118] Quintino, L., Costa, A. ,Miranda, R. ,Yapp, D. ,Kumar, V. ,Kong, C., "Welding with high power fiber lasers-A preliminary study," *Materials & Design,* vol. 28, pp. 1231-1237, 2007.

[119] Kaplan, A., Wouters,M., Nilsson,K. ,Powell,J., "Fundamental analysis of hybrid laser-MIG welding," in *EUROJOIN 5,* Vienna (Austria), 2004.

[120] Cam, G., Erim, S. ,Yeni, C. ,Kocak, M., "Determination of mechanical and fracture properties of laser beam welded steel joints," *WELDING JOURNAL-NEW YORK-,* vol. 78, p. 193, 1999.

[121] Watkins, K., "Laser welding of magnesium alloys," in *TMS (The Minerals, Metals & Materials Society)*, 2003, p. 4.

[122] Katayama, S. and Kawahito Y., "Elucidation of phenomena in high-power fiber laser welding and development of prevention procedures of welding defects," in *Proc. of SPIE* 2009, p. 9.

[123] Cao, X., Jahazi, M., Immarigeon, J., Wallace, W., "A review of laser welding techniques for magnesium alloys," *Journal of Materials Processing Technology,* vol. 171, pp. 188-204, 2006.

[124] Kim, J., Watanabe,T. ,Yoshida,Y., "Effect of the beam-defocusing characteristics on porosity formation in laser welding," *Journal of materials science letters,* vol. 14, pp. 1624-1626, 1995.

[125] Zhang, X., Ashida, E. ,Katayama, S., Mizutani, M., "Development of ultra deep penetration welding with 10 kW fiber laser," in *ICALIO,* USA, 2008, p. 6.

[126] Bachmann, F., "Industrial applications of high power diode lasers in materials processing," *Applied Surface Science,* vol. 208, pp. 125-136, 2003.

[127] Chae, H., Kim C., Kim J., and Rhee S., "The effect of shielding gas composition in CO2 laser—gas metal arc hybrid welding," *Proceedings of the Institution of Mechanical Engineers, Part B: Journal of Engineering Manufacture,* vol. 222, p. 1315, 2008.

[128] Salminen, A., Piili,H. , Purtonen, T., "The characteristics of high power fibre laser welding," *Mechanical Engineering Science,* vol. Vol. 224 Part C, p. 11, 2010.

[129] Kawahito, Y., Mizutani, M., Katayama, S., "Elucidation of high-power fibre laser welding phenomena of stainless steel and effect of factors on weld geometry," *Journal of Physics D: Applied Physics,* vol. 40, p. 5854, 2007.

[130] Thomy, C., Seefeld, T., Vollertsen, F., "High-power fibre lasers–Application potentials for welding of steel and aluminium sheet material," *Advanced Materials Research,* vol. 6, pp. 171-178, 2005.

[131] Narikiyo, T., Fujinaga, S., Takenaka, H., Ohmori, A., Inoue, K., "Optimisation of welding using two Nd-YAG laser beams combined at workpiece surface," *Science and Technology of Welding &# 38; Joining,* vol. 5, pp. 113-119, 2000.

[132] Nguyen, T., Weckman D., Johnson D., and Kerr H., "High speed fusion weld bead defects," *Science and Technology of Welding &# 38; Joining,* vol. 11, pp. 618-633, 2006.

[133] Lee, J.Y., Ko, S.H., Farson, D.F., Yoo, C.D., "Mechanism of keyhole formation and stability in stationary laser welding," *Journal of Physics D: Applied Physics,* vol. 35, p. 1570, 2002.

[134] Zhao, H., White D., and DebRoy T., "Current issues and problems in laser welding of automotive aluminium alloys," *International materials reviews,* vol. 44, pp. 238-266, 1999.

[135] Pastor, M., Zhao H., Martukanitz R., and DebRoy T., "Porosity, Underfill and Magnesium Lose during Continuous Wave Nd: YAG Laser Welding of

Thin Plates of Aluminum Alloys 5182 and 5754," ***WELDING JOURNAL-NEW YORK-*****, vol. 78, p. 207, 1999.**

[136] Katayama, S., Mizutani, M., Matsunawa, A., "Development of porosity prevention procedures during laser welding - First International Symposium on High-Power Laser Macroprocessing, Isamu " in *Proceedings of SPIE* 2003, p. 8.

[137] Ishide, T., Tsubota S., Nayama M., Shimokusu Y., Nagashima T., and Okimura K., "10-kW-class YAG laser application for heavy components," in *SPIE Optics and Photonics*, 2000, p. 8.

[138] Tani, G., Campana, G., Fortunato, A., Ascari, A., "The influence of shielding gas in hybrid LASER-MIG welding," *Applied Surface Science,* vol. 253, pp. 8050-8053, 2007.

[139] Tsukamoto, S., Kawaguchi, I., Arakane, G., Honda, H., "Keyhole behavior in high power laser welding - First International Symposium on High-Power Laser Macroprocessing, Isamu," in *SPIE Optics and Photonics*, 2003, p. 6.

[140] David, S. and DebRoy T., "Current issues and problems in welding science," *journal of science,* vol. 257, p. 6, 1992.

[141] Zhu, J., Li L., and Liu Z., "CO2 and diode laser welding of AZ31 magnesium alloy," *journal of Applied Surface Science,* vol. 247, pp. 300-306, 2005.

[142] Park, H. and Rhee S., "Analysis of mechanism of plasma and spatter in CO2 laser welding of galvanized steel," *Optics & Laser Technology,* vol. 31, pp. 119-126, 1999.

[143] Li, L., Brookfield, D.J., Steen, W.M., "Plasma charge sensor for in-process, non-contact monitoring of the laser welding process," *Measurement Science and Technology,* vol. 7, p. 615, 1996.

[144] Vollertsen, F., Grünenwald, S., "Defects and process tolerances in welding of thick plates," in *Proceedings of Laser Materials Processing Conference ICALEO*, 2008, pp. 489-497.

[145] Page, C.J., Devermann, T., Biffin, J., Blundell, N., "Plasma augmented laser welding and its applications," *Science and Technology of Welding &# 38; Joining,* vol. 7, pp. 1-10, 2002.

[146] Mahrle, A. and Beyer E., "Hybrid laser beam welding—Classification, characteristics, and applications," *Journal of laser applications,* vol. 18, p. 169, 2006.

[147] Vitek, J.M., David, S.A.,Richey, M.W., Biffin, J., Blundell, N., Page, C.J., "Weld pool shape prediction in plasma augmented laser welded steel," *Science and Technology of Welding &# 38; Joining,* vol. 6, pp. 305-314, 2001.

[148] Ono, M., Shinbo, Y., Yoshitake, A., Ohmura, M., "Development of laser-arc hybrid welding," *NKK TECHNICAL REVIEW,* pp. 8-12, 2002.

[149] **Bagger, C., Olsen, F.O., "Review of laser hybrid welding,"** ***Journal of laser applications,*** **vol. 17, p. 13, 2005.**

[150] **Starling, C., Marques, P.V., Modenesi, P.J., "Statistical modelling of narrow-gap GTA welding with magnetic arc oscillation,"** ***Journal of Materials Processing Technology,*** **vol. 51, pp. 37-49, 1995.**

[151] **Abe, N., Agano Y., Tsukamoto M., Makino T., Hayashi M., and Kurosawa T., "High speed welding of thick plates using a laser-arc combination system,"** ***Transactions of the JWRI(Japan Welding Research Institute)(Japan),*** **vol. 26, pp. 69-75, 1997.**

[152] **Phaoniam, R., Shinozaki, K., Yamamoto, M., Kadoi, K., Tsuchiya, S., Nishijima, A., "Development of a highly efficient hot-wire laser hybrid process for narrow-gap welding—welding phenomena and their adequate conditions,"** ***Welding in the World,*** **pp. 1-7, 2013.**

[153] **Salminen, A., "The filler wire-laser beam interaction during laser welding with low alloyed steel filler wire,"** ***Journal of Mechanika*** **vol. 84, pp. p.67-74, 2010.**

[154] **Salminen, A.S., "Effects of filler wire feed on the efficiency of laser welding," in** ***LAMP 2002: International Congress on Laser Advanced Materials Processing,*** **2003, pp. 263-268.**

[155] **Jean-Pierre. (2008), Narrow gap welding of heavy wall thickness materials in nuclear and fossil fuel industries. Available: http://www.polysoude.com/documents/english/press-releases/NARROW_GAP_WELDING_EN.pdf. 3/2013**

[156] **Reisgen, U., Schleser M., Mokrov O., and Ahmed E., "Optimization of laser welding of DP/TRIP steel sheets using statistical approach,"** ***Optics & Laser Technology,*** **vol. 44, pp. 255-262, 2012.**

[157] **Reisgen, U., Schleser, M., Mokrov, O., Ahmed, E., "Statistical modeling of laser welding of DP/TRIP steel sheets,"** ***Optics & Laser Technology,*** **vol. 44, pp. 92-101, 2012.**

[158] **Manonmani, K., Murugan, N., Buvanasekaran, G., "Effects of process parameters on the bead geometry of laser beam butt welded stainless steel sheets,"** ***The International Journal of Advanced Manufacturing Technology,*** **vol. 32, pp. 1125-1133, 2007.**

[159] **Torkamany, M., Hamedi M., Malek F., and Sabbaghzadeh J., "The effect of process parameters on keyhole welding with a 400 W Nd: YAG pulsed laser,"** ***Journal of Physics D: Applied Physics,*** **vol. 39, pp. 4563-4567, 2006.**

[160] **Benyounis, K. and Olabi A., "Optimization of different welding processes using statistical and numerical approaches–A reference guide,"** ***Advances in Engineering Software,*** **vol. 39, pp. 483-496, 2008.**

[161] **Box, G. and Wilson K., "On the experimental attainment of optimum conditions.,"** ***Journal of Royal Statistical Society,*** **pp. 1-45, 1951.**

[162] **Murugan, N., Parmar, R. S., "Effects of MIG process parameters on the geometry of the bead in the automatic surfacing of stainless steel," *Journal of Materials Processing Technology,* vol. 41, pp. 381-398, 1994.**

[163] **Anawa, E.M., Olabi, A.G., "Using Taguchi method to optimize welding pool of dissimilar laser-welded components," *Optics & Laser Technology,* vol. 40, pp. 379-388, 2008.**

[164] **Leigh, S., Sezer, K., Li, L., Grafton-Reed, C., Cuttell, M., "Statistical analysis of recast formation in laser drilled acute blind holes in CMSX-4 nickel superalloy," *The International Journal of Advanced Manufacturing Technology,* vol. 43, pp. 1094-1105, 2009.**

[165] **Palani, P.K. and Murugan N., "Optimization of weld bead geometry for stainless steel claddings deposited by FCAW," *Journal of Materials Processing Technology,* vol. 190, pp. 291-299, 2007.**

[166] **BRITISH STAINLESS STEEL ASSOCIATION. (2007). *Heat tint temper colours on stainless steel surfaces heated in air*. Available: http://www.bssa.org.uk/topics.php?article=140. 9/2011**

[167] **Ruggiero, A., Tricarico L., Olabi A., and Benyounis K., "Weld-bead profile and costs optimisation of the CO< sub> 2</sub> dissimilar laser welding process of low carbon steel and austenitic steel AISI316," *Optics & Laser Technology,* vol. 43, pp. 82-90, 2011.**

[168] **Kim, T.H., Albright, C.E., Chiang, S., "The energy transfer efficiency in laser welding process," *Journal of Laser Applications,* vol. 2, pp. 23-28, 1990.**

[169] **Nath, A.K., Sridhar, R., Ganesh, P., Kaul, R., "Laser power coupling efficiency in conduction and keyhole welding of austenitic stainless steel," *Sadhana,* vol. 27, pp. 383-392, 2002.**

[170] **Collings, N., Wong, K.Y., Guile, A.E., "Efficiency of tungsten-inert-gas arcs in very-high-speed welding," *Electrical Engineers, Proceedings of the Institution of,* vol. 126, pp. 276-280, 1979.**

[171] **Khalfallah, I.Y., Rahoma, M.N., Abboud, J.H., Benyounis, K.Y., "Microstructure and corrosion behavior of austenitic stainless steel treated with laser," *Optics & Laser Technology,* vol. 43, pp. 806-813, 2011.**

[172] **Regis, G. (2013) Estimating Total Welding Costs. *Fabricatrion Metal Working*. 6.**

[173] **Lin, Y., Cheng,L.K., "Effect of preheating on the residual stress in type 304 stainless steel weldment," *Journal of Materials Processing Technology,* vol. 63, pp. 797-801, 1997.**

[174] **ASTM, "International Standarad. E8M-04 Standard test methods for tension testing of metallic materials," ed.**

[175] **Tsuchiya, K., Kawamura H., and Kalinin G., "Re-weldability tests of irradiated austenitic stainless steel by a TIG welding method," *Journal of nuclear materials,* vol. 283, pp. 1210-1214, 2000.**

[176] Read, D.T., McHenry, H.I., Steinmeyer, P., Thomas,J., R., "Metallurgical Factors Affecting the Toughness of 316 L SMA Weldments at Cryogenic Temperatures," *Welding journal,* vol. 59, p. 104, 1980.

[177] Yuri, T., Ogata, T., Saito, M., Hirayama, Y., "Effect of welding structure and δ-ferrite on fatigue properties for TIG welded austenitic stainless steels at cryogenic temperatures," *Cryogenics,* vol. 40, pp. 251-259, 2000.

[178] Kumar, D.H., T.Shaktivelu, M. N. Gopal, K.S. Chandravathi, K. Laha, S.K. Albert, H. Kumar, B. Shanmugarajan, A. SomiReddy, "Creep Failures in Laser Welded 316L (N) Stainless Steel Joints," *Journal of Materials Science Research,* vol. 2, p. p124, 2012.

[179] Tang, W. and Wang Y., "Fractal characterization of impact fracture surface of steel," *Applied Surface Science,* vol. 258, pp. 4777-4781, 2012.

[180] Hornbach, D.J., Prevéy, P.S., "The effect of prior cold work on tensile residual stress development in nuclear weldments," *Journal of Pressure Vessel Technology. Transactions of the ASME,* vol. 124, pp. 359-365, 2002.

[181] Turski, M., Bouchard, P.J., Smith, M., Edwards, L., Withers, P.J., "Spatially resolved materials property data from a cross-weld tensile test," *Journal of Pressure Vessel Technology. Transactions of the ASME,* vol. 131, pp. 1-7, 2009.

[182] Katayama, Y., Tsubota M., and Saito Y., "Effect of the plastic strain level quantified by EBSP method on the stress corrosion cracking of L-grade stainless steels," in *12th International Conference on Environmental Degradation of Materials in Nuclear Power System–Water Reactors,* Salt Lake City, Utah, August 14–18, 2005, pp. 31-36.

[183] Weeks, J.R., Vyas, B.,Isaacs, H.S., "Environmental factors influencing stress corrosion cracking in boiling water reactors," *Corrosion science,* vol. 25, pp. 757-768, 1985.

[184] Radaj, D., "Heat effects of welding: temperature field, residual stress, distortion," *Recherche,* vol. 67, p. 02, 1992.

[185] Withers, P.J., "Residual stress and its role in failure," *Reports on Progress in Physics,* vol. 70, p. 2211, 2007.

[186] Zhang, Y., Pratihar, S., Fitzpatrick, M.E., Edwards, L., "Residual stress mapping in welds using the contour method," *Materials Science Forum,* vol. 490, pp. 294-299, 2005.

[187] Cheng, X., Fisher, J.W., Prask, H.J., Gnäupel, T., Yen, B.T. Roy, S., "Residual stress modification by post-weld treatment and its beneficial effect on fatigue strength of welded structures," *International Journal of fatigue,* vol. 25, pp. 1259-1269, 2003.

[188] Francis, J.A., Bhadeshia, H. K. H. and Withers, P.J. , "Welding residual stresses in ferritic power plant steels," *Materials Science and technology,* vol. 23, pp. 1009-1020, 2007.

[189] Yoshinori, K., Tsubota, M., Saito,Y. , "Combination of Cold Work and Heat Treatment on Stress Corrosion Cracking Susceptibility of L-Grade Stainless Steel," *Corrosion* pp. 1-13, 2003 , paper No. 03665.

[190] Zhuang, W.Z., Halford, G. R., "Investigation of residual stress relaxation under cyclic load," *International Journal of fatigue,* vol. 23, Supplement 1, pp. 31-37, 2001.

[191] Bang, H.S., Kim Y.C., and Oh I.H., "A study on mechanical and microstructure characteristics of the STS304L butt joints using hybrid CO2 laser-gas metal arc welding," *Materials & Design,* 2010.

[192] Prime, M.B., "Cross-sectional mapping of residual stresses by measuring the surface contour after a cut," *Transections of AMSE, Journal of Engineering Materials and Technology,* vol. 123, pp. 162-168, 2001.

[193] Pagliaro, P., Prime, M.B., Swenson, H., Zuccarello, B., "Measuring multiple residual-stress components using the contour method and multiple cuts," *Experimental mechanics,* vol. 50, pp. 187-194, 2010.

[194] Prime, M.B., Hughes, D. J., Webster, P. J., "Weld application of a new method for cross-sectional residual stress mapping," in *Proceedings of 2001 SEM Annual Conference on Experimental and Appplied Mechanics (Portland, OR),* 2001, pp. 608-611.

[195] Kartal, M.E., Liljedahl, C. M., Gungor, S., Edwards, L., Fitzpatrick, M. E., "Determination of the profile of the complete residual stress tensor in a VPPA weld using the multi-axial contour method," *Acta Materialia,* vol. 56, pp. 4417-4428, 2008.

[196] Withers, P.J., Turski, M., Edwards, L., Bouchard P.J., Buttle, D.J., "Recent advances in residual stress measurement," *International Journal of Pressure Vessels and Piping,* vol. 85, pp. 118-127, 2008.

[197] DeWald, A.T., Hill, M.R., "Multi-axial contour method for mapping residual stresses in continuously processed bodies," *Experimental mechanics,* vol. 46, pp. 473-490, 2006.

[198] Hosseinzadeh, F., Ledgard, P., Bouchard, P. J., "Controlling the Cut in Contour Residual Stress Measurements of Electron Beam Welded Ti-6Al-4V Alloy Plates," *Experimental mechanics,* vol. 53, pp. 829-839, 2013.

[199] Cheng, W., Finnie, I., Gremaud, M., Prime, M.B., "Measurement of near surface residual stresses using electric discharge wire machining," *Journal of engineering materials and technology,* vol. 116, pp. 1-7, 1994.

[200] Turski, M., Edwards, L., "Residual stress measurement of a 316l stainless steel bead-on-plate specimen utilising the contour method," *International Journal of Pressure Vessels and Piping,* vol. 86, pp. 126-131, 2009.

[201] Shin, S.H., "FEM analysis of plasticity-induced error on measurement of welding residual stress by the contour method," *Journal of mechanical science and technology,* vol. 19, pp. 1885-1890, 2005.

[202] Casavola, C., Pappalettere, C., Tursi, F., "Residual Stress on Ti6Al4V Hybrid and Laser Welded Joints," *Engineering Applications of Residual Stress,* vol. 8, pp. 111-118, 2011.

[203] Pirling, T.B., Giovanni. Withers, Philip J, "SALSA—A new instrument for strain imaging in engineering materials and components," *Materials Science and Engineering: A,* vol. 437, pp. 139-144, 2006.

[204] Mark, A.F., JA. Dai, H. Turski, M. Hurrell, PR. Bate, SK. Kornmeier, JR. Withers, PJ, "On the evolution of local material properties and residual stress in a three-pass SA508 steel weld," *Acta Materialia,* vol. 60, pp. 3268-3278, 2012.

[205] Hutchings, M.T.W., Philip J. Holden, Thomas M. Lorentzen, Torben, *Introduction to the characterization of residual stress by neutron diffraction*: CRC Press, 2005.

[206] Ranjbarnodeh, E., Serajzadeh, S., Kokabi, A.H., Fischer, A., "Effect of welding parameters on residual stresses in dissimilar joint of stainless steel to carbon steel," *Journal of materials science,* vol. 46, pp. 3225-3232, 2011.

[207] Teng, T.L., Chang, P.H., Tseng,W.C., "Effect of welding sequences on residual stresses," *Computers & structures,* vol. 81, pp. 273-286, 2003.

[208] Sudnik, W., Radaj, D., Erofeew, W., "Computerized simulation of laser beam welding, modelling and verification," *Journal of Physics D: Applied Physics,* vol. 29, p. 2811, 1996.

[209] Hodgson, D., Gill,C., Pellereau, B., Hurrell, P., Mark, A., "Simulation of Multi-Pass Welds Using ABAQUS 2D Weld GUI and Comparison with Experimental Results," 2011.

[210] Dong, P., "Residual Stress Analyses of a Multi-Pass Girth Weld: 3-D Special Shell Versus Axisymmetric Models," *Journal of Pressure Vessel Technology,* vol. 123, pp. 207-213, 2000.

[211] Shanmugam, N.S., Buvanashekaran, G., Sankaranarayanasamy, K., Manonmani, K., "Some studies on temperature profiles in AISI 304 stainless steel sheet during laser beam welding using FE simulation," *The International Journal of Advanced Manufacturing Technology,* vol. 43, pp. 78-94, 2009.

[212] Balasubramanian, K.R., Siva S. N., Buvanashekaran, G., Sankaranarayanasamy, K., "Numerical and experimental investigation of laser beam welding of AISI 304 stainless steel sheet," *Adv Prod Eng Manage J,* vol. 3, pp. 93-105, 2008.

[213] Chandrasekhar, N., Vasudevan, M., Bhaduri, A.K., Jayakumar, T., "Intelligent modeling for estimating weld bead width and depth of penetration from infra-red thermal images of the weld pool," *Journal of Intelligent Manufacturing,* pp. 1-13, 2013.

[214] Yang, Z.G., Paxton, D.M.,Weil, K.,Stevenson, J.,Singh, P., *Materials Properties Database for Selection of High-Temperature Alloys and Concepts*

***of Alloy Design for SOFC Applications*: Pacific Northwest National Laboratory Richland, WA, 2002.**

[215] Lu, B., Chen Z., Luo J., Patchett B., and Xu Z., "Pitting and stress corrosion cracking behavior in welded austenitic stainless steel," *Electrochimica acta,* vol. 50, pp. 1391-1403, 2005.

[216] Marshall, P. and Gooch T., "Effect of composition on corrosion resistance of high-alloy austenitic stainless steel weld metals," *Corrosion,* vol. 49, pp. 514-526, 1993.

[217] scheel, J. (2010), Eliminating Stress Corrosion Cracking in Stainless Steels - *MFN Metal Finishing News Vol. 11*. Available: http://www.mfn.li/article/?id=898. 4/2013

[218] NACE. (2010), Stress corrosion cracking Available: http://events.nace.org/library/corrosion/Forms/scc.asp. 12/2012

[219] John, H. (2009), Low-Plasticity Burnishing *NASA Tech Briefs*. Available: http://www.techbriefs.com/index.php?option=com_staticxt&staticfile=Briefs/Aug02/LEW17188.html. 6/2012

[220] Parvathavarthini, N., Subbarao, R.V., Dayal, R.K., Khatak, H.S., Kumar, S., "Elimination of intergranular corrosion susceptibility of cold-worked and sensitized AlSl 316 SS by laser surface melting," *Journal of materials engineering and performance,* vol. 10, pp. 5-13, 2001.

[221] Syed, S., "Atmospheric corrosion of materials," *Emirates Journal for Engineering Research,* vol. 11, pp. 1-24, 2006.

[222] Ryan, M.P., Williams, D.E., Chater, R.J., Hutton, B.M., McPhail, D.S., "Why stainless steel corrodes," *Nature,* vol. 415, pp. 470-474, 2002.

[223] Frankel, G., "Pitting corrosion of metals a review of the critical factors," *Journal of the Electrochemical Society,* vol. 145, pp. 2186-2198, 1998.

[224] Mahmood, K., Stevens N., and Pinkerton A.J., "Laser surface modification using Inconel 617 machining swarf as coating material," *Journal of Materials Processing Technology,* vol. 212, pp. 1271-1280, 2012.

[225] Guerre, C., Raquet, O., Herms, E. Le Calvar, M., Turluer, G., "SCC growth behavior of austenitic stainless steels in PWR primary water conditions," in *Proc. 12th Int. Conf. Environmental Degradation of Materials in Nuclear Systems, Salt Lake City*, 2005.

[226] Speidel, M.O., Magdowski,R., "Stress corrosion cracking of stabilized austenitic stainless steels in various types of nuclear power plants," in *Proc. 9th Int. Symp. on Environmental Degradation of Materials in Nuclear Power Systems—Water Reactors, eds. FP Ford, SM Bruemmer, GS Was (Warrendale, PA: Metallurgical Society of The American Institute of Mining, Metallurgical, and Petroleum Engineers [AIME], 1999)*, 1999, p. 325.

[227] ASTM.G129-00, "Standard Practice for Slow Strain Rate Testing to Evaluate the Susceptibility of Metallic Materials to Environmentally Assisted Cracking," 2004.

[228] Haruna, T., Shibata, T., "Initiation and growth of stress corrosion cracks in type 316L stainless steel during slow strain rate testing," *Corrosion,* vol. 50, pp. 785-791, 1994.

[229] Robertson, J., "The mechanism of high temperature aqueous corrosion of steel," *Corrosion science,* vol. 29, pp. 1275-1291, 1989.

[230] Nelis, T. and Pallosi J., "Glow discharge as a tool for surface and interface analysis," *Applied Spectroscopy Reviews,* vol. 41, pp. 227-258, 2006.